Civil
Engineering
Infrastructures
Journal

CEIJ

Available online at
http://ceij.ut.ac.ir/

Civil Engineering Infrastructures Journal (CEIJ)
Semiannual Publication

CONTENTS
Volume 55, Number 2, December 2022

Economic Analysis and Economic Leakage Level in Water Loss Management and Paths for Future Evaluation: A Review

Firat, M.[1]* , Ateş, A.[2] , Yılmaz, S.[3] and Özdemir, Ö.[4]

[1] Professor, Inonu University, Civil Engineering Department, Malatya, Türkiye
[2] Associate Professor, Inonu University, Computer Engineering Department, Malatya, Türkiye
[3] Assistant Professor, Çankırı Karatekin University, Civil Engineering Department, Çankırı, Türkiye
[4] Associate Professor, Kayseri Water and Sewerage Administration, Kayseri, Türkiye

ABSTRACT: Operational and investment costs increase due to aging of the network, increasing the failure rate, leakage and the water demand, new investments and energy consumption. Several methods and tools with different initial investment and operating costs are proposed for reducing water losses in the related literature. The aim of this study is to make detailed evaluations within the framework of economic components for effective and sustainable water loss management and provide a reference for further studies. The most important advantage is that there has not been a detailed assessment and discussion in this context within the framework of economic analysis and the economic leakage level. The methods and tools for reducing the water losses such as district metered areas, passive leakage control, active leakage control, pressure management, pipe management and network renewal methods, were evaluated economically and discussed. The most important issues in water loss management are the definition of the economic leakage level and the cost components that are the maintenance and break repair, methods applied to detect and control the leaks and automation systems for monitoring, control and data transfer. Moreover, the priority, suitability, applicability and economic impact of the methods should be considered to decide the methods for more efficient use of resources.

Keywords: Economic Analysis, Economic Level of Leakage, Water Distribution System, Water Loss.

1. Introduction

In urban water management, the increasing in failures and leaks, aging of the network, decreasing in useful life, excessive water demand, and insufficient capacity of the existing system increase operational and maintenance costs. In addition, the initial installation and operational and maintenance costs of the methods and tools used for reducing and monitoring the water losses in many utilities also reach significant levels. For this reason, it is crucial to carry out economic analysis and

---

* Corresponding author E-mail: mahmut.firat@inonu.edu.tr

elaborate the benefits and cost assessments of the Water Loss Management (WLM) components in terms of effective and sustainable management. In the literature, the cost and benefits and economic effects of the water loss management methods and tools are analyzed and evaluated (Fanner and Lambert, 2009; Lambert et al., 1999). These studies have focused on planning and applying the Pressure Management (PM) (Gomes et al., 2011; Creaco and Walski, 2017), defining the District Metered Areas (DMA) (Ferrari and Savic, 2015; Campbell et al., 2016; di Nardo et al., 2017), planning the Active Leakage Control (ALC) (Lambert et al., 1999; Berardi et al., 2016; Cabral et al., 2019; Lipiwattanakarn et al., 2019), reduction of failure rate, passive leakage control, asset management (Deidda et al., 2014; Farley and Liemberger, 2005; Loganathan et al., 2002; Suribabu and Neelakantan, 2012; Tricarico et al., 2006). Barandouzi and Kerachian (2016) proposed a methodology based on Probabilistic Support Vector Machines (PSVMs) for identifying the contamination source location in WDSs. The efficiency and versatility of the proposed methodology were examined using the available data and information from water distribution network of the City of Arak in the western part of Iran. In general, specific targets are defined for the Non-Revenue Water (NRW) rate and significant investments are made to achieve these targets. However, in many cases, these investments are not economic since they are not supported by Cost-Benefit Analysis (CBA). The main reason can be explained as; water losses are dependent on many factors that are the physical, operational, hydraulic and environmental variables, and the intervention and prevention method is not chosen considering the current conditions of each system. Therefore, the current condition of the system should be considered in the management of the water losses and the Economic Leakage Level (ELL) should be defined for selecting the most appropriate of prevention strategy

(Haider et al., 2019; Lambert and Lalonde, 2005; Molinos-Senante et al., 2016). Deidda et al. (2014) define the ELL is that a balance between the costs of water saved and the marginal costs of an additional reduction from leakage. This idea was used for a reference area in order to intervene the system in large WDSs. During the development of the most appropriate renewal strategy to reduce leakage levels in WDSs, a balance should be provided between the ELL, the marginal benefits of saved water and operating/investment costs.

The aim of this study is to make detailed evaluations within the framework of economic components for effective, efficient and sustainable urban water management and prevention activities applied in managing the water losses. The most important advantage of this study is economic assessment of water loss prevention methods which are evaluated and discussed under the ELL concept. For this purpose, the water loss management methods and tools such as ELL calculation, the district metered areas, passive leakage control and network maintenance, ALC, PM, asset management and network renewal, automation systems for monitoring and database, are evaluated economically and discussed by considering the current literature.

2. Economic Components in Water Loss Management

Leakage occurs in water transmission and distribution systems due to physical, environmental, operational and hydraulic factors and indirectly causes significant economic impacts for the utilities. Apparent losses including the volume of unbilled water, constitute the direct loss of revenue for the utilities. The economic impacts of NRW are (Lambert and Lalonde, 2005; May, 1994): i) leakage cost; ii) maintenance and repair costs of failures; iii) energy cost; iv) new resource cost' and v) apparent losses cost. Several methods and tools that are establishment and monitoring of water

balance, DMA definition, customer management, PM, Minimum Night Flow (MNF) analysis, factor analysis for failures, asset management, Geographical Information System (GIS), Supervisory Control and Data Acquisition (SCADA), customer management, automation systems, are applied in WLM.

The following issues should be considered in the selection of methods order to use technical, economic and available resources more efficiently; i) priority, suitability, applicability, economic impact of the selected methods; ii) current status of the personnel, economic, technical in the utility; iii) device, automation, data transfer, operational and maintenance cost; and iv) the maintenance costs and expected benefits from the selected methods. Therefore, in this study, detailed analysis and evaluations were made within the framework of economic components for the methods and tools applied in WLM.

2.1. Passive Leakage Control

The pipe breaks density in the system increases due to the decrease in the resistance of pipes against environmental, hydraulic and operational factors (Farley et al., 2008). The increasing in the break rate leads to increasing in the cost of operating, repairing and maintenance. Moreover, the frequency of water interruptions for repairing the pipes increases and customer satisfaction level decreases and the operating conditions of the system deteriorate. Several factors such as fluctuations and variations in operating

pressure, pipe age, material fatigue and environmental factors have effect on failure rate (Islam and Babel, 2013). Reducing the failure repairing time and performing repair and maintenance activities in a shorter time and reducing personnel expenses, failure management system and establishing the appropriate teams make significant contributions in order to reduce the leakage costs. Loganathan et al. (2002) defined failure threshold rate for operating the system and the failure management in WDS by considering the costs of the maintenance, repair and renovation and inflation rate.

A significant relationship between pipe diameter and failure threshold value based on cost analysis was defined. Farley and Liemberger (2005) reported that the existing systems in developing countries are weaker in terms of technological and current condition than developed countries and the water loss reduction methods should be developed specifically for the systems. Wang et al. (2009) used the annual break rate as the main criterion for the determination of the current status of the network and proposed that the administrations should evaluate the maintenance, renewal or replacement activities and determine the priority by evaluating the status of the existing pipes with the limited budgets. Tricarico et al. (2006) conducted a cost-based study highlighting hydraulic reliability for the rehabilitation of WDSs where the frequency of failure is high. In this context, a network operating model was proposed based on the lowest cost and maximum benefit approach.

(a)

(b)

(c)

(d)
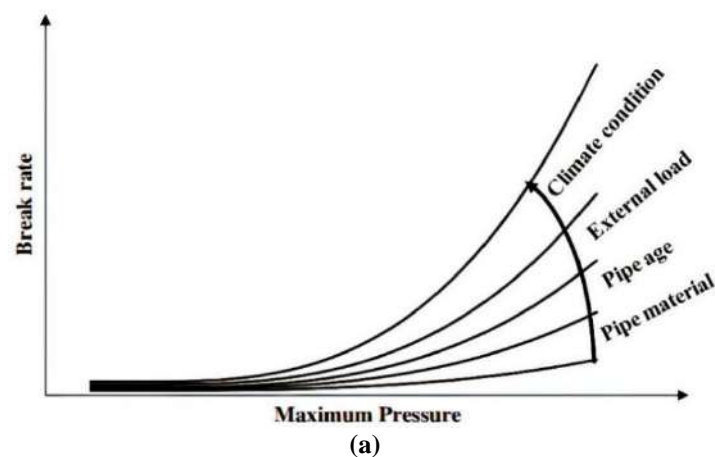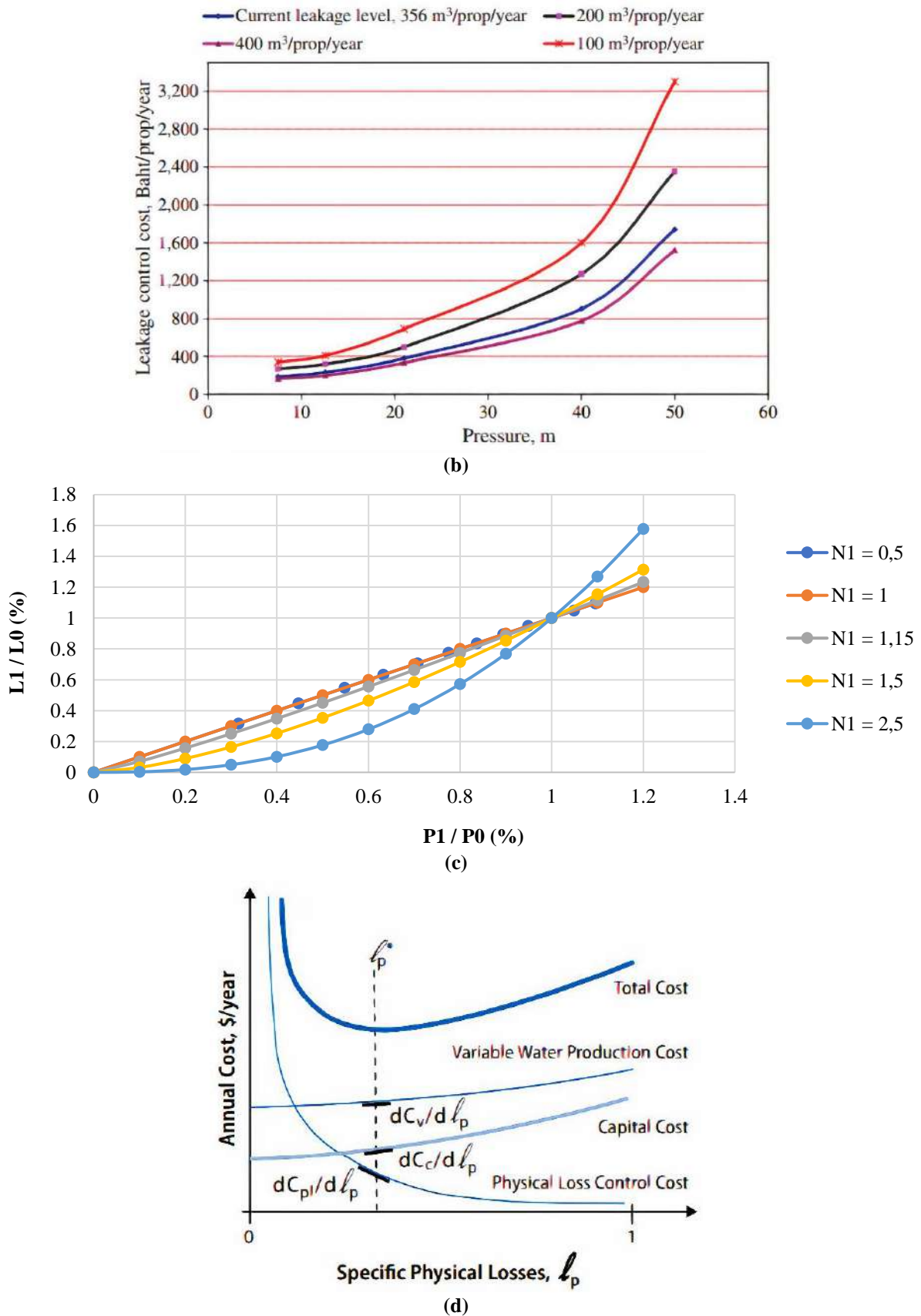
Fig. 1. a) Hypothetical shapes of break rate functions influenced by factors contributing to pipe breaks (Ghorbanian, Guo and Karney, 2016); b) Cost of active leakage control with pressure for different leakage levels (Islam and Babel, 2013); c) Pressure-leakage relationship for different coefficients N1 (May, 1994); and d) Optimality condition for physical losses (Wyatt, 2010)

Ghorbanian et al. (2016) focused that the pressure, pipe type, pipe age, external load, climatic conditions are effective on the failure rate of the pipe (Figure 1a). Suribabu and Neelakantan (2012) emphasized the necessity for economic analysis during the design and operation of WDSs. A performance-oriented model was developed and proposed by considering the maintenance and repair costs during the useful life of the designed networks. According to Zamenian et al. *(2017)*, the failures in WDSs cause significant water losses as well as significant social, economic and environmental impacts, and have significant impacts on energy consumption and cost, particularly in systems where water is delivered by pumps. For this reason, development of the strategic asset management plans was proposed to determine the potential damage of the pipes, evaluate the current situation, estimate the failure rate and prioritize the regions to be renovated.

2.2. District Metered Areas

Monitoring, controlling and implementing an effective water loss strategy in a large and complex WDS is time-consuming and costly. For this reason, the DMA approach was firstly planned and applied by International Water Association (IWA) in England in 1980. The DMA is a region where boundaries are precisely defined, usually have an inlet and are separated from other regions by isolation valves to control water losses (Farley et al., 2008). The DMA provides important contributions in the successful implementation of tools and methods such as minimum MNF, leak detection, customer management, and passive leakage control to reduce water losses (Gomes et al., 2013). The most appropriate size and number of the DMA should be determined by considering the main length, the number of service connections and making economic analysis (Lambert and Morrison, 1996).

Although the small size of the DMA provides an advantage in terms of managing the water loss components and controlling the system, the costs of the device-equipment, workmanship for isolation and field works and data transfer will increase. On the other hand, in the case of large planning, the investment and operating costs will be reduced while the operational components will be difficult as the size of the system components will increase (Farley et al., 2008). However, the following issues and field works can cause significant costs: i) determination of the number and location for isolation valves and identification of boundaries; and ii) room construction for flow-meter and pressure valves at DMA entrance, purchase and installation of flow-meters and pressure gauges and automation systems.

Gomes et al. (2013) emphasized that economic conditions and assessments are crucial parameters for planning and defining the boundaries of the DMAs in WDSs. In the study, an algorithm was proposed for minimization of the total cost and maximization of the benefit during the creation of DMA. Thus, the ELL is determined for DMA planning and implementation. Ferrari and Savic (2015) proposed that the expected benefits from the DMA (reduction of leakage and failures, reduction of energy and water consumption and efficiency) should be analyzed and evaluated under the economical perspective for planning and implementation DMA. Significant economic benefits in terms of pressure-dependent consumption reduction, failure frequency and leakage reduction was obtained by applying the efficiency analysis for DMA. As a result, the cost-benefit analysis and an economic performance evaluation framework was provided for comparing different DMA schemes and identification of the best solution from different options.

Kanakoudis and Gonelas (2015) expressed that the most important component for reducing the NRW rate is estimation of the ELL which is basically defined based on network conditions, pressure, NRW rate, consumption, water

price and water production cost etc. Campbell et al. (2016) analyzed the benefits of the DMA methodology in terms of economic and control capability in WDSs. Genetic algorithm based model was developed and the most suitable options for the practitioner were defined for determination of the usage places and number of isolation valves and flow-meters in the most appropriate way. According to di Nardo et al. (2017), the DMA planning is quite complex and therefore the system should be analyzed in detail in terms of hydraulic, economic and topological aspects. An algorithm was developed by considering the economic and energy components for determining the boundaries of isolated zones and the locations of the devices to measure the hydraulic parameters. The developed algorithm aims for minimization of the operating costs by using the least possible flow-meter and simplifies the calculation of water balance by improving the hydraulic performance.

2.3. Active Leakage Control

In WDSs, the recoverable leakage volume, system operating and water production costs increase due to the awareness, recognizing and locating time the unreported leakages which is a significant part of leaks. The ALC strategy including awareness of these leakages, locating, repairing and preventing activities, plays an important role in reducing the volume of leakage (Lambert and Lalonde, 2005; Farley et al., 2008; Islam and Babel, 2013). However, in order to obtain benefits from the ALC method, it is very important to create isolated zones, monitor the minimum night flow and determine the recoverable leakage volume. In ALC methodology, leak location should be determined with devices and equipment such as ground microphone, regional recorder, and regional correlator. However, the costs of devices and equipment with different characteristics, sensitivities and prices are quite important component (Suribabu and Neelakantan, 2012;

Kanakoudis and Gonelas, 2015; Zamenian et al., 2017; Cabral et al., 2019). Lambert et al. (1999) stated that ALC plays an important role in leakage management, and the cost-benefit analysis should be performed for ALC works during the definition of ELL. Li et al. (2015) examined the methods and devices used for detection and location of the leakages, and evaluated the advantages, disadvantages and costs of the methods. The working ranges of the ground microphones with low operating cost are between 200 to 500 m. The accuracy rate of this device is low and the efficiency is dependent on the personnel experience. On the other hand, regional noise logger and correlator equipment has a scanning range of up to 2000 m and automatic detection with high accuracy, whereas these devices cost were high.

Fantozzi (2006) pointed that ALC has an important role in the reduction and control of water losses as a result of technological developments. An approach is proposed by considering the water cost, intervention cost and the natural degradation rate of the network to determine economically the frequency of intervention for ALC method. Islam and Babel (2013) emphasized that the total costs including the system operating and water production should be considered to determine the ELL (Figure 1b). It was argued that the cost of ALC method depends on the duration of the screening and inspection activities which include the cost of inspection activities (leak detection and detection in the field with devices) and the break repair. Berardi et al. (2016) stated the importance of faster detection and repairing of unreported leakages due to the implementation of ALC for reduction of water losses.

It is argued that the implementation of the ALC strategy will reduce the operating costs and potential damage of the failures and leakages and provide the significant benefits. Lipiwattanakarn et al. (2019) analyzed the effects of leakage prevention and reduction on energy and system operating costs. After the repair of the

leakages in the DMA, the inlet flow rate was decreased by 9% and the system input energy was reduced by 8% and the efficiency of the system was improved with ALC. Moslehi et al. (2020a) proposed a methodology based on the field data for the short-run economic leakage level with respect to ALC method. The proposed methodology was applied to a large WDS and the short-run ELL was estimated to be 27 m^3/service connection/year based on the current ALC policy and operating pressure.

2.4. Pressure Management

The system operating pressure is an effective parameter in the occurrence of new reported or unreported failures or leakage rate per unit time in existing failures in WDS (Farley et al., 2008). May (1994) developed a function between the leakage and pressure based on direct measurements for pipes with different diameters (Figure 1c). Lambert and Morrison (1996) developed a model, background and burst estimates (BABE) that calculates standard failure frequencies and flow rates for background losses. The fixed and varied area discharge (FAVAD) method was proposed as the most basic and widely used approach that expresses a relationship between leakage flow and failure rate with operating pressure (Lambert et al., 1999). PM contributes significantly to the reduction of leakage volume in existing failures, reduction of the risk of new leaks, extending the economic life of the pipe and reduction of operating and initial investment cost (Fanner and Lambert, 2009). Tabesh et al. (2011) proposed a demand-driven and pressure-based hydraulic design model by using the genetic algorithm. Authors expressed that more realistic data can be obtained by integrating possible leakages into hydraulic systems. However, components that are the room construction, device and equipment selection and placement, and automation system for monitoring the data, constitute significant costs.

Therefore, before applying PM in a system, answering the following questions is very important for system efficiency under the economic aspects (Kanakoudis and Gonelas, 2015): i) Is PM required? Is it applicable? What are the expected benefits?; ii) Is there information about network behavior, customer water demand characteristics? Has the hydraulic model been simulated? and iii) Have the cost components, equipment, installation, workmanship, and field work costs been determined? Has the CBA been performed?

Gomes et al. (2011) stated that the failure frequency and leakages can be reduced by applying PM. Consequently, the water production and transmission costs could be decreased. Moreover, it was determined that effect of PM on decreasing water consumption is very low. Thornton and Lambert (2007) investigated the benefits of PM in WDS. Firstly, pressure zones were established in the network then appropriate PRV was selected. It was stated that if a successful system is installed, the number of failures and instant water loss values will decrease. Creaco and Walski (2017) implemented an active pressure control strategy to reduce leakage and losses and analyzed the economic outcomes by comparing the results of the conventional and remote controlled PRVs. The results showed that active pressure control is not needed in areas where leakage level is low and maintenance and operating costs are low.

The remote controlled pressure control systems are more suitable in complex and large systems. Fontana et al. (2018) proposed a real-time pressure control system for the prevention and reduction of leaks. It was expressed that real-time pressure control provides significant gains in reducing the minimum night flow rate, minimizing pressure fluctuations and regulating pressure. Moslehi et al. (2020b) presented an economic evaluation framework to support the decision-making process relating to alternative PM schemes. The methodology was applied to a DMA by changing the existing fixed–outlet to time-

based (TM-PRV) and flow-based modulation.

2.5. Network Renewal and Asset Management

The network renewal method, which creates a very high cost for reduction the water losses, is preferred primarily in many cases. Therefore, in a WDS firstly, the parameters that are current failure rates, the costs of the network operating, maintenance and repair, new water resource and energy and initial investment in current conditions should be considered. Moreover, in case of network renewal, medium and long term operational costs should be also analyzed (Kanakoudis and Gonelas, 2015).

Since the cost of pipe material, workmanship and construction are at very high levels, detailed cost-benefit analysis and alternatives should be evaluated before the network renewal approach. Therefore, ALC and other reduction methods for WLM should be firstly implemented and monitored then priority regions in network renewal should be identified to reduce the initial investment costs (Suribabu and Neelakantan, 2012). Tricarico et al. (2006) proposed two factors that are reducing costs and maximizing hydraulic reliability which should be considered for the design of WDSs. In this context, the reliability of all points in the system to reach expected minimum pressure required to meet every hour of the day, while the amount of unsold water and losses are evaluated economically.

Wu et al. (2010) analyzed the pipe failure records to determine the network leakage rate in WDSs, and presented a curve representing the relationship between pipe ages and leakage amount. The ELL was determined by calculating the optimum replacement period and costs for the pipes. Romaniuk (2016) carried out Monte Carlo simulation for different material and failure records to provide a reference in obtaining maintenance costs. Zangenehmadar and Moselhi (2016) developed a model for estimating the remaining useful life of pipes

as well as predicting the degradation rates. According to existing literature studies, generally the concept of useful life for networks is widely studied topic. This concept is quite important in cases where network leakage control cannot be economically managed by network repair, maintenance activities, pressure management or other basic methods. In other words, in cases where the cost spent per unit pipe to operate the network is greater than the cost spent to replace the pipe, it can be evaluated as having completed its useful life for the network. Shahangian et al. (2019) analyzed the effects of flow hydraulics, pipe structure (particularly elastic behavior) and submerged jet on leak behavior based on the numerical and experimental study. The results Showed that the leakage exponent is close to the theoretical value of 0.5, considering the effect of pressure head on leak area behavior.

3. Economic Leakage Level

The methods applied to reduce and control water losses cause direct economic costs for utilities. In order to reduce leakages, four basic methods (PM, asset management, ALC and failure repair speed and quality), which require the detailed information about the current network conditions and technological tools have been used (Lambert et al., 1999). In WDSs, PRV or new water tanks are required for pressure management. The state-of-the-art equipment such as acoustic listening and regional monitoring devices are needed for active leak control. In this case, a new problem arises for utilities is that will there be a financial return to the utility for the expenditures to reduce water loss? In order to answer this question, the utilities should determine the optimal level of leakages based on the current network conditions. The most important issue in WLM and managing leakages is defining the ELL (Islam and Babel, 2013; Haider et al., 2019). For this aim, making a regional

based evaluation and considering the current network and economic conditions, local costs, benefits, engineering parameters and other factors rather than universal assumptions will provide a more realistic approach (Deidda et al., 2014). The ELL can be changed with system characteristics such as water production and operating costs, type of transmission (pump-fed and treated or gravity-fed and non-treated). Therefore, the ELL should be calculated by considering the status of the existing network. Since the network conditions will not remain the same during this time, the ELL will also vary. Therefore, deterioration rates in the networks and materials used should be calculated as well as economic changes.

In defining the ELL, firstly, the leakage reduction methods should be well understood and analyzed. Each method will create a cost and benefit due to the current condition and characteristics of the network. Two different approaches were proposed in the literature, namely Short-Run (SRELL) and Long-Run ELL (LRELL). SRELL is considered to be the ELL that should be reached at the current pressure. In the SRELL theory, the ELL is generally evaluated on the whole system. For this reason, making separate calculations for different pressure zones provides an advantage in determining the economic level (Lambert and Lalonde, 2005). On the other hand, the LRELL includes less theoretical assumptions in dealing with leaks and several basic parameters that are the pressure management, network rehabilitation, team number optimization are considered. The LRELL will be more useful for utilities in the framework of long-run planning. In the LRELL methodology, four methods used in leakage management are considered (Lambert and Lalonde 2005).

Rudolph (2008) argued that water losses should be assessed separately for developed and developing countries. It was emphasized that the water loss rate, which is 8% in Germany, can reach up to 90% in developing countries and the main reason for this is the difference between the budgets allocated for water management. The results demonstrated that 30% loss rate is economical in regions where water production and operation costs are low. Moreover, the economic repair level and the point where the lost water value is equal to the detection and repair cost, were was calculated as 6.9 m³/day/km. Wyatt (2010) defined the ELL as the point where the total amount spent to reduce water loss is equal to the slope of the unit production cost of water (Figure 1d). This optimum point is where the marginal utility of the leak is equal to the marginal costs of detection. For this purpose, three basic calculations were used: i) the cost of leakage directly proportional to the level of leakage; ii) the cost of detecting inversely proportional to the level of leakage; and iii) cost of repair independent of leakage level.

Lambert and Fantozzi (2005) proposed a practical and rapid approach for economic evaluation of financial and physical parameters to develop and implement an ALC strategy. In this context, marginal cost of water, cost of prevention method, leakage rate and related costs are considered. Fanner and Lambert (2009) presented a method for identifying and predicting the ELL by considering the main components of leakages. Islam and Babel (2013) emphasized that the most important component of the leak control strategy is the determination of the ELL which depends on network conditions, operating pressure, marginal water cost and all costs spent for leakage control. Molinos-Senante et al. (2016) envisaged that environmental and resource costs will be evaluated within the ELL. In the determination of the costs, the costs on which many parameters, such as the number of employees called shadow costs, and the number of interventions, are calculated. Considering the aforementioned studies, there is a need to establish a model that can take into account all technical and economic variables for the strategy to should be determined for struggling water

losses. As it is known, four basic components such as pressure management, ALC, improving fault repair speed-quality and asset management affect WLM. These four basic structures should be solved simultaneously in problem solving.

4. Conclusions

In this review, detailed literature review was conducted within the framework of economic components for effective, efficient and sustainable urban water management and prevention activities implemented for struggling water losses. Evaluations that can serve as a reference for subsequent studies are made and basically the following basic results are obtained:

- The economic analysis and elaboration of benefit-cost assessments (CBA) for both operational and water loss management (WLM) components of the system are very important for effective, efficient and sustainable management of the system.
- The main cost components that come to the forefront in WLM can be given as follows; the costs of leakage maintenance and repair of reported and unreported leakages, the cost of methods used for detection, control and prevention of unreported leakages, the costs of energy and searching for new water resources, and the cost of automation systems for monitoring, control and transfer of data.
- Deciding on methods for preventing, monitoring and controlling the water losses in order to use more efficiently for economic and infrastructure resources; the priority, suitability, applicability and economic impact of the method should be considered. Furthermore, it was emphasized that factors such as devices, automation systems, data transfer, operation and maintenance cost, expected benefit from the method, operating cost and possible costs on maintenance costs should be taken into consideration.

- The main and service connection failures in water distribution systems (WDSs) have significant social, economic and environmental effects, cause significant water losses and have significant effects on energy consumption especially in pump-fed systems. Therefore, it has come to the fore that it is necessary to determine the damage potential of the pipes, evaluate the current situation, estimate the failure rate, prioritize the regions in rehabilitation and formulate strategic asset management plans.
- The district metered areas (DMA) approach is widely used in water loss management and provides significant gains in the fight against unreported leaks. In addition, it is underlined that it provides important contributions for minimum night flow (MNF), acoustic leak detection, customer management, passive leakage control and other means-methods applied to prevent and reduce water losses. However, in addition to the benefits of the district metered areas, it was reported that system design and field productions constitute significant costs.
- The recoverable leakage volume increases due to awareness and locating periods of the unreported leaks, and system operating and water production costs also increase. It was emphasized that active leakage control (ALC) strategy, which includes awareness of these leaks, locating, repairing and preventing activities, plays an important role in reducing the volume of physical losses. It was reported that the ground microphones were in the range of 200-500 m in the inspection range and the accuracy percentage was low and the efficiency was dependent on the personnel experience, whereas they had a low operating cost. On the other hand, it was emphasized that regional noise logger and noise correlator equipment has a scanning range of up to 2000 m and automatic detection with high accuracy, whereas these devices are costly.
- The system operating pressure is

influential factor in the occurrence of reported or unreported breaks in water distribution systems and in increasing the leakage volume lost per unit time in existing breaks. By applying pressure management schemes, the benefits can be obtained the reduction of leakage volume in existing faults, the reduction of the risk of new failures and new leakages, the reduction of the volume of water consumed per unit and the prolongation of the pipe's economic life.

- Defining the economic leakage level (ELL) is the most important issue in water loss management and fight against leaks. While determining this level, it was emphasized that making a regional based evaluation and taking into consideration the current network condition, economic conditions, local costs, benefits, engineering parameters and other factors rather than universal assumptions will provide a more realistic approach.

As a result, in the light of the examinations and evaluations carried out in detail in the previous parts of the paper, according to indicated literature survey: there are methods with different characteristics and costs in water loss management, the importance of economic analysis in deciding these methods, choosing suitable and applicable method according to the current system conditions and defining the economic leakage level. In the following studies, it is thought that the economic analysis of the economic effects of water loss components, defining the detailed benefit and cost standards for the methods to be applied for the prevention of the components, the determination of the optimum leak level and optimization and the use of mathematical based models will make important contributions in the determination of the economic leakage level.

List of Abbreviations

WLM	Water Loss Management
PM	Pressure Management
DMA	District Metered Areas
ALC	Active Leakage Control
NRW	Non-Revenue Water
CBA	Cost-Benefit Analysis
ELL	Economic Leakage Level
WDS	Water Distribution System
SCADA	Supervisory Control and Data Acquisition
GIS	Geographical Information System
IWA	International Water Association
MNF	Minimum Night Flow
AWWA	American Water Work Association
BABE	Background And Burst Estimates
FAVAD	Fixed And Varied Area Discharge
PRV	Pressure Reduction Valve
TM-PRV	Time-Based Pressure Reduction Valve
LRELL	Long-run Economic Leakage Level
SRELL	Short-run Economic Leakage Level

5. Acknowledgement

6. References

N.W.C. (NWC). (1980). *Leakage control policy and practice*, NWC Technical Working Group on Waste of Water Publication, London.

Agathokleous, A. and Christodoulou, S. (2017). "Component-holistic condition assessment of water distribution networks", *Journal of Water Supply: Research and Technology,* AQUA, 64(7), 509-519.

Al-Aghbar, A. (2005). *Automated selected trenchless technology for the rehabilitation of water mains*, M.Sc. Thesis, Concordia University, Canada.

Al-Ghamdi, A.S. (2011). "Leakage-pressure relationship and leakage detection in intermittent water distribution systems", *Research and Technology,* AQUA, 60(3), 178-183.

AL-Washali, T., Sharma, S. and Kennedy, M. (2016). "Methods of assessment of water losses in water supply systems: A review", *Water Resources Management*, 30(14), 4985-5001.

Al-Zahrani, M. Abo-Monasar, A. and Sadiq, R. (2016). "Risk-based prioritization of water main failure using fuzzy synthetic evaluation technique", *Journal of Water Supply: Research and Technology,* AQUA, 65(2), 145-161.

Alvisi, S., Luciani, C. and Franchini, M. (2019). "Using water consumption smart metering for water loss assessment in a DMA: A case study",

Urban Water Journal, 18(1), 77-83.

Berardi, L., Laucelli, D.B., Simone, A., Mazzolani, G. and Giustolisi, O. (2016). "Active leakage control with WDNetXL", *Procedia Engineering*, 154, 62-70.

Cabral, M., Loureiro, D., Almeida, M.D.C. and Covas, D., (2019). "Estimation of costs for monitoring urban water and wastewater networks", *Journal of Water Supply: Research and Technology,* AQUA, 68(2), 87-97.

Cabrera, E., Pardo, M.A. and Arregui, F.J. (2013). "Tap water costs and service sustainability, A close relationship", *Water Resources Management*, 27(1), 239-253.

Campbell, E., Izquierdo, J., Montalvo, I. and Pérez-García, R. (2016). "A novel water supply network sectorization methodology based on a complete economic analysis, including uncertainties", *Water (Switzerland)*, 8(5), 179.

Candelieri, A., Soldi, D. and Archetti, F. (2015). "Cost-effective sensors placement and leak localization, The Neptun pilot of the ICeWater Project.", *Journal of Water Supply: Research and Technology,* AQUA, 64(5), 567-582.

Charalambous, B. and Kanellopoulou, S. (2010). "Applied pressure management techniques to reduce and vontrol leakage", *Proceedings of the IWA International Specialised Conference 'Water Loss 2010'*, 1-12.

Christodoulou, S. and Deligianni, A. (2009). "A neurofuzzy decision framework for the management of water distribution networks", *Water Resources Management*, 24, 139-156.

Creaco, E. and Walski, T. (2017). "Economic analysis of pressure control for leakage and pipe burst reduction', *Journal of Water Resources Planning and Management*, 143(12), 1-11.

Deidda, D., Sechi, G.M. and Zucca, R. (2014). "Finding economic optimality in leakage reduction: A cost-simulation approach for complex urban supply systems', *Procedia Engineering*, 70, 477-486.

De Paola, F., Galdiero, E. and Giugni, M. (2016). "A jazz-based approach for optimal setting of pressure reducing valves in water distribution networks", *Engineering Optimization*, 48(5), 727-739.

Di Nardo, A., Di Natale, M., Giudicianni, C., Santonastaso, G.F., Tzatchkov, V. and Varela, J.M.R. (2017). "Economic and energy criteria for district meter areas design of water distribution networks", *Water (Switzerland)*, 9(7), 1-13.

Fallis, P., Hübschen, K., Oertle, E., Ziegler, D., Klingel, P., Baader, J., Trujillo, R. and Laures, C. (2011). *Guidelines for water loss reduction*, Eschborn, Germany: Deutsche Gesellschaft für International Zusammenarbeit (GIZ), Germany, p. 236.

Fanner, P., Thornton, J., Liemberger, R. and Sturm, R. (2007). "Evaluating water loss and planning loss reduction strategies", *AWWA Research Foundation*, AWWA, Denver, USA; IWA, London, UK.

Fanner, P. and Lambert, A. (2009). "Calculating SRELL with pressure management, active leakage control and leak run-time options, with confidence limits", *Proceedings of WaterLoss 2009, IWA International Conference,* IWA Publishing, 373-380.

Fantozzi, M. (2006). "Some international experiences in promoting the recent advances in practical leakage management", *Water Practice and Technology*, 1(2), 1-10.

Farley, M., Wyeth, G., Ghazali, Z.B.M., Istandar, A., Sigh, S. (2008). "The manager's non-revenue water handbook, A guid to understanding water losses", *Ranhill Utility Bernhad and United States Agency for International Development (USAID)*, Washington DC.

Farley, M. and Liemberger, R. (2005). "Developing a non-revenue water reduction strategy: Planning and implementing the strategy", *Water Science and Technology: Water Supply*, 15(1), 41-50.

Farley, M. and Trow, S. (2003). *A practitioner's guide to assessment, monitoring and control*, IWA Publishing, ISBN 9781780402642, UK, p. 296.

Ferrari, G. and Savic, D. (2015). "Economic performance of DMAs in water distribution systems", *Procedia Engineering*, 119(1), 189-195.

Fontana, N., Giugni, M., Glielmo, L., Marini, G. and Zollo, R. (2018). "Real-time control of pressure for leakage reduction in water distribution network: Field experiments", *Journal of Water Resources Planning and Management*, 144(3), 1-12.

Francisque, A., Tesfamariam, S., Kabir, G., Haider, H., Reeder, A. and Sadiq, R. (2017). "Water mains renewal planning framework for small to medium sized water utilities: A life cycle cost analysis approach", *Urban Water Journal*, 14(5), 493-501.

Ghorbanian, V., Guo, Y. and Karney, B. (2016). "Field data-based methodology for estimating the expected pipe break rates of water distribution systems", *Journal of Water Resources Planning and Management*, 142(10), 1-11.

Giustolisi, O., Laucelli, D. and Savic, D.A. (2006). "Development of rehabilitation plans for water mains replacement considering risk and cost-benefit assessment", *Civil Engineering and Environmental Systems*, 23(3), 175-190.

Gomes, R., Marques, A.S.A. and Sousa, J. (2013). "District metered areas design under different decision makers' Options: Cost analysis", *Water Resources Management*, 27(13), 4527-4543.

Gomes, R., Marques, A.S. and Sousa, J. (2011). "Estimation of the benefits yielded by pressure

management in water distribution systems", *Urban Water Journal*, 8(2), 65-77.

Haider, H., Al-Salamah, I.S., Ghazaw, Y.M., Abdel-Maguid, R.H., Shafiquzzaman, M. and Ghumman, A.R. (2019). "Framework to establish economic level of leakage for intermittent water supplies in arid environments", *Journal of Water Resources Planning and Management*, 145(2), 1-12.

Hardeman S. (2008). "A cost-benefit analysis of leak detection and the potential of real water savings for New Mexico water systems", Water Resources Professional Project Report Albuquerque, NM: UNM Digital Repository, University of New Mexico.

Islam, M. S. and Babel, M. S. (2013). "Economic analysis of leakage in the Bangkok water distribution system", *Journal of Water Resources Planning and Management*, 139(2), 209-216.

Kanakoudis, V. and Gonelas, K. (2015). "Estimating the economic leakage level in a water distribution system", *Water Resources Management in a Changing World: Challenges and Opportunities*, Europan Water Resources Association (EWRA) Publications, Istanbul, Turkey, 1-7.

Kanakoudis, V. and Gonelas, K. (2016). "Non-revenue water reduction through pressure management in Kozani's water distribution network: from theory to practice", *Desalination and Water Treatment*, 57(25), 11436-11446.

Kim, E.S., Baek, C.W. and Kim, J.H. (2005). "Estimate of pipe deterioration and optimal scheduling of rehabilitation", *Water Science and Technology: Water Supply*, 5(2), 39-46.

Kleiner, Y., Adams, B.J. and Rogers, J.S. (1998). "Selection and scheduling of rehabilitation alternatives for water distribution systems", *Water Resources Research*, 34(8), 2053-2061.

Lambert, A. and Lalonde, A. (2005). "Using practical predictions of economic intervention drequency to calculate short-run economic leakage level, with or without pressure management", *Proceeding of the IWA Leakage 2005 Conference*, Halifax, Nova Scotia, Canada, 1-12.

Lambert, A. and Morrison, J.A.E. (1996). "Recent developments in application of "Bursts and Background Estimates" concepts for leakage management", *Journal of International Water and Environmental Management*, 10(2), 100-104.

Lambert, A.O., Brown, T.G., Takizawa, M. and Weimer, D. (1999). "A review of performance indicators for real losses from water supply systems", *Journal of Water Supply: Research and Technology, AQUA*, 48(6), 227-237.

Lambert, A.O. (2002). "International report: Water losses management and techniques", *Water Science and Technology: Water Supply*, 2(4), 1-

20.

Lambert, A.O. and Fantozzi, M. (2005). "Recent advances in calculating economic intervention frequency for active leakage control, and implications for calculation of economic leakage levels", *Water Science and Technology: Water Supply*, 5(6), 263-271.

Lambert, A.O. and Mckenzie, R. (2001). "Econoleak: Economic model for leakage management for water suppliers in South Africa", Pretoria, Republic of South Africa: South African Water Research Commission, 169(02).

Lambert, A. and Thornton, J. (2012). "Pressure-bursts relationships: Influence of pipe materials, validation of scheme results, and implications of extended asset life", *Water Loss 2012*, Manila, Philippines, 2-11.

Laucelli, D.B., Simone, A., Berardi, L., Giustolisi, O. (2017). "Optimal design of district metering areas for the reduction of leakages", *Journal of Water Resources Planning and Management*, 143(6), 04017017.

Lee, H., Kong, M. and Kang, S. (2015). "Economic evaluation of leak monitoring system in water supply system", 99, 71-74.

Li, R., Huang, H., Xin, K., Tao, T. (2015). "A review of methods for burst/leakage detection and location in water distribution systems", *Water Science and Technology: Water Supply*, 15(3), 429-441.

Frauendorfer, R., Liemberger, R. (2010). "The issues and challenges of reducing non-revenue water", Asian Development Bank, Manila, Philippines.

Liemberger, R., Kingdom, B. and Marin, P. (2006). "The challenge of reducing non-revenue water (NRW) in developing countries", *The World Bank, Water Supply and Sanitation Sector Board, PPIAF*, 8, 1-40.

Lim, E., Savic, D. and Kapelan, Z. (2015). "Development of a leakage target setting approach for South Korea based on economic level of leakage", *Procedia Engineering*, 119(1), 120-129.

Lipiwattanakarn, S., Kaewsang, S., Pornprommin, A. and Wongwiset, T. (2019). "Real benefits of leak repair and increasing the number of inlets to energy", *Water Science and Technology*, 14(3), 714–725.

Loganathan, G.V., Park, S. and Sherali, H.D. (2002). "Threshold break rate for pipeline replacement in water distribution systems", *Journal of Water Resources Planning and Management*, 128(4), 271-279.

Marchionni, V., Cabral, M., Amado, C. and Covas, D. (2016). "Estimating water supply infrastructure cost using regression techniques", *Journal of Water Resources Planning and Management*, 142(4), 04016003.

May, J. (1994). "Pressure dependent leakage; world water and environmental engineering", Water Environment Federation: Washington DC, USA.

Mesquita, A.M. and Ruiz, M. (2013). "A financial economic model for urban water pricing in Brazil", *Urban Water Journal*, 10(2), 85-96.

Molinos-Senante, M., Mocholí-Arce, M. and Sala-Garrido, R. (2016). "Estimating the environmental and resource costs of leakage in water distribution systems: A shadow price approach", *Science of the Total Environment*, 568, 180-188.

Mondaca, M., Andrade, M.A., Choi, C.Y. and Lansey, K.E. (2015). "Development of a cost function of water distribution systems for residential subdivisions", *Urban Water Journal*, 12(2), 145-153.

Morrison, J., Tooms, S. and Rogers, D. (2007). *District metered areas: Guidance notes*, IWA Water Loss Task Force; IWA Publishing: London, UK.

Moslehi, I., Jalili-Ghazizadeh, M., Yousefi-Khoshqalb, E. (2020). "Developing a framework for leakage target setting in water distribution networks from an economic perspective", *Structure and Infrastructure Engineering*, 17(6), 821-837.

Moslehi, I., Jalili-Ghazizadeh, M., Yousefi-Khoshqalb, E. (2020). "An economic valuation model for alternative pressure management schemes in water distribution networks", *Utilities Policy*, 67, 101129.

Muhammetoglu, A., Nursen, C., Karadirek, I.E. and Muhammetoglu, H. (2018). "Evaluation of performance and environmental benefits of a full-scale pump as turbine system in Antalya water distribution network", *Water Science and Technology: Water Supply*, 18(1), 130-142.

Mutikanga, H.M., Sharma, S.K. and Vairavamoorthy, K. (2013). "Methods and tools for managing losses in water distribution systems", *Journal of Water Resources Planning and Management*, 139(2), 166-174.

Neelakantan, T.R., Suribabu, C.R. and Lingireddy, S. (2008). "Pipe-sizing optimization including break-repair and replacement economics", *Water SA*, 34(2), 217-224.

Park, S.W. and Loganathan, G.V. (2002). "Methodology for economically optimal replacement of pipes in water distribution systems: 2. Applications", *KSCE Journal of Civil Engineering*, 6(4), 545-550.

Pearson, D. and Trow, S.W. (2005). "Calculating the Economic Levels of Leakage", *Proceeding of the IWA Leakage 2005 Conference*, Halifax, Nova Scotia, Canada, 294-309.

Puust, R., Kapelan, Z., Savic, D.A. and Koppel, T. (2009). "A review of methods for leakage management in pipe networks", *Urban Water Journal*, 7, 25-45.

Rahman, A. and Wu, Z.Y. (2018). "Multistep simulation-optimization modeling approach for partitioning water distribution system into district meter areas", *Journal of Water Resources Planning and Management*, 144(5), 04018018.

Rogers, D. and Calvo, B. (2015). "Defining the rehabilitation needs of water networks", *Procedia Engineering*, 119(1), 182-188.

Romaniuk, M. (2016). "On simulation of maintenance costs for water distribution system with fuzzy parameters", *Eksploatacja i Niezawodnosc - Maintenance and Reliability*, 18(4), 514-527.

Rudolph, K.U. (2008). "Economic aspects for water loss reduction", *International Workshop on Drinking Water Loss Reduction, Developing Capacity for Applying Solutions, 03.-05.,* September 2008, United Nations University, UN Campus, UNW-DPC, Bonn.

Sarrate, R., Blesa, J., Nejjari, F. and Quevedo, J. (2014). "Sensor placement for leak detection and location in water distribution networks", *Water Science and Technology: Water Supply*, 14(5), 795-803.

Seago, C.J., McKenzie, R.S. and Liemberger, R. (2005). "International benchmarking of leakage from water reticulation systems", *Proceeding of the IWA Leakage 2005 Conference*, Halifax, Nova Scotia, Canada, 48-61.

Sechi, G.M. and Zucca, R. (2017). 'A Cost-Simulation Approach to Finding Economic Optimality in Leakage Reduction for Complex Supply Systems', *Water Resources Management*, 31(14), 4601-4615.

Suribabu, C.R. and Neelakantan, T.R. (2012). "Sizing of water distribution pipes based on performance measure and breakage-repair-replacement economics", *ISH Journal of Hydraulic Engineering*, 18(3), 241-251.

Tabesh, M., Jamasb, M. and Moeini, R. (2011). "Calibration of water distribution hydraulic models: A comparison between pressure dependent and demand driven analyses", *Urban Water Journal*, 8, 93-102.

Tabesh, M., Yekta, A.H. and Burrows, R. (2008). "An integrated model to evaluate losses in water distribution systems", *Water Resources Management*, 23, 477-492.

Thornton, J. and Lambert, A.O. (2007). "Pressure management extends infrastructure life and reduces unnecessary energy costs", *IWA Conference Proceedings, Water Loss 2007*, Bucharest, Romania, 1-9.

Tricarico, C. Gargano, R., Kapelan, Z., Savic, D. and De Marinis, G. (2006). "Economic level of reliability for the rehabilitation of hydraulic networks", *Civil Engineering and Environmental Systems*, 23(3), 191-207.

Venkatesh, G. (2012). "Cost-benefit analysis-leakage reduction by rehabilitating old water

pipelines: Case study of Oslo (Norway)", *Urban Water Journal*, 9(4), 277-286.

Vicente, D.J., Garrote, L., Sánchez, R. and Santillán, D. (2016). "Pressure management in water distribution systems: Current status, proposals, and future trends", *Journal of Water Resources Planning and Management*, 142(2), 1-13.

Wang, Y., Zayed, T. and Moselhi, O. (2009). "Prediction models for annual break rates of water mains", *Journal of Performance of Constructed Facilities*, 23(1), 47-54.

Wegelin, W. and McKenzie, R.S. (2010). "Scope for pressure management in South Africa", *Proceedings of the IWA Conference 'Water Loss 2010'*, São Paulo, Brazil, 1-5.

Wu, S., Yang, L., Zhou, C. and Zhang, J. (2013). "Analysis of benefits yielded by pressure management in the area based on temperature revision", *ICPTT 2013 ASCE*, 127-141.

Wu, Z.Y., Sage, P. and Turtle, D. (2010). 'Pressure-dependent leak detection model and its application to a district water system', *Journal of Water Resources Planning and Management*, 136(1), 116-128.

Wyatt, A. and Alshafey, M. (2012). "Non-revenue water: Financial model for optimal management in developing countries", *Water Science and Technology: Water Supply*, 12(4), 451-463.

Wyatt, A.S. (2010). "Financial model for optimal management of non-revenue water in developing countries", *Proceedings of the IWA International Specialised Conference, Water Loss 2010*, São Paulo, Brazil, 1-11.

Xin, K., Tao, T., Lu, Y., Xiong, X. and Li, F. (2014). "Apparent losses analysis in district metered areas of water distribution systems", *Water Resources Management*, 28, 683-696.

Zamenian, H., Mannering, F.L., Abraham, D.M. and Iseley, T., (2017). "Modeling the frequency of water main breaks in water distribution systems: Random-Parameters Negative-Binomial approach", *Journal of Infrastructure Systems*, 23(2), 04016035.

Zangenehmadar, Z. and Moselhi, O. (2016). "Assessment of remaining useful life of pipelines using different Artificial Neural Networks models", *Journal of Performance of Constructed Facilities*, 30(5), 04016032.

Lime Stabilization of Expansive Clay Soil of Jimma Town, Ethiopia

Sorsa, A.[1]* and Agon, E.[2]

[1] Ph.D. Candidate, Department of Civil Engineering, Jimma Institute of Technology, Jimma University, Jimma, Ethiopia.
[2] M.Sc. Stident, Department of Civil Engineering, Jimma Institute of Technology, Jimma University, Jimma, Ethiopia.

ABSTRACT: The engineering properties of stabilized soils are varied for many factors such as soil heterogeneity, soil composition, soil structures, geological conditions, and the difference of interaction between the soil and stabilizers. These variations required the consideration of stabilization at a specific site option. These natural materials, therefore, critically influence the success of a construction project. The reason for this study was to quantify the improvements achieved in the engineering properties of expansive soils due to lime stabilization. This study considered quantitative experimental to determine lime-stabilized expansive clay soil's engineering properties using a laboratory program. Laboratory tests were to determine Atterberg Limits, compaction test, free swell test, California Bearing Ratio (CBR), and pH values of the mixtures. The collected soil samples were stabilized using 2, 4, 5, 6, and 8% of hydrated lime by weight. The optimum lime for the stabilization of expansive soils was 5% using hydrated lime. As percentages of hydrated lime increased, there were improvements in stabilized subgrade soil properties. The more significant upgrade in engineering properties was observed on California Bearing Ratio (CBR), and lower improvements were on maximum dry density. The result indicated that the stabilizer is very effective in improving strength parameters than index parameters. The hydrated lime stabilized soils under the optimum ratio fulfill the standard requirements as subgrade soils.

Keywords: Engineering Properties, Expansive Soil, Laboratory Tests, Lime Stabilization, Optimum Lime Content.

1. Introduction

Soils are naturally occurring materials used for road construction and other civil engineering works, such as the structure of all pavement layers except the surface made of concrete or asphalt. Therefore, these natural materials critically influence the success of a construction project (USDA, USAF, USN, 2004). There are different methods of minimizing structural damages due to the high swelling potential of expansive soils. The most common forms are reducing expansive soil swelling, using a solid structure that cannot be damaged for soil swelling, not constructing structures on swelling soil (Kalantari, 2012). Expansive soils are predominant soil in various parts of the world. Lime has been widely used to reduce the expansiveness of the soil by

---

* Corresponding author E-mail: soorummaa@gmail.com

forming pozzolanic products such as calcite and calcium-silicate-hydrate (Akula and Little, 2020). The expansiveness of soils is because of the presence of clay minerals. Clay particles have sizes of 0.002 mm or less. However, according to Chen (1984), the grain size alone does not determine clay minerals, and he highlighted that the essential property of fine-grained soils is their mineralogical composition. The most common clay minerals in engineering studies are Kaolinite, Illite, and Montmorillonite. Expansive soils can be recognized using mineralogical identification, indirect index property tests, or direct expansion potential tests. The expansiveness of soil is governed by the type and proportion of clay minerals it contains. Knowing the type and ratio of the clay mineral in the soil indicates the swelling potential (Chen, 1984). However, Lytton (1999) observed that the small size of clay grains makes the minerals challenging to distinguish in either hand specimens or petrographic microscopy. He also indicated the absence of a single or straightforward procedure for identifying clay minerals or their quantification and recommended the application of several methods for even approximate identification and rough quantification. Rao et al. (2007) pointed out the nature and characteristics of the expansive soils. The nature of expansive soil is water-absorbing, swelling, shrinking, and weak strength. These soils are stiff when dry, easily compressible when it gets water, and highly expansive when the Free Swell Index (FSI) is higher than 50 percent.

Soil stabilization is a method of soil modification by physical and chemical means in density increment, reinforcement, cementation, and volume control of the soil for construction purposes (Fang, 2019; Negi et al., 2013). Soil stabilization is a process by mechanical or chemical soil improvement to increase the strength and stability of the soil. The improvements mainly attained are increased soil gradation, reduction of swelling and shrinkage

potential, increased shear strength, and stability (Islam et al., 2019; USDA, USAF, USN, 2004). The purposes of lime used in construction engineering are to dry, modify, stabilize medium to fine-grained soils (ARBA, 2004; NASEM, 2009; Negi et al., 2013). A long-term pozzolanic reaction among flocculates and agglomerates of soil particles increases the strength based on the amounts of pozzolanic products and the reactivity of the soil minerals with lime used for stabilization (NASEM, 2009). Several procedures like the Illinois procedure, Thompson procedure, Eades and Grim procedure, and the Texas procedure, as summarized by the NRC and TRB (1987), involve comparing strength testing results using various lime contents till a lime content provides the maximum strength is obtained. For the Thompson and Eades and Grim procedures, the optimum lime ratio is estimated by evaluating the pH of several soil lime mixtures with changing lime contents. The lowest lime content that provides a pH of 12.4 is then used as the starting point for determining the optimum lime content. The Texas procedure, as summarized by the NRC and TRB (1987), first estimates the optimum lime content using the plasticity index of the soil and the percentage of soil passing the No. 40 sieves. After evaluating the optimum lime content, strength testing is then used to verify the actual optimum lime content. While the procedures outlined above help identify the lime content that will provide the greatest strength, many factors influence the strength of soil-lime mixtures. The variability of these factors makes it practically impossible to pinpoint the strength achieved for the lime stabilization of a particular soil. Therefore, the strengths of soil-lime mixtures through strength tests such as CBR, unconfined compressive strength, or resilient modulus must be verified. Lime contents between 2 to 10 percent can produce significant strength gains (Ikeagwuani et al., 2019). Jawad et al. (2016) reviewed previous studies on lime-treated soil and suggested that lime is the

oldest and traditional soil stabilization system.

Soil treated using lime makes the soil particles agglomerate and flocculation that results in a pozzolanic reaction. Lime stabilization of soil efficiently increases soil strength, workability, and durability. The properties of lime-treated soil depend on many factors, such as soil type, lime type, lime percentage, curing time, and temperature conditions (Ali and Mohamed, 2019; Balaji et al., 2018; Di Sante et al., 2014). However, according to Kassim and Chern (2004), soil stabilization depends on the lime quality, clay fraction, soil mineralogy, and alkalinity. The influence of lime on the physical-mechanical properties of black cotton soils was studied using laboratory tests including Atterberg limits, California Bearing Ratio (CBR), swell percent, Unconfined Compressive Strength (UCS), X-Ray Diffraction (XRD), and pH test. The result revealed that lime significantly improved the physical-mechanical properties of the soil (Cheng et al., 2018; Dang et al., 2016). Alkali-activated materials are more sustainable and environmentally friendly construction materials in improving durability, strength, corrosion resistance, and a high degree of reaction when appropriate amounts are used (Wang et al., 2020).

The engineering properties of stabilized soils vary for many factors such as soil heterogeneity, soil composition, soil structures, geological conditions, and the interaction difference between the soil and stabilizers. These variations required the stabilization of a specific site option (NASEM, 2009). The envisioned transportation system in the future will be characterized as a "five-zero" system, such as zero casualties, zero delays, zero emissions, zero maintenance, and zero failure. The realization of the system needs the coordination and interaction between each element in the transportation system (i.e., peoples, vehicles, the road, and the environment) to be considered for systematic optimization (Sun et al., 2018).

In Ethiopia, as a general practice, the conventional method of removing expansive soil and replacing it with quality fill material has been common practice for a problem of expansive subgrade soils. This method is also practical around Jimma Town due to the lack of knowledge on stabilizing and reusing weak soils. Ikeagwuani and Nwonu (2019) stated that soil replacement might not be considered adequate when the soil condition is very critical; for the case of expansive soils, it involves prolonged physical activity to execute in situ when quality control is essential and thus could be time-consuming. According to Sarkar et al. (2016), using 5% of lime for expansive soil stabilization saved a cost of 32.5% than using quality material replacement. Stabilizing clays with lime can improve subgrade soils at a lower cost than removing and replacing materials (Prusinski and Land, 1999). Therefore, this study quantifies the improvements achieved on the engineering properties of expansive soils due to lime stabilization and determines the optimum lime content required for the stabilization of Jimma expansive clay. The stabilization of expansive soil is essential to ensure the stability of soil that can successfully sustain the load of the superstructure without failure. This research determines the proper ratio of stabilizer to be used in future construction on Jimma Town expansive clay soil. In designing a better sub-grade of road pavements, the laboratory results and the statistical analysis from this study can be helpful.

2. Materials and Methods

2.1. Description of the Study Area

This study considered the expansive clay soil of Jimma city of Ethiopia. Jimma town is one of the old and largest towns of the country, located in the southwestern part of the country at 354 km distance from Addis Ababa, the capital city of the country. The town is in the Jimma Zone of Oromia state; its geographical coordinates are

approximately 7°41'N latitudes and 36°50'E longitudes. The city has an average temperature range from 20–30 °C, annual rainfall of average ranges from 800-2500 mm, and an elevation of 1718-2000 m above mean sea level. From Ethiopia's Central Statistical Agency (CSA) 2007 census report, the city's total population is 130,254. Its climate is in the climatic zone, which is very suitable for agriculture and the life of a human (Sun et al., 2018).

2.2. Materials

2.2.1. Soils

The type of soil considered for the stabilization using lime is expansive clay soil characterized by Sorsa et al. (2020) and summarized in Table 1.

2.2.2. Lime

Hydrated lime used for this study was obtained from Sankale Lime Factory. The chemical composition of Sankale hydrated lime was tested by (Solomon, 2011). The composition result is presented in Table 2.

2.3. Experimental Design

To characterize and understand the engineering properties of lime stabilized expansive clay soil laboratory experimental methods of (AASHTO T193-93, 1993; ASTM D3282-93, 1993; ASTM D422-98, 1998; ASTM D4318-00, 2000; ASTM D4643-00, 2000; ASTM D6276-99a, 1999; ASTM D698-00a, 2000; ASTM D854-02, 2002) procedures were considered. The soil specimens were from the Jimma city around Kidane-Mihret Church as shown in Figure 1 and Rift Valley University Jimma Campus (Sample 2).

2.3.1. Lime and Expansive Soil Mixing Ratios

As proposed in most of the previous studies conducted on soil stabilization using lime, the ratio of lime should be from 2%-10% by weight. The stabilization was done using 2, 4, 5, 6, and 8% of hydrated lime by weight for this study. The optimum amount of lime added to expansive clay was estimated using the pH test method (ASTM D6276-99a, 1999). This test method gives a means for evaluating the soil-lime proportion requirement for the stabilization of soil.

Table 1. Engineering properties of Jimma town soft, expansive clay soil (Sorsa et al., 2020)

Parameters/Samples name	S1	S2
Moisture content (%)	40.77	54.50
Specific gravity	2.7	2.77
Percentage Finer # 200 (%)	78	78
Liquid limit (%)	81	67
Plastic limit (%)	41	31
Plasticity index (%)	40	36
Classification	A-7-5	A-7-5
MDD (gm/cm^3)	1.41	1.48
OMC (%)	33.5	32
CBR (%)	1.8	2.4

Table 2. Sankale hydrated lime chemical composition

Constituent	SiO_2	Al_2O_3	Fe_2O_3	CaO	MgO	Na_2O	K_2O	TiO_2	P_2O_5	MnO	SO_3
Percentage (%)	6.21	2.18	3.57	59.47	3.91	0.61	0.79	0.3286	0.208	0.2785	0.58

Fig. 1. Photo of expansive soil observed at Kidane-Mihret (Jimma) Church Site (S1)

2.3.1. Laboratory Testing Procedures for Lime Stabilization

The collected soil samples should be first air-dried and sieved through a 425 μm sieve. Next, prepare hydrated lime of 2, 3, 4, 5, 6, and 8% of the soil samples. Finally, conduct laboratory tests by mixing hydrated lime with soil based on ASTM C977-02 (2002) that is dry mixing of hydrated lime with soil, then adds distilled water and thoroughly distributed throughout the soil.

3. Results and Discussions

3.1. Laboratory Results of Lime Stabilized Expansive Clay Soil

For this study, two subgrade soil samples were collected along the road section to evaluate the effects of hydrated lime for expansive subgrade soil. The most critical parameters used to assess the impact of chemical additives for this study were the Atterberg limit and CBR tests.

3.1.1. Atterberg Limits

The Atterberg limit tests were conducted at different ratios of lime. Based on the soil type and added chemicals, there were changes in index properties of stabilized soil. The variation of Atterberg limit values for the present study was reported in Figure 2.

As observed from Figure 2, changing stabilization ratio changes liquid limit, plastic limit, and plasticity index values of the soil. The highest reduction in plastic index occurred when stabilized with maximum percentages, and the minimum

reduction occurred at minimum ratios. For example, the liquid limit, plastic limit, and plasticity index of natural soils of sample 1 were 67%, 31%, and 36%, respectively, whereas 5% hydrated lime stabilized soil 53%, 45%, and 8%, respectively. This study agrees with previous findings (Islam et al., 2019; Phanikumar and Raju, 2020; Solomon, 2011). According to Islam et al. (2019), adding 12% of lime to expansive soil reduced the liquid limit from 54.6% to 52.2% and increased the plasticity index from 24.3% to 34.6%. According to Phanikumar and Raju (2020), there were decreases in LL and PI, from 84% to 72% and 58% to 40.5%, respectively, when the lime content was increased from 0% to 12%. In general, from Figure 2 for lime stabilization, the following observation has been made. The liquid limit and plasticity index reduce with increasing lime ratios, but the plastic limit increases with increasing lime ratios. The purpose of reducing the liquid limit with increasing lime content is calcium silicate in a hydrated lime with absorbing water.

On the other hand, the plastic limit shows the opposite trend. The plastic limit increases with an increasing percentage of lime, as shown in Figure 2. The plasticity index drops as lime content increases due to the rapid occurrence of flocculation and pozzolanic reaction. Lime has been widely used to reduce the expansiveness of the soil by forming pozzolanic products such as calcite and calcium-silicate-hydrate (Akula and Little, 2020).

Table 3. Laboratory testing procedures used for this study

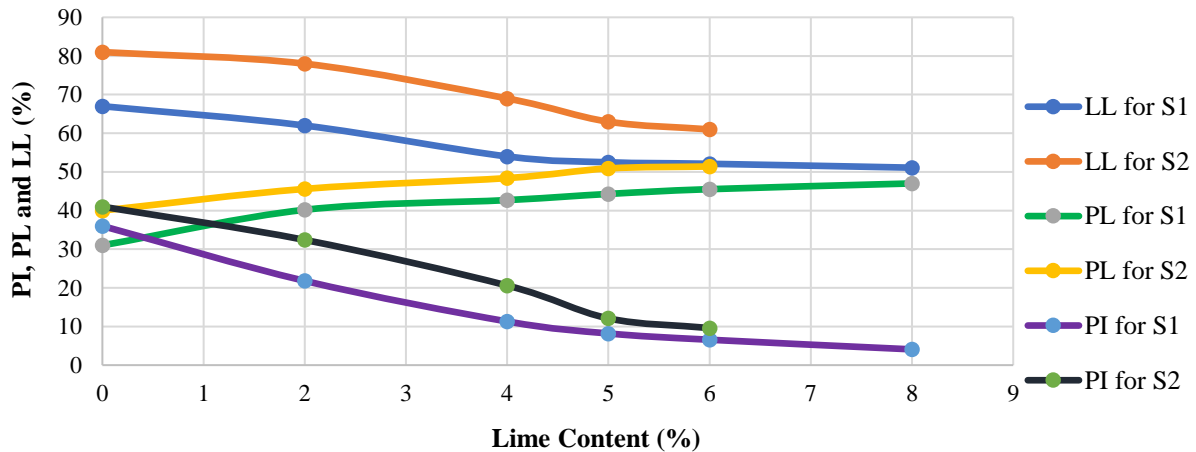| Laboratory test	ASTM standards	AASHTO standards
Natural moisture content	D 4643-00	
Specific gravity	D 854-83	
Grain size analysis	D 422-63	
Atterberg limits	D 4318-98	
pH	D 6276-99a	
Standard compaction	D 698-98	
CBR		T 193-93

Fig. 2. Atterberg limit test result of hydrated lime stabilized expansive clay soils

3.1.2. Free Swell Test Result of Lime Stabilized Expansive Clay Soil

Free swell tests result indicated the potential expansiveness of soil samples without being loaded was very high. The Free Swell (FS) of the stabilized soil sample is presented in Figure 3.

The swelling potential of expansive soils was greater than 50% (Figure 3). This result indicated that the two soils were highly expansive soil. It was supported by Rao et al. (2007) soils are highly expansive when the free swell index exceeds 50%. Such soils undergo volumetric changes, leading to pavement distortion, cracking, and general unevenness due to seasonal wetting and drying. The soil samples' expansiveness for this study was identified based on parameters obtained from the test results of free swell and CBR swell percentage results. As indicated in Figure 3, increasing the proportion of stabilizers reduces the swelling of soils. For instance, the stabilization of expansive clay soil with 5% hydrated lime decreased the swelling potential of the soil from 85% to 29%, which is a very significant improvement. Thus, the result showed a stabilizer is effective in reducing the swelling potential of expansive soils.
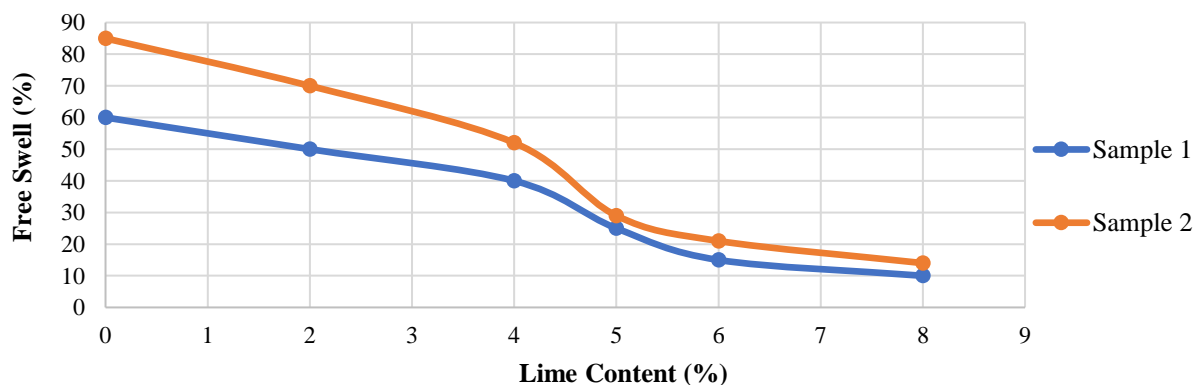

Fig. 3. Free swell result of stabilized soils

3.1.3. Moisture–Density Relationship

Moisture-density relationships were determined using the standard proctor compaction test according to ASTM D698-98. The OMC and maximum dry density of stabilized soils are presented in Table 4.

OMC and MDD showed that the stabilization proportion increased, optimum moisture content decreased, and maximum dry density increased. The results show that OMC decreases with increasing lime content due to fine and light particles in the mixtures. The pozzolanic reaction between clay and lime also reduces the OMC and increases MDD (Phanikumar and Raju, 2020). The use of 5% lime decreased OMC from 33.5% to 31% and increased MDD from 1.41 g/cm^3 to 1.48 g/cm^3. This concept is the same as Darsi et al. (2021) and Solomon (2011) concept, was concluded that the addition of chemical stabilizers to subgrade soils has decreased the OMC and has increased MDD of stabilized subgrade expansive clay soils. According to Solomon (2011), OMC decreases from 31% to 26%, and MDD increases from 1.44 g/cm^3 to 1.48 g/cm^3, when the lime content was increased from 0% to 6%. The decreasing moisture content had a significant influence on the stiffness of improved ground and the soil bearing capacity (Toufigh et al., 2017).

3.1.4. California Bearing Ratio (CBR) Result

California bearing ratio (CBR) is an essential parameter in pavement design (Nasrizar and Muttharam, 2019). This CBR test was conducted using the AASHTO procedure T193-93. The CBR value is a value at 2.54 mm penetration and 95% of MDD. The soils stabilized by hydrated lime showed an improvement in strength. Therefore, CBR is one of the parameters used to measure strength.

According to Nasrizar and Muttharam (2019), the CBR values can be affected by the lime content, curing period, and curing temperature. For example, stabilizing expansive soil by 5% lime improves CBR values from 1.8% to 18.1% for Sample 1. From Table 5, the following observations have been made:

➢ CBR increased with increased hydrated lime proportions.
➢ CBR values of natural subgrade soils of the two samples did not fulfill the requirement of subgrade soils as per the ERA standard (CBR > 5%).
➢ The improvement done at 5% hydrated lime fulfills the ERA standard (CBR > 5%) for sub-grade.

The increasing and decreasing of different parameters with an increasing percentage of lime were agreed with (Karatai et al., 2017; Phanikumar and Raju, 2020). Based on the finding of Gunjagi et al. (2016), adding 10% lime improved the CBR of expansive soil from 0.36% to 27.65%. The improvement in the CBR values of lime stabilized expansive soil is due to a cation exchange, flocculation, and agglomeration produced by lime (Nasrizar and Muttharam, 2019). The reason for soil strength increase after stabilization was there is a higher energy at the initial stage of reaction and a faster hydration process, resulting in the completion of their pozzolanic reactions in a short period (Bargi et al., 2021). According to the Ethiopian Road Authority (ERA) (2013), it is not allowed to use CBR values less than 5% because, from both a technical and economic perspective, it would generally be inappropriate to lay a pavement on soils of such bearing capacity.

Table 4. OMC and MDD of stabilized soil for typical ratios stabilizer

Sample	Lime percentage (%)	0	4	5
S1	OMC (%)	33.5	32	31
	MDD (g/cm^3)	1.41	1.45	1.48
S2	OMC	32	30.6	28.7
	MDD (g/cm^3)	1.48	1.50	1.54

Table 5. CBR values of stabilized and natural sub-grade soil

Sample name	lime percentage	CBR (%)	CBR requirements (%)
S1	0%	1.8	> 5
	5%	18.1	
S2	0%	2.4	
	4%	3.4	
	5%	8.4	

3.1.5. CBR Swell Result

The hydrated lime-soil mixtures compacted in CBR molds at optimum moisture content with maximum dry density gauged for swelling characteristics before and after soaking for four days to evaluate the swell percent. The test results at different ratios are presented in Table 6.

The CBR and CBR swell percentage test results, as shown in Tables 5 and 6, conclude that the subgrade soils have a low load-bearing capacity and high swelling potential, making the soils unsuitable for subgrade without improvement. The comparison above confirms that both soil samples did not fulfill the ERA standard requirements as subgrade soils, which are CBR should be greater than 5%, and CBR swell should be less than 2%. Therefore, treating expansive soils using appropriate improving methods before using the soil for subgrade materials is better. For this study, hydrated lime stabilization was considered. Chemicals such as lime and cement

improve the low load-bearing capacity of poor subgrade soil and lower the plasticity index and percent swell of highly expansive subgrade soils (NASEM, 2009). The use of 5% lime reduced the swelling potential of an expansive soil from 4.30% to 1.08%, which is a very significant improvement. According to Cheng et al. (2018), adding 6% lime to expansive clay soil reduced the free swell percent of soil from 15.8% to 1.3%.

3.1.6. Estimation of the Optimum Lime for Expansive Soil Stabilization

One of the aims of this study was to determine the optimum lime ratio to stabilize the expansive soil of Jimma Town. The optimum lime was estimated for Jimma Town expansive clay based on laboratory test analysis and literature review. The optimum ratio of hydrated lime was calculated based on the pH meter method according to ASTM D6276. The optimum proportion is determined at a pH of 12.4.

Table 6. CBR swell test result of stabilized and natural subgrade soils

Sample name	CBR swell (%)	CBR Swell (%) minimum requirements
Natural S1	2.26	< 2%
5% stabilized S1	1.40	
Natural S2	4.30	
5% stabilized S2	1.08	
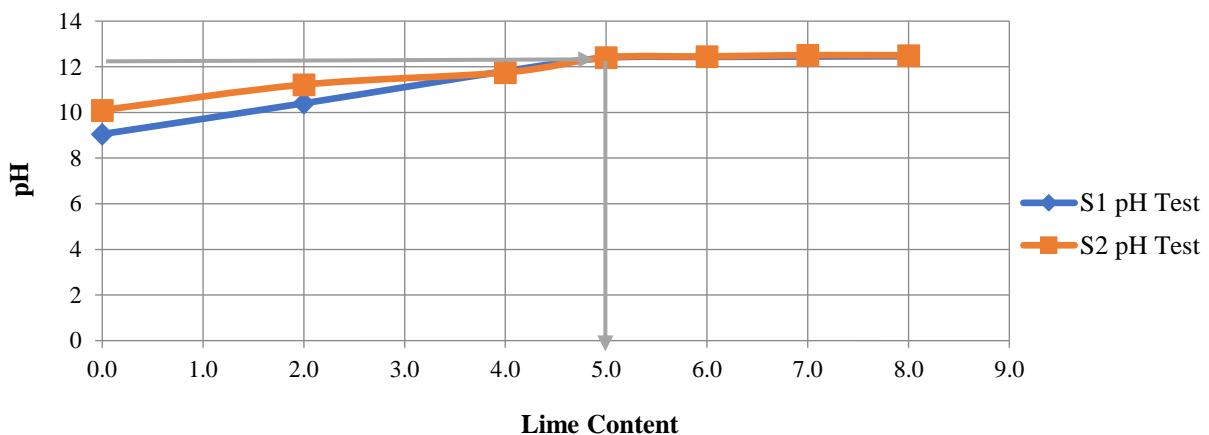
Fig. 4. Estimation of optimum lime ratio using pH method

As shown in Figure 4, the optimum ratio at 12.4 pH value is 5% of hydrated lime for both soils considered for this study. This result has similar trends observed in the study of (Mahedi et al., 2020). Different researchers found various optimum lime content for the stabilization of expansive soil. Based on the finding of Islam et al. (2019), 7% lime, Sarkar et al. (2016), 5% lime, Gunjagi et al. (2016), 10% lime, Nikookar et al. (2016), 9–12% lime is the optimum lime content for lime stabilization in short-term and long-term curing. The difference was because of soil property variation from place to place. The spatial variability of the soil had significant effects on the bearing capacity of the shallow foundations (Chenari, 2014). The mixture of expansive soil with lime increased the pH and salinity, creating a suitable environment for pozzolanic reactions (Kumar and Thyagaraj, 2020). Elsharief et al. (2013) suggested that soils having different mineralogical constituents had different optimum lime content. As the study conducted on three different Sudan tropical soil showed, the optimum lime was 4%, 6.5%, and 7%, which were different.

This study evaluated the effects and performance of hydrated lime on expansive soils based on the laboratory test results of Atterberg limits, free swell, CBR, and CBR swell percentage.

The test result in Table 7 shows that the more significant improvements were observed on CBR, and lower improvements were on maximum dry density. The degree of improvements for CBR and MDD are 905.5% and 4.1%, respectively. Thus, the result indicated that the hydrated lime improved strength parameters more effectively than index parameters. The reason is all index parameter tests considered immediate effects of lime. However, CBR depends on curing time effects. CBR was soaked for seven days for this study, so a more significant change was observed in CBR values. Therefore, the analysis shows lime is more effective when it takes time to react with soils. Nasrizar and Muttharam (2019) stated that soil engineering properties' improvement depends on the percentage of lime, curing period, and curing temperature.

4. Conclusions

This study was to quantify the improvements achieved in the engineering properties of expansive soils due to lime stabilization. Stabilizing soils with lime is now a cost-effective method of converting poor-quality soil into a strong, impermeable medium. The laboratory tests conducted for this study were Atterberg limits, compaction test, free swell test, California Bearing Ratio, and CBR swell tests. The test methods were based on AASHTO and ASTM laboratory test standards. The stabilization was done using 2, 4, 5, 6, and 8% of hydrated lime by weight. From the study, the following findings are concluded:

Table 7. Summary of the improvements on engineering properties at the optimum ratio

Sample name	Parameters	Natural soil	Improved soil using 5% lime	Degree of Improvements (%)
S1	LL (%)	67	52.5	21.6
	PL (%)	31	45.46	46.6
	PI (%)	36	7.04	80.4
	Free Swell (%)	60	25	58.3
	CBR (%)	1.8	18.1	905.5
	CBR Swell (%)	2.26	1.4	38.1
	OMC (%)	33.5	31	8.1
	MDD (g/cm^3)	1.41	1.48	4.96
S2	LL (%)	81	63	22.2
	PL (%)	41	50.9	24.1
	PI (%)	40	12.1	69.8
	Free Swell (%)	85	24	71.8
	CBR (%)	2.4	8.4	250
	CBR Swell (%)	4.3	1.08	74.9
	OMC (%)	32	28.7	10.3
	MDD (g/cm^3)	1.48	1.54	4.1

- The engineering properties of natural subgrade soils studied, the two soils were expansive clay of A-7-5 class soil.
- The subgrade soils considered for this study have a low load-bearing capacity and high swelling potential, making the soils unsuitable for subgrade without improvement. The CBR and CBR swell of natural soil was 1.8% and 2.26%, respectively.
- The optimum ratio for the expansive soils is at 5% hydrated lime using the pH meter method.
- The higher improvements in engineering properties were observed on CBR, and lower improvements were on maximum dry density. The result indicated that the hydrated lime was very effective in improving strength parameters than index parameters. Stabilizing expansive soil by 5% lime improves CBR values from 1.8% to 18.1% for Sample 1. The use of 5% lime increased MDD from 1.41 g/cm^3 to 1.48 g/cm^3.
- The two soil samples stabilized using hydrated lime at optimum ratio fulfilled the standard requirements as subgrade soils.
- The finding of this study is a potential solution to improve expansive clay soil by adding the optimum lime before constructing any structure. However, further investigation is recommended on different stabilization methods to select the suitable stabilizer.

5. Declaration of Interests

The authors declare no conflict of interest or financial conflicts to disclose.

6. References

AASHTO T193-93. (1993). *Standard method of test for California bearing ratio*, AASHTO, Washington D.C.

Akula, P. and Little, D.N. (2020). "Analytical tests to evaluate pozzolanic reaction in lime stabilized soils", *MethodsX*, 7(4), 100928.

Ali, H. and Mohamed, M. (2019). "Assessment of lime treatment of expansive clays with different mineralogy at low and high temperatures",
Construction and Building Materials, 228, 116955.

American Road Builders Association (ARBA). (2004). *Lime-treated soil construction manual: Lime stabilization and lime modification*, 11th Edition, National Lime Association, Virginia.

ASTM C977-02. (2002). *Standard specification for quicklime and hydrated lime for soil stabilization 1*, ASTM International, West Conshohocken.

ASTM D3282-93. (1993). *Standard practice for classification of soils and soil-aggregate mixtures for highway construction purposes*, ASTM International, West Conshohocken.

ASTM D422-98. (1998). *Standard test method for particle-size analysis of soils*, ASTM International, West Conshohocken.

ASTM D4318-00. (2000). *Standard test methods for liquid limit, plastic limit, and plasticity index of soils*, ASTM International, West Conshohocken.

ASTM D4643-00. (2000). *Standard test method for determination of water (moisture) content of soil by the microwave oven heating*, ASTM International, West Conshohocken.

ASTM D6276-99a. (1999). *Standard test m for using pH to estimate the soil-lime proportion requirement*, ASTM International, West Conshohocken.

ASTM D698-00a. (2000). *Standard test methods for laboratory compaction characteristics of soil using standard effort*, ASTM International, West Conshohocken.

ASTM D854-02. (2002). *Standard test methods for specific gravity of soil solids by water pycnometer*, ASTM International, West Conshohocken.

Balaji, S., Wadhave, M.D., Waghe, A.P., Rathod, D.C. and Razvi, S.S. (2018). "Soil stabilization by using lime", *International Journal of Engineering and Management Research*, 8(02), 79-86.

Bargi, M.M., Rasouli Ghahroudi, O. and Tajdini, M. (2021). "An investigation on the effects of adding nano-Sio_2 particles and silica fume with different specific surface areas on the physical and mechanical parameters of soil-cement materials", *Civil Engineering Infrastructures Journal*, 51(1), 93-109.

Chen, F.H. (1984). *Foundations on expansive soils*, Elsevier, New York.

Chenari, J. (2014). "The effect of spatial variability and anisotropy of soils on bearing capacity of shallow foundations", *Civil Engineering Infrastructures Journal*, 47(2), 199-213.

Cheng, Y., Wang, S., Li, J., Huang, X., Li, C. and Wu, J. (2018). "Engineering and mineralogical properties of stabilized expansive soil compositing lime and natural pozzolans", *Construction and Building Materials*, 187, 1031-1038.

Dang, L.C., Hasan, H., Fatahi, B., Jones, R. and

Khabbaz, H. (2016). "Enhancing the engineering properties of expansive", *International Journal of GEOMATE*, 11(25), 2447-2454.

Darsi, B.P., Molugaram, K., Vamshi, S. and Madiraju, H. (2021). "Subgrade black cotton soil stabilization using Ground Granulated Blast-Furnace Slag (GGBS) and lime, an inorganic mineral †", *Environmental Sciences Proceedings*, 6(15), 1-15.

Di Sante, M., Fratalocchi, E., Mazzieri, F. and Pasqualini, E. (2014). "Time of reactions in a lime treated clayey soil and influence of curing conditions on its microstructure and behavior", *Applied Clay Science*, 99, 100-109.

Elsharief, A.M., Elhassan, A.A.M. and Mohamed, A.E.M. (2013). "Lime stabilization of tropical soils from Sudan for road construction", *International Journal of GEOMATE*, 4(2), 533-538.

Ethiopian Road Authority (ERA). (2013). *Pavement design manual Volume 1: Flexible pavements*, Ethiopian Road Authority, Addis Ababa.

Fang, H.-Y. (2019). *Foundation engineering handbook: Volume II,* 2nd Edition, Springer Science and Business Media, Berlin.

Gunjagi, D.A., Kore, S.B., Lole, A.A. and Kadam, S.R. (2016). "Assessment of use of lime in expansive soil subgrade for Sangli – Kolhapur highway", *International Research Journal of Engineering and Technology (IRJET)*, 3(11), 720-723.

Ikeagwuani, C.C., Obeta, I.N. and Agunwamba, J.C. (2019). "Stabilization of black cotton soil subgrade using sawdust ash and lime", *Soils and Foundations*, 59(1), 162-175.

Ikeagwuani, C.C. and Nwonu, D.C. (2019). "Emerging trends in expansive soil stabilization: A review", *Journal of Rock Mechanics and Geotechnical Engineering*, 11(2), 423-440.

Islam, S., Hoque, N.M.R., Hoque, M.A., Mishra, P.N., Mamun, M.M.H. and Dey, S. (2019). "Strength development in fine-grained paddy field soil by lime addition", *Journal of Building Engineering*, 26(100857), 1-7.

Jawad, I.T., Taha, M.R., Majeed, Z.H. and Khan, T.A. (2014). "Soil stabilization using lime: Advantages, disadvantages and proposing a potential alternative", *Research Journal of Applied Sciences, Engineering and Technology*, 8(4), 510-520.

Kalantari, B. (2012). "Foundations on expansive soils: A review", *Research Journal of Applied Sciences, Engineering and Technology*, 4(18), 3231–3237.

Karatai, T.R., Kaluli, J.W., Kabubo, C. and Thiong'O, G. (2017). "Soil stabilization using rice husk ash and natural lime as an alternative to cutting and filling in road construction", *Journal of Construction Engineering and Management*, 143(5), 4-8.

Kassim, K.A. and Chern, K.K. (2004). "Lime stabilized Malaysian cohesive soils", *Malaysian Journal of Civil Engineering*, 16(1), 13-23.

Kumar, K.S.R. and Thyagaraj, T. (2020). "Comparison of lime treatment techniques for deep stabilization of expansive soils", *International Journal of Geotechnical Engineering*, 15(8), 1021-1039.

Lytton, R. (1999). "Expansive soils problems and practice in foundation and pavement engineering", *International Journal for Numerical and Analytical Methods in Geomechanics*, 23, 1067-1069.

Mahedi, M., Cetin, B. and White, D.J. (2020). "Cement, lime, and fly ashes in stabilizing expansive soils: Performance evaluation and comparison", *Journal of Materials in Civil Engineering*, 32(7), 1-16.

Nasrizar, A.A. and Muttharam, M. (2019). "Effect of lime on California bearing ratio (CBR) of soft soils", *International Journal of Innovative Science and Research Technology*, 4(6), 287-293.

National Academies of Sciences, Engineering and Medicine (NASEM). (2009). *Recommended practice for stabilization of subgrade soils and base materials*, The National Academies Press, Washington D.C.

National Research Council (NRC) and Transportation Research Board (TRB). (1987). *Lime stabilization – reactions properties, design and construction*, Transportation Research Board and National Research Council (U.S), Washington D.C.

Negi, A.S., Faizan, M. and Siddharth, D.P. (2013). "Soil stabilization using lim", *International Journal of Innovative Research in Science, Engineering and Technology*, 2(2), 448-453.

Nikookar, M., Arabani, M., Mirmoa'Zen, S.M. and Pashaki, M.K. (2016). "Experimental evaluation of the strength of peat stabilized with hydrated lime", *Periodica Polytechnica Civil Engineering*, 60(4), 491-502.

Phanikumar, B.R. and Raju, E. (2020). "Compaction and strength characteristics of an expansive clay stabilised with lime sludge and cement", *Soils and Foundations*, 60(1), 129-138.

Prusinski, J.R. and Land, S. (1999). "Effectiveness of Portland cement and lime in stabilizing clay soils", *Transportation Research Record*, 1652(1), 215-227.

Rao, A.S., Phanikumar, B.R., Babu, R.D. and Suresh, K. (2007). "Pullout behavior of granular pile-anchors in expansive clay beds in situ", *Journal of Geotechnical and Geoenvironmental Engineering*, 133(5), 531-538.

Sarkar, R., Daalia, A., Narang, K., Garg, S., Agarwal, P. and Mudgal, A. (2016). "Cost-effectiveness of flexible pavement on stabilized expansive soils", *International Journal of*

GEOMATE, 10(1), 1595-1599.

Solomon, H. (2011). "Chemical stabilization of expansive sub-grade soil performance evaluation on selected road section in Northeastern Addis Ababa*"*, M.Sc. Thesis, Addis Ababa University.

Sorsa, A., Senadheera, S. and Birru, Y. (2020). "Engineering characterization of subgrade soils of Jimma Town, Ethiopia, for roadway sesign", *Geosciences*, 10(2), 1-17.

Sun, L., Zhao, H., Tu, H. and Tian, Y. (2018). "The smart road: Practice and concept", *Engineering*, 4(4), 436-437.

Toufigh, V., Bagheri, B., Asadi, R., Sadir, A. and Toufigh, M.M. (2017). "Relatively large-scale experimental study on behavior of Compacted Lime Mortar (CLM) columns: Influence of moisture content", *Civil Engineering Infrastructures Journal*, 1(2), 355-371.

United States Department of the Army, United States Air Force, and United States Navy

USDA, USAF, USN. (2004). *Soil stabilization for pavements*, University Press of the Pacific, Washington D.C.

Wang, A., Zheng, Y., Zhang, Z., Liu, K., Li, Y., Shi, L. and Sun, D. (2020). "The durability of Alkali-activated materials in comparison with ordinary Portland cements and concretes: A review", *Engineering*, 6(6), 695-706.

Numerical Study of the Failure in Elbow Components of Buried Pipelines under Fault Movement

Salimi Firoozabad, E.[1] , Samadzad, M.[2] and Rafiee-Dehkharghani, R.[2]*

[1] Ph.D., School of Civil Engineering, College of Engineering, University of Tehran, Tehran, Iran.
[2] Assistant Professor, School of Civil Engineering, College of Engineering, University of Tehran, Tehran, Iran.

© University of Tehran 2021

ABSTRACT: Faults have large impact on the mechanical behavior of soil in pipeline's construction. These pipelines have been embedded to supply vital resources such as water, oil, and gas for consumers. To prevent damage, it is highly recommended not to construct pipelines around active faults. However, it is generally inevitable to cross the fault due to wide extension of pipelines. In this paper, a numerical analysis and parametric study on an underground water pipeline in Tehran, Iran, under the fault-induced displacement is presented. It is important to note that the main focus of this study is on elbow components which are the most critical sections in pipeline systems. The effects of crossing angle, distance to elbow and various soil properties on the elbow response are investigated. It is aimed at finding a safe regulation to embed pipelines with the lowest level of risk expected in elbow components after fault movement. The results show that the elbow component does not suffer serious damage when the crossing angle is 90°, provided they are not located in the close vicinity of the fault rupture surface. However, when the crossing angle decreases to 60 and 45 degrees, these components are much more vulnerable.

1. Introduction

Buried pipelines are considered as lifelines that human's life highly depends on them. These lifelines carry water, oil, and gas throughout residential areas in major cities for consumers. They are mostly steel made and manufactured in different pieces (for convenient transportation) including straight parts, elbows, and tee sections to be assembled and welded in sites. Steel pipe elbows are one of the most common sections used in pipelines to convey fluids. Pipelines are often exposed to existing fault movement as they are expanded all around under the ground passing through the fault lines. Therefore, they could be damaged or even failed to supply consumers. It is observed that the elbow components are one of the most critical parts in pipeline systems that are very vulnerable to fault rupture.

Elbow components have been reported to be the most critical points of different pipelines and piping systems including

---

* Corresponding author E-mail: rezarafiee@ut.ac.ir

nuclear power plants (Salimi Firoozabad et al., 2015), subsea pipelines (Pouraria et al., 2017) and buried pipelines (Vazouras and Karamanos, 2017). The failure analysis of various types of steel pipe elbow due to the cyclic loading by Salimi Firoozabad et al. (2016), and low-cycle fatigue (Varelis and Karamanos, 2015; Hassan et al., 2015) has been studied in the literature. Extensive experimental studies on the structural behavior of steel elbows (Varelis et al., 2013; Hassan et al., 2015; Kiran et al., 2018; Kim et al., 2019) have been also performed.

There are numerous studies in the literature on analysis of buried pipelines crossing active faults. Newmark and Hall (1975) developed a method for analyzing the effect of a fault movement on a pipeline. They found that the pipeline capacity in buried soil depends mainly on the fault movement, soil characteristics, fault angle, slip length, and pipe material specifications. Karamitros et al. (2011), proposed an analytical methodology for the strain analysis of elbows subjected to permanent ground deformation. More recently, Tsatis et al. (2019) studied failure modes of buried pipeline and effective parameters crossing normal and reverse faults. Sabermahani and Bastami (2019) considered rotation between the cross-section and the bending line due to the shear deformations for the stress analysis of a buried pipeline. These few available FEA studies on pipe elbows in the literature are either analytical or scaled, they propose an application process, surrounding soil modeling, and loading condition, quite difficult (time consuming) to be applied on a real pipeline case. Furthermore, Majrouhi Sardroud et al. (2021) indicated the importance of having BIM adopted for urban piping systems to evaluate the risk of rupture in case of an earthquake.

The pipe-soil interaction was studied by Kokavessis and Anagnostidis (2006). they used the finite element method and contact elements to describe the soil-pipe interaction and analyzed buried pipes under permanent motion of the earth. More

recently, Vazouras, et al. (2015, 2017) studied the mechanical behavior of buried straight pipes and also pipe bends crossing different fault angles by using the Finite Element Method (FEM), considering different failure criteria. Bildik and Laman (2015) performed experiments on buried pipes in sand box subjected to a vertical static load in order to conduct a parametric study on soil's bearing capacity. In addition, Castiglia et al. (2018) studied the performance of buried pipelines in liquefied soil considering the effect of pore water pressure and structure's floatation.

Elbow components have been reported to be one of the most critical points of different pipelines and piping systems although, their behavior under fault movement has not been much investigated. Therefore, the structural behavior of pipe elbow components in a real buried pipeline crossing fault line has been studied in this paper. Various parameters have taken into considerations including soil mechanical properties, soil-pipe interaction properties, fault angle, and distance to elbow. Full scale three dimensional existing pipelines and surrounding soil are modeled. A real water transmission pipeline geometry (used in Tehran metropolitan city, Iran) is taken as a case study for numerical simulation. The reliability of the simulations has been verified by two different experiments: 1) A centrifuge test on a buried polyethylene pipeline under fault movement; and 2) A test on a steel pipe elbow under monotonic and cyclic loading.

2. Finite Element (FE) Modeling

The structural response of the steel pipe under fault movement is studied using numerical calculations. For this purpose, the general finite element method (FEM) program ABAQUS/Implicit (2016) is used for simulating the mechanical behavior of the steel pipeline, the surrounding soil environment, and their interaction in a precise manner, considering the detailed geometry of the soil and pipe along their

nonlinear material properties.

2.1. Pipeline Description

A small part of real water transition pipeline (used in district 4 of Tehran metropolitan city, Iran) is taken as a case study for numerical simulation as shown in Figure 1. The pipeline has a total length of 197.75 meters (m), including two straight parts 63, 133 m, and an elbow, with curvature radius to diameter ratio of $r/D = 2.5$, connecting those two parts (Figure 2). The pipeline diameter (D) and thickness (t) are 0.5 m and 5.2 mm, respectively, which has the diameter to thickness ratio of $D/t = 96$. The pipeline's material is Carbon Steel ASTM (ASTM, 2011) SA-53 GR-A with

the material properties (given by Salimi Firoozabad et al., 2015): ρ = mass density = 7850 kg/m^3, E = Young's Modulus = 203509 MPa, ν = Poisson's Ratio = 0.3. It is assumed that the material has plastic behavior with Kinematic Hardening rule, and first yielding occurs at 310 MPa. The pipeline is meshed using an 8-node linear brick solid element (element C3D8R from ABAQUS element library). Using a mesh convergence analysis, the minimum mesh size is selected to be equal to 0.0625 m in cross section. However, the mesh size increased linearly to 0.125 m in farther regions from the elbow to alleviate the computational burden.
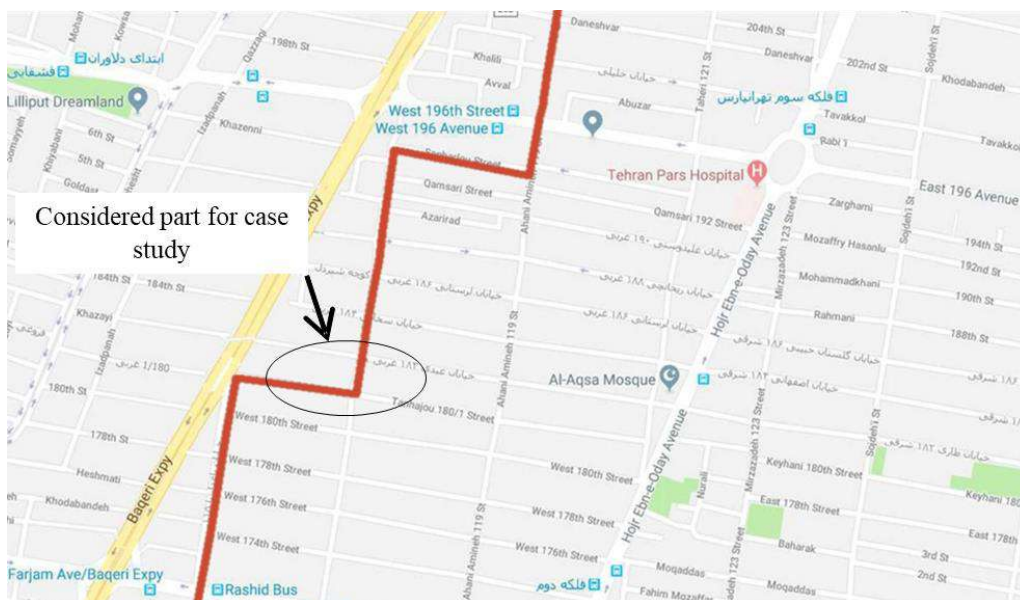
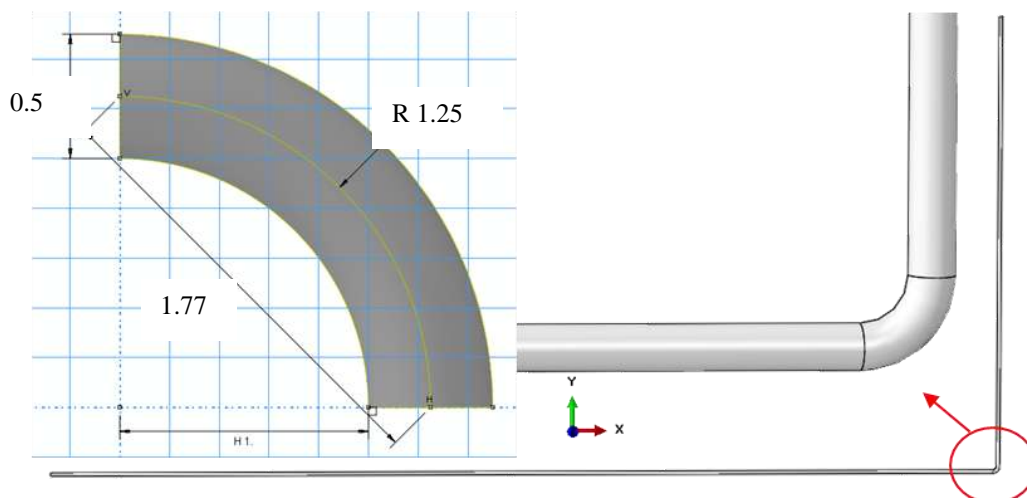**Fig. 1.** Tehran's pipeline map and the section considered in this research

Fig. 2. The pipeline and the elbow geometry (numbers unit is m)

2.2. Soil Characteristics

The soil material properties are selected considering the geotechnical reports about different locations in Tehran, Iran. Within this context, the density, elastic modulus, and Poisson's ratio parameters are considered to be 2000 kg/m^3, 50.5 MPa, and 0.35, respectively. The soil is modeled as a block with a rectangular cross section having the width and height of 6 and 2.5 m, respectively, which allows the pipe's burial depth to be equal to 2D as suggested in Vazouras et al. (2015). It should be noted that the ground should be first excavated for embedding the pipe and filled later to cover it. This causes the change in material properties of the soil above the pipe. To consider this issue, the filled soil is modeled with the new properties as: ρ = 1600 kg/m^3, E = 30 MPa and ν = 0.35. This is shown schematically in Figure 3. The soil plastic behavior is based on Mohr-Coulomb plasticity criteria which have been reported to be well matched to real soil characteristics in the literature by Anastasopoulos et al. (2007) and Loukidis et al. (2009). Considering the geotechnical

data, the friction angle (φ) and cohesion is selected to be 34° and 15 kPa (Motallebiyan et al., 2020), respectively. The dilation angle (ψ) is considered to be zero. The soil is modeled using 8-node linear brick solid C3D8R elements with a mesh size range of 0.25 (in cross section) to 0.5 m (along the model).

The procedure to draw the surrounding soil proposed in the literature (Vazouras et al., 2015) is that the soil is drawn as a complete rectangular box. However, the soil in this study is taken with a constant geometry along the pipeline's length in order to significantly reduce the number of soil elements. It should be noted that the soil section size is taken based on the recommendations available in the literature and also the sensitivity analysis performed to ensure that the boundaries do not affect the results. For example, the pipe's burial depth is selected to be equal to 2D as suggested in Vazouras et al. (2015). Furthermore, the obtained results also confirm that such soil size is sufficient as stress contour tend to be negligible at the soil surface.
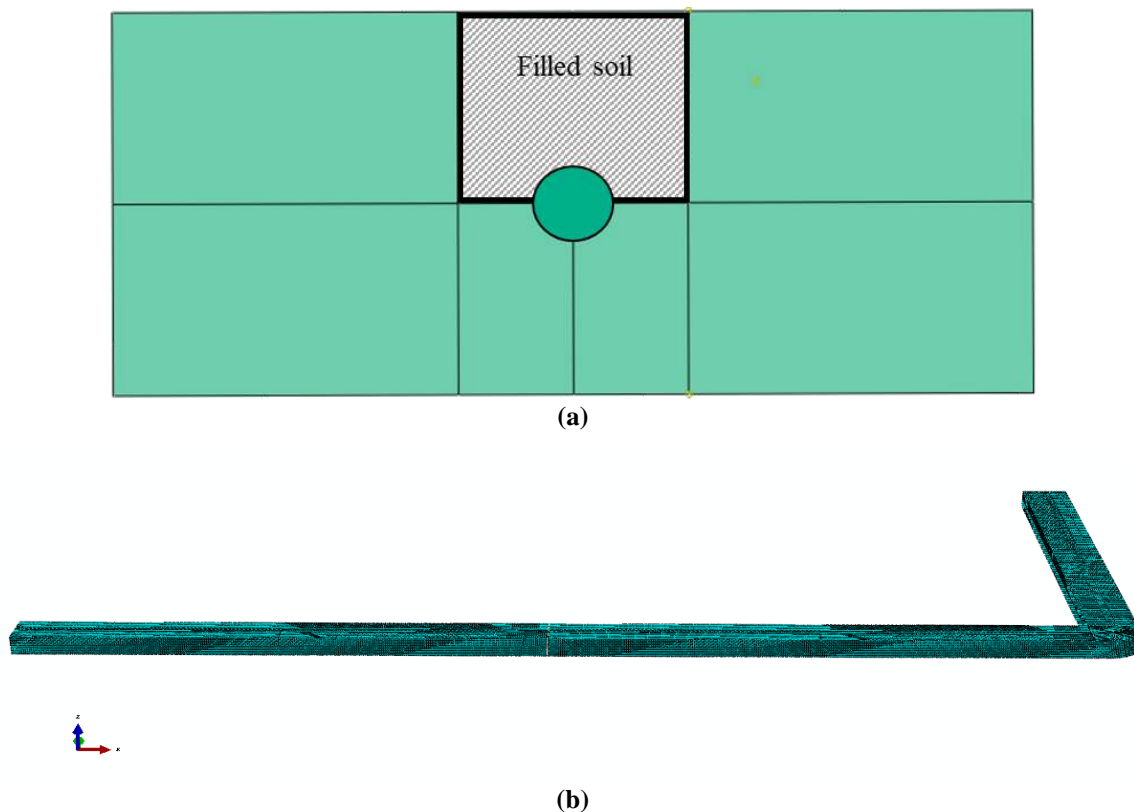

(a)

(b)

Fig. 3. Soil domain in FE analyses: a) Cross section; and b) Geometry

2.3. Loading and Boundary Conditions

Faults are fractures in the earth crust, with rocks on both sides moving against each other. Each fault (inclined) can be considered a surface, which divides rocks on its both sides into two parts. Tehran is surrounded and cut by several major faults (shown with redlines in Figure 4 according to Ritz et al., 2012). Therefore, it is very probable that any buried lifeline system would certainly cross one of those faults. Faults, based on the nature of their movement, are categorized into four types as strike-slip, normal, reverse, and oblique. It is generally stated (Hessami and Jamali, 2006) that the existing faults in Iran are mostly fall into strike-slip types, cause damages on the elbow crossing over them due to the axial deformation. Hence, a strike-slip fault is considered in this paper for investigating its effect on the pipeline passing through it. In this case, the soil is divided into two parts (exactly in the middle of the longer straight part) including the fixed part and the movable part. Therefore, the fault movement is applied horizontally (Y axis) on the vertical surface (Y-Z surface) of the movable part (see Figure 5). The movement was applied statically as the fault moves slowly in real cases and it is assumed to be equal to one meter (in total). It must be noted that the location of the fault and its crossing angle is subjected to change in the simulations in order to investigate the influence of these parameters on the behavior of elbow.

Generally, the FE analysis is divided into major three steps. First the geostatic step is run to establish the interaction between soil and pipe and calculating the geostatic stresses. The second step relates to applying the internal pressure of the pipe which is equal to 2 MPa according to the design pressure for these pipelines (ASME Boiler and Pressure Vessel Code II Part D, 2007). Finally, in the third step, the fault movement is applied as a displacement loading with the total value of 1 m in 10 seconds (with maximum increments set at 0.1 m). Note that the effect of nonlinear geometry is also accounted in the modeling.
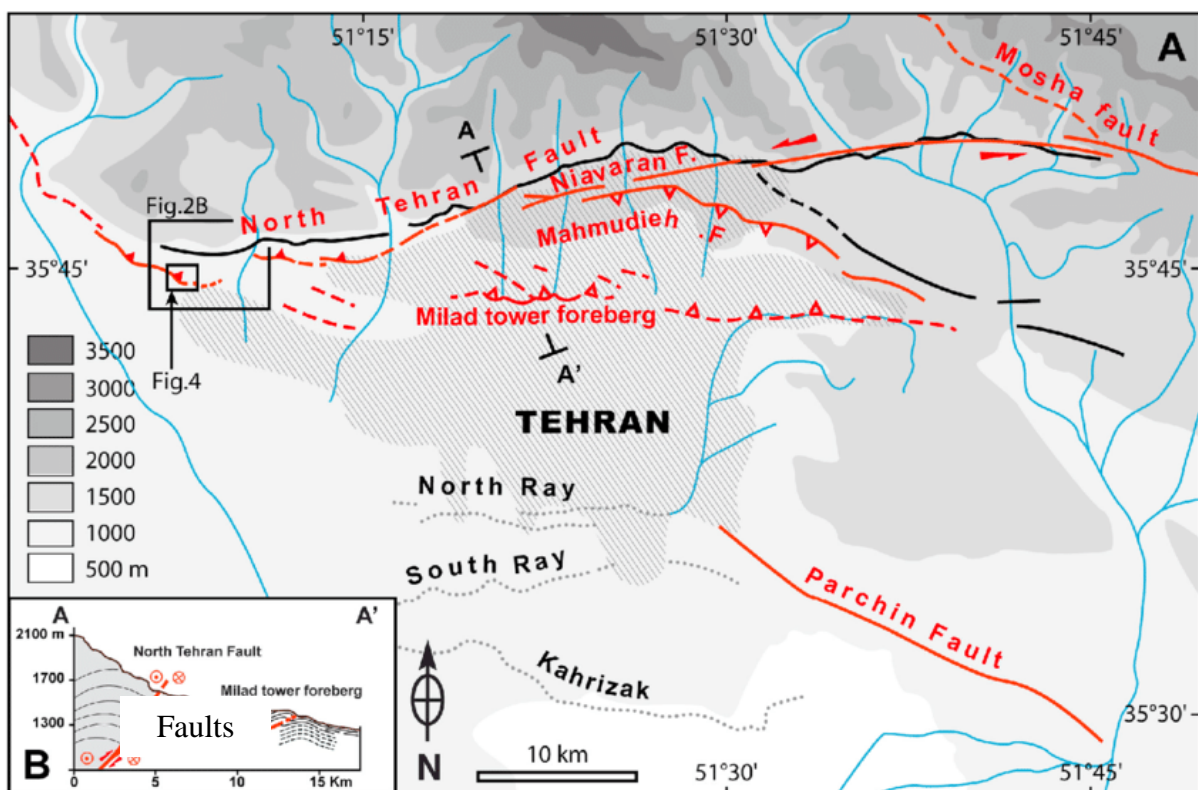

Fig. 4. Tehran's fault lines map (Ritz et al., 2012), (the red lines are the major fault lines)

Different types of boundary conditions are carefully applied to various parts of the model in order to represent the physics behind the model. Within this context, the boundary of the soil domain is fixed in all simulation steps. In addition, the horizontal movement of vertical surfaces of the soil was also constrained at the first two steps and set to be free in only movable part in the last step when the fault movement was applied. The pipeline was also horizontally constrained at both ends in the first two steps (since it is assumed that it is connected to the rest of the pipeline) while it is set as free at the end of the moving part at the last step.

One of the most important parameters in the analysis of buried pipelines is the interaction between the soil and pipe. It is mostly due to this parameter that fault movement affects the pipelines, which can lead to minor and major damages in these lifelines. A surface to surface interaction between soil and pipe material has been defined for this purpose, and a penalty based friction formulation has been adopted for the tangential behavior of the interaction with the friction coefficient set to 0.44 ($\tan(0.7\ \varphi)$) by Dash and Jain (2007).

3. FE Model Verification

In order to ensure the reliability of the FE simulation steps, which requires proper selection of material properties, soil-pipe interaction characteristics, and load/boundary conditions, it is required to compare and validate the results with a series of related analytical, laboratory or field works. For this purpose, a qualitative comparison is presented between the results of an experiment conducted in RPI, USA by Ha et al. (2008) on a polyethylene buried pipe subjected to normal fault and the FE numerical model generated in this research. In addition, the numerical results related to the behavior of a steel pipe elbow component under static load is verified with that of an experiment performed in South Korea by Salimi Firoozabad et al. (2016).

3.1. Verification for a Buried Pipe

In order to ensure the validity of numerical simulations, its results should be compared to those of the experiments. As it was not possible to conduct a test in this study, the reported experiments available in literature are used for verification. Consequently, the results of the tests conducted in RPI, USA on polyethylene pipes and surrounding soil subjected to a normal fault were extracted and compared with the simulations' results in this paper. The numerical simulations are performed using commercial ABAQUS FE software (2016). The details of the simulations are selected according to the specifications and characteristics presented in Ha et al. (2008) study. The experiment setup and soil surface deformation are shown in Figure 6. The specification of the pipe and the soil and the characteristics of its materials are as follows:
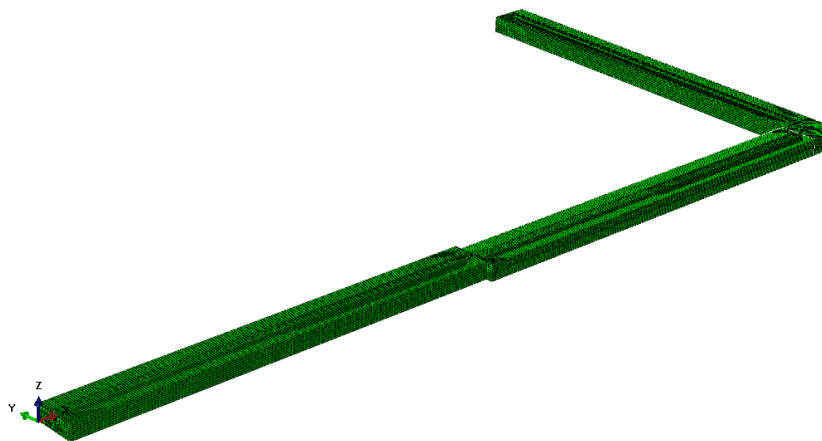

Fig. 5. The deformed FE model after applying the fault movement

High Density Polyethylene (HDPE) pipe for water service (AWWA Standard C901, 2003) with the diameter of 33.4 mm, thickness of 1.96 mm, and length of 1.14 m. The material properties are given in Table 1. The soil around the pipe was modeled as a solid cube, with the length, width, and thickness of 1.14 m, 0.76 m, and 0.2 m, respectively. The soil domain is divided (from the mid-point) into two fixed and moving parts. The soil domain was then assigned a material with the properties as given in Table 1.

The fault is normal and a 40 mm displacement was applied downward and perpendicular to the soil surface. To simulate the fault movement, a displacement loading is applied at the bottom of the soil in the movable part while

the bottom of the fixed part was restrained in all directions. The simulation results, after applying the fault movement, are shown in Figure 7. Considering the element sizes of the soil and pipe in Figure 7, and significance of the mesh size in interaction analysis, it should be noted that a robust verification is made through the experiments, and it is observed that the mesh size needs to be selected carefully to capture the structural behavior of the soil and the pipe accurately. As for the soil-pipe interaction, the mesh size of soil is the same through the connected surface with the pipe and double the size through the pipe length. The same size was used in simulation verification with the experiment conducted in RPI, USA by Ha et al. (2008).

Table 1. The material properties of the performed experiment in Ha et al. (2008)

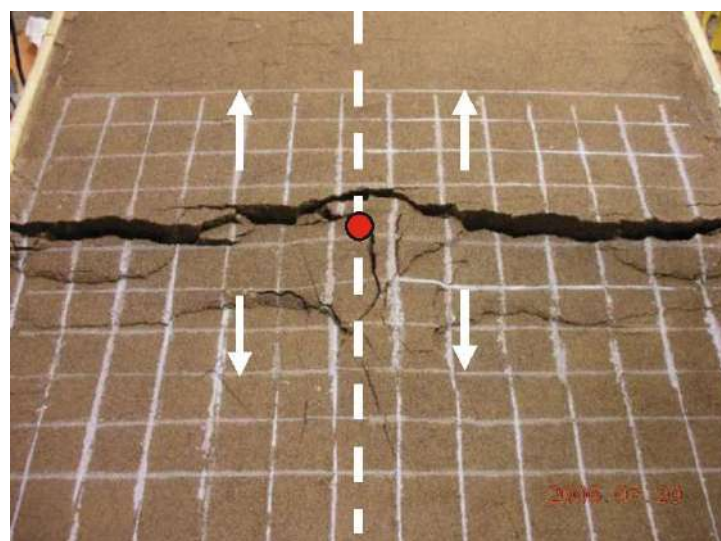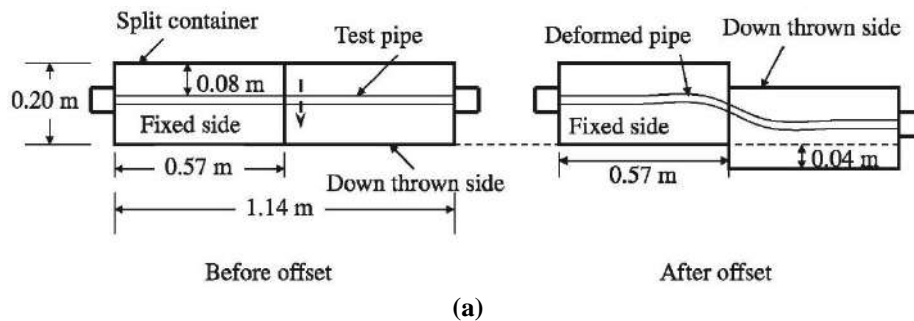| Material	Density (kg/m^3)	Elastic modulus (MPa)	Poisson's ratio	Friction angle (degree)	Cohesion coefficient (kPa)
HDPE Pipe	958	880	0.4	N/A	N/A
Soil	1498	42.747	0.35	0	15

(a)

(b)

Fig. 6. a) Experiment setup; and b) Soil surface deformation at the end of experiment (Ha et al., 2008)
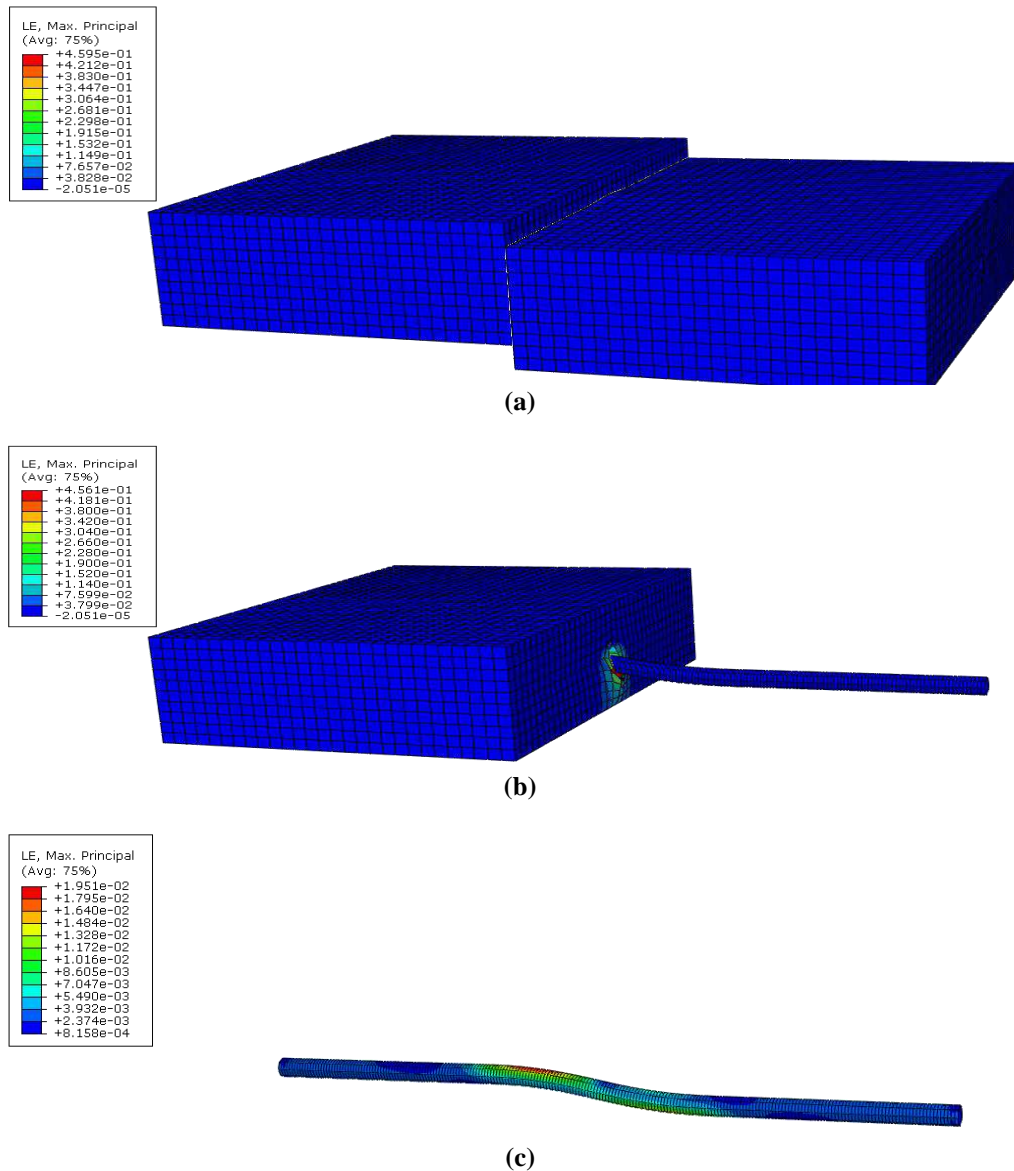
Fig. 7. Maximum principal stain after application of fault movement: a) Soil; b) Soil and pipe; and c) Pipe
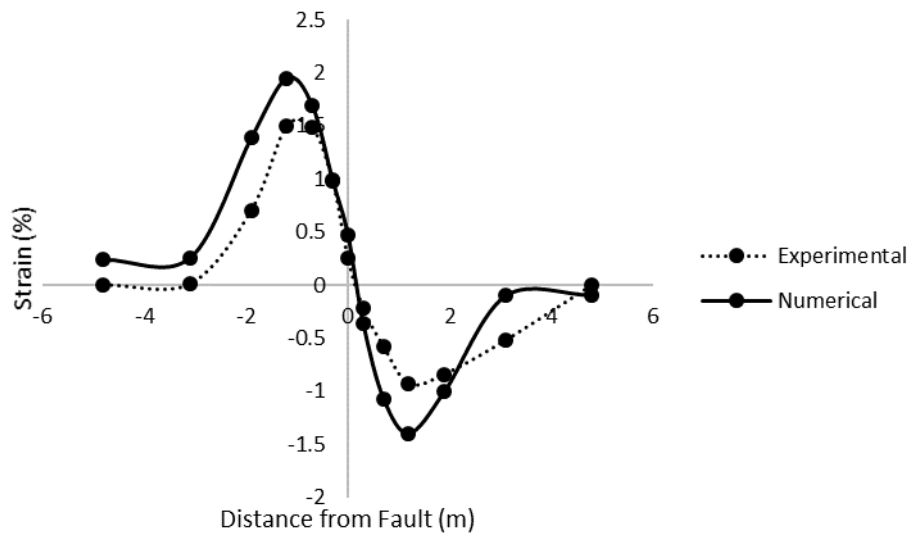
The axial and flexural strain across the pipe were compared with that of the experiment as shown in Figure 8. Note that the experiment was carried out under the gravity acceleration of 12.2g, and the same gravity value is employed in the numerical simulation. Due to this reason, the axial and flexural strains extracted along the pipe at different locations, the distance between these points, and the distance from the fault location, are multiplied by the scaling factor of 12.2.

According to the results in Figure 8 and considering the uncertainties associated with the difference between the real material properties, loading and boundary conditions, and other modeling details, it can be concluded that there is a good agreement between the experimental and numerical simulations, which proves the fidelity of the FE simulations. One of the major reasons of the existing difference between the results can be attributed to the plastic behavior of polyethylene pipes. This type of behavior is modeled using a simple kinematic plastic behavior due to the lack of information for using more complex material properties. Besides, in our simulations, a steel pipeline was used which is separately verified and discussed subsequently. Hence, it could be reasonably implied that the FE simulation was reliable enough to be used in the presented case study.
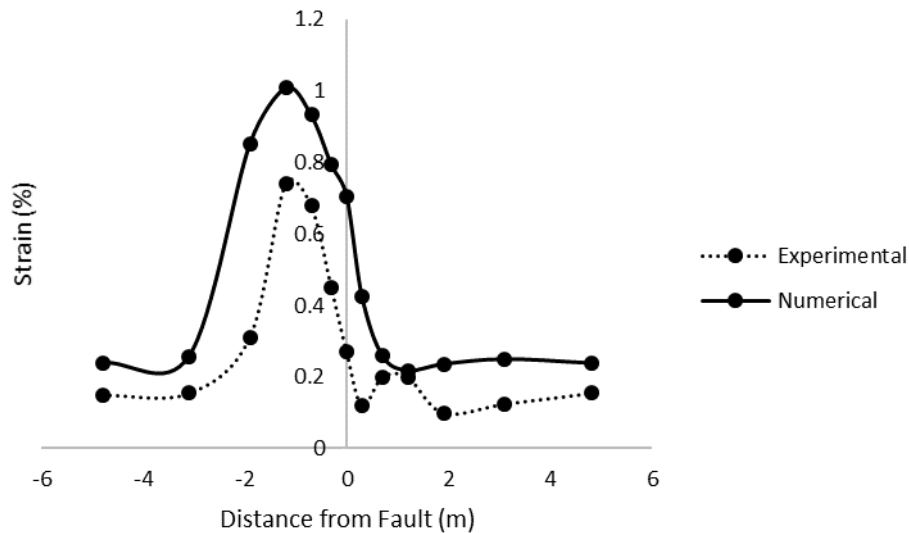
(a) Comparison of axial strain

(b) Comparison of bending strain

Fig. 8. The axial and flexural strain comparison between experimental and numerical analysis

3.2. Verification of Steel Pipe Elbow Simulation

The pipeline simulation has been verified by comparing it with a series of experiments performed on actual test specimens. The experiments were performed by the first author (of this paper) in the Department of Civil Engineering at Pusan University, Pusan, South Korea. The specimen was a 0.075 m (3 inches) elbow component (Figure 9) with similar characteristics as our case study pipeline (Carbon Steel ASTM SA-53 GR-A) with the density of $\rho = 7850$ kg/m^3, elastic modulus of E = 203509 MPa, and a Poisson's ratio of $\nu = 0.3$. The test setup and detailed descriptions are provided in Salimi Firoozabad et al. (2016). The component was first subjected to an internal pressure of 3 MPa and thereafter a series of various monotonic and cyclic displacement loadings are applied. The elbow is fixed in all directions except the rotation along its axis. The other end of the elbow is the location where it is subjected to gradual displacement loading with the maximum speed of 36 mm/min.

The mechanical properties of the elbow, its geometry, boundary conditions, and loading are simulated in accordance with the experiments performed. Kinematic hardening rule is used in order to simulate

the plastic behavior of the component, as this rule is more accurate as the elbow is loaded cyclically both in tension and compression. In the numerical analysis, an internal pressure is first applied in a static step then, a cyclic displacement equal to 60 mm is applied as the next step. Similar to the pipeline, the elbow is modeled using C3D8R solid elements from ABAQUS element library. It should be noted that shell elements can also be used for modeling the pipeline. However, it is found that for contact (interaction) simulation between soil and pipe, solid elements provide more accurate results and are computationally more efficient. Furthermore, solid elements are used for modeling the elbow and they are tied to the beam elements as shown in

Figure 9. The mesh size is selected to be 5 mm even though it converged at 10 mm. The difference is not that much but for dynamic analysis, 5 mm would be the better choice. It is worthwhile to mention that tying the end nodes of solid elements to the beam constrains all displacements of the nodes of the exposed faces of the solid elements to remain to the cross-sectional plane. The cross-sectional plane is in turn characterized by six degrees of freedom and constrained to the six degrees of freedom on the end node of the beam element. This is performed in order to be able to handle boundary conditions at the fixtures which are connected to the ends of the elbowed pipe.
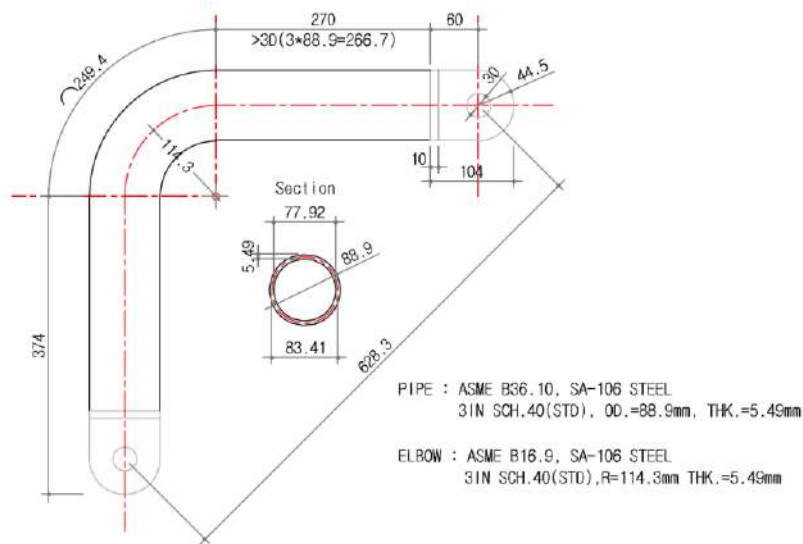
(a)
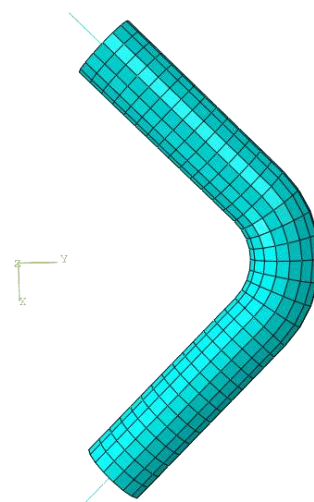
(b)

Fig. 9. a) The elbow specimen in Salimi Firoozabad (2016); and b) FE numerical model

The result of numerical static analysis is compared with the experiments using $\pm$ 60 mm cyclic displacement in the X direction to one end of the elbows while the other end is fixed. The results are shown in Figure 10 as the force-displacement graph at the point of applied displacement, in the experiment and simulation. It can be seen that the difference between numerical result and the actual sample is negligible. This proves the reliability of the used kinematic hardening model, and therefore, it is used for FE modeling of the buried pipeline in this paper.

4. Failure/Yield Criterion

The exact structural failure point of a steel pipe elbow has not yet been fully estimated. Therefore, various criteria have been defined, expressed and examined in the literature and standard code provisions. These criteria are mostly expressed for straight pipes based on a limit state defined in tension and compression. Consequently, tensile and compressive stress and/or strain capacities are evaluated. A cross sectional distortion limit is also defined in some cases due to local buckling. It must be noted that fault movement causes large plastic strains; therefore, pipeline performance is better to be evaluated in terms of longitudinal strain, rather than stress. This means that the fault movement is clearly governed by a displacement-controlled based scenario.

The tensile strain capacity of the steel pipe is highly dependent on the fracture of pipe wall and it is controlled by the strength of pipe at the welding point, so that the stress and strain rate at the weakest point in the pipe results in defective welding. This capacity has been considered in a range of approximately 2 to 5 percent in the literature as explained in the following references. Canadian Standard Association (CSA Z662) (2007) proposes an empirical equation based on parameters including: weld toughness, the yield-tensile strength ratio, and defect height and length ratio over the pipe wall thickness. This value would lay in a range of 3 to 5 percent based on general values. EN1998-4 provisions (1998) and ASCEMOP119 (2009) also suggest 3% in the case of buried steel pipelines subjected to fault movement. ASME code provision for Boiler and Pressure Vessel (2007) adopts a so-called Twice Elastic Slope (TES) method for strain limit calculations. Furthermore, a value of 1 to 2 percent is recommended for normal operation of hydrocarbon pipelines by Pipeline Research Council International (2004).
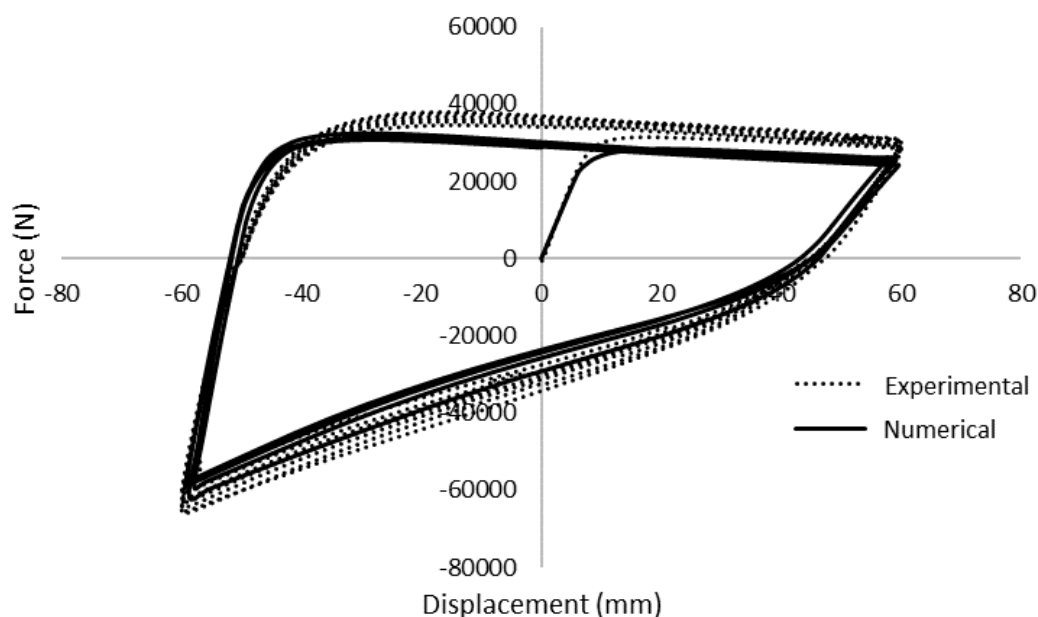

Fig. 10. Comparison of experimental and numerical results in force-displacement graph

Due to the vital importance of elbow components, the capacity limit in this study is considered to be the lowest of the above-mentioned values. For this purpose, it is required to calculate the capacity of the elbow based on TES method. Hence, a numerical simulation has been performed on a steel pipe elbow with the exact same geometry and material properties, as the pipeline elbow in this research. An internal pressure equal to 2 MPa is firstly applied and then a gradually increasing static load is applied to one end as an incremental increasing displacement. Accordingly, the elbow is free to move at one end and fixed on the other. Figure 11 shows the geometry, loading, and boundary conditions (BCs) of the simulated elbow and stress contour after load application.

As it can be seen in Figure 11, the location of the critical point is in the internal part of the curvature at the middle of the elbow. The same location is identified as maximum stress critical point in the numerical simulation of buried pipeline, which verifies the correct application of load and BCs. Accordingly, the force and strain of that point is extracted, and the corresponding graph is derived and shown in Figure 12. The line in which the slope is twice the elastic line's slope is drawn. Hence, the intersection of this line and the stress-strain curve would indicate the strain limit which in this case is 0.009 (shown in Figure 12). Given that this amount is less than the other indicated values for tensile limit state, 0.009 is selected as the final capacity in this study and the results of the failure analysis of the pipeline crossing over the fault is compared with this value.
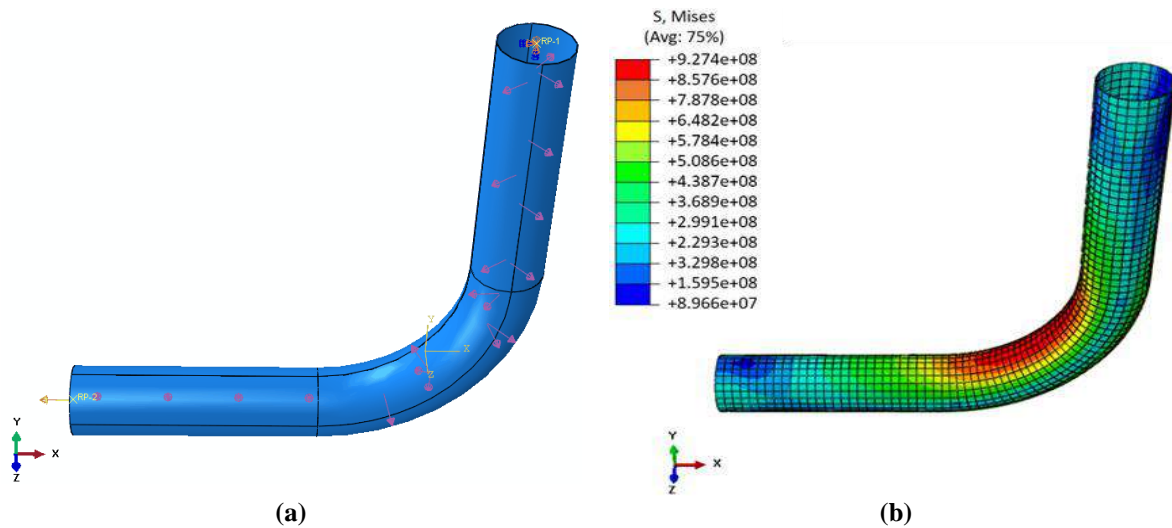

(a)   **(b)**

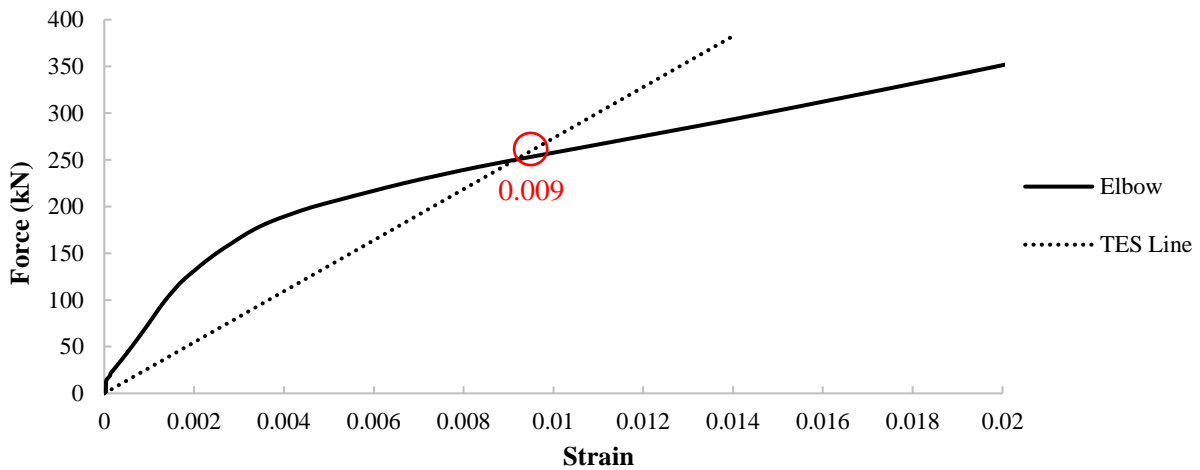**Fig. 11.** a) Geometry; and b) Von Mises stress contour results of the elbow

Fig. 12. Force-strain graph at the critical point of the elbow

5. Results and Discussion

5.1. Effect of Angle and Distance to Elbow

In this section, the results of numerical simulation of the pipeline under displacements induced by a strike-slip fault are presented. The effect of two important parameters on the behavior of elbow joint in the pipeline has been investigated. These two parameters are: the angle of fault crossing the pipeline and the elbow joint distance from the fault location. For this purpose, three fault line angles of 90, 60, and 45 degrees are considered with respect to the axis of the pipeline. In addition, three values for the distance of the fault location to the elbow is considered: 68 m (middle of the soil length), 53 m, and 38 m from the elbow. Therefore, a total of 9 simulations (given in Table 2) have been performed. The distances are not taken further closer to the elbow as the study is more focused on the strain in elbow caused by the soil-pipe interaction rather than the results caused by bending due to the fault movement itself. The affected range of pipeline in length crossing over a fault proposed by Karamitros et al. (2011) is 35 to 45 times of pipe diameter (17.5 to 22.5 m in this study) on both sides of the fault. Hence, the minimum distance of fault to elbow is taken 38 m which is outside of the range to be influenced by fault movement.

The structural behavior of the elbow is then expressed as its maximum principal strain response for each simulation case. Then, the results are compared with the failure criterion in order to identify the most critical case. This critical case is next taken for evaluation of the effect of soil properties on the elbow component response. Finally, some practical recommendations are presented for engineering practice.

The fault movement is uniformly applied perpendicular to the horizontal surface of the soil in the moving part. It should be noted that the maximum displacement of 100 cm is considered for fault movement and it is gradually applied in 1000 increments.

In the FE simulations where the fault line is perpendicular to the soil, the elbow did not show any displacement due to the fault movement. It happened in all cases even when the fault is in the nearest considered distance to elbow (38 m). It is observed that the pipeline suffers no damage approximately 10 m from the fault line on each side. Consequently, the elbow would be safe unless it is well close to the fault line. In addition, the maximum Von Mises stress (480 MPa) and strain (0.02) observed is around the fault line on both sides as it is expected. Figure 13 shows the maximum Von-Mises stress of the pipeline after the fault movement is applied in the simulation case in which the fault line is occurred at the distance of 38 m from the elbow.

In the next three cases, the fault movement is applied to the soil with crossing angle of 60°, and three different distances from the elbow. The maximum strain within the elbow in the first two cases is insignificant. However, in the last case (Figure 14), where the fault distance to elbow is 38 m, it reaches to 0.0045.

Table 2. Simulation cases

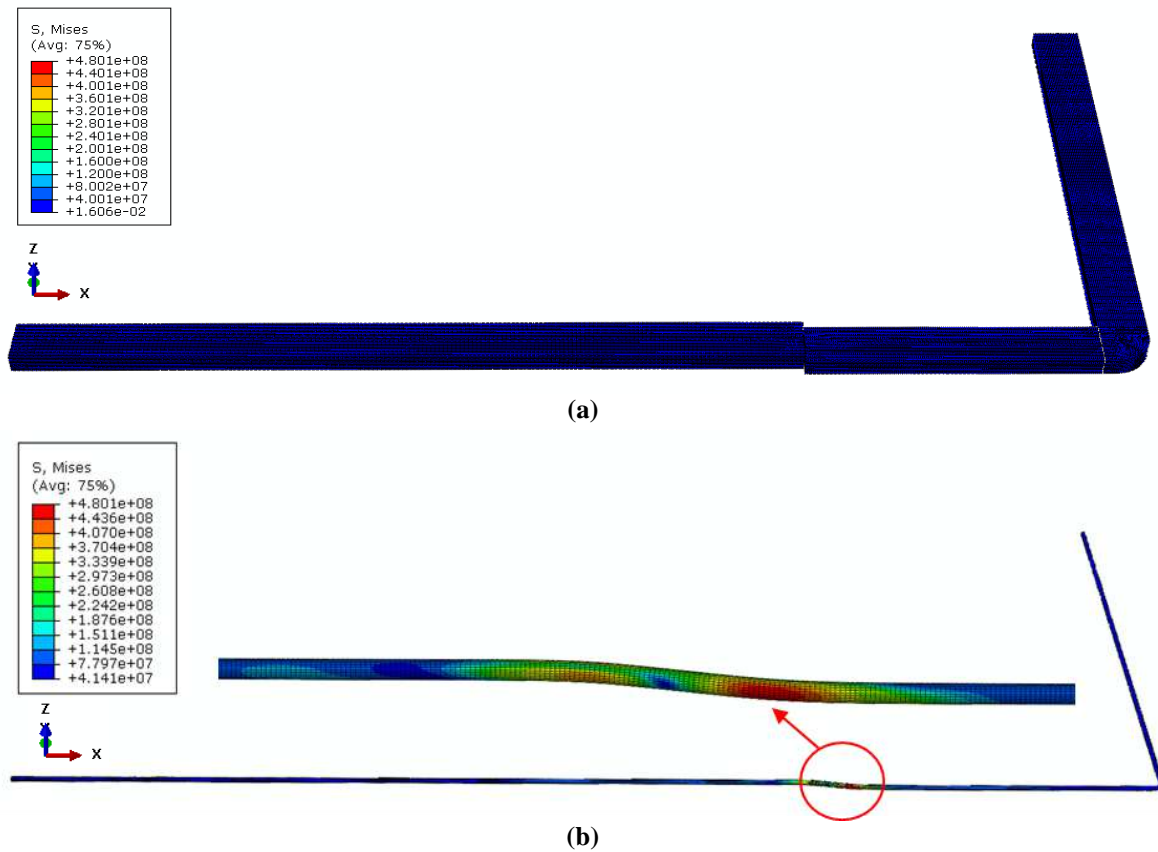| Simulation No.	Simulation name	Fault crossing angle	Distance to elbow
1	A1	90	68
2	A2	90	53
3	A3	90	38
4	B1	60	68
5	B2	60	53
6	B3	60	38
7	C1	45	68
8	C2	45	53
9	C3	45	38

(a)

(b)

Fig. 13. The Von Mises stress contour in: a) Soil; and b) Pipeline (simulation A3)

Finally, three more simulations with the fault distance to elbow of 68, 53, and 38 m are performed for crossing angle of 45°. It is observed that the elbow undergoes no strain in the first case, then the strain reaches to 0.001 in the second case, and it reaches to the peak of 0.01 when the distance to elbow is 38 m. Hence, the elbow suffers a significant damage beyond the failure criterion when the fault crosses the pipeline at 38 m from the elbow with 45°. Figure 15 shows the stress contour for pipeline subjected to fault movement in the last simulation case, along the logarithmic strain contour in elbow. It can be seen that the most critical point of the elbow is exactly the same point as the one identified in failure criterion estimation of the elbow (given in Section 3).

Different simulations and analysis scenarios indicate that when the pipeline passes through the fault perpendicularly, the deformations and strains in the pipeline vanishes at short distances from the fault (about 7.5 m), so the rest of the pipeline would be safe. The reason could be attributed to the effect of soil continuity on both sides of the fault and the pipe flexibility along its length. On the other hand, when the pipeline crosses the fault with an angle less than 90°, the fault movement has both vertical and horizontal components. The horizontal component, considering the volume of soil and its interaction with the pipe, loads the pipe in the axial direction, which causes significant increase in the strain rate of the elbow.

5.2. Effect of Soil Properties

It is observed in the previous section that the most critical simulation case is when the crossing angle is 45° and it is located at the distance of 38 meter from the elbow. Therefore, this case is selected for the parametric study on the effect of soil properties on the elbow performance. The varying soil properties considered for the parametric study are: elastic modulus, cohesion, and friction angle. All these parameters considered as two different values (within the range for sandy clay type of soil based on Unified Soil Classification

System (USGS) (2011)) other than the original values. The elastic modulus is taken as 35 and 70 MPa, the cohesion is selected to be 30 and 45 kPa, and the friction angles are set to be 30 and 40 degrees. It must be noted that the friction coefficient, for the interaction between soil and pipe, changes accordingly for each friction angle value. Hence, another six simulations are performed and their corresponding principal strains are extracted and compared.
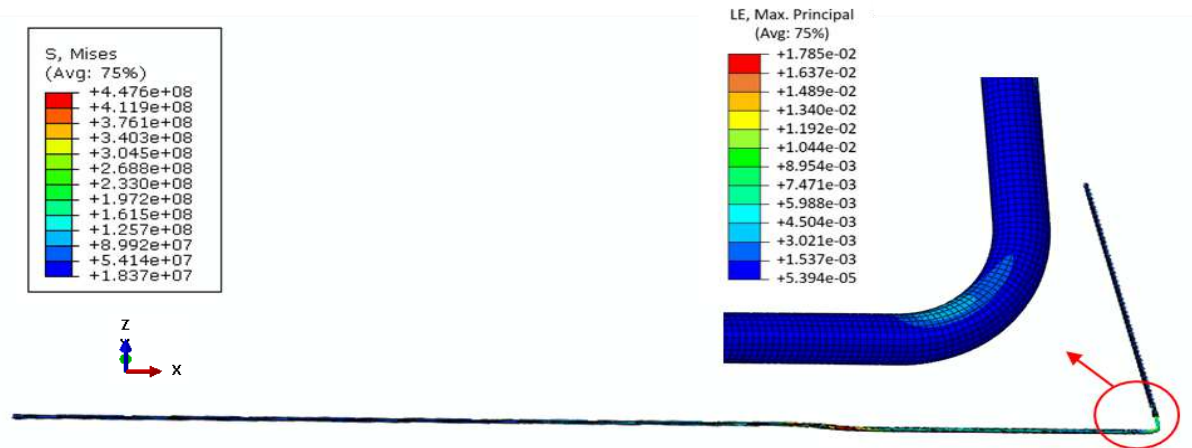

Fig. 14. The stress and strain contour in pipeline and elbow (Simulation B3)
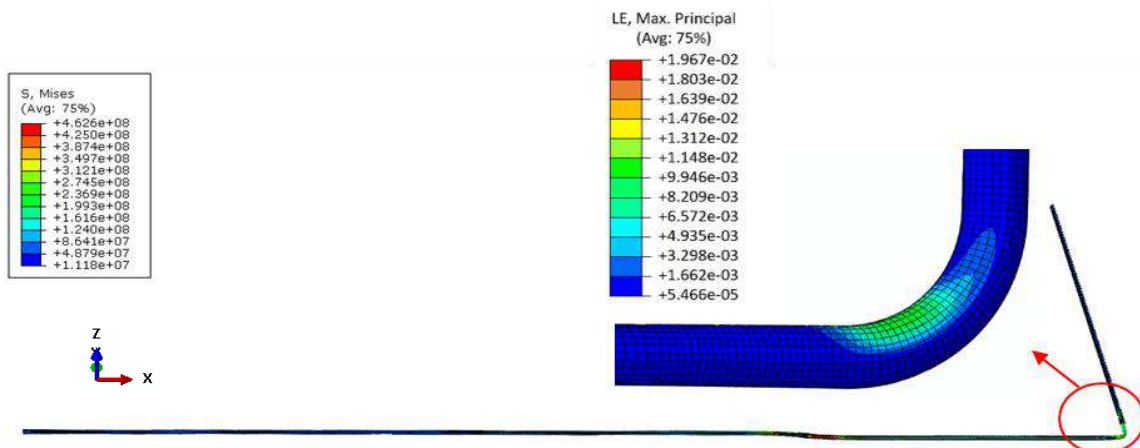
Fig. 15. The stress and strain contour in pipeline and elbow (Simulation C3)
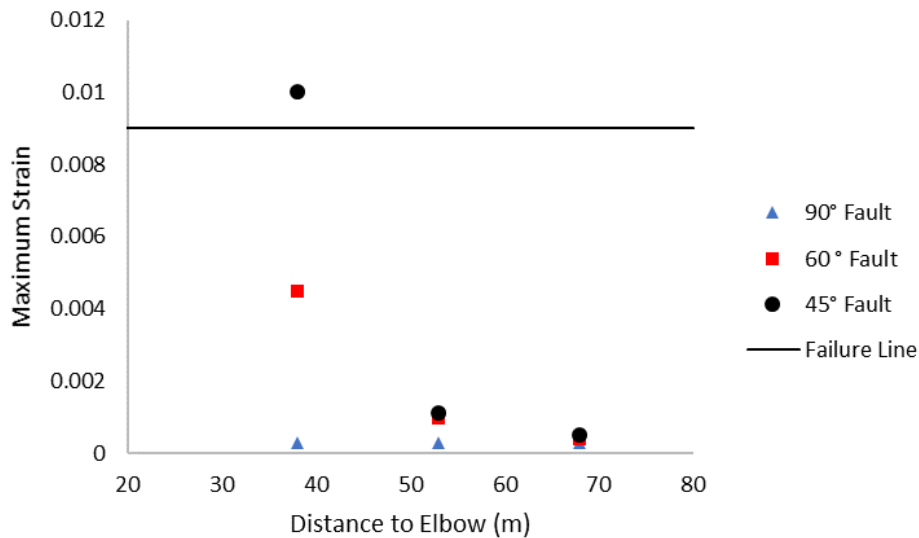

Fig. 16. Results of all simulations

It is observed that the cohesion changes would not significantly affect the elbow performance. Then, the elastic modulus which is originally 50.5 MPa, changed to 35 and 70 MPa. In this case also, an increase in elastic modulus did not make a significant change in final results. The friction angle on the other hand, has a considerable impact on the elbow, approximately 85 percent in ten degrees. The strain value is 0.007 at friction angle 30°, 0.013 at 40° friction angle. Therefore, the higher value of friction angle leads to higher strain level as it is expected because it changes the friction coefficient which increases the applied displacement at elbow due to fault movement.

It is noted that the strain variation in straight part of pipeline around the fault in different cases are more significant. Figure 17 shows the strain versus distance from fault results for all six simulation cases for different soil properties. Strain variation can be seen for each soil properties and it can be compared with the original soil properties.

Most standard provisions highly recommend not constructing around any active fault due to the severity of the damage as a result of fault movement. However, in the case of pipelines construction, it is inevitable to cross the fault due to the large length of these pipelines. One of the most common sections used in pipelines are steel pipe elbows.

These sections must be analyzed and checked with an extra care as they are more vulnerable (due to less failure capacity) than straight sections in pipelines. However, their behavior under fault movement has not been much investigated. Therefore, there are not much of any recommendations on their safety evaluation crossing over active faults. Accordingly, available recommendations for straight pipes in the literature have been expanded on the elbow sections.

The numerical analysis and parametric study conducted on a real case of water transmission pipelines indicated the importance of elbow failure analysis. For instance, it is understood that the elbow could be damaged at the farther distance to a fault as much as 38 m (68D, i.e. 68 times of pipe diameters), which is quite significant. Other researchers such as Karamitros et al. (2011) have reported smaller ranges of 35 to 45D on either side of the crossing fault. It is observed when the pipeline crosses over a fault, the safe distance to fault line for elbow to be placed, is highly dependent on crossing angle. Another effective parameter in elbow safe performance is the internal angle of friction of soil. On the contrast, the soil's cohesion, and elastic modulus has a negligible effect on the pipeline behavior.
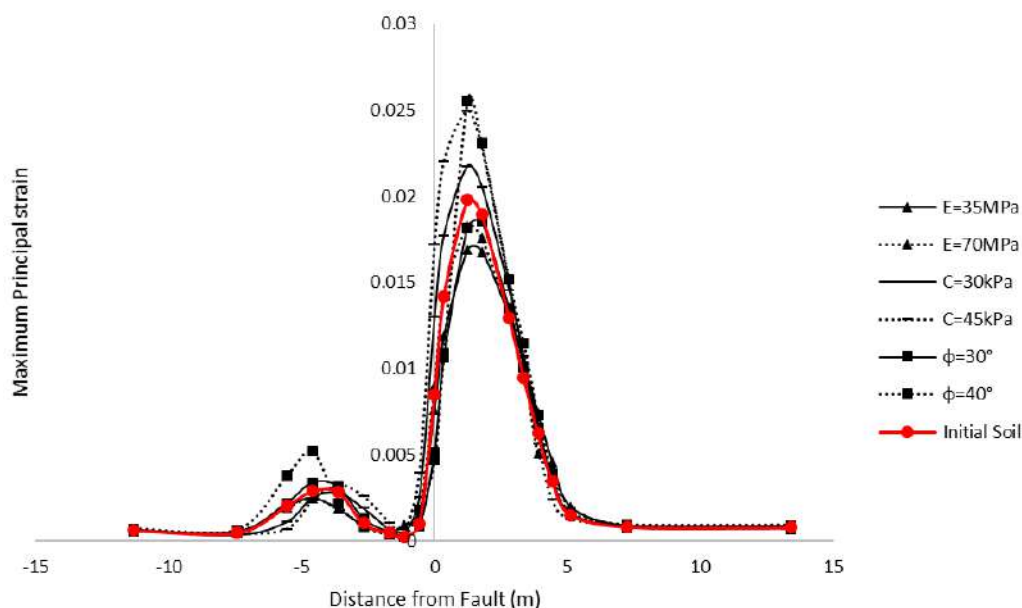

Fig. 17. Strain variation around the fault line for all soil properties

6. Conclusions

A numerical analysis was performed on a buried water transmission pipeline. The simulations were verified with the experimental data reported in the literature. The elbow component's behavior was investigated through a defined failure criterion. The effects of fault crossing angle and distance to elbow was also investigated. Furthermore, the soil characteristics effects on the elbow's response was evaluated.

Different simulations and analysis scenarios indicated that: when the pipeline crosses perpendicular to a strike-slip fault, the deformations and strains in the pipeline vanishes at short distances from the fault (about 7.5 m) so an elbow would be safe in a distance more than 7.5 m. On the other hand, when the pipeline crosses the fault with an angle less than 90°, the fault movement had both vertical and horizontal component. The horizontal component applied displacement loading on the pipe in the horizontal direction, which caused the strain rate to increase in the elbow. A safe distance for the elbow from the fault was then estimated as 38 and 53 m for the crossing angle of 60 and 45°, respectively.

It was observed that the soil cohesion changes would not significantly affect the elbow performance. In the case of elastic modulus also, the variations did not make a significant change in the final results. The friction angle on the other hand, had a considerable impact on the elbow, approximately 85 percent in ten degrees. The strain value was 0.007 at friction angle 30°, 0.013 at 40° friction angle.

7. Recommendation for Future Study

A more comprehensive study including more numerical analysis considering other crossing angles, pipe and elbow geometry and soil properties can lead to comprehensive recommendation and safety regulations for underground pipelines design.

8. References

ABAQUS/Standard. (2016) *User's manual*, Providence, RI, USA: Simulia.

American Society of Mechanical Engineers (ASME). (2007). *Boiler and pressure vessel code,* NY, United States.

American Water Works Association. (2003). *AWWA standard for polyethylene (PE) pressure pipe and tubing, 1/2 in. (13 mm) through 3 in. (76 mm), for water service*, ANSI/AWWA C901-02, Denver, Colorado, United States.

Anastasopoulos, I., Gazetas, G., Bransby, M.F., Davies, M.C.R. and El Nahas, A. (2007). "Fault rupture propagation through sand: finite-element analysis and validation through centrifuge experiments", *Journal of Geotechnical and Geoenvironmental Engineering*, 133(8), 943-958.

ASTM Committee D-18 on Soil and Rock. (2011). *Standard practice for classification of soils for engineering purposes (Unified Soil Classification System)*, ASTM International, West Conshohocken, PA, USA.

Bildik, S. and Laman, M. (2015). "Experimental investigation of the effects of pipe location on the bearing capacity", *Geomechanics and Engineering*, 8(2), 221-235.

Canadian Standard Association. (2007). *Oil and gas pipeline system*, Z662–07, Ottawa, ON, Canada.

Castiglia, M., Santucci de Magistris, F. and Napolitano, A. (2018). "Stability of pipelines in liquefied soils: Overview of computational methods", *Geomechanics and Engineering*, 14(4), 355-366.

Dash, S.R. and Jain, S.K. (2007). *Guidelines for Seismic Design of buried pipelines*, IITK-GSDMA Codes, National Information Center of Earthquake Engineering, Indian Institute of Technology, Kanpur, India.

De Normalisation, Comité Européen. (1998). *Eurocode 8, Part 4: Silos, tanks and pipelines*, CEN EN 4, European Committee for Standardization, Brussels, Belgum.

Firoozabad, E.S., Jeon, B.G., Choi, H.S. and Kim, N.S. (2015). "Seismic fragility analysis of seismically isolated nuclear power plants piping system", *Nuclear Engineering and Design*, 284, 264-279.

Firoozabad, E.S., Jeon, B.G., Choi, H.S. and Kim, N.S. (2016). "Failure criterion for steel pipe elbows under cyclic loading", *Engineering Failure Analysis*, 66, 515-525.

Ha, D., Abdoun, T.H., O'Rourke, M.J., Symans, M.D., O'Rourke, T.D., Palmer, M.C. and Stewart, H.E. (2008). "Buried high-density polyethylene pipelines subjected to normal and strike-slip faulting, A centrifuge investigation", *Canadian Geotechnical Journal*, 45(12), 1733-1742.

Hassan, T., Rahman, M. and Bari, S. (2015). "Low-cycle fatigue and ratcheting responses of elbow piping components", *Journal of Pressure Vessel Technology*, 137(3), 031010-1 to 12.

Hessami, K. and Jamali, F. (2006). "Explanatory notes to the map of major active faults of Iran", *Journal of Seismology and Earthquake Engineering*, 8(1), 1-11.

Honegger, D.G. and Nyman, D.J. (2004). *Guidelines for the seismic design and assessment of natural gas and liquid hydrocarbon pipelines*, Pipeline Research Council International, Inc., Arlington, Va. Catalogue, (L51927).

Karamitros, D.K., Bouckovalas, G.D., Kouretzis, G.P. and Gkesouli, V. (2011). "An analytical method for strength verification of buried steel pipelines at normal fault crossings", *Soil Dynamics and Earthquake Engineering*, 31(11), 1452-1464.

Kim, S.W., Jeon, B.G., Hahm, D.G. and Kim, M.K. (2019). "Seismic fragility evaluation of the base-isolated nuclear power plant piping system using the failure criterion based on stress-strain", *Nuclear Engineering and Technology*, 51(2), 561-572.

Kiran, A.R., Reddy, G.R. and Agrawal, M.K. (2018). "Experimental and numerical studies of inelastic behavior of thin walled elbow and tee joint under seismic load", *Thin-Walled Structures*, 127, 700-709.

Kokavessis, N.K. and Anagnostidis, G. (2006). "Finite element modelling of buried pipelines subjected to seismic loads: Soil structure interaction using contact elements", In: *Proceedings of the ASME PVP conference*, Vancouver, BC, Canada.

Loukidis, D., Bouckovalas, G.D. and Papadimitriou, A.G. (2009). "Analysis of fault rupture propagation through uniform soil cover", *Soil Dynamics and Earthquake Engineering*, 29(11-12), 1389-1404.

Majrouhi Sardroud, J., Fakhimi, A., Mazroi, A., Ghoreishi, S.R., Azhar, S. (2021). "Building information modeling deployment in oil, gas and petrochemical industry: An adoption roadmap", *Civil Engineering Infrastructures Journal*, 54(2), 281-299.

Motallebiyan, A., Bayat, M. and Nadi, B. (2020). "Analyzing the effects of soil-structure interactions on the static response of onshore wind turbine foundations using Finite Element method", *Civil Engineering Infrastructures Journal*, 53(1), 189-205.

Newmark, N.M. and Hall, W.J. (1975). "Pipeline design to resist large fault displacement", In: *Proceedings of US National Conference on Earthquake Engineering,* pp. 416-425.

Pouraria, H., Seo, J.K. and Paik, J.K. (2017). "Numerical study of erosion in critical components of subsea pipeline: Tees vs bends", *Ships and Offshore Structures*, 12(2), 233-243.

Ritz, J.F., Nazari, H., Balescu, S., Lamothe, M., Salamati, R., Ghassemi, A., Shafei, A., Ghorashi, M. and Saidi, A. (2012). "Paleoearthquakes of the past 30,000 years along the North Tehran Fault (Iran)", *Journal of Geophysical Research: Solid Earth*, 117(B6).

Sabermahany, H. and Bastami, M. (2019). "Refinement to the existing analytical methods of analysis of buried pipelines due to strike-slip faulting", *Civil Engineering Infrastructures Journal*, 52(2), 309-322.

Tsatsis, A., Loli, M. and Gazetas, G. (2019). "Pipeline in dense sand subjected to tectonic deformation from normal or reverse faulting", *Soil Dynamics and Earthquake Engineering*, 127, 105780.

Varelis, G.E., Karamanos, S.A. and Gresnigt, A.M. (2013). "Pipe elbows under strong cyclic loading", *Journal of Pressure Vessel Technology*, 135(1), 011207.

Varelis, G.E. and Karamanos, S.A. (2015). "Low-cycle fatigue of pressurized steel elbows under in-plane bending", *Journal of Pressure Vessel Technology*, 137(1), 011401-1 to 10.

Vazouras, P. and Karamanos, S.A. (2017). "Structural behavior of buried pipe bends and their effect on pipeline response in fault crossing areas", *Bulletin of Earthquake Engineering*, 15(11), 4999-5024.

Vazouras, P., Dakoulas, P. and Karamanos, S.A. (2015). "Pipe–soil interaction and pipeline performance under strike, Slip fault movements", *Soil Dynamics and Earthquake Engineering*, 72, 48-65.

Effectiveness of Reusing Steel Slag Powder and Polypropylene Fiber on the Enhanced Mechanical Characteristics of Cement-Stabilized Sand

Ghanbari, M.[1] and Bayat, M.[2]*

[1] M.Sc., Department of Civil Engineering, Najafabad Branch, Islamic Azad University, Najafabad, Iran.
[2] Assistant Professor, Department of Civil Engineering, Najafabad Branch, Islamic Azad University, Najafabad, Iran.

ABSTRACT: Waste generated by steel industry cases environmental and economic problems. Therefore, it becomes very important to utilize steel industrial waste material in a proper manner. One promising use for this huge amount of industrial waste is soil improvement. In this work, Unconfined Compressive Strength (UCS) tests were conducted to study the influence of steel slag on the mechanical characteristics of cement-stabilized sand. The UCS tests were conducted on the compacted specimens which prepared in the laboratory at their Optimum Moisture Content (OMC) and modified proctor Maximum Dry Density (MDD). The results indicate that use of steel slag powder as a partial replacement of chemical stabilizer such as cement in soil stabilization has advantages from economic, environmental and technical points of view. The highest value of UCS was observed in the sample containing 7.2% cement and 0.8% steel slag powder. Beyond optimum steel slag powder dosage, the UCS value decreased. The addition of polypropylene fiber into the specimens treated with cement or steel slag powder improves significantly the mechanical behavior of specimens and significantly increases the UCS and strain corresponding to the maximum compressive strength. The specimen containing 0.2% of polypropylene fiber, 6.4% of cement and 1.6% steel slag exhibits the highest UCS value when the sum of the amounts of cement and steel slag was 8%. The failure pattern of specimen indicates a transition from ductile to brittle behavior with addition of cement and steel slag. However, the addition of polypropylene fiber changes the brittle response of treated specimens to a more ductile behavior.

Keywords: Cement, Sand, Soil Stabilization, Steel Slag, Unconfined Compressive Strength.

1. Introduction

In situ soil improvement with pozzolanic additives and other agents is a method of improving the soil characteristics to solve the problem of civil construction. The effectiveness of the soil stabilization technique including physical stabilization and chemical stabilization depends on the mechanical characteristics of soil (Nicholson, 2014). Lime and cement are the oldest materials which used in

---

* Corresponding author E-mail: bayat.m@pci.iaun.ac.ir

soil stabilization. So far, extensive experimental studies have been done on the mechanical behavior soil stabilized with addition of cement or lime (Hosseini et al., 2014; Moghal et al., 2020; Deneele et al., 2016; Kwon et al., 2010; Kim et al., 2018; Yoon and Abu-Farsakh, 2009; Saeed et al., 2015; Yin et al., 2019; Bayat et al., 2013; Saadat and Bayat, 2019). The formation of cemented aggregates which is caused by chemical bonds in cement- or lime-stabilized soil would lead to improve the mechanical characteristics of the weak soil.

In the short stabilization period, the strength properties of stabilized soil could be significantly improved by filling the pore spaces and development of inter-cluster cementation bonding (Horpibulsuk et al., 2010). While the utilization of conventional stabilizers is well established in civil engineering projects, natural and synthetic fibers were also used as a reinforcement additives in cement-fiber composites to enhance the shear strength capacity and also reduce the swelling and compressibility potential (Eshaghzadeh et al., 2021; Anagnostopoulos et al., 2013; Tomar et al., 2020; Wei et al., 2018; Syed et al., 2020; Sharma, 2018; Eldesouky et al., 2016). Various synthetic fibers such as polyester fiber, polyethylene fiber, basalt fiber, and polypropylene fiber with a higher durability than the natural fibers have been used in the soil reinforcement applications (Hejazi et al., 2012). Polypropylene fiber is a synthetic fiber which is made by extrusion of a thermoplastic polymer of propylene. Polypropylene fiber is an effective additive to enhance the shear strength characteristics and ductility of cement-based materials (Olgun, 2013).

The Unconfined Compressive Strength (UCS) test is one of the major and convenient laboratory method to investigate the strength characteristics of cohesive or stabilized specimens (Eme et al., 2016). Tang et al. (2007) indicated that the UCS value, shear strength parameters, and failure strain increased when the fiber added to the cement-stabilized specimen. Sharma (2018)

studied the geotechnical characteristics of dredged reservoir material which stabilized with a mixture of fiber, cement and fly ash. They showed that UCS or split tensile strength increased after stabilization and it improved further with addition of fiber.

The formulation of cement causes severe environmental pollution (Uwasu et al., 2014). The use of waste materials such as steel slag as a partial replacement for chemical stabilizer such as cement in geotechnical projects can be useful for environmental management. Many efforts have already been initiated to reduce the use of cement in soil stabilization to avoid environmental issues. Previous studies indicated that pozzolanic materials such as natural pozzolan and fly ash could be used to soil stabilization materials projects which can be useful for environmental management (Haddad et al., 2020; Salamatpoor et al., 2018; Mousavi and Wong, 2016; Vakili et al., 2013; Kumar, 2011; Stefanidou et al., 2017; Cheng et al., 2018). Most recently studies have been made to reduce the industrial wastes (Hanumantharao and Ramana, 2008; Rajput, 2018; Grenney et al., 1990). Researchers have been challenged to convert industrial wastes to construction materials. This includes soil stabilization (Gholipoor Norozi et al., 2015; Al-Bared et al., 2018; Panfilova et al., 2020; Salehi et al., 2021), concrete additives (Kim et al., 2020; Al-Bared et al., 2018), and road construction applications (Fırat et al., 2012; Jafar, 2016; Singh et al., 2018; Li et al., 2019).

Steel slag is a solid waste and one among the industrial by-products available in large quantity which is generated during the iron refining process. Steel slag has been utilized in previous studies as road and building materials (Baalamurugan et al., 2019; Dhoble and Ahmed, 2018; Yi et al., 2012; Kumar and Varma, 2020; Siddique et al., 2020). Shen et al. (2009) used steel slag and other solid wastes as effective additives for road base material. They indicated that the composite has higher early strength than the

other composites having lime-fly ash or lime-soil. It has also higher the long-term shear strength than the composite contaninig cement. Wu et al. (2019) used waste steel slag as alternative material to modify expansive soil properties. Mozejko and Francisca (2020) showed that the utilization of steel slag in the compaction of clay soils as a new and cost effective approach which resulted in significant increase of UCS. Bahadori et al. (2019) studied using of natural pozzolan for stabilization of marl soil. The tests results indicated that the efficiency of stabilized marl soil increases and the expansion and ductility decreases due to increasing volcanic ash content. Bahadori et al. (2019a) investigated the effects of fly ash content and volcanic ash content on the mechanical behaviour of peat soils using UCS and CBR tests. The results showed that UCS of specimens increases due to addition of fly ash or volcanic ash. Furthermore, the CBR results showed that the filling property of the stabilizer (fly ash and volcanic ashes) can be useful as its pozzolanic activity for soil stabilization. Zare et al. (2020) investigated the effect of waste tire textile fibers on the mechanical behaviour of cement-stabilized specimens. The results showed that waste tire textile fibers can be used with and without additive cement to improve the strength and brittle response of rammed earth structures.

Lang et al. (2020) studied the influences of cement content and type, acid content, steel slag powder content and curing period time on the strength characteristics of cement stabilized specimens. The results showed that the cement content and type have important effects on the mechanical characteristics of cement-steel slag-stabilized specimens. The results indicated that the use of 5% to 10% steel slag powder could be benefit to increase the strength characteristics of cement-stabilized dredged sludge, but for stabilized specimens containing HA, the 15-20% steel slag powder was recommended. The microstructural analyses by scanning electron microscopy indicated that the addition of steel slag powder can contribute to increase of cementitious matrix products in stabilized specimens.

As maintained above, most previous studies have focused on the mechanical characteristics of cement-stabilized specimens when cement replaced by industrial waste material. In other words, the effect of addition of different amounts and types of fibers on the mechanical behaviour of specimens treated with cement and steel slag powder has not been widely studied. The objective of this study is the utilization of steel slag, polypropylene fiber and cement for soil stabilization. The UCS were conducted on specimens with various steel slag, polypropylene fiber and cement contents.

2. Experimental Program

2.1. Materials and Testing Program

So far, many researchers have proved that the UCS is a strength index which has strong positive relationship with resistance of cohesive or stabilized-soils. In this study, a series of UCS tests were performed on stabilized specimens of Varzane sand. The soil collected from the Varzaneh desert in Isfahan, Iran. The grain-size distribution curve of Varzaneh sand is presented in Figure 1. Table 1 shows the physical and geotechnical properties of Varzaneh sand. According to the Unified Soil Classification System (USCS), Varzaneh sand is classified as poorly graded sand (SP).

Table 1. Physical and geotechnical properties of soil

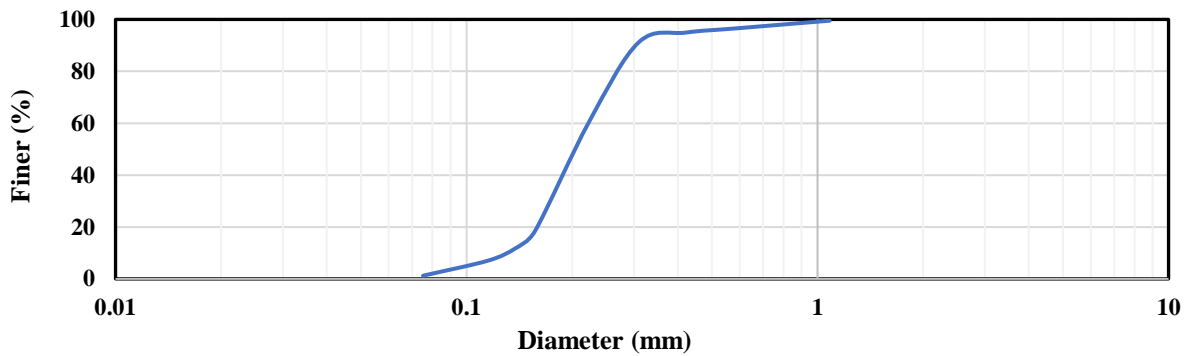| Characteristics	Values and descriptions
Specific gravity	2.66
Passing No. 200 sieve (%)	4
Plasticity index (%)	NP
Unified Soil Classification System (USCS)	SP
Optimum water content (%)	8
Maximum dry unit weight (kN/m^3)	17.8

Fig. 1. Grain-size distribution curve of Varzaneh sand

Polypropylene fiber was used for reinforcing the cement-stabilized specimens. The physical and mechanical properties of the polypropylene fiber is presented in Table 2. Ordinary Portland cement was also used in the testing program for stabilization. The physical and chemical properties of cement are shown in Table 3. In this study, Electric Arc Furnace (EAF) steel slag waste produced in Mobarakeh steel company (located in Isfahan, Iran) was used. X-ray diffraction (XRD) technique was used for structural characterization and mineralogical composition of the steel slag. The chemical composition of Mobarakeh EAF steel slag is shown in Table 4. The steel slag was crushed in a laboratory then sieved. The particle size fraction finer than 149 µm was used for this work.

The mechanical behavior of treated specimens has been investigated in this work. For this purpose, an experimental program comprising UCS tests was conducted. The effects of cement content, steel slag content, and polypropylene fiber content on the mechanical behavior of specimens have been investigated. Table 5 shows a summary of the performed tests. The first and second groups of the tests were intended to evaluate the effects of addition of cement or steel slag on the mechanical

behavior of reinforced specimens.

Table 2. Physical and mechanical properties of the Polypropylene fiber

Property	Values
Cut length (mm)	12
Filament diameter (µm)	13
Density (g/cm^3)	0.915
Elastic modulus (GPa)	5.51
Tensile strength (MPa)	680

Table 3. Physical and chemical properties of cement

Property/composition	Value
Specific gravity	3.14
Specific surface area (m^2/kg)	320
CaO (%)	60.4
SiO$_2$ (%)	15.9
Al$_2$O$_3$ (%)	9.5
SO$_3$ (%)	6.4
Fe$_2$O$_3$ (%)	4.1
MgO (%)	0.9
K$_2$O (%)	0.7
TiO$_2$ (%)	0.1

Table 4. Chemical composition of Mobarakeh EAF steel slag

Composition	Value (%)
FeO	29.8
CaO	31.2
SiO$_2$	19.2
MgO	12.2
AL$_2$O$_3$	4.1
MnO	0.6
P$_2$O$_5$	0.5

Table 5. A summary of the test details

Test Group	Cement content (%)	Steel slag content (%)	Polypropylene fiber content (%)
Group-1	0, 0.5, 1, 1.6, 1.8, 2	0, 0.2, 0.4, 1, 1.5, 2	0
Group-2	0, 2, 4, 6.4, 7.2, 8	0, 0.8, 1.6, 4, 6, 8	0
Group-3	2, 8	0	0, 0.1, 0.2, 0.5, 1
Group-4	0	2, 8	0, 0.1, 0.2, 0.5, 1
Group-5	1, 1.6, 4, 6.4	0.4, 1, 1.6, 4	0.1, 0.2

As shown from Table 5, in the first and second groups, steel slag has been partially replaced instead of cement. The third group of tests was performed to study the effect of cement and fiber contents on the UCS of specimens. The fourth group of tests was to study the effect of steel slag and fiber contents. The last group of tests was performed to investigate the effect of cement, steel slag and fiber contents on the UCS of treated specimens with varying contents of additives. It is worth noting that all specimens were subjected loading after 28 days of curing.

2.2. Specimen Preparation and Testing Method

In this work, the modified Proctor compaction tests were conducted to study the Maximum Dry Density (MDD) and Optimum Moisture Content (OMC) of specimens containing various additives (cement, steel slag and polypropylene fiber) in accordance with ASTM D1557. UCS tests were also performed for remolded specimens prepared in the laboratory at OMC and MDD using a cylindrical mould with height and diameter of 20 cm and 10 cm, respectively. Afterwards, the materials were first dried and then the required amounts of soil, steel slag and fibers were calculated and weighted. The required amounts of additives and soil were mixed before the OMC was added. The required water content was added into the specimen to reach the OMC of each specimen based on the modified Proctor results. The specimen was compacted into the UCS

mould into ten layers and then the specimen was taken out of the mould. The compacted specimen was wrapped in sealed container and cured in a curing room for 28 days with 95% humidity and 23 ± 2 °C temperature. In this work, the UCS tests were performed on the specimens after curing time of 28 days.

3. Results and Discussion

3.1. Compaction Characteristics

The results of compaction tests indicated that cement content has a more important effect than steel slag content on OMC and MDD. Steel slag content has not important influence on the OMC and MDD of specimens treated with steel slag. The results of compaction tests of specimens treated with steel slag and cement are presented in Figure 2. The results show that adding more cement slightly decreases the MDD and increases the OMC. At the addition of 8% cement, the maximum value of OMC and the minimum value of MDD were obtained. Generally, the MDD of the specimens treated with steel slag and cement is lower than that of untreated soil. However, the OMC of the treated specimens is higher than that of untreated soil. Figure 3 shows the variation of OMC and MDD of specimens treated with cement and polypropylene fiber. As shown from the results, the OMC and MDD decrease with increase of polypropylene fiber content. Increasing cement content from 2% to 8% leads to decrease MDD and increase OMC for a given polypropylene fiber content.
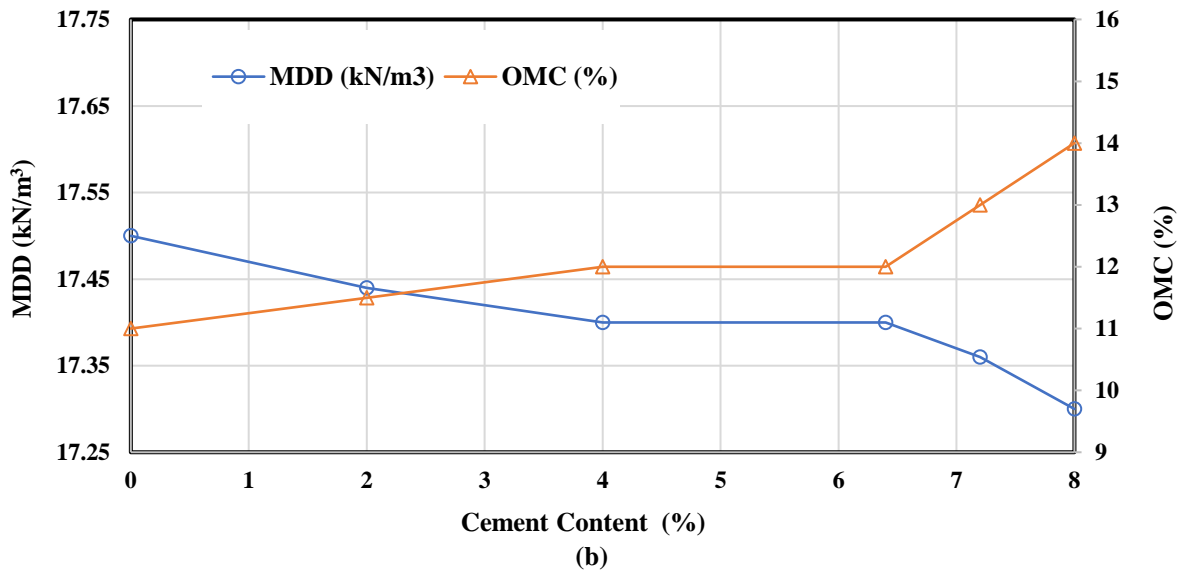

(a)
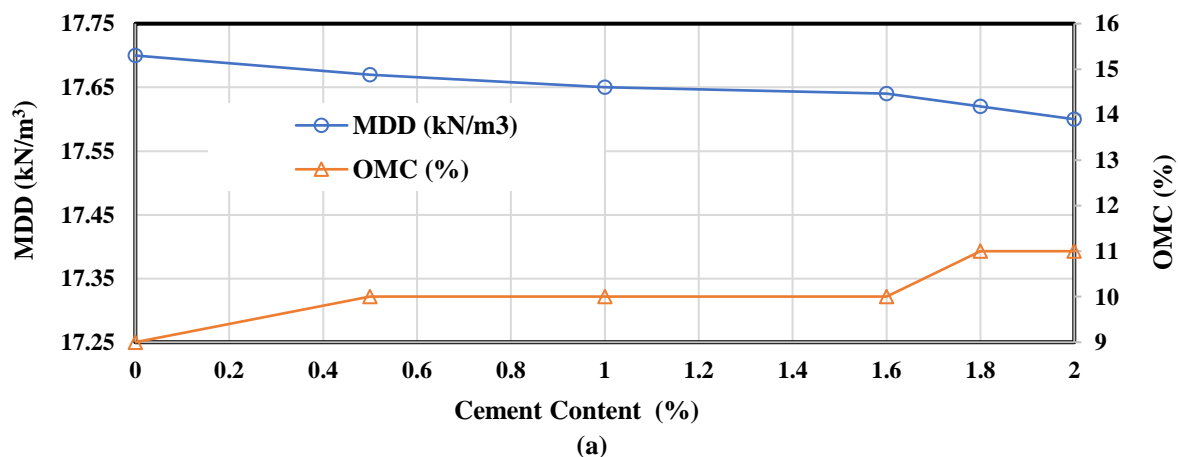
Fig. 2. Variation of OMC and MDD of specimens treated with cement and steel slag: a) Additive content of 2%; and b) Additive content of 8%
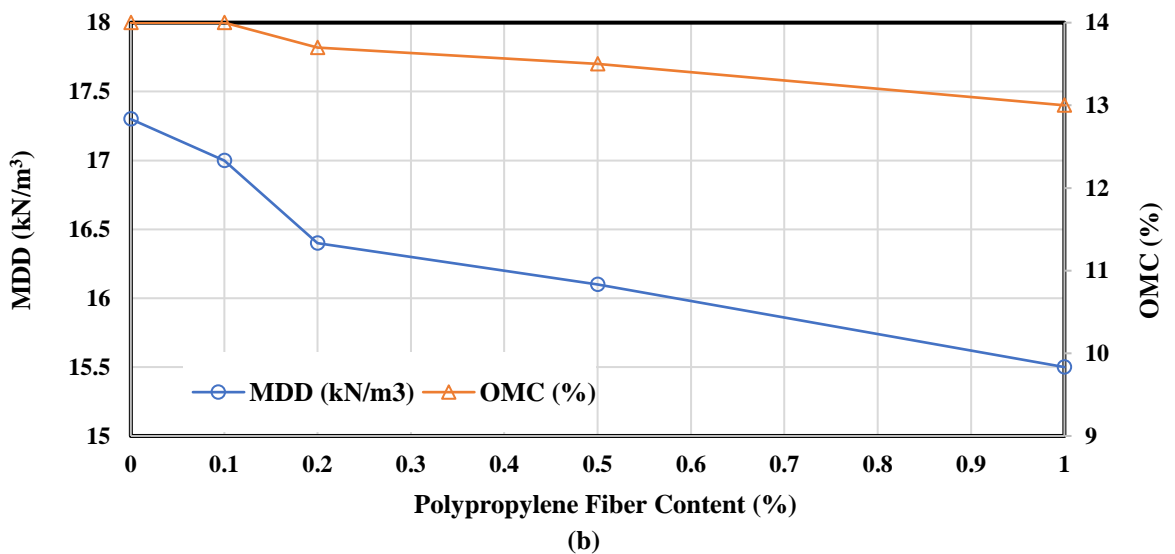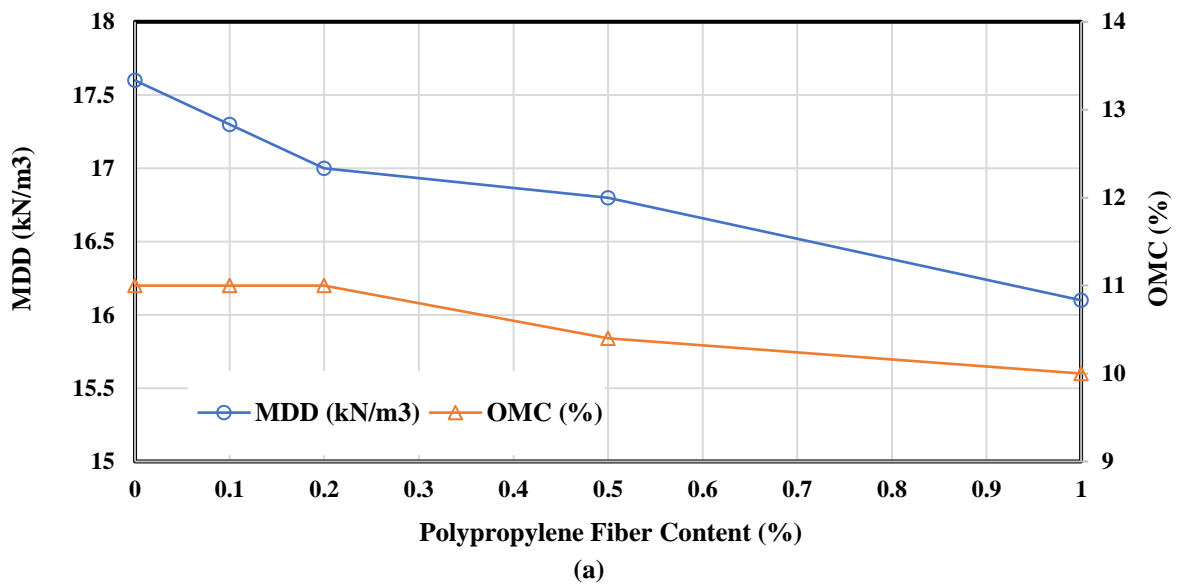

Fig. 3. Variation of OMC and MDD of specimens treated with cement and polypropylene fiber: a) Cement content of 2%; and b) Cement content of 8%

3.2. Unconfined Compressive Tests

In this study, the controlling parameters evaluated were cement content (C), steel slag content (S), and polypropylene fiber content (P). Figures 4a and 4b show the axial stress versus axial strain curves during unconfined compressive tests for the 2% and 8% additives (steel slag and cement) content, respectively. The UCS and strain corresponding to the maximum compressive strength of specimens either increase or decrease when cement replaced by steel slag powder depending on cement and steel slag contents. The UCS values of specimens treated with steel slag and cement are presented in Figure 5. As shown from the results, compressive strength increases when cement replaced by 20% (the specimen containing S=0.4% and C=1.6%) or 10% (the specimen containing S=0.8% and C=7.2%) of steel slag for the 2% and 8% additives contents, respectively. Similar results have been reported by previous studies when cement replaced by other waste materials (Ilieş et al., 2017; Jayasinghe et al., 2016; Ahmadi Chenarboni et al., 2021; Haddad et al., 2020; Kordnaeij et al., 2019).

The axial stress versus axial strain curves of cement stabilized specimens obtained from the unconfined compression tests are presented in Figure 6. It can be seen from the results that the strain corresponding to the maximum compressive strength of the cement stabilized fiber-reinforced specimens is higher than that of the specimens treated with cement and steel slag, and increases as polypropylene fiber content increases. The cement-stabilized specimen reinforced with 1% polypropylene fiber has the highest strain corresponding to the maximum compressive strength. The UCS values of improved specimen with cement and fiber are shown in Figure 7.
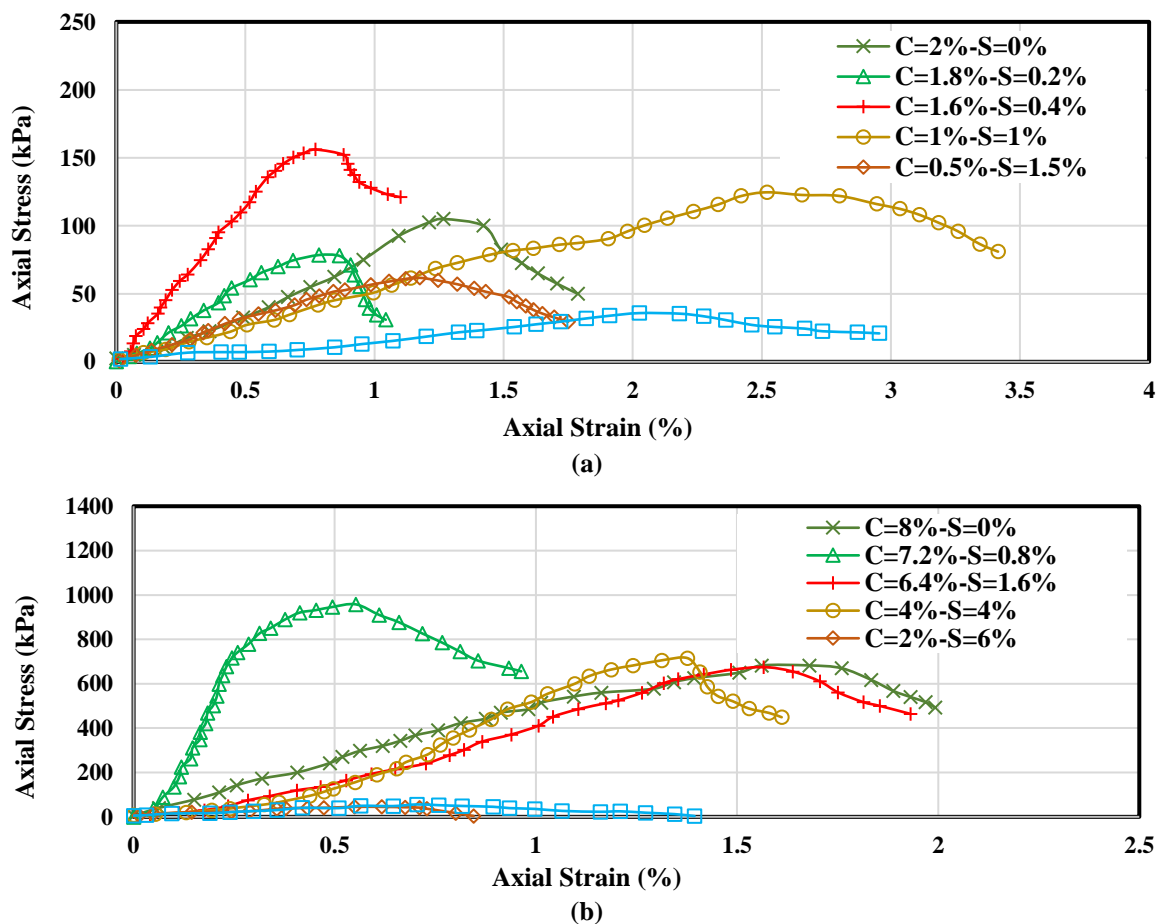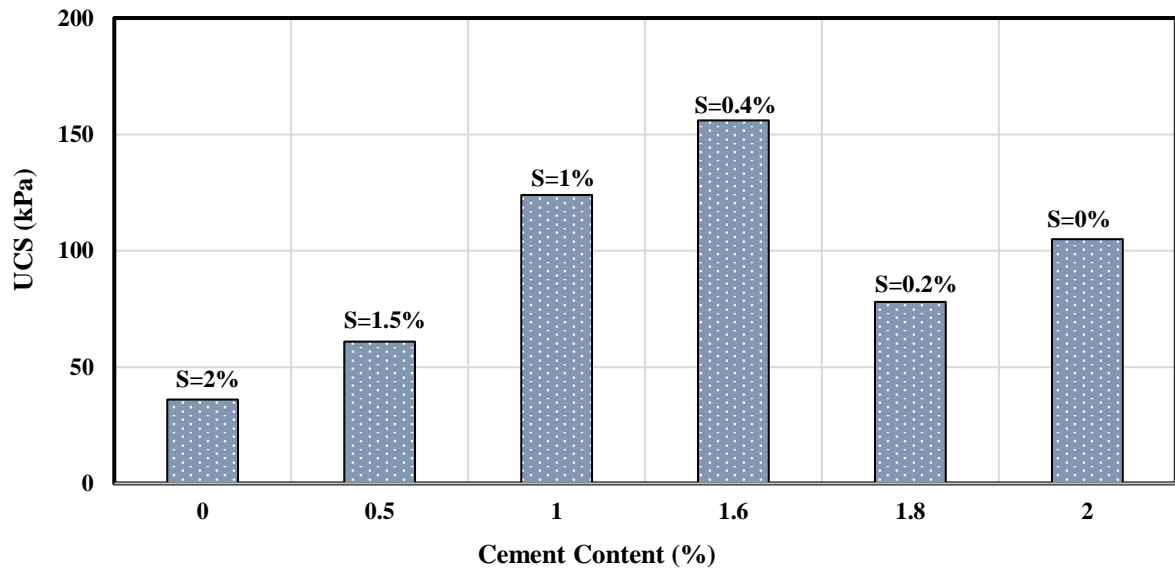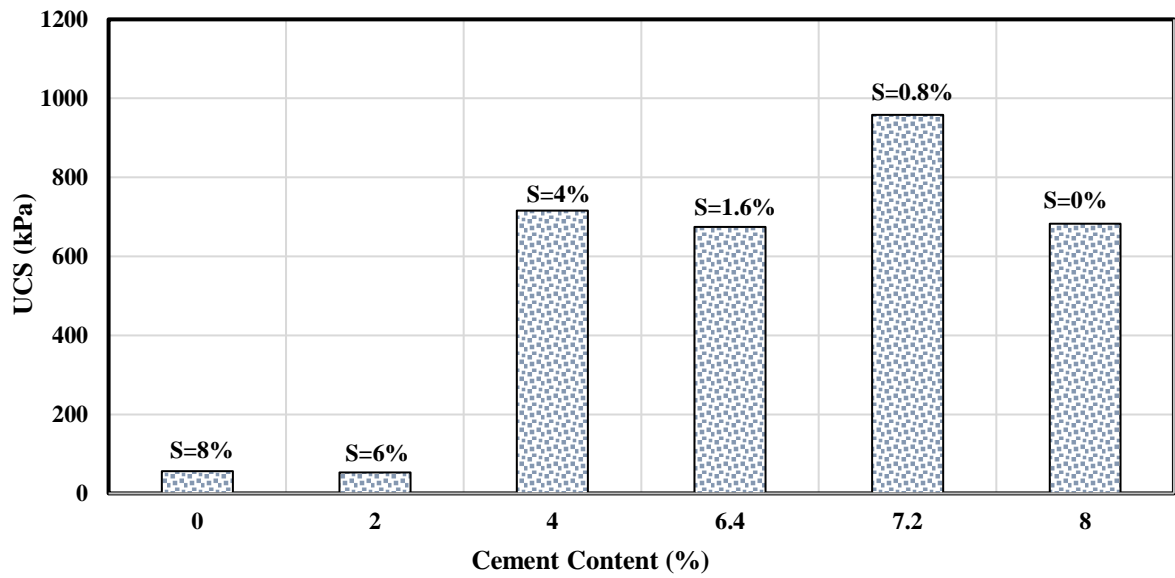

Fig. 4. Stress-strain curves of the specimens treated with cement and steel slag mixture: a) Additives content of 2%; and b) Additives content of 8%
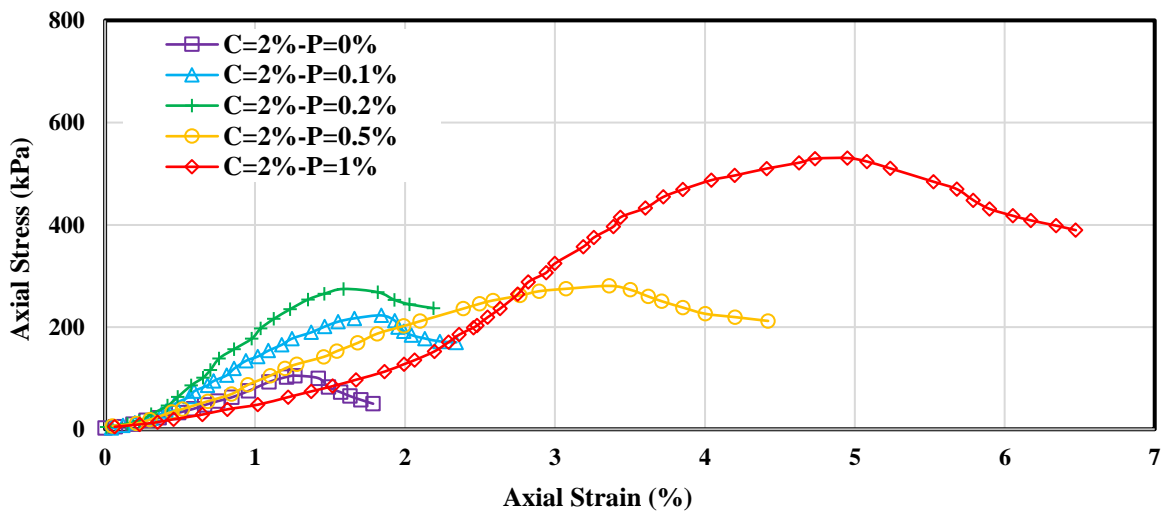
Fig. 5. UCS values of the specimens treated with cement and steel slag mixture: a) Additives content of 2%; b) Additives content of 8%
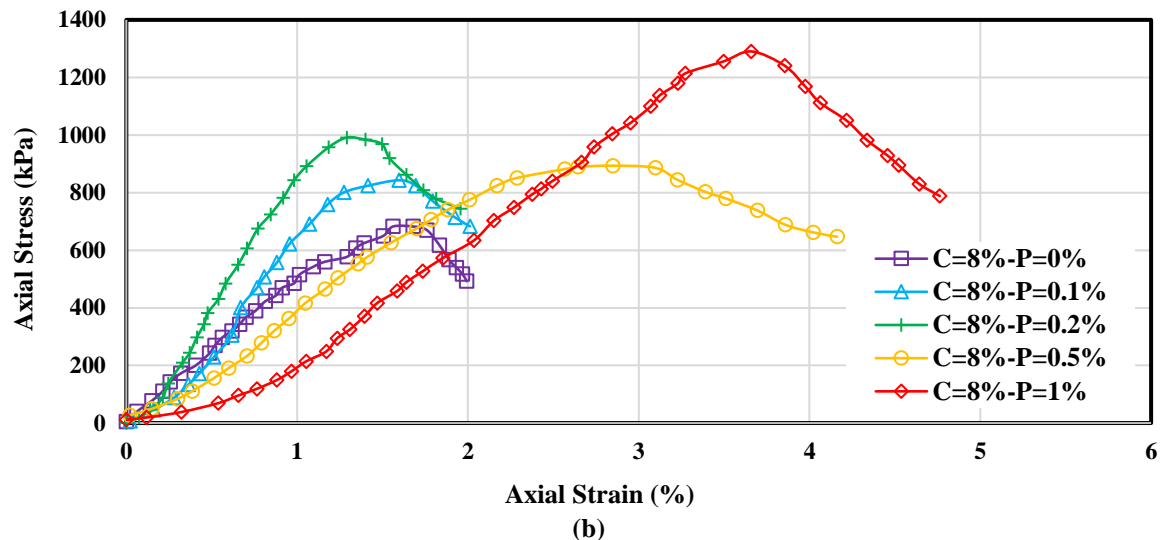
Fig. 6. Stress-strain curves of the fiber-reinforced cement-stabilized specimens: a) Cement content of 2%; b) cement content of 8%

As shown, the UCS values of cement-stabilized polypropylene fiber-reinforced specimens are greater than those of cement-stabilized specimens. The simultaneous use of cement and polypropylene fibers as an effective method to improve the mechanical behaviour of soils has been suggested by previous studies (Arabani and Haghsheno, 2020; Wang et al., 2020; Park, 2011; Khattak and Alrashidi, 2006; Kaniraj and Havanagi, 2001; Park, 2009). A comparison between Figures 5 and 7 reveals that the addition of polypropylene fiber lower than 1% is not effective compared to the case where cement is replaced with steel slag. However, the UCS values increased significantly when fiber content was further increased to 1%.

Figures 8 and 9 show the axial stress versus axial strain curves and the corresponding UCS values of treated specimens with varying contents of steel slag and polypropylene fiber, respectively. Although the addition of steel slag and fiber increased the UCS, the UCS values of all specimens treated with steel slag and fiber mixture are much smaller than those of specimens treated with cement and fiber mixture. Here too, the specimens containing 1% polypropylene fiber have the highest UCS values.
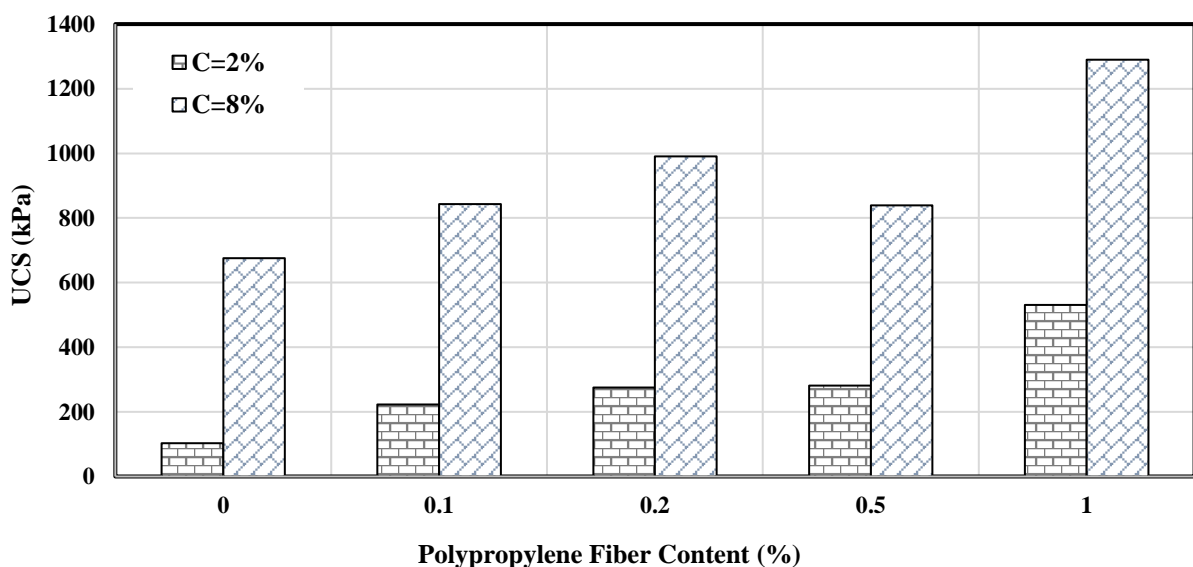

Fig. 7. UCS values of the fiber-reinforced cement-stabilized specimens
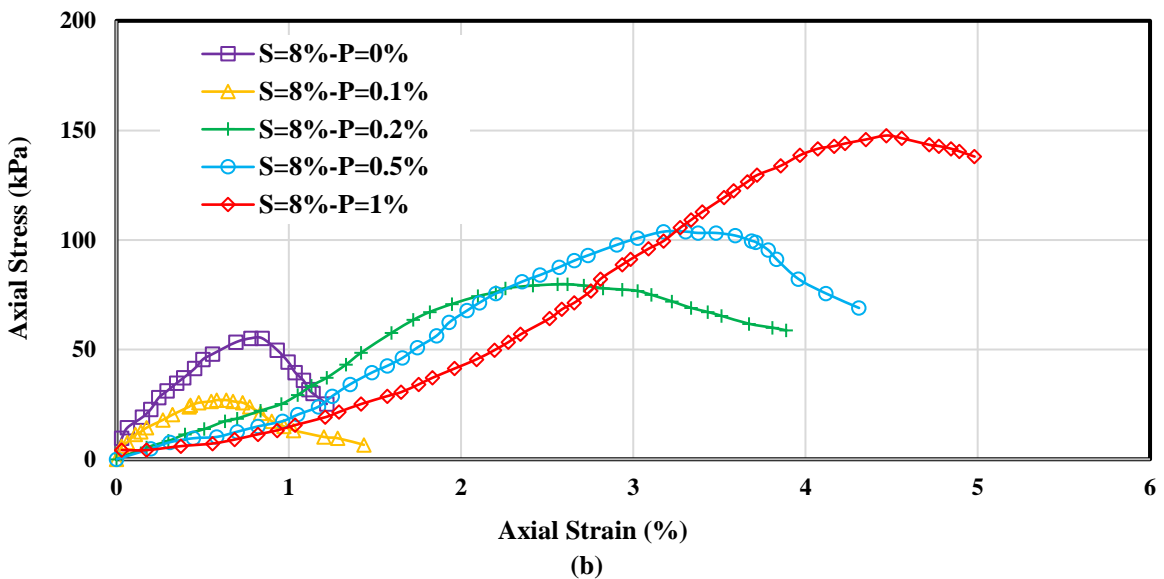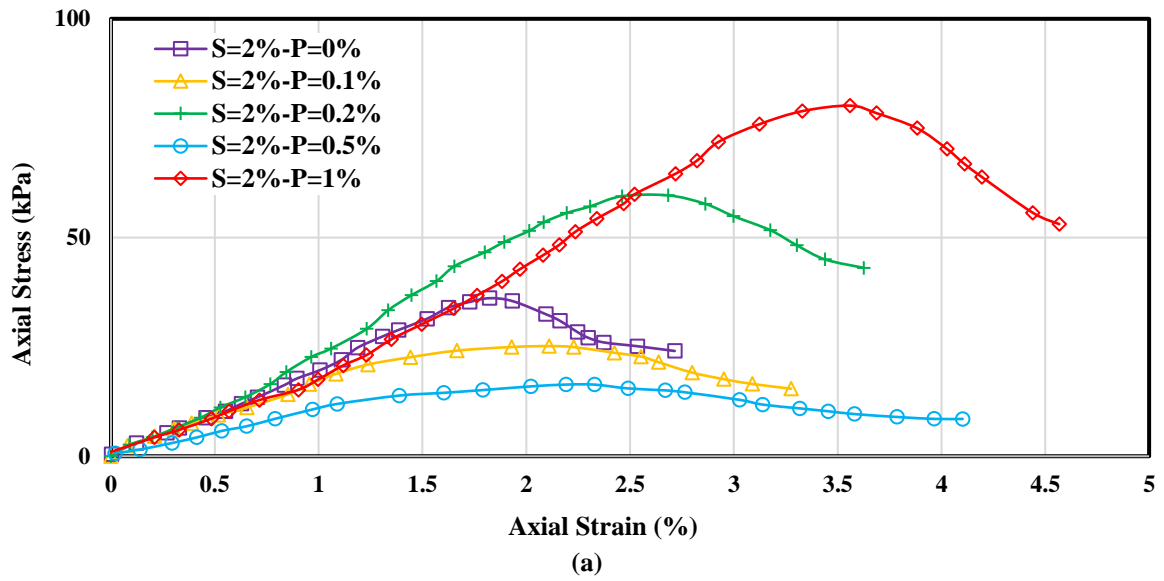
Fig. 8. Stress-strain curves of the fiber-reinforced steel slag-stabilized specimens: a) Steel slag content of 2%; b) Steel slag content of 8%
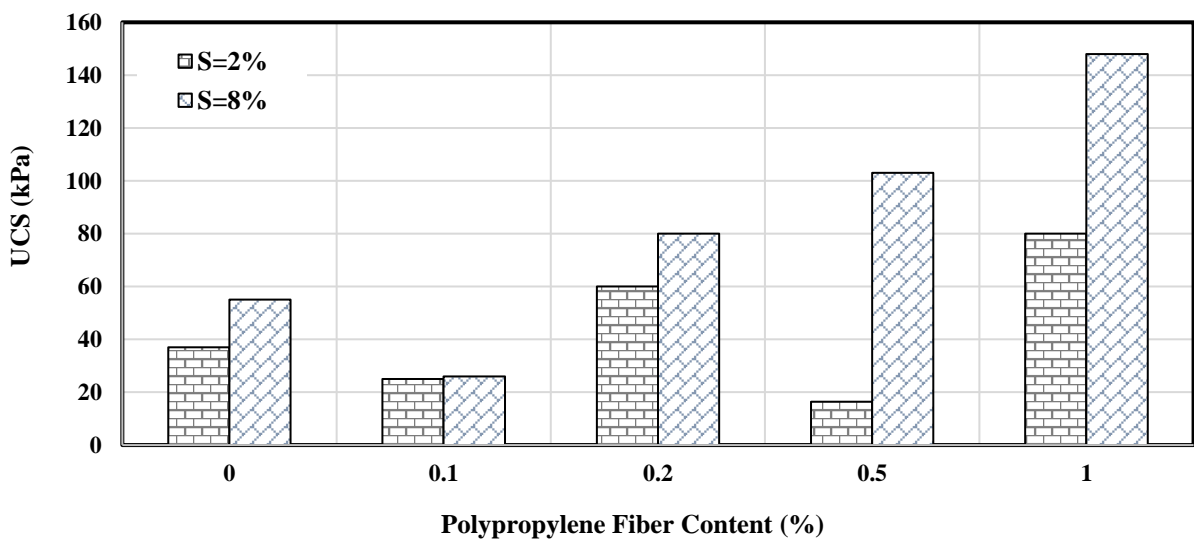

Fig. 9. UCS values of the fiber-reinforced steel slag-stabilized specimens

The axial stress versus axial strain curves of treated specimens with varying contents of steel slag, cement and polypropylene fiber contents are shown in Figure 10. The corresponding values of the UCS are also presented in Figure 11. As shown from the results, the brittleness of the specimens is reduced and ductility and UCS enhanced obviously with higher polypropylene fiber content. It can be conducted from the results that the specimen containing 0.1% of polypropylene fiber, 1.6% of cement, and 0.4% steel slag exhibits the highest UCS value when the sum of the amounts of cement and steel slag was 2%. On the other hand, the specimen containing 0.2% of polypropylene fiber, 6.4% of cement, and 1.6% steel slag exhibits the highest UCS value when the sum of the amounts of cement and steel slag was 8%.
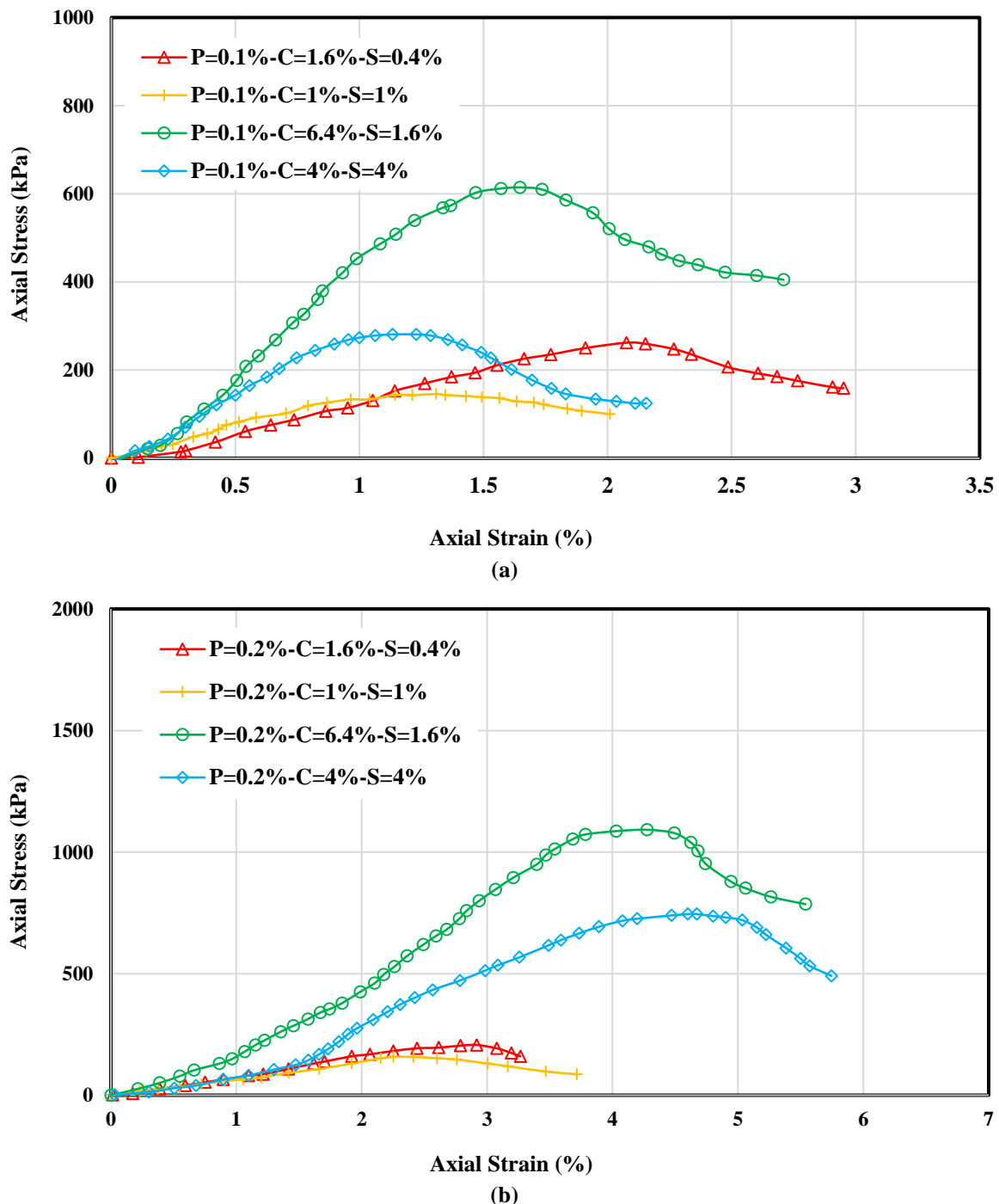

Fig. 10. Stress-strain curves of the specimens treated with fiber, cement and steel slag mixture: a) Fiber content of 0.1%; b) Content of 0.2%
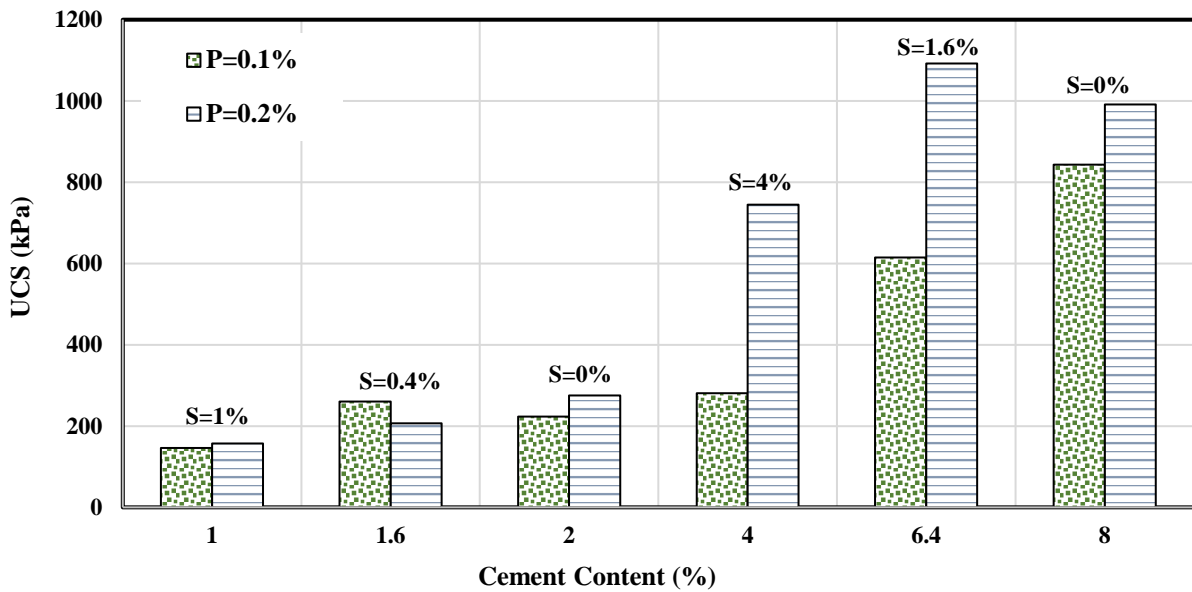
Fig. 11. UCS values of the specimens treated with fiber, cement and steel slag mixture

3.3. Failure Patterns of Specimens

The compressive failure patterns and fracture resistance of fiber-reinforced or cement-stabilized specimens under axial loading are a macro embodiment of the variation of deflection and internal particles stresses (Yang et al., 2017). Thus, it is necessary to study the failure patterns of specimens. The failure patterns of stabilized specimens with cement and steel slag powder are presented in Figure 12. The failure mechanisms of steel slag-stabilized specimens, specimens treated with fiber and cement and specimens treated with fiber, steel slag and cement are shown in Figure 13.
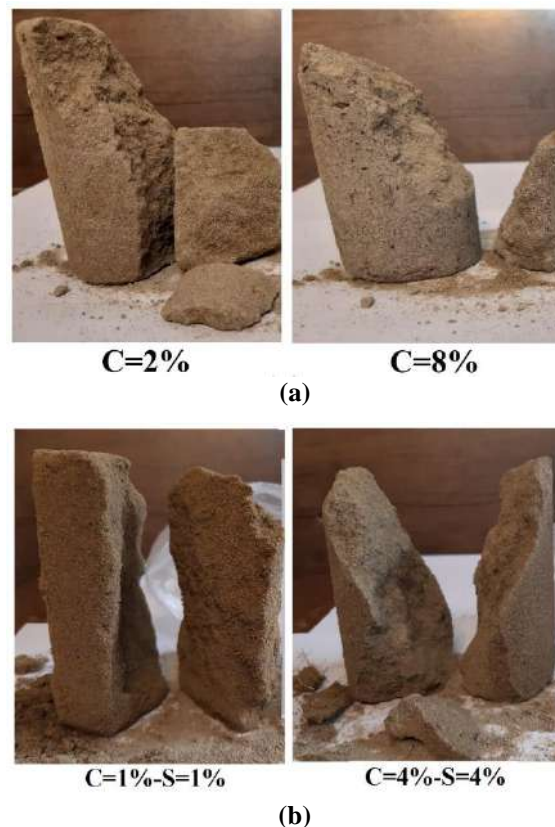

C=2%   C=8%

(a)

C=1%-S=1%   C=4%-S=4%

(b)

Fig. 12. Failure patterns of the: a) Specimens treated with cement; and b) specimens treated with cement and steel slag mixture

As shown in Figure 12, the longitudinal cracks have been formed in the cement-stabilized and cement-steel slag-stabilized specimens. The cracks developed rapidly through the specimen. As shown from the results, the cracks became longer and deeper from the surface. The specimens exhibited loose structure accompanied by debris and soil blocks. The results indicate a transition from ductile to brittle response due to addition of cement and steel slag. As shown in Figure 13, thin and dense cracks have been formed in the specimens containing fibers. The results show that the brittle failure characteristics of the specimens have been significantly improved by addition of fibers. Polypropylene fibers showed an apparent 'bridging' function and could form a stable three-dimensional network in the fiber-reinforced soil, which was able to disperse the stress and prevent the development of cracks effectively. Previous studied have been reported that the addition of fibers modified the pattern of fracture in the specimens from brittle to ductile (Yang et al., 2017; Kaniraj and Havanagi, 2001; Estabragh et al., 2012; Correia et al., 2015).

3.4. Microstructures of Specimens

In this work, the microstructures of treated specimens were studied by SEM analysis. SEM images obtained from cut-up sections of steel slag-stabilized specimen, cement-stabilized specimen, and fiber-reinforced cement-stabilized specimens. SEM images are presented in Figure 14. The SEM images were taken after curing of 28 days. As shown in Figure 14, the sand particles are coated by the cement or steel slag paste. It can be observed that the sand is composed of angular to subangular particles, while the surface of the polypropylene fibers is almost smooth. Some sand particles interlock with the polypropylene fiber surface and improve the interaction between the polypropylene fibers and sand particles. The soil particle and polypropylene fiber surfaces are enwrapped by the cement paste and the surface of the polypropylene fiber is rough with pronounced scales. The sand and polypropylene fiber are connected by the cement membrane thus to shape firmly together as a whole. It can be seen that the cement paste covered the surfaces of sand particles and increased the interlocking force between sand particles.

S=8%-P=0.1%   S=8%-P=0.2%   S=8%-P=0.5%   S=8%-P=1%

(a)

C=0.8%-P=0.1%   C=8%-P=0.2%   C=8%-P=0.5%   C=8%-P=1%

(b)

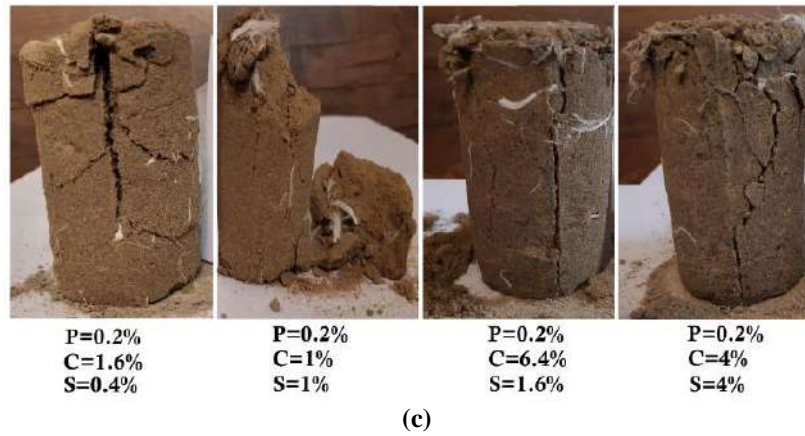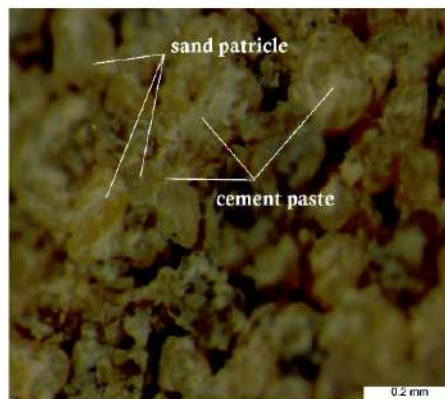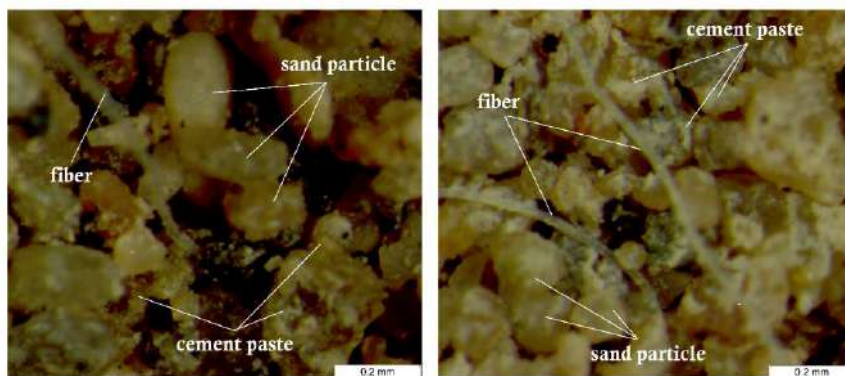| P=0.2% | P=0.2% | P=0.2% | P=0.2% |
| C=1.6% | C=1% | C=6.4% | C=4% |
| S=0.4% | S=1% | S=1.6% | S=4% |

(c)

Fig. 13. Failure patterns of the: a) Specimens treated with steel slag and fiber mixture; b) Specimens treated with cement and fiber mixture; and c) Specimens treated with cement, steel slag and fiber mixture

(a)   S=8%

(b)   C=8%

(c)   C=8%-P=1%

Fig. 14. SEM images of specimen treated with: a) Steel slag; b) Cement; and c) Cement and fiber mixture

4. Conclusions

The application of industrial wastes such as steel slag for civil projects with environmentally friendly can be useful for environmental protection. The use of steel slag powder in civil project such as soil stabilization has many economic and environmental benefits. In this paper, a series of UCS tests was done to investigate the effects of steel slag powder, cement and polypropylene fiber contents on the mechanical behavior of treated specimens. Based on the experimental results, the following conclusions were reached:

- The UCS of stabilized specimens could be improved strongly by the cement-steel slag mixture. While the total additives (cement and steel slag) content is a constant, the UCS of specimens first increases and then has a downward trend when the cement content increases. Hence, beyond optimum steel slag powder dosage, the UCS value decreased. The sample treated with 7.2% cement and 0.8% steel slag powder has a highest UCS of 958 kPa. Furthermore, the UCS values of treated specimens increase with increasing additives content from 2% to 8%.
- The addition 1% polypropylene fiber in the specimens treated with cement, steel slag powder or a mixture of them improves significantly the mechanical behavior of specimens. In other words, the addition of polypropylene fiber increases UCS and the strain corresponding to the maximum compressive strength.
- Polypropylene fiber content has significant effect on the UCS value of specimens treated with a mixture of cement, steel slag powder when additives (steel slag and cement) content increases from 2% to 8%. The specimen containing 0.2% of polypropylene fiber, 6.4% of cement, and 1.6% steel slag exhibits the highest UCS value when the sum of the amounts of cement and steel slag was 8%. Greater cement content of up 6.4% resulted in considerable drop in compressive strength.
- The longitudinal cracks have been formed in the specimens treated with cement, steel slag powder or a mixture of them. A transition from ductile to brittle behavior was observed due to addition of cement and steel slag. The specimen's brittle failure characteristics have been improved significantly due to addition of polypropylene fibers.

5. References

Ahmadi Chenarboni, H., Hamid Lajevardi, S., MolaAbasi, H. and Zeighami, E. (2021)."The effect of zeolite and cement stabilization on the mechanical behavior of expansive soils", *Construction and Building Materials*, 272, 121630,

Al-Bared, M.A.M., Marto, A. and Latifi, N. (2018). "Utilization of recycled tiles and tyres in stabilization of soils and production of construction materials, A state-of-the-art review", *KSCE Journal of Civil Engineering*, 22(10), 3860-3874.

Arabani, M. and Haghsheno, H. (2020). "The effect of polymeric fibers on the mechanical properties of cement-stabilized clay soils in Northern Iran", *International Journal of Geotechnical Engineering*, 14(5), 557-568.

Baalamurugan, J., Ganesh Kumar, V., Chandrasekaran, S., Balasundar, S., Venkatraman, B., Padmapriya, R. and Bupesh Raja, V.K. (2019). "Utilization of induction furnace steel slag in concrete as coarse aggregate for gamma radiation shielding", *Journal of Hazardous Materials*, 369(February), 561-568.

Bahadori, H., Hasheminezhad, A. and Mohamadi asl, S. (2019a). "Stabilisation of Urmia Lake peat using natural and artificial pozzolans", *Proceedings of the Institution of Civil Engineers-Ground Improvement*, 175(2), 104-113.

Bahadori, H., Hasheminezhad, A., and Taghizadeh, F. (2019b). "Experimental study on marl soil stabilization using natural pozzolans", *Journal of Materials in Civil Engineering*, 31(2), 04018363.

Bayat, M., Asgari, M.R. and Mousivand, M. (2013). "Effects of cement and lime treatment on geotechnical properties of a low plasticity clay", *International Conference on Civil Engineering Architecture and Urban Sustainable Development*, November, Tabriz, Iran.

Cheng, Y., Wang, S., Li, J., Huang, X., Li, C. and

Wu, J. (2018). "Engineering and mineralogical properties of stabilized expansive soil compositing lime and natural pozzolans", *Construction and Building Materials*, 187, 1031-1038.

Correia, A.A.S., Venda Oliveira, P.J. and Custódio, D.G. (2015). "Effect of polypropylene fibres on the compressive and tensile strength of a soft soil, artificially stabilised with binders", *Geotextiles and Geomembranes*, 43(2), 97-106.

Eme, D.B., Nwofor, T.C. and Sule, S. (2016). "Correlation between the California Bearing Ratio (CBR) and Unconfined Compressive Strength (UCS) of stabilized sand-cement of the Niger Delta", *International Journal of Civil Engineering*, 3(3), 7-13.

Eshaghzadeh, M., Bayat, M., Ajalloeian, R. and Mahdi, S. (2021). "Mechanical behavior of silty sand reinforced with nanosilica-coated ceramic fibers nanosilica-coated ceramic fibers", *Journal of Adhesion Science and Technology*, 35(23), 2664-2683.

Haddad, A., Jafarian, Y. and Amiri, I. (2020). "Evaluation of mechanical properties of cement and zeolite-stabilized sand using monotonic simple shear test", *Journal of Civil and Environmental Engineering*, DOI: 10.22034/JCEE.2020.39108.1931.

Hanumantharao, C. and Ramana, G.V. (2008). "Dynamic soil properties for microzonation of Delhi, India", *Journal of Earth System Science*, 117(SUPPL.2), 719-730.

Hejazi, S.M., Sheikhzadeh, M., Abtahi, S.M. and Zadhoush, A. (2012). "A simple review of soil reinforcement by using natural and synthetic fibers", *Construction and Building Materials*, 30, 100-116.

Horpibulsuk, S., Rachan, R., Chinkulkijniwat, A., Raksachon, Y. and Suddeepong, A. (2010). "Analysis of strength development in cement-stabilized silty clay from microstructural considerations", *Construction and Building Materials*, 24(10), 2011-2021.

Hosseini, P., Hosseinpourpia, R., Pajum, A., Khodavirdi, M.M., Izadi, H. and Vaezi, A. (2014). "Effect of nano-particles and aminosilane interaction on the performances of cement-based composites, An experimental study", *Construction and Building Materials*, 66, 113-124.

Ilieş, N.M., Cîrcu, A.P., Nagy, A.C., Ciubotaru, V.C. and Kisfaludi-Bak, Z. (2017). "Comparative study on soil stabilization with Polyethylene waste materials and binders", *Procedia Engineering*, 181, 444-451.

Jalili, M., Ghahroudi, R., Tajdini, M., Zadeh, K. and Zaeim, N. (2020). "Experimental investigation of the effective parameters on the strength of soil-cement", *Civil Engineering Infrastructures Journal*, 53(2), 407-416.

Kim, S.K., Jang, I.Y. and Yang, H.J. (2020). "Strength development characteristics of concrete replaced with different waste glasses from display industry as a cementitious material", *KSCE Journal of Civil Engineering*, 24(8), 2485-2494.

Kordnaeij, A., Moayed, R.Z. and Soleimani, M. (2019). "Unconfined compressive strength of loose sandy soils grouted with zeolite and cement", *Soils and Foundations*, 59(4), 905-919.

Kumar, H. and Varma, S. (2020). "A review on utilization of steel slag in hot mix asphalt", *International Journal of Pavement Research and Technology*, 14(2), 232-242.

Lang, L., Song, C., Xue, L. and Chen, B. (2020). "Effectiveness of waste steel slag powder on the strength development and associated micro-mechanisms of cement-stabilized dredged sludge", *Construction and Building Materials*, 240, 117975.

Li, J., Xiao, F., Zhang, L. and Amirkhanian, S.N. (2019). "Life cycle assessment and life cycle cost analysis of recycled solid waste materials in highway pavement, A review", *Journal of Cleaner Production*, 233, 1182-1206.

Moghal, A.A.B., Mohammed, S.A.S., Almajed, A. and Al-Shamrani, M.A. (2020). "Desorption of heavy metals from lime-stabilized arid-soils using different extractants", *International Journal of Civil Engineering*, 18(4), 449-461.

Mousavi, S. and Wong, L.S. (2016). "Compressibility characteristics of compacted clay treated with cement, peat ash and silica sand", *Civil Engineering Infrastructures Journal*, 49(1), 149-164.

Mozejko, C.A. and Francisca, F.M. (2020). "Enhanced mechanical behavior of compacted clayey silts stabilized by reusing steel slag", *Construction and Building Materials*, 239, 117901.

Olgun, M. (2013). "Effects of polypropylene fiber inclusion on the strength and volume change characteristics of cement-fly ash stabilized clay soil", *Geosynthetics International*, 20(4), 263-275.

Panfilova, M.I., Zubrev, N.I., Efremova, S.Y., Yakhkind, M.I. and Gorbachevskii, V.P. (2020). "Strengthening of water-saturated soils of the bases of underground structures with composite solutions modified by industrial waste, boehmite", *Case Studies in Construction Materials*, 12, e00323.

Park, S.S. (2011). "Unconfined compressive strength and ductility of fiber-reinforced cemented sand", *Construction and Building Materials*, 25(2), 1134-1138.

Rajput, S.P.S. (2018). "An experimental study on crushed stone dust as fine aggregate in cement concrete", *Materials Today Proceedings*, 5(9), 17540-17547.

Saadat, M. and Bayat, M. (2019). "Prediction of the unconfined compressive strength of stabilised soil by Adaptive Neuro Fuzzy Inference System (ANFIS) and Non-Linear Regression (NLR)", *Geomechanics and Geoengineering*, 17(1), 80-91.

Salamatpoor, S., Jafarian, Y. and Hajiannia, A. (2018). "Physical and mechanical properties of sand stabilized by cement and natural zeolite", *European Physical Journal Plus*, 133(5), 1-13.

Salehi, M., Bayat, M., Saadat, M. and Nasri, M. (2021). "Experimental study on mechanical properties of cement-stabilized soil blended with crushed stone waste", *KSCE Journal of Civil Engineering*, 25(6), 1974-1984.

Sharma, R. (2018). "Laboratory study on sustainable use of cement-fly ash-polypropylene fiber-stabilized dredged material", *Environment, Development and Sustainability*, 20(5), 2139-2159.

Shen, W., Zhou, M., Ma, W., Hu, J. and Cai, Z. (2009). "Investigation on the application of steel slag-fly ash-phosphogypsum solidified material as road base material", *Journal of Hazardous Materials*, 164(1), 99-104.

Siddique, R., Singh, M. and Jain, M. (2020). "Recycling copper slag in steel fibre concrete for sustainable construction", *Journal of Cleaner Production*, 271, 122559.

Singh, S., Ransinchung, G.D., Debbarma, S. and Kumar, P. (2018). "Utilization of reclaimed asphalt pavement aggregates containing waste from Sugarcane Mill for production of concrete mixes", *Journal of Cleaner Production*, 174, 42-52.

Syed, M., GuhaRay, A., Agarwal, S. and Kar, A. (2020). "Stabilization of expansive clays by combined effects of geopolymerization and fiber reinforcement", *Journal of The Institution of Engineers (India), Series A*, 101(1), 163-178.

Tang, C., Shi, B., Gao, W., Chen, F. and Cai, Y. (2007). "Strength and mechanical behavior of short polypropylene fiber reinforced and cement stabilized clayey soil", *Geotextiles and Geomembranes*, 25(3), 194-202.

Tomar, A., Sharma, T. and Singh, S. (2020). "Strength properties and durability of clay soil treated with mixture of nano silica and Polypropylene fiber", *Materials Today", Proceedings*, 26, 3449-3457.

Uwasu, M., Hara, K. and Yabar, H. (2014). "World cement production and environmental implications", *Environmental Development*, 10(1), 36-47.

Vakili, A.H., Selamat, M.R., Moayedi, H. and Amani, H. (2013). "Stabilization of dispersive soils by pozzolan", *Forensic Engineering 2012, Gateway to a Better Tomorrow - Proceedings of the 6th Congress on Forensic Engineering*, 726-735.

Wang, D., Wang, H., Larsson, S., Benzerzour, M., Maherzi, W. and Amar, M. (2020). "Effect of basalt fiber inclusion on the mechanical properties and microstructure of cement-solidified kaolinite", *Construction and Building Materials*, 241, 118085.

Wei, L., Chai, S.X., Zhang, H.Y. and Shi, Q. (2018). "Mechanical properties of soil reinforced with both lime and four kinds of fiber", *Construction and Building Materials*, 172, 300-308.

Wu, J., Liu, Q., Deng, Y., Yu, X., Feng, Q. and Yan, C. (2019). "Expansive soil modified by waste steel slag and its application in subbase layer of highways", *Soils and Foundations*, 59(4), 955-965.

Yang, B. han, Weng, X. zhong, Liu, J. zhong, Kou, Y. nan, Jiang, L., Li, H. lei, and Yan, X. cheng (2017). "Strength characteristics of modified polypropylene fiber and cement-reinforced loess", *Journal of Central South University*, 24(3), 560-568.

Zare, P., Sheikhi Narani, S., Abbaspour, M., Fahimifar, A., Mir Mohammad Hosseini, S.M. and Zare, P. (2020). "Experimental investigation of non-stabilized and cement-stabilized rammed earth reinforcement by Waste Tire Textile Fibers (WTTFs)", *Construction and Building Materials*, 260, 120432.

Outrigger Braced System Placement Effect on Seismic Collapse Probability of Tall Buildings

Tavakoli, H.R.[1]* [iD]**, Moradi, M.[2]** [iD]**, Goodarzi, M.J.[3]** [iD] **and Najafi, H.[4]** [iD]

[1] Associate Professor, Department of Civil Engineering, Babol Noshirvani University of Technology, Babol, Iran.
[2] Ph.D. Candidate, Department of Civil Engineering, Babol Noshirvani University of Technology, Babol, Iran.
[3] Instructor, Department of Civil Engineering, Technical and Vocational University (TVU), Tehran, Iran.
[4] M.Sc. Student, University of Azad, Ghaemshahr Branch, Ghaemshahr, Iran.

© University of Tehran 2022

ABSTRACT: The placement of bracing can affect the seismic response and energy balance in the outrigger braced systems. In this study, it is attempted to investigate the effect of placement optimization of outrigger braced system on the seismic response of a 50-story structure. IDA curves are used to investigate the seismic responses. Sa and Sd are considered as intensity measure (IM) Parameters. Maximum story drift and inelastic strain energy considered as Engineering Demand Parameters (EDP). At first, IDA curves are derived based on maximum story drift in the structures. When the performance level is determined, their fragility curves are derived and compared. In the next step, the energy balance is investigated in the structures and the strain energy parameter is selected as EDP, which the damage level is determined in accordance with. Fragility curves are plotted and the results are assessed using the plastic strain energy. The results show that the placement optimization of outrigger braced system improves all structural parameters and reduces the collapse probability. Moreover, the fragility curves obtained from plastic strain energy as EDP are quite similar to the fragility curve derived from the selection of story drift as EDB.

Keywords: Fragility Curve, IDA Curve, Inelastic Energy, Outrigger Braced System, Tall Building.

1. Introduction

Outrigger braced structures have a central core consisted of shear walls or braced frames; the central core is attached to the outer columns by outrigger trusses or girders (Ding et al., 2018). When the structure is subjected to lateral loads, rotations of the core are restrained by the outriggers through tension in windward columns and compression in leeward columns (Gorji and Cheng, 2017). Given the considerable effective depth of these structures, the lateral stiffness increases and the lateral displacement and moment of the core decline significantly (Gorji and Cheng,

---

* Corresponding author E-mail: tavakoli@nit.ac.ir

2017). Outrigger braced structures are used for buildings of 40 to 70 stories. If the lateral resistance system of a structure is merely based on a braced core, its deformation under a lateral force is like that of a cantilevered beam in the bending mode; but if the core is connected to the outer columns by a relatively stiff truss (outrigger braced system), the rotation of the core under lateral loading causes the rotation of outrigger braced system and the outer columns are tensioned on one side and compressed on the other side. This process involves columns in lateral load-bearing. In this case, the core approximately shows an S-shaped deformation (Zhao et al., 2017).

Involving the columns, the performance of outrigger braced system reduces the moment of the core and axial forces of core columns under lateral loading, although it does not affect the core shear and shear loads must be entirely borne by the core. The performance of outrigger bracing in structural core is like the performance of torsion spring on a cantilevered beam under distributed loading (Patil and Sangle, 2016). The concentrated moment applied by the spring reduces the moment of cantilevered beam and displacement of its tip.

Using compatibility equations of a cantilevered beam and a torsion spring based on linear elastic behavior and uniform cross-section, Stafford Smith and Coull (1991) found that the tip displacement function of the beam can be expressed in terms of the distance between the tip of the beam and the location of torsion spring and the optimal location of spring can be determined by its derivative with respect to x in order to minimize the tip displacement of the beam. Various research has been done in this regard. Tan et al. (2015) studied Dynamic characteristics of energy dissipation systems with damped outriggers. Lee and Tovar (2014) studied outrigger placement in tall buildings using topology optimization. (Jiang et al., 2017) studied seismic performance of high-rise buildings with energy-dissipation outriggers. Mashhadiali and Kheyroddin

(2014) studied progressive collapse assessment of new hexagrid structural system for tall buildings. They illustrate that resisting progressive collapse capacity, in both hexagrid and diagrid structures, is increased by using the buckling-restrained elements. He and Lu (2019) studied seismic fragility assessment of a super tall building with hybrid control strategy using IDA method.

Studies on the fragility analysis using Peak Ground Velocity (PGV) demonstrate that, for tall buildings, PGV is not only suitable for IDA but also works well in fragility analysis based on its high efficiency and reasonable exceeding probabilities. Mashhadiali and Kheyroddin (2013) studied on proposing the hexagrid system as a new structural system for tall buildings. According to the results, the hexagrid system has a better architectural view and more ductility and stiffness sensitivity, which are about three times than that of the diagrid system. Finally, in comparison with the diagrid system, the hexagrid system has enough potential to push the height limit.

In this study, a 50-story structure is designed with an outrigger braced steel core system. Structures are considered in both modes of the original structure and the structure optimized in terms of outrigger braced system placement. The study is mainly aimed to evaluate the response of structures during near-field earthquakes.

1.1. Performance-Based Earthquake Engineering (PBEE) Provisions

Fragility curve commonly described by using a log-normal CDF, whose characteristic parameters are C and β collected in the vector $\vartheta = (C,)$. In particular parameter C: is the intensity measure producing 50% of failure (median) and β: is the logarithmic standard deviation describing the dispersion of results due to both record-to-record variability and uncertainties about the system response. Therefore, the conditional probability of failure can be obtained by the convolution

integral $P_f(v) = \int_R F_C(i,v)f_I(i)di$; where R+ represents the set of positive real numbers and i: is the intensity (Dall'Asta et al., 2021).

The fragility curve is plotted for the structure by drawing different values of Probability for each IM (Mobinipour and Pourzeynali, 2020). These curves indicate the increasing probability of damage conditions for structures exposed to earthquake. Engineering demand parameters are generally considered as story drift, axial deformations of column and plastic hinges rotations. Various parameters such as PGA, PGD, PGV, spectral acceleration (Sa), etc. are also considered for intensity measure (Nazari and Saatcioglu, 2017). To assess the PBEE, a set of analyses must be conducted using Incremental Dynamic Analysis (IDA) (Asgarian and Ordoubadi, 2016). IDA involves a set of nonlinear dynamic analyses under a series of scaled earthquake records whose intensities should ideally cover the entire range from elasticity to general dynamic instability. In this study, the maximum story drift and plastic strain energy dissipated in each structure are considered as EDP and the spectral acceleration (Sa) and spectral displacement (Sd) are considered as IM.

1.2. Plastic Strain Energy in the Structure

The seismic energy input applied to the structure can be converted into a set of internal energies. Strain energy, kinetic energy (E_k) and the energy dissipated by structural damping (E_ξ) are a set of internal energies in structure, mobilized against the input energy (E_i). The strain energy is divided into elastic strain energy (E_e) and plastic strain energy (E_{in}) in the structure. According to Eq. (1), input energies and internal energies are balanced in the structure:

$$E_i = E_k + E_\xi + E_e + E_{in} \qquad (1)$$

$$E_k = \frac{m\dot{u}^2}{2} \qquad (2)$$

$$E_\xi = \int C \dot{u}^2 dt \qquad (3)$$

$$E_e + E_{in} = \int f_s du \qquad (4)$$

$$E_i = - \int m\ddot{u}_g du_g \qquad (5)$$

where m: is mass of the structure, C: is the damping coefficient, f_s: is the restoring force, u: is the displacement of the mass, $\dot{u}$: is the velocity of the mass, $\ddot{u}$: is the acceleration of the mass, u_g: denotes the foundation displacement, and t: is time (Jamnani et al., 2018).

If the sum of elastic strain energy, energy dissipated by damping and kinetic energy is not balanced with the input energy, the structure uses the plastic strain energy to reach an energy balance (Shin and Kim, 2016). Plastic strain energy causes permanent deformations and damages in the structure (Tavakoli and Afrapoli, 2018). Therefore, if energy is used as a criterion for assessing the seismic performance of structure, plastic strain energy can be considered as EDP which can lead to a damaged in the structure if exceeds the IM.

As stated previously, in this study, a 50-story structure is considered in both original mode and the optimized outrigger braced structure to evaluate their behavioral differences, performances and failures during near-field earthquakes. In this study, IDA (Mohammadizadeh and Jafarzadeh, 2021) and fragility curves are used to achieve the research objectives. The parameters Sa and Sd are considered as IM and the maximum story drift and plastic strain energy are considered as EDP to derive IDA and fragility curves. The specification of proposed models, the seismic loading and the research results are then presented.

2. Introduction to Original Structural Model

In this study, a 50-story structure is modeled and designed initially for time history dynamic analysis. For designing this

structure it was assumed that the structure has a 49 × 49 m plan in the 1st to 5th stories, 35 × 35 m plan in the 6th to 26th stories, 28 × 35 m plan in the 27th to 41st stories and 21 × 35 m plan in the 42nd to 50th stories. The height of stories is considered constant, equal to 3.7 m (Figure 1). The dead load is 700 Kgf/m² for the structure and the live load is also considered 350 Kgf/m² for the 5 first floors and 200 Kgf/m² for other floors. The snow load is 150 Kgf/m² for the proposed structure. The ASCE (2016) is employed for the loading. The base wind speed is considered 41.7 m/s for the region in Iran. The structure is designed for both seismic and wind loads. A spectral dynamic analysis is used for the seismic analysis. It is assumed that the structure is located in a high-risk seismic zone with a peak ground acceleration of 0.3 g, on the soil type 2. Since the Iranian Seismic Code No. 2800 is used for seismic loading and it does not provide behavioral and dynamic magnification factors for outrigger braced structures, linear and nonlinear modeling are applied simultaneously for structural design. Figure 1 Shows the flowchart of design procedure.
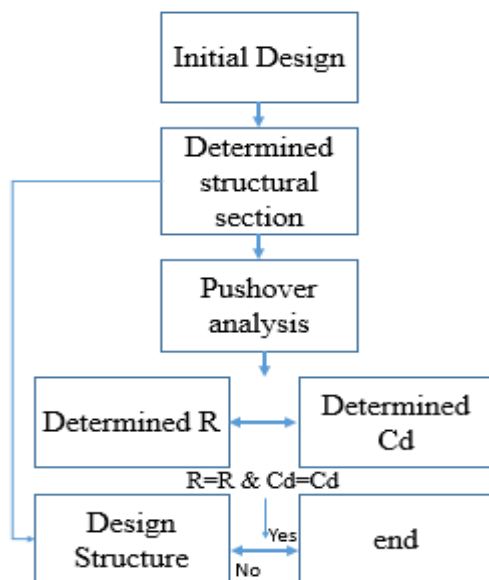

Fig. 1. Design flowchart

After initial design of the structure, the behavioral factor and displacement amplification factor (Cd) are calculated and the design is modified and this process

continues until achieving convergence (4 steps). In Table 1, behavioral and Cd factors are shown for the design steps. The ST37 steel with yield stress of 2400 kg/cm², specific weight of 7850 Kg/m³ and ultimate stress of 3700 Kg/cm² is used.

Table 1. Determining the values of R and Cd factors

| Step	Cd	R	Outrigger braced placement
1	2.17	2.32	Original
2	2.5	2.45	Original
3	2.65	2.59	Original
4	2.69	2.61	Original
5	2.71	2.68	Optimized

2.1. Determining Optimal Placement of Outrigger Bracing

The structure is analyzed and designed after the loading and appropriate sections are then derived. In initial design of the structure, it is assumed that the outrigger braces are placed on the roof and the middle of the structure. Then, the structure is designed. In design process, box sections are used for column and bracing elements and I-shaped sections are used for beams. The suitable sections are shown in Table 2. Figure 2a shows the modeling of original structure. The original structure is designed and then exposed to the triangular load applied by wind and earthquake to calculate the optimal displacement of outrigger bracing. In calculations of the outrigger bracing assumed that the structure behaves linearly, just axial forces are borne by the columns and the outrigger brace connected to the core and columns using fixed and pinned connections, respectively. The geometric properties of the core, columns and outrigger truss are assumed fixed along the height and the lateral load is considered for triangular mode.

Accordingly, in this research assuming two outrigger braces, the ratio of optimum outrigger bracing placement to the entire height of structure (x/H) is calculated 0.52 and 0.188 using the equation. Therefore, the placement of braces is shifted to upper stories 42 and 41 as well as middle stories 26 and 25 in the optimized structure

Table 2. Structural sections in original model of 50-story structure

Story	Column (Box) (cm)		Brace (Box) (cm)		Beam	
	Core	Other	Outrigger	Core	Outrigger	Other
1-5	200×10	80×35		100×5		IPE 300
6-20	180×8	80×3		100×5		IPE 300
20-25	150×7	80×3		80×4		IPE 300
25-30	150×5	70×3	100×5	80×4	HEA 1000	IPE 300
30-35	120×4	50×3		80×4		IPE 300
35-40	80×3	40×2		80×3		IPE 300
40-45	80×3	35×2		60×3		IPE 300
45-50	80×3	30×1	80×2	60×2	HEA 1000	IPE 300
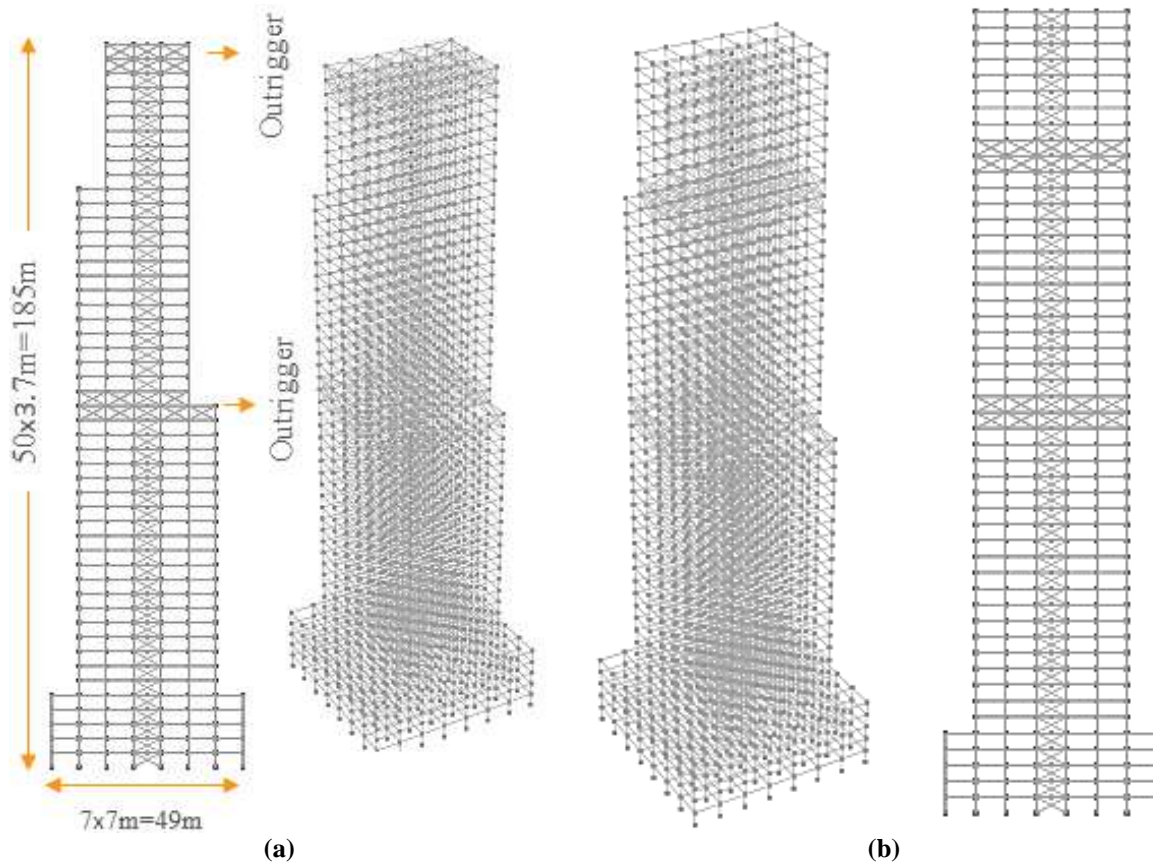
Fig. 2. Finite element models of 50-story outrigger braced structure: a) Original model; and b) Optimized outrigger braced model

2.2. Nonlinear Modeling

The proposed structure is modeled by Perform-3D software for the nonlinear dynamic time history analysis. A concentrated plastic hinge is used for the nonlinear modeling. Force-displacement relationships are defined for beam, column and bracing elements based on the FEMA 356 (FEMA, 2000). FEMA-Beam element is used for nonlinear modeling of the beams and FEMA-Column element is employed to model the columns. A schematic of plastic hinges is shown in Figure 3, according to the FEMA 356. In Table 3, the modeling parameters and performance levels are shown for the elements. To evaluate the seismic performance of the structure using the plastic hinges rotation, three limit modes have been defined. The three performance levels including Immediate Occupancy (IO), Life Safety (LS) and Collapse Prevention (CP) have been selected as criteria for low, medium and high failure, respectively, based on different references (Jiang et al., 2017).

2.3. Seismic Loading

In this study, 18 earthquakes are used for seismic analysis. The characteristics of records are listed in Table 4. The records are

scaled up and applied to the structures. At first, the acceleration response spectrum and the displacement response spectrum are extracted. In Figure 4, the acceleration response spectrum (for a damping ratio equal to 5%) and its corresponding displacement response spectrum are shown in the periods of both structures. Since the structure has a long period, the acceleration response spectrum (Sa) of the structure shows that it has a low sensitivity to the acceleration values. However, a comparison of Sa and Sd values indicates that the structure has a very high sensitivity to the values of acceleration spectrum.

Different authorities introduce different seismic parameters for IM, each with its own characteristics. However, Sd indicates the displacement response of the system is one degree free and is used in tall structures that are more sensitive to displacement than

acceleration. But in general, the acceleration response parameter is a fundamental parameter that gives an easier understanding of the magnitude of the earthquake. Therefore, both Sd and Sa have been used in this research.

To reach a reasonable response in this study, the structural responses are investigated as a function of Sa and Sd values in the incremental dynamic analysis. Because it seems that the acceleration response spectrum (Sa) does not change significantly as the PGA rises, but the displacement response spectrum values increase much more. Therefore, it is more reasonable to use the displacement response spectrum to explain and compare the results, but the responses of structures to the both parameters Sa and Sd are examined for a better comparison.

Table 3. Modeling values and performance levels for definition of plastic joints in structural members based on FEMA 356

Component type	Characteristic parameters			Deformation limit		
	a	b	c	IO	LS	CP
Column	$9\theta_y$	$11\theta_y$	0.6	$1\theta_y$	$6\theta_y$	$8\theta_y$
Beam	$4\theta_y$	$6\theta_y$	0.2	$0.25\theta_y$	$2\theta_y$	$3\theta_y$
Bracing in compression	$0.5\Delta_c$	$8\Delta_c$	0.2	$1.25\Delta_c$	$6\Delta_c$	$8\Delta_c$
Bracing in tension	$11\Delta_T$	$14\Delta_T$	0.8	$1.25\Delta_T$	$8\Delta_T$	$10\Delta_T$

Table 4. Specifications of earthquake records considered for incremental dynamic analysis (IDA) (Tajammolian et al., 2018)

| No.	Record	Station	Max. PGA (g)	Mw
1	Cape Mendocino	Cape Mendocino	1.43	7
2	Chi-Chi, Taiwan	TCU084	1.16	7.6
3	Chi-Chi, Taiwan	TCU065	0.789	7.6
4	Coalinga-05	Oil City	0.841	5.8
5	Gazli, USSR	Karakyr	0.71	6.8
6	Imperial Valley-06	Elcentro#5	0.528	6.5
7	Imperial Valley-06	Elcentro#8	0.602	6.5
8	Kocaeli, Turkey	Izmit	0.22	7.5
9	Loma Prieta	BRAN	0.64	6.9
10	Morgan Hill	Coyote Lake Dam	1.3	6.2
11	Nahanni	Site 2	0.45	6.8
12	Northridge	Converter Station	0.897	6.7
13	Northridge	Sylmar	0.843	6.7
14	San Fernando	Pacoima Dam	1.24	6.6
15	Bam	Bam	0.8	6.6
16	Tabas	Tabas	0.85	7.35
17	Manjil	Abhar	0.51	7.37
18	Duzce	Bolu	0.822	7.1
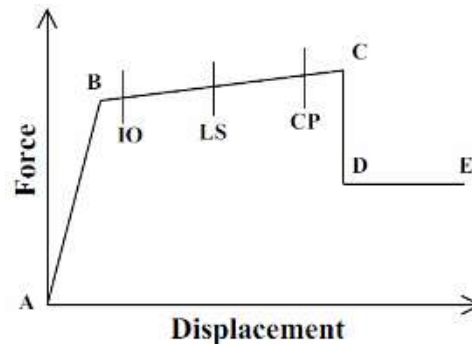
Fig. 3. Modeling parameters and performance levels in plastic joints based on FEMA 356 (Jiang et al., 2017)
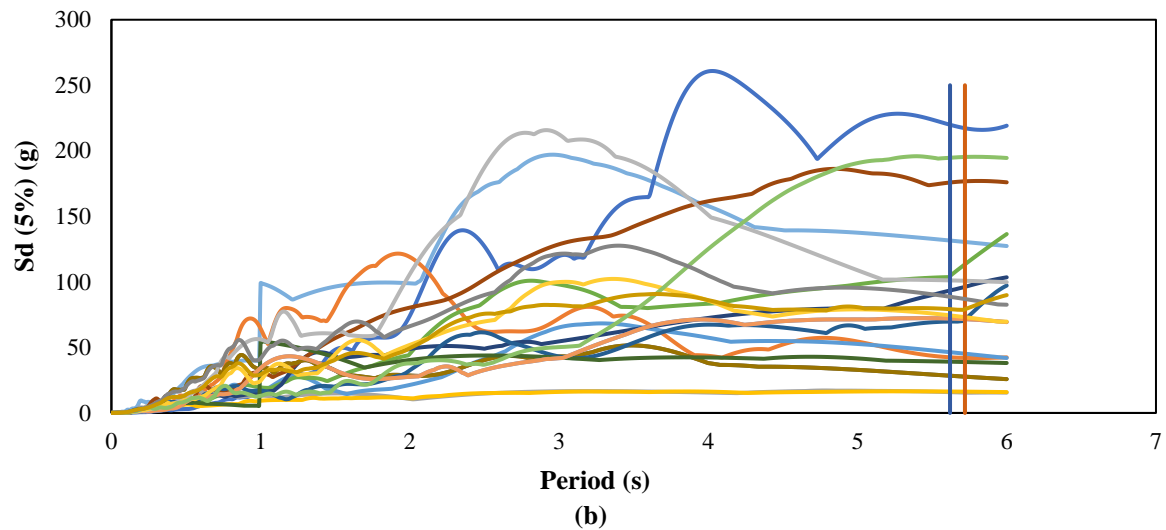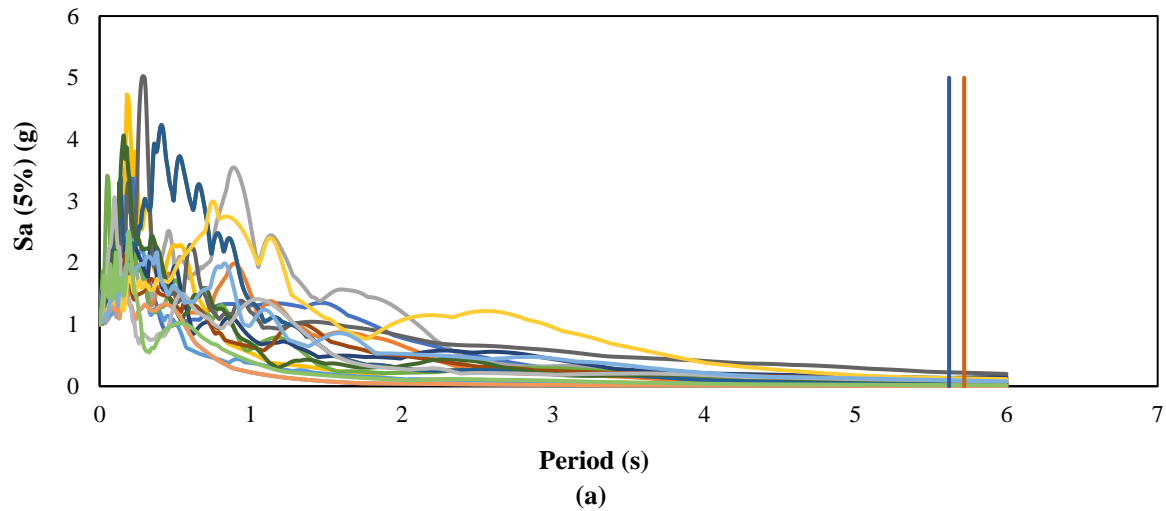

(a)

(b)

Fig. 4. Spectral response: a) Acceleration spectrum; and b) Displacement spectrum

3. Results of Analysis

After nonlinear modeling, outrigger braced structures are subjected to the dynamic seismic load in both original and optimized conditions in order to evaluate their responses. The dynamic load is applied to structures incrementally and the drift and plastic strain energy are derived as research parameters and presented based on parameters S_a and S_d. Initially, the performances of structures are partially compared in some particular earthquakes.

At first drift ratio curves for Chi-Chi earthquake with PGA of 0.2 to 1.4g are illustrated (in 0.2g steps in X and Y

directions for both structures) (Figures 5 and 6). Then rotations of plastic hinges are compared. The results of analysis show that the 47th stories experiences the maximum drift during the earthquake in both structures. As the PGA rises, the response of the structure and the drifts increase. This increase is more in the original structure than the optimized outrigger braced structure. The optimization of outrigger bracing placement causes maximum acceleration of the structure at the applied PGAs to be less than the original structure. Maximum drift is a symbol of structural stability, so the structure is more stable if the outrigger is placed in its optimum position. In addition, the results show that

as outriggers are less spaced apart, the drifts between two outriggers are reduced. In fact, reducing the distance between two belts and inserting an outrigger belt in the middle of the structure decrease the total drift of the structure as well as the story drift between two belts. In Figure 7, the plastic hinge rotations are compared at LS performance level (red elements) during Chi-Chi earthquake at PGA = 1g. The results show number of hinges reach to the LS performance level in optimized structure is less than the original structure. In fact, the role of outrigger bracing in reducing the torsion of steel core causes the optimized outrigger braced structure to perform better than the original structure.
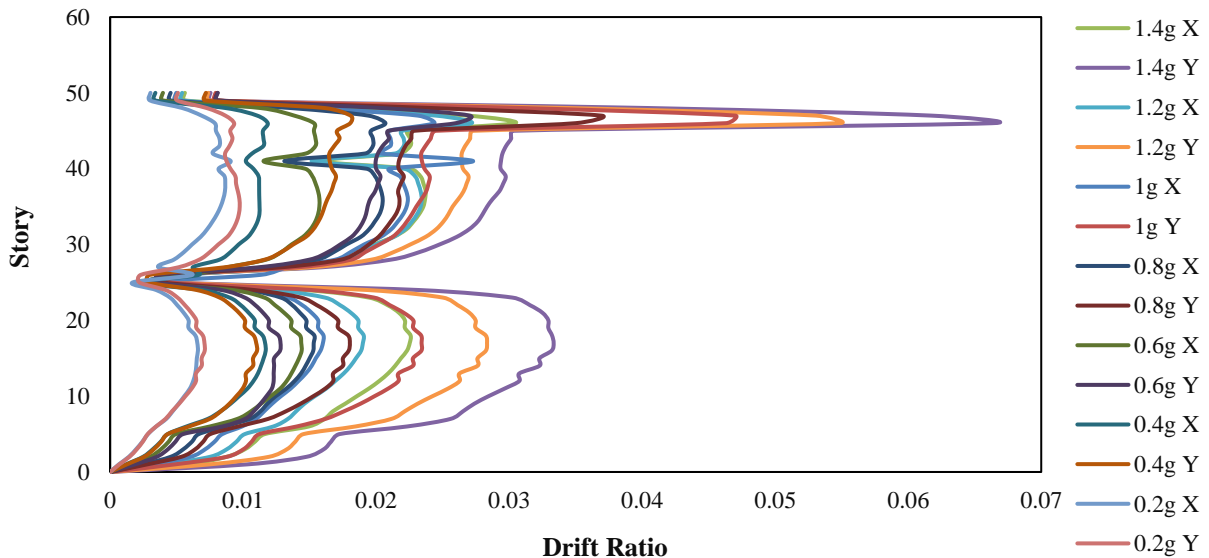
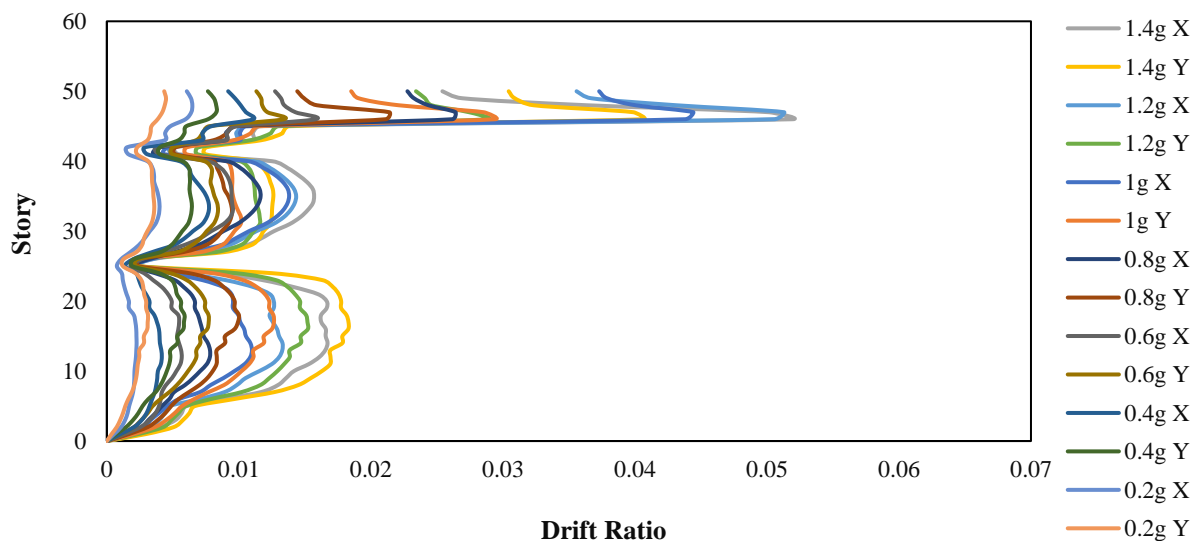**Fig. 5.** Maximum story drift curve for original structure under Chi-Chi earthquake

Fig. 6. Maximum story drift curve for optimized outrigger braced structure under Chi-Chi earthquake

(a)   **(b)**
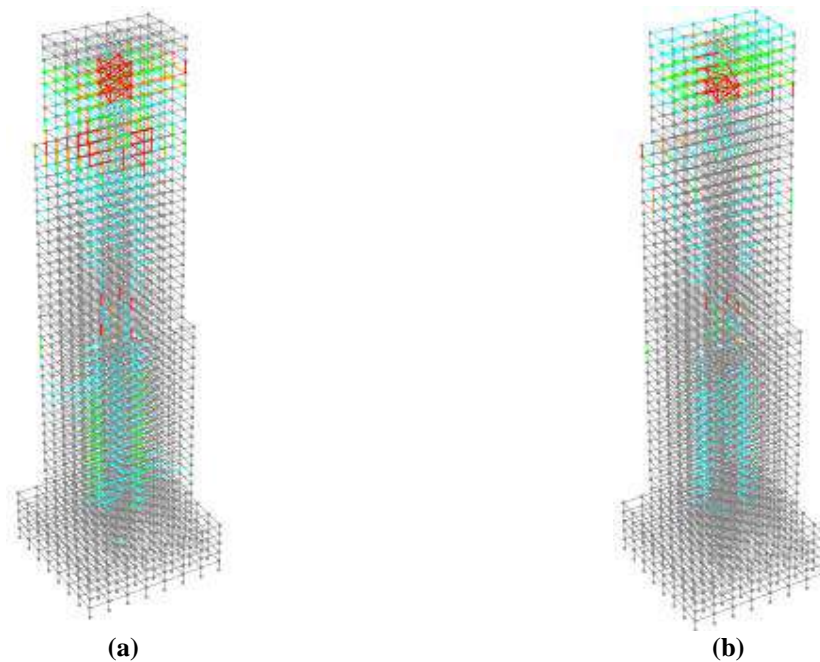
Fig. 7. Rotation of plastics hinges at LS performance level in Chi-Chi earthquake with PGA = 1g: a) Original structure; and b) Optimized structure
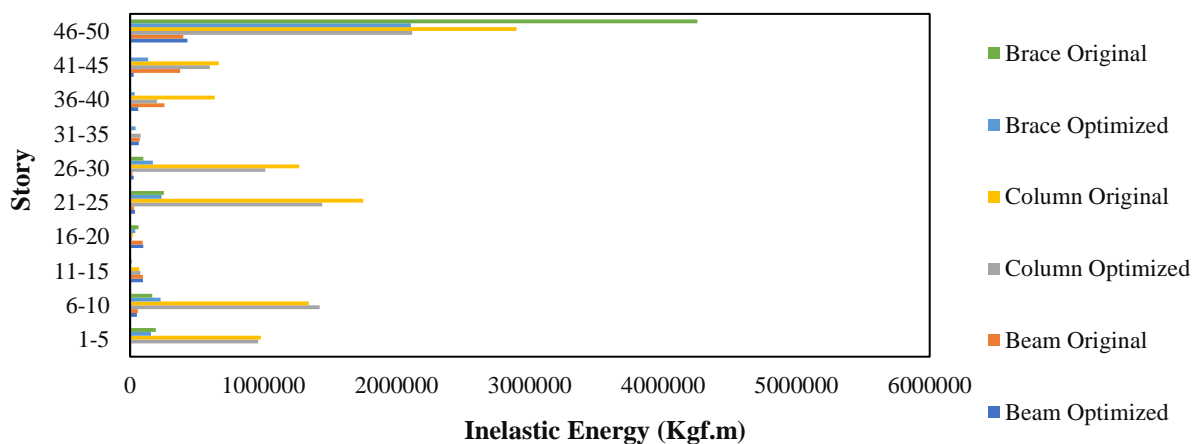

Fig. 8. Plastic strain energy in original and optimized structures in Chi-Chi earthquake with PGA = 1g

Figure 8 represents the dissipated strain energy for beam, column and bracing elements in the both structures. According to the figure, the highest dissipated strain energy is observed in the steel core braces and columns. The beams have the least plastic strain energy. In fact, the steel core in the center of structure causes the strain energy of other elements to be negligible and the structural damage to be minimized in other elements. An investigation into plastic strain energy in the original and optimized outrigger braced structure shows that the strain energy dissipated in the original structure is usually more than that of the optimized structure. In fact, transferring the braces to the optimal position reduces plastic strain energy and, consequently, decreases structural damage due to the earthquake. The IDA curves are presented for the proposed structures. Initially, the drift curves are presented for different values of Sa and Sd. Figure 9 demonstrates the IDA curves for the drift parameter in both original and optimized outrigger braced structures. According to the figure, as Sa and Sd increase, maximum drifts rise to reach the failure boundary; in the failure boundary, drift values significantly surge as the Sa and Sd increase slightly. An investigation of fragility curves shows that the structure experiences stiffening and softening irregularly as IM values increase. This means that the

structure sometimes is faced with a decrease in EDP as IM increases (Sa and Sd). This can be a positive factor for increasing the structural strength and preventing damage. In fact, in these structures, the structural performance is a non-uniform function of IM growth. When an ultimate softening zone emerges in the IDA curve, a dynamic instability is created in the structure. Generally, the mean or median is used to sum up IDA curves. In this study, the median IDA curves are employed to better evaluate and compare the IDA curves. In Figure 10, the median IDA curves are presented for both structures.

(a)

(b)

(c)

(d)
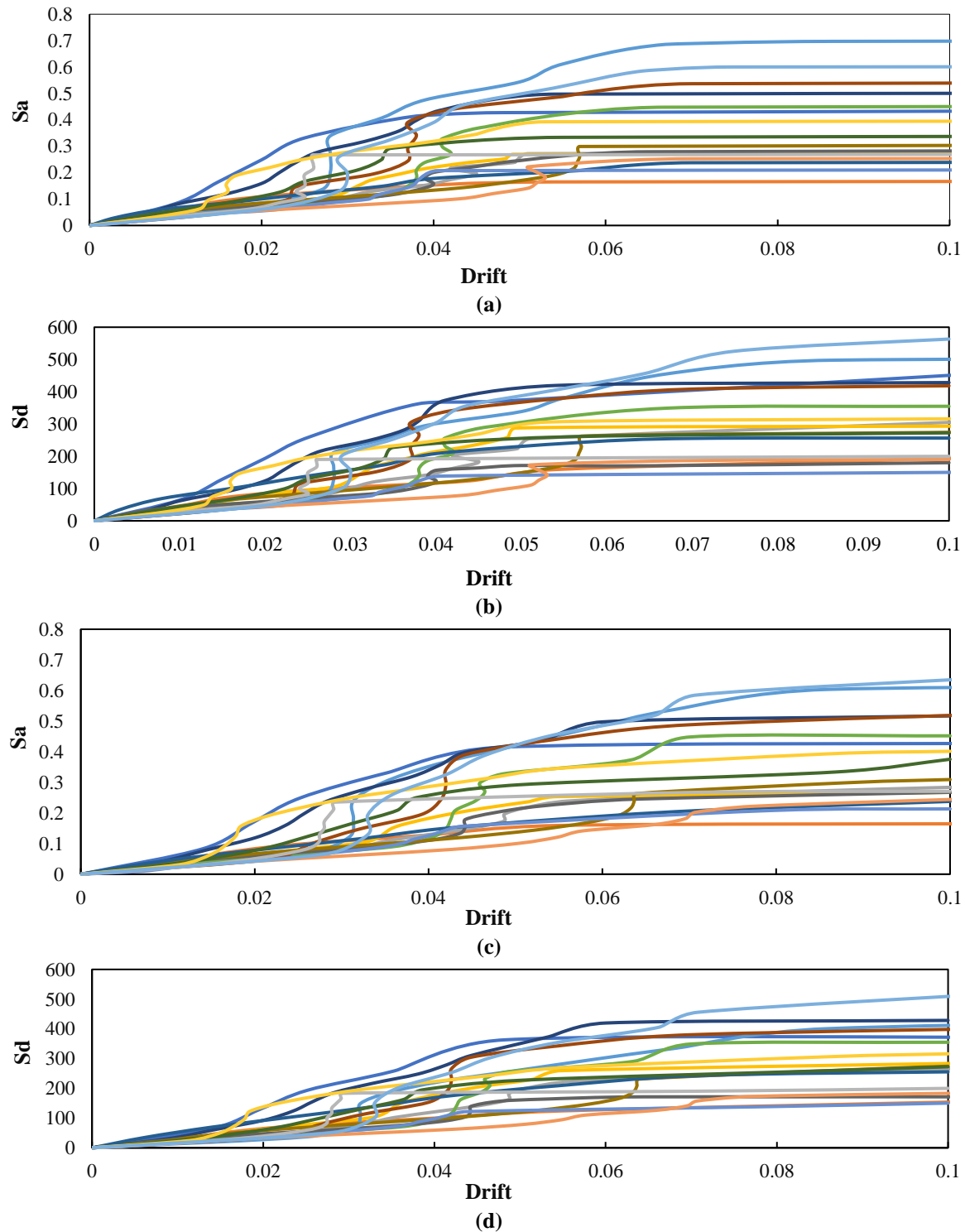
Fig. 9. IDA curves for drifts as EDB: a) Structure optimized by Sa; b) Structure optimized by Sd; c) Structure initialized by Sa; and d) Structures initialized by Sd
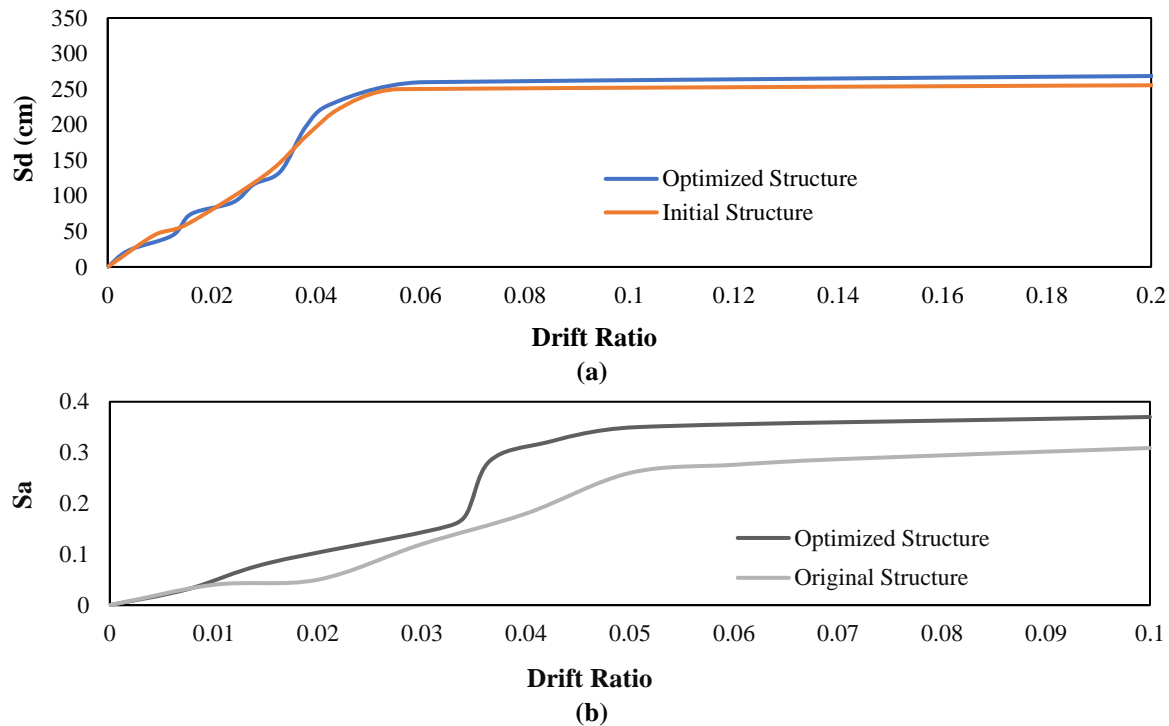
Fig. 10. Median curves derived from IDA analysis for both structures: a) Based on Sd; and b) Based on Sa

An investigation into the variations of IDA curves versus Sa and Sd shows that, in both structural models, the median IDA curve has a softer state versus Sd changes and varies through a significant trend, while the curve shows a hardening state versus Sa changes. Comparison of the curves of both structures also shows that the EDP values of original structure are greater in a given IM, which indicates that the overall performance of optimized outrigger braced structure is better than the conventional structure. Although the ratio of 20% of IDA curve slope to the initial slope is defined as CP performance level according to the FEMA 356, the maximum drift of 0.053 is calculated as CP performance level considering the parameter Sd as IM for both structures. If the parameter Sa is considered IM, the CP performance level is 0.055 for the optimized structure and 0.05 for the original structure. If the end point of elastic range is considered as IO performance level, the drift of IO is 0.0152 with the IM considered in terms of Sd and 0.01 with the IM considered in terms of Sa. For the optimized outrigger braced structure, they are calculated 0.0152 and 0.0154, respectively. Given these two performance

levels, Figure 11 shows fragility curves of the structures with Sa and Sd separately considered as IM. According to the figure, the exceedance probability of IO and CP performance levels in the optimized outrigger braced structure is less than that of original structure. An examination of both IMs suggests that if the Sd value is considered as a criterion, the structures have a 10% exceedance probability of IO performance level in near-field earthquakes with an Sd greater than 10 cm; it would equal 100% for the original structure at Sd = 80 cm and for the optimized structure at Sd = 101 cm. In the original structure, the exceedance probability of CP performance level is 10% at Sd = 130 cm and 100% at Sd = 350 cm. In the optimized outrigger braced structure, the exceedance probability of CP performance level is 9% at Sd = 150 cm and 100% at Sd = 400 cm. The results show that the optimization of outrigger bracing placement has a significant effect on the reduction of exceedance probability of IO and CP performance levels in near-field earthquakes. An investigation into fragility curves of the IMs also shows that exceedance probability of CP performance level starts to increase in low Sa values in

both structures; this phenomenon indicates the selection of Sa as IM cannot be a good choice for tall buildings, because the exceedance of CP performance level is probable in very small values of Sa.

4. Evaluation of IDA Curve Considering Plastic Strain Energy as EDP

According to Eq. (1), the input seismic energy applied to the structure is converted into kinetic energy, potential energy and dissipated energy. The potential energy is stored in form of elastic strain energy in the structure (Szyniszewski and Krauthammer, 2012; Moradi and Abdolmohammadi, 2020). The dissipated energy includes the plastic strain energy and the energy dissipated by damping in the structure (Song et al., 2018). If the sum of kinetic, stored and dissipated energies is in balance with the energy input induced by earthquake, the structure remains stable; otherwise the structure is faced with

instability. On the other hand, the plastic strain energy causes damage in the structure; the greater the amounts of energy, the more structural members are damaged. Internal energy curves are studied in an earthquake. Figure 12 represents the values of plastic strain energy, elastic strain energy, energy dissipated by damping and kinetic energy in the original and optimized outrigger braced structures in Imperial Valley earthquake at PGA = 1g. The analysis was performed in the range of forced vibration and free vibration was omitted in this study. But since in all records the most drift occurred in the forced vibration range, it makes perfect sense to avoid free vibration. However, the time history curve of plastic strain energy also shows that the curve is horizontal at the end of the analysis, which indicates that the energy lost in the structure was also in the range of forced vibration. Therefore, the hypothesis of not considering free vibration is a correct hypothesis in this research.
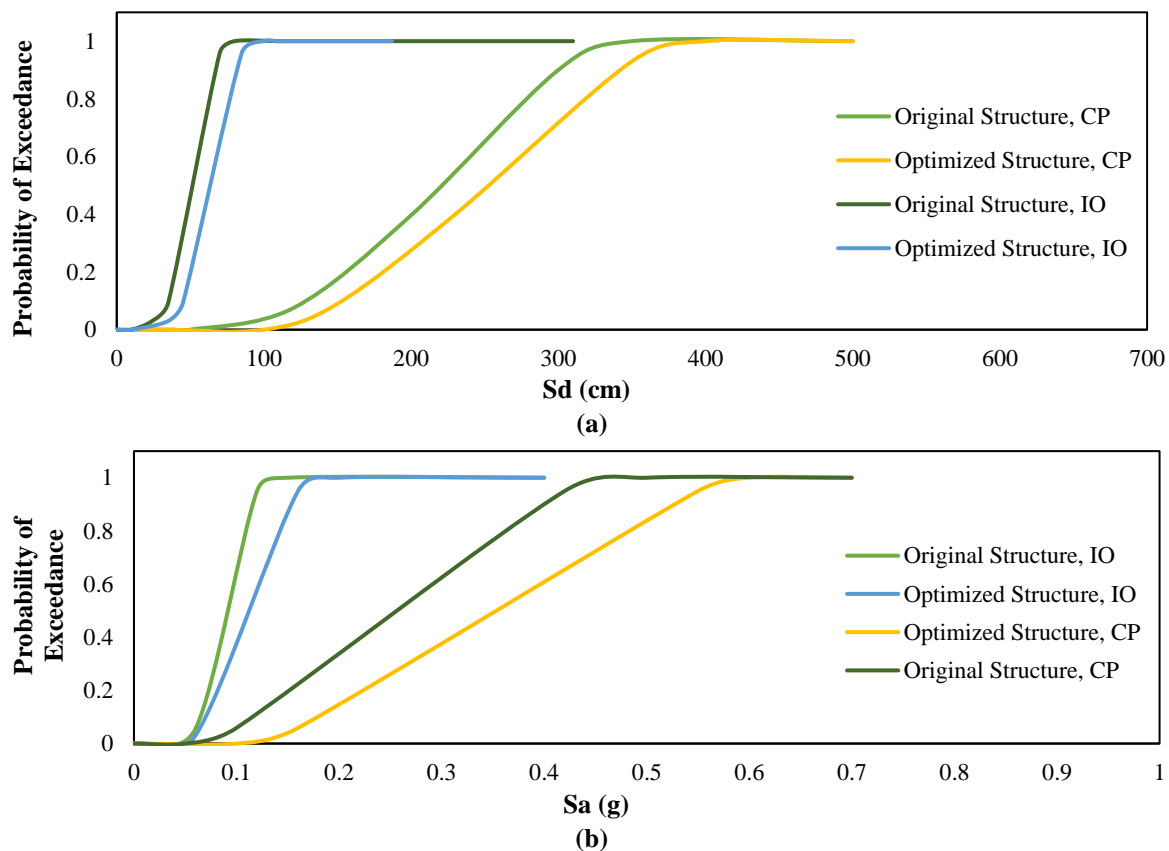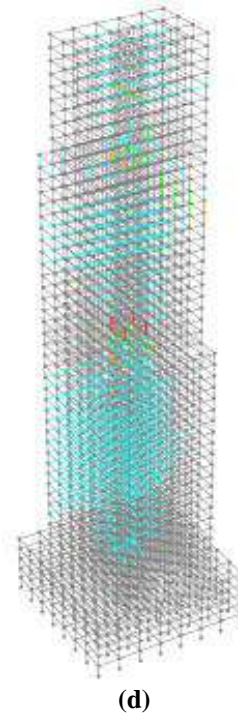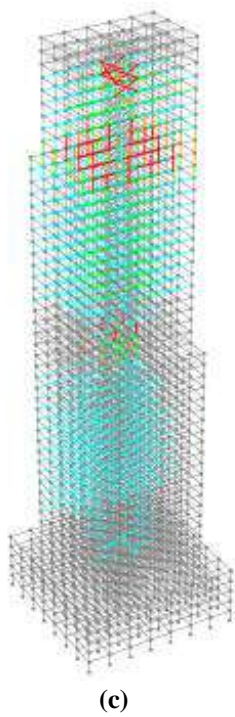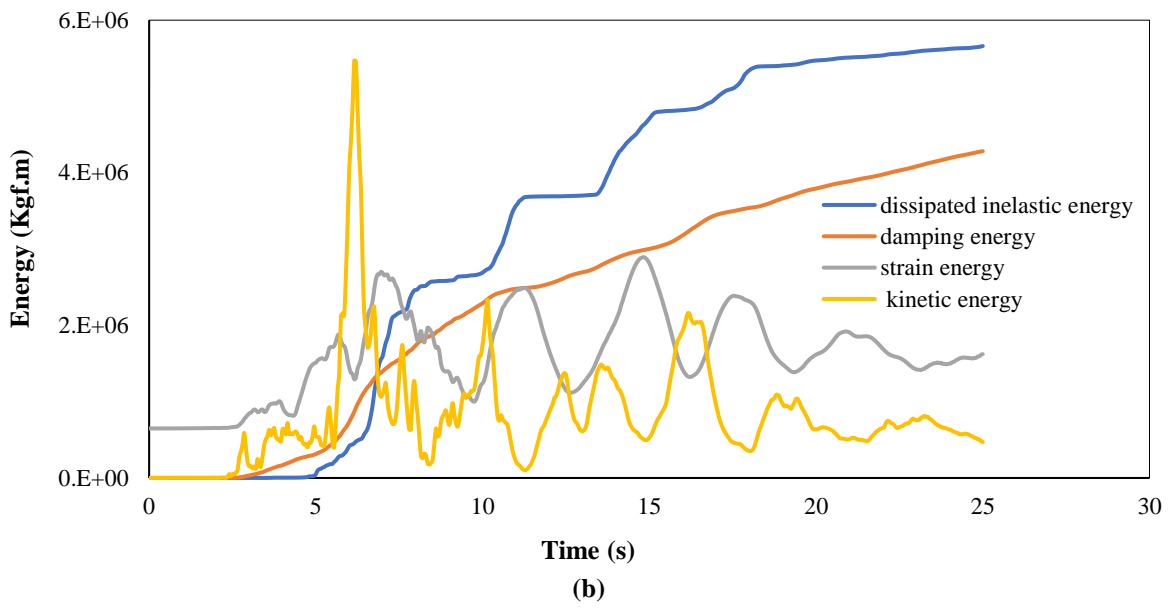

Fig. 11. Fragility curves: a) Considering Sd as IM; and b) Considering Sa as IM

(a)

(b)

(c)   **(d)**
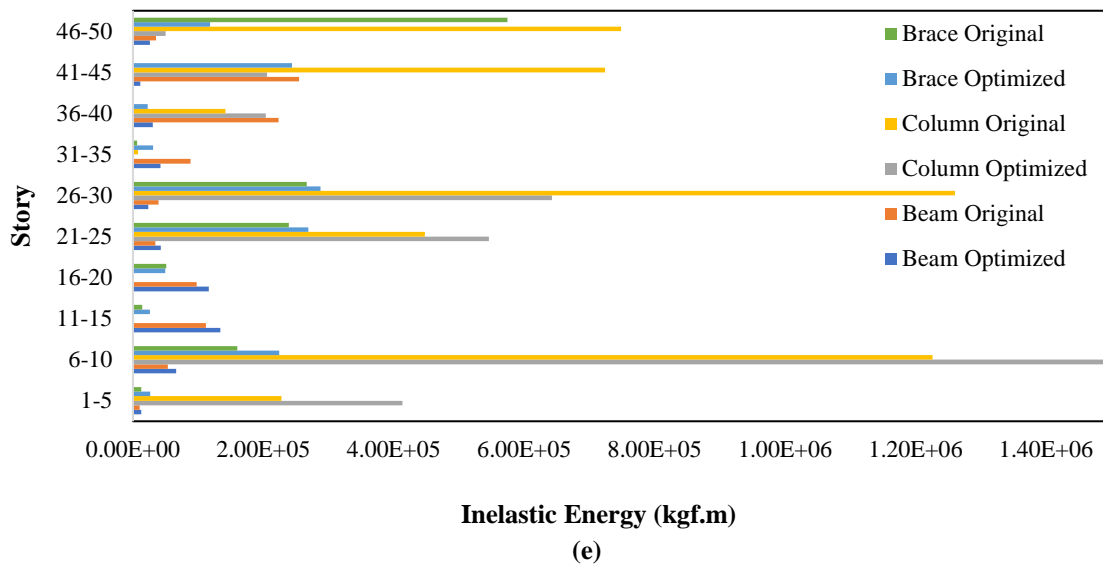
(e)
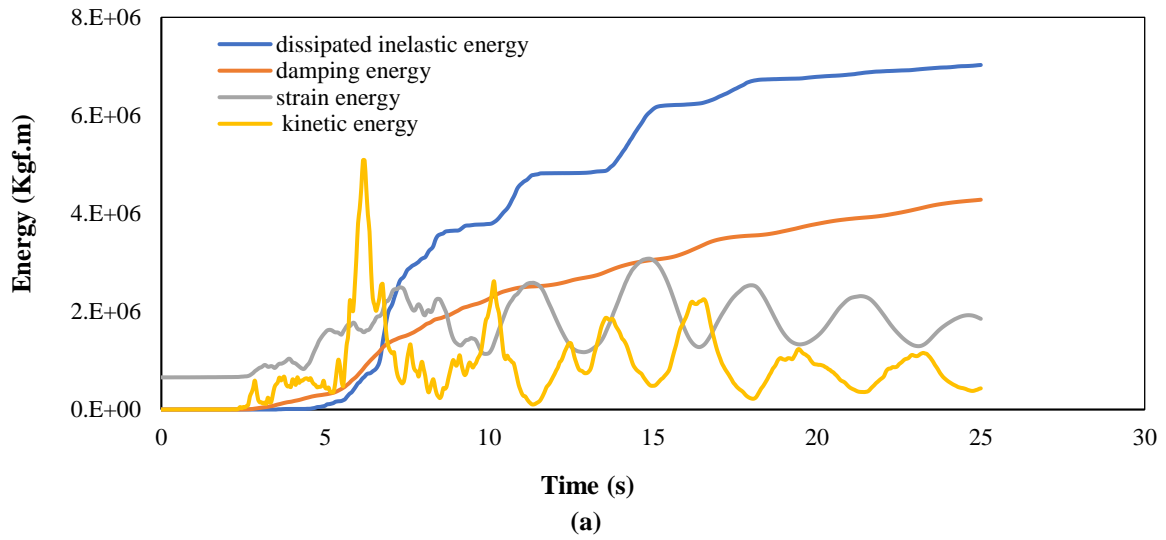
Fig. 12. a) Energy balance in original structure; b) Energy balance in optimized structure; c) Plastic hinge rotations at LS performance level in original structure; d) Plastic hinge rotations; and e) Distribution of plastic strain energy on floors at LS performance level in optimized structure in Imperial Valley earthquake

The assessment of energy curves in both structures shows that the dissipated energy, the sum of the plastic strain energy and the energy dissipated by damping in the structure has an ascending trend in the energy balance. Elastic strain energy has a limited capacity within the elastic range of structure, partly stored by gravity load of the structure. Hence the elastic strain energy of the structure starts from a non-zero value in the energy balance. An investigation into the energy curves in both structures shows that less energy is dissipated by plastic strain energy in the optimized outrigger braced structure in comparison with the original structure, which indicates that this structure suffers less damage than the original structure. The total strain energy dissipated due to the plastic strain energy is calculated as 5.7e6 kgf.m for the optimized outrigger braced structure and 7e+6 Kgf.m for the original structure. An investigation into the amount of plastic strain energy in the structures shows that the increase of plastic strain energy by 1.3e6 kgf.m causes more elements to enter the LS performance level in the original structure and their periods to exceed the LS performance level. Accordingly, these elements suffer more damage in the original structure in comparison with the optimized outrigger braced structure.

Figure 12e shows the distribution of plastic strain energy for beam, column and bracing elements on different floors. According to the figure, in the original structure, the plastic strain energy of structural elements on most floors is more than that of optimized structure. However, the maximum strain energy occurs in the columns of 6th-10th floors in the optimized structure, which indicates that the structural damage on these floors is more than that for the original structure. But the overall performance of structure in accordance with total plastic strain energy criterion in structures shows that the original structure dissipates more plastic strain energy, resulted in greater structural damage. Two views can be adopted to evaluate the structural performance using plastic strain energy. The first view is to investigate the amount of plastic strain energy on each floor of the structure. The amount can indicate the damage induced to each floor of the structure. The second view is related to the strain energy dissipated in the entire structure, which can also reflect the overall damage to the structure. Therefore, two criteria of EDP and IM can be considered for the strain energy dissipated in each structure. The first criterion is determined

by the energy dissipated on each floor of the structure versus the IM of each floor and the second criterion is determined according to the total energy dissipated in the structure versus the total IM of the structure. The second view can reflect the overall damage to the structure and the exceedance probability of each IM may indicate the collapse probability of the structure. In the following, the strain energy dissipated in the whole structure is considered as EDB and its IDA curves are plotted versus the Sd for both structures (Figure 13).

In Figure 13, an examination of IDA curves shows that the plastic strain energy-Sd curves are composed of three sections. The first section is related to the strain energy of about zero. The plastic strain energy of zero on the IDA curve shows that the structure has elastic behavior at corresponding Sd. In these Sds, the input energy applied to the structure is in the balance with the elastic strain energy, the energy dissipated by damping and the kinetic energy and the elements do not enter the nonlinear range. The IDA curve has an infinite slope in the first section. In the second section of IDA curves, the plastic strain energy occurs in the structure as the Sd increases and the structure enters the plastic range. At this stage, the structure is stable but exposed to damage and the plastic joints emerge in the structure. In this section, the infinite slope of IDA curve decreases gradually. In the third section, the slope of IDA curve moves towards zero. In the third section of this curve, the strain energy increases abruptly and the structure is exposed to instability as the Sd increases. The third section actually represents the plastic strain energy corresponding to the point of structural rupture.

In Figure 14, the median IDA curves are shown versus plastic strain energy in the both structures discussed in this study. According to the figure, the median curves are also composed of three sections, like the main curves. This curve shows that the amount of plastic strain energy for each Sd is greater in the original structure than the optimized outrigger braced structure. If the distance between the second and third sections of median curve is considered as strain energy for the collapse limit, the value can be noticed as a failure criterion in the structure. In fact, the behavior of plastic strain energy versus increasing IM in the structure corresponds to zero in a range, an incremental trend in another range and a sudden increase in the other range; the boundary between the increasing trend and the sudden increase can be considered as a the collapse limit of the structure, which indicates the entire collapse of the structure. In Figure 14, the value is equal to 5.8e7 Kgf.m for both structures. Considering the limit as the collapse limit, the fragility curve can be plotted based on plastic strain energy as EDP.
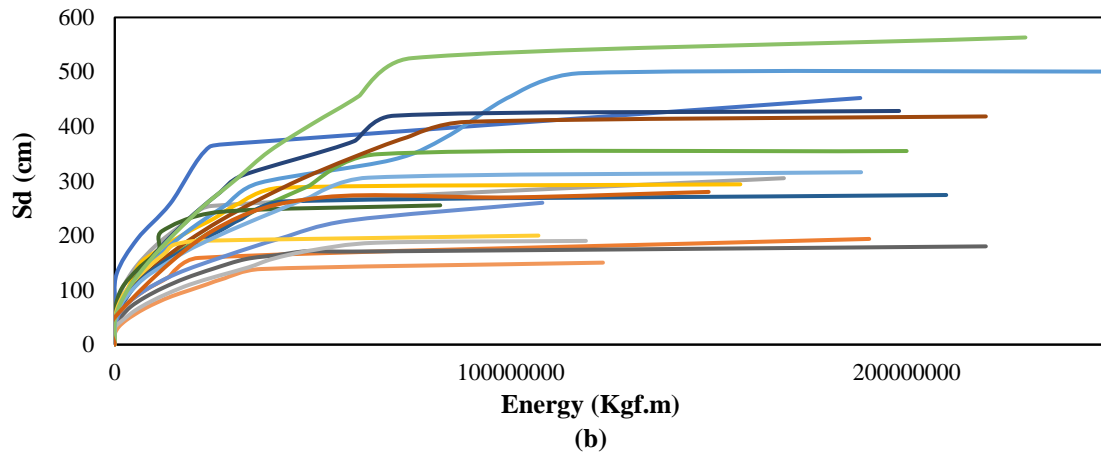

(a)
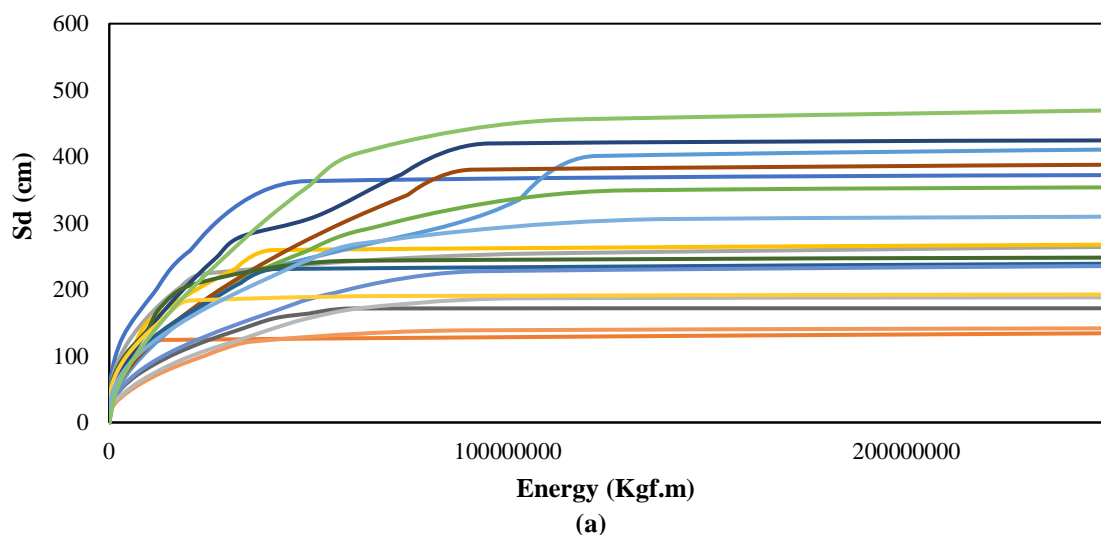
Fig. 13. IDA curve based on plastic strain energy: a) Original structure; b) Optimized structure
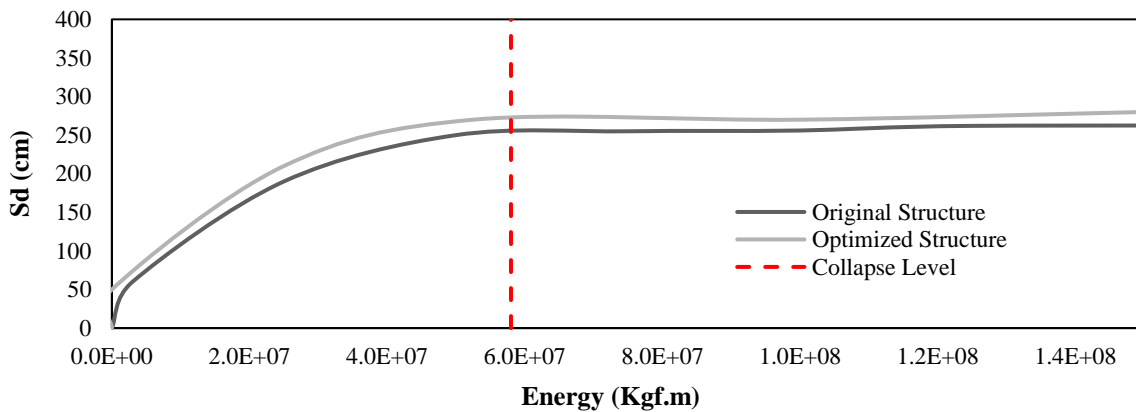

Fig. 14. Median curves derived from IDA curves based on Sd and plastic strain energy

In Figure 15, the fragility curve obtained from the parameter Sd as IM and the plastic strain energy as EDP are derived and presented for both structures discussed in this study. According to the figure, like previous fragility curves, the optimized structure has a lower probability of failure in the same IMs in comparison with the original structure. In the following, the fragility curves of the structures are compared with the drift considered as EDP

and the plastic strain energy considered as EDP. According to Figures 11 and 15, the fragility curves with plastic strain energy considered as EDP almost have a good convergence with the fragility curves with drift considered as EDP in the rupture of structure. Therefore, to evaluate the collapse probability in structures, the drift can be substituted by the strain energy criterion as an effective parameter in the assessment of structural damage.
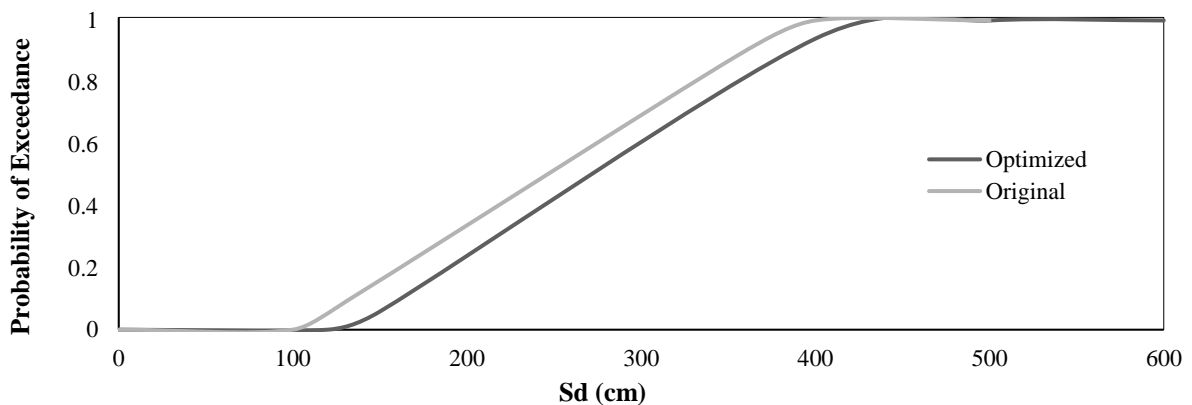

Fig. 15. Fragility curve based on energy and Sd in original and optimized structures

5. Conclusions

Aimed to investigate the effect of optimizing outrigger bracing placement in tall structures, the behavior of this structural system is studied in two structures of 50 floors in this article. In the original model, outrigger braces are placed on the last two and the middle two floors; while in the optimized model, the outrigger braces of the last two floors are transferred to the 42nd and 41st floors after calculations. Many parameters are used to assess the behavior of structures. IDA curves are the most important parameter for evaluating the behavior of structures in this research. Two parameters of maximum story drift and plastic strain energy are considered as EDB and two parameters of Sa and Sd are also considered as IM in fragility curves. The results of analyses are summarized as follows:

- The plastic hinge rotations and maximum story drift show that the optimization of outrigger bracing placement improves the behavior of structure. The process is obvious in the median curves derived from the IDA curves.
- The energy balance shows that the placement of outrigger bracing system is optimized in the structure, the plastic strain energy declines, while the elastic strain energy and the energy dissipated by damping do not change significantly and the kinetic energy may increase. In the optimized structure, the plastic strain energy of most floors is less than that for the original structure.
- The results show that if maximum story drift is selected as EDB and the Sa is considered as IM, the collapse limit in the optimized structure is 5% higher than that of the original structure. However, if the Sd is chosen as IM, the collapse limit is the same in both structures.
- An investigation of fragility curves for both structures shows that the collapse probability of the optimized structure is less than that of the original structure for

the same IM. The results of fragility analysis suggest that the collapse probability of 100% is at Sd = 400 cm for the optimized structure and at Sd = 350 cm for the original structure.
- The selection of total plastic strain energy as EDB and its corresponding fragility curves demonstrate that the collapse probability equals 100% at Sd=400 cm in the original structure and at Sd=500 cm in the optimized structure.

6. Acknowledgements

7. References

ASCE. (2016). *Minimum design loads for buildings and other structures*, American Society of Civil Engineers.

Asgarian, B. and Ordoubadi, B. (2016). "Effects of structural uncertainties on seismic performance of steel moment resisting frames", *Journal of Constructional Steel Research*, 120, 132-142.

Dall'Asta, A., Dabiri, H., Tondi, E. and Morci, M. (2021). "Influence of time-dependent seismic hazard on structural design", *Bulletin of Earthquake Engineering*, 19(6), 2505-2529.

Ding, R., Nie, X., Tao, M.-X. and Fan, J.-S. (2018). "Fishbone-shaped beam–column model for steel outrigger truss-concrete wall composite joints", *Journal of Constructional Steel Research*, 145, 386-396.

FEMA 356, Federal Emergency. (2000). *Prestandard and commentary for the seismic rehabilitation of buildings*, Federal Emergency Management Agency: Washington, DC, USA.

Gorji, M.S. and Cheng, J.R. (2017). "Steel plate shear walls with outriggers, Part I: Plastic analysis and behavior", *Journal of Constructional Steel Research*, 134, 148-159.

Gorji, M.S. and Cheng, J.R. (2017). "Steel plate shear walls with outriggers, Part II: Seismic design and performance", *Journal of Constructional Steel Research*, 137, 311-324.

Jamnani, H.H., Amiri, J.V. and Rajabnejad, H. (2018). "Energy distribution in RC shear wall-frame structures subject to repeated earthquakes", *Soil Dynamics and Earthquake Engineering*, 107, 116-128.

Jiang, H., Li, S. and Zhu, Y. (2017). "Seismic performance of high-rise buildings with energy-

dissipation outriggers", *Journal of Constructional Steel Research*, 134, 80-91.

Lee, S. and Tovar, A. (2014). "Outrigger placement in tall buildings using topology optimization", *Engineering Structures,* 74, 122-129.

Mobinipour, S.A. and Pourzeynali, S. (2020). "Assessment of near-dault ground motion effects on the fragility curves of tall steel moment resisting frames", *Civil Engineering Infrastructures Journal*, 53(1), 71-88.

Mohammadizadeh, M.R. and Jafarzadeh, A. (2021). "Comparison of nonlinear dynamic analysis of time history and endurance time method in tall structures with frame-wall system", *Civil Engineering Infrastructures Journal*, 54(2), 405-421.

Moradi, M. and Abdolmohammadi, M. (2020). "Seismic fragility evaluation of a diagrid structure based on energy method", *Journal of Constructional Steel Research*, 174, 106311.

Nazari, Y.R. and Saatcioglu, M. (2017). "Seismic vulnerability assessment of concrete shear wall buildings through fragility analysis", *Journal of Building Engineering*, 12, 202-209.

Patil, D.M. and Sangle, K.K. (2016). "Seismic behaviour of outrigger braced systems in high rise 2-D steel buildings*",* In *Structures,* Elsevier, 8, 1-16.

Shin, D.-H. and Kim, H.-J. (2016). "Influential properties of hysteretic energy dissipating devices on collapse capacities of frames", *Journal of Constructional Steel Research,* 123, 93-105.

Song, Z., Frühwirt, T. and Konietzky, H. (2018). "Characteristics of dissipated energy of concrete subjected to cyclic loading", *Construction and Building Materials,* 168, 47-60.

Stafford Smith, B. and Coull, A. (1991). *Tall building structures: Analysis and design*, Wiley-Interscience.

Szyniszewski, S. and Krauthammer, T. (2012). "Energy flow in progressive collapse of steel framed buildings", *Engineering Structures,* 42, 142-153.

Tajammolian, H., Khoshnoudian, F., Rad, A.R. and Loghman, V. (2018). "Seismic fragility assessment of asymmetric structures supported on TCFP bearings subjected to near-field earthquakes", In *Structures,* Elsevier, 13, 66-78.

Tan, P., Fang, C., Chang, C. Spencer, B. and Zhou, F. (2015). "Dynamic characteristics of novel energy dissipation systems with damped outriggers", *Engineering Structures,* 98, 128-140.

Tavakoli, H. and Afrapoli, M.M. (2018). "Robustness analysis of steel structures with various lateral load resisting systems under the seismic progressive collapse", *Engineering Failure Analysis,* 83, 88-101.

Zhao, E., Cheng, K., Sun, W., Zhou, Z. and Zhao, J.

(2017). "Buckling failure analysis of truck mounted concrete pump's retractable outrigger", *Engineering Failure Analysis*, 79, 361-370.

Effect of Surface Condition on the Skid Performance of the Stone Matrix Asphalt

Davari, M.[1] , Khabiri, M.M.[2]* and Fallah Tafti, M.[2]

[1] M.Sc. Student, Department of Civil Engineering, Yazd University, Yazd, Iran.
[2] Associate Professor, Department of Civil Engineering, Yazd University, Yazd, Iran.

ABSTRACT: Road traffic accidents are one of the major issues that have been investigated by many researchers in transportation communities. One of the effective factors in reducing accidents is to improve the surface friction of the road pavements, which is often measured by the skid resistance. The presence of dust would reduce drivers' field of view and also the skid resistance of the road surface, and thereby contributes many road accidents in these areas. In this research, the existing dust particles were collected from the surface of the roads. These fine dust with variable amounts were scattered as contaminants on the surface of asphalt samples and skid resistance was measured for HMA and SMA asphalt samples with different gradations and temperatures. The results showed that dust deposition on the pavement surface in three months causes pavement skid resistance in the two types of HMA and SMA asphalt mixtures, decreasing 9 to 16% in the dry state and 25 to 35% in the wet state. According to the obtained results, it is recommended to apply SMA asphalt with a nominal size of 19 mm as a Topeka layer in the areas that are exposed to fine dust, especially in conditions of high traffic and high ambient temperature.

Keywords: British Pendulum, Dust, Road Surface Pollutants, Skid Resistance, Stone Matrix Asphalt.

1. Introduction

Skid-resistance is one of the important properties of road pavements. Lack of enough friction and skid resistance of the pavement surface are known as important factors in traffic accidents(Jalalkamali et al., 2021; Jalal-Kamali et al., 2019). Extensive research on pavement friction has been conducted for decades. Pavements constructed with conventional, unmodified asphalt binders and aggregates grading may not sustain the adverse environmental

conditions and traffic load (Raufi et al., 2020; van Bijsterveld and del Val, 2016). Skid-resistance property is defined as a deterrent and resistive force that prevents the vehicle's wheels from skidding on the road surface during the wheels' lock. On the wet surface, it also plays a decisive role in controlling vehicles by their drivers. There are various pollutants on the road surface, which contribute to the skiddiness of the road surface (Chan et al., 2010; Dan et al., 2017). The natural pollutants include sand dune on the surface of roads located in the

* Corresponding author E-mail: mkhabiri@yazd.ac.ir

desert areas and also the dust caused by the pollutants. The variation in the road surface temperature and humidity would also affect the skid-resistance of road pavements.

There could be a direct link between the roughness or skid resistance of a road surface and its accident rates. Dust has caused severe environmental problems in many countries with roads passed through desert areas, e.g. Iran. In a situation where the dust in the air is too high, the road surface would likely be skiddy and the sight vision of drivers would also be reduced. For instance, in research conducted in an area closely located to the city of Zabol in the sought-east of Iran, it was found that the maximum accidents in this area have occurred in the summer and during the annual 120 days' storm period. Dust storms, which mostly occur in the arid and semi-arid regions of the world carrying a large amount of suspended particles and therefore are considered as one of the most important international environmental issues. Dust is very small and light particles with a diameter lower than 10 μm, which are moved and transported to a very long distance as a result of wind erosion and desertification. Over the last four decades, the dust phenomenon has been observed in vast areas of the world, e.g. in Southwest Asia, Central Asia, North America, and North Africa, which is called the "global dust belt" (Sharafati and Mishmast Nahi, 2017).

Wallman and Astrom (2001) carried out comprehensive research on the friction and rate of accidents and concluded that increasing road friction would greatly decrease the accident rate (Wallman and Åström, 2001). Xiao et al. (2000) proposed a model to predict the accidents in the wet condition. This research was performed under the supervision of the Pennsylvania Department of Transportation. They found that if the skid value increases from 33.4 to 48, the accidents could be reduced by about 60%. Kamel and Gartshore (1982) researched on the hazardous highways of Ontario, Canada. They found out that

friction should be increased in these locations, which could then lead up to 29% reduction in accident rates.

For the effect of the dust on the accidents, Sharafati and Mishmast Nahi (2017) concluded that the maximum number of accidents in Zabol city have occurred in the summer and during the 120-days storms. Abdoulahi (2016) investigated the quantitative changes of the dust in Zahedan province, using a marble sediment trap for sampling. The results showed that the average weight of the dust fall in Zabol city over the winter of 2014 and spring 2015 were 9.625 and 6.319 gr/m^2, respectively.

Cao et al. (2010) investigated the effect of pollutants on the skid-resistance and found out that the skid-resistance of the asphalt pavement will be affected when the surface is covered with the pollutants, and the maximum effect of the pollutants on the skid-resistance occurs when all the surface covers with the pollutants. Wang et al. (2015) investigated the effect of the sand and gravel materials, sprinkled on the road surface of an asphalt pavement during the winter service, on the skid-resistance. They realized that the quartz sand powder as an anti-freeze factor would only eliminate a fraction of bitumen from the top of the aggregates in the asphalt pavement, and also noticed that the micro-texture of the aggregates would also slowly be polished. By using the quartz sand, the bitumen is completely eliminated from the surface, and the sharpening edge of the aggregates will highly be eliminated. Also, Tyfour (2009) investigated the effect of pollutants on the skid-resistance of the wet surface and concluded that the rain would reduce the surface skid-resistance of the pavement and that the existence of the other pollutants has an important role in a further reduction of the skid-resistance. In research conducted by Do et al. (2014) the effect of pollutants on the skid-resistance was investigated. The pollutants of this research were selected from a filling level near Nantes, France. Their selected sample was a 450 × 210 × 35 mm rectangular slab, and since their

objective was to investigate the effect of the pollutants, only one asphalt mixture sample was used. The surface of the test was a 100 × 150 mm rectangle with an area of 0.015 m^2. Three weights of 1.25 gr, 2.5 gr, and 5 gr of pollutants were used for the test.

Blake et al. (2017) investigated the effect of volcanic ash from four different volcanic resources in New Zealand on the skid-resistance of the airport and road surfaces. The result indicated that road markings in either dry or wet conditions when covered with a thin layer of ash led to a reduction in friction and more importantly the biggest change in the skid-resistance of a surface covered with ash occurred at dry conditions. In research carried out by Zhang et al. (2015) the effect of the aggregates' size on the skid-resistance of the porous asphalt was numerically investigated. The results of the numerical simulation showed that the asphalt pavements constructed from the higher size aggregates produced higher skid-resistance than lower sized aggregates. This was attributed to the better drainage and lower thickness of water flowing on the pavement surface.

One conclusion that can be drawn from this literature review is that the macro and micro texture of a road surface is an initiation factor in the friction force between the wheel and surface of the road pavement. This is affected by the roughness, type, size, classification, and grading of the aggregates. To measure the roughness, the sand patch method, and to measure friction, the English friction pendulum was used at different temperatures. The main objectives of this study were therefore to evaluate the effect of the aggregates grading on the skid -resistance of the SMA asphalt mixtures using coarse- and fine-grained mixtures, to evaluate the effect of changes in ambient temperature, and also combined effects of the temperature changes and dust on the skid -resistance of the asphalt mixtures.

2. Research Methodology

One of the main objectives of this research was to investigate the effect of dust on the skid-resistance of the SMA asphalt mixtures comprising three different grading with a maximum nominal size of 9.5, 12.5, and 19 mm, respectively. For this purpose, an experimental method was used by Irfan et al. (2019). The optimal bitumen content for making the samples was obtained using the Marshall Strength test (ASTM D-1559), and then the samples were produced. At first, the coarse texture of the samples was measured using the sand distribution method, and then the skid-resistance of the samples was measured in the desired conditions using a British Pendulum skid resistance tester. These conditions include the presence or the absence of dust. Also, the effect of the dust at different temperatures was investigated, and the effect of dust and temperature changes and the combination of these two factors on the skid-resistance were measured and compared to each other. The required aggregates were obtained from the crushed local limestone rocks used in the highway construction projects crashed to the required size. Rock wool fibers were also obtained from a producer and used in making the SMA asphalt. The dust was collected from the surface of the Zahedan-Iranshahr highway that is passed through the deserts in the southeast of Iran. The bitumen used to produce SMA samples was a PG-grade binder (ASTM D7643-16), with the specifications indicated in Table 1.

To prevent bitumen flow in the mixture, the fibers are used in the SMA asphalt mixtures. The fibers used in these types of asphalt mixtures can be organic or mineral types such as mountain cotton, stone wool, glass wool, and cellulose (Terrones-Saeta et al., 2020). In this research, due to the ease of access and compliance with safety, health, and environmental issues, Rockwool was used which is a mineral fiber. To comply with the SMA standards, the amount of the Rockwool fiber used to make the samples was 0.4% of the total weight of the mixture, the length of the fibers was about 1 mm.

The technical specifications of the aggregate materials used in the asphalt samples have an important effect on their skid-resistance; as a result, the relevant standard tests were performed to determine their technical specifications (Kogbara et al., 2016). The results of the tests are presented in Table 2 and compared with their corresponding standard limits. In this research, three grading types with the maximum aggregate nominal size of 19%, 12.5%, and 9.5% were used to produce the SMA samples. The SMA mixture design was conducted to determine the optimal grading for different mixtures (grading with different nominal size) and optimal bitumen content under the method provided in NCHRP Report 425 (1999). Four different grading are proposed for the SMA asphalt mixtures, comprising maximum nominal sizes of 19%, 12.5%, 9.5%, and 4.75% (NCHRP Report 425, 1999).

For each mixture, the optimal grading was obtained to comply with the following triple requirements. The first requirement is the value of the Voids in the Mineral Aggregates (VMA). The value of the VMA should be more than 17%. Because of the

failure possibility during compaction and a reduction in VMA, the minimum value of the VMA was selected in the range between 17.5 to 18%. The second criterion is to ensure the existence of stone-stone contact in the coarse-grained mixture. For this purpose, the ratio of air void available in the mixture to the dry case was considered to be equal to or less than 1.

As it was likely that two and/or even all three considered grading could meet the desired conditions; therefore, the optimal grading was selected so that the minimum value of the bitumen content is used whilst the desired air void ratio ($V_a = 3$ to 4%) is also met.

Figure 1 shows the resulting grading for mixtures corresponding to each maximum nominal size used in this research. The curve with power 0.45 is linear which according to the Fowler formula, shows the maximum grading density, indicating that the density of the mixture would be increased as it gets closer to this line. Following the determination of optimal grading, the optimal bitumen content for the mixture was also determined.

Table 1. Results of the tests done on the consumed bitumen

Test title	Dim.	Result min	Standard max
Humidity	Prec.	18%	
Viscosity @ 135 (RV)	°C	0.332	---	3 Pa.s
Flash point temperature	°C	334	230	---
Original dynamic shear	Kpa	1	1.14	---
RTFO, percent change of mass	Prec.	5.7	---	1
MSCR test, standard traffic"s", Jnr3.2		3.9	---	4.5
MSCR Test, Standard traffic"s", Jnrdiff%	Prec.	19	---	75
RTFO, dynamic shear	Kpa	2.31	2.2	---
PAV, dynamic shear @25 °C	Kpa	1632	---	5000
PAV, creep stiffness @-12 °C	Mpa	96.23	---	300
m-value, (slope) @-12 °C		0.302	0.3	---
PAV, direct tension	Prec.	---	1	---

Table 2. Technical specifications of the aggregates

| Specification	Standard	Results	Regulations limit
	coarse aggregates		
Actual specific weight (g/cm^3)	ASTM C127	2.594	-
Specific gravity (g/cm^3)	ASTM C127	2.672	-
Water absorption (%)	ASTM C127	0.6	2.5Max
Los Angeles Wwear (%)	ASTM C131	17.1	25 Max
Weight loss with sodium sulfate (%)	ASTM C88	3.6	8 Max
Fracture value (%)	ASTM D5821	97	90 Min
	Fine aggregates		
Actual specific weight (g/cm^3)	ASTM C127	2.689	-
Specific gravity (g/cm^3)	ASTM C127	2.734	-
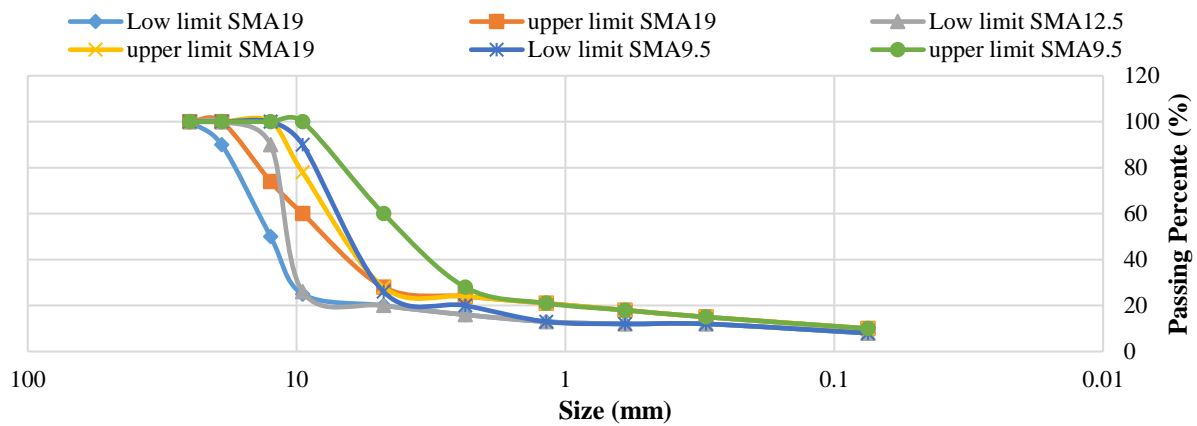
Fig. 1. Grading curves of the mixtures used in the present study

2.1. Optimum Bitumen Content

To determine the optimal bitumen content, its content should be varied to obtain the optimal bitumen content. In this stage, 9 Marshall samples include 3 samples at three different bitumen content levels were produced using optimal grading. The variation in bitumen content was considered 0.4%. Then, given the real specific weight of the compressed sample and the maximum theoretical specific weight of the mixture, the air void was obtained, and the *Va* curve was plotted against the bitumen and the optimal bitumen content at a point where the air content is 4% was selected using the interpolation. The optimal bitumen content for different mixtures was obtained as presented in Table 3.

It can be seen from Table 3 that by increasing the nominal size, the optimal bitumen content would increase. It should be noted that in designing the SMA mixtures, the flow and Marshall strength can not be used, because the Marshall strength is not an appropriate criterion for designing these mixtures. In NCHRP Report 425 (1999), the minimum value of Marshall strength for SMA mixtures is specified as 6200 N.

Moreover, the performance of the Marshall method in designing SMA mixtures has been promising. Table 4 shows the Marshall strength of the different mixtures produced in this research.

2.2. Measuring the Coarse Texture and Determining the Skid Value

The SMA samples produced with the 6-inch diameter Marshal test molds were used to conduct the skid-resistance test (see Figure 2). The reason for using 6 in diameter samples, is that according to the ASTM E303 Standard, the path needed for passage of the rubber slider of the British Pendulum is in the range of 12.4-12.7 cm (Zealand, 2002).

Table 3. The optimum bitumen content of different mixtures

Bitumen content (%)	Maximum nominal size (mm)
6.12	19 (Up-Limit)
6.3	12.5 (Med.-Limit)
6.5	9.5 (Dow.--Limit)

Table 4. The results of the Marshall test

Maximum nominal size (mm)	Bitumen content (%)	Marshall strength (N)
19 (Up-Limit)	5.7	6250
	6.1	6600
	6.5	6400
12.5 (Med.-Limit)	6.1	7300
	6.5	7550
	6.9	7430
9.5 (Dow.--Limit)	6.2	8200
	6.6	8730
	7.0	8600

The sand patch distribution test was conducted on the samples with different grading. The sand patch distribution test measures the coarse texture of the pavement surface (Mean Texture Depth) using the volumetric method according to the ASTM E465 Standard. To determine the skid value, the British Pendulum test was performed (ASTM E303-93, 2018). This test has been described in different standards; e.g. a comprehensive description of this test is provided by the UK Transport and Road Research Laboratory (TRRL) and ASTME-303 Standard. In this research, the ASTME-303 Standard has been used. In Figure 3, the British Pendulum available in the Asphalt and Bitumen Laboratory of the Yazd university is shown. In this research, the dust and dust as pollutants were collected from the surface of the Zahedan-Iranshahr Highway (Figure 3). According to the previous researches, the dust has a diameter of less than 100 μm; therefore, the collected dust was sieved using a sieve No. of 200 (75 mμm) (ASTM E303-93, 2018).

The British Pendulum test was performed on the samples in various desired humidity, pollutant, and temperature conditions, and the skid resistance value was obtained. For scattering dust on samples, first, they were weighted, and then dust was scattered on them in a specific amount, and then distributed on the samples with a knife and brush. For obtaining assurance, every experiment was repeated three times.

- To obtain the skid value in the dry condition, three gradings were used each of the SMA asphalt mixtures, and for each related grading, two samples were made. Therefore, in total, 12 samples were made for dry condition.
- The skid value for each case in dry condition was measured at three temperatures including 10, 35, and 60 °C and three different dust values on the surface of the sample were measured. Temperatures 10 °C, 35 °C, and 60 °C were the average winter temperature, average summer temperature, and maximum temperature, respectively.
- Then, the skid value was measured for all samples in the wet condition, at 10 °C, and three different values of the dust on the sample surface.

Fig. 2. The surface image of the 6 in samples made

Fig. 3. The images of the tests' process

According to the definition of ASTM Standard, a skid number is a resistive force created between the wheel and the surface of the pavement during the braking and the wheel lock situation, which prevents the wheel from slipping. Also, the skid number has been defined as follows (ASTM E465, 2017).

$$SN = 100\,\mu = 100\left(\frac{F}{N}\right) \qquad (1)$$

where μ: is friction coefficient, F: is friction force (the horizontal force applied on the wheel in the wheel-pavement contact location) and N: is the vertical force applied on the surface. For the samples used in this research, SN can be calculated using the following relation (Liu et al., 2019):

$$\begin{aligned} SN &= (1.38BPN \\ &- 31)e^{\left[-0.96V\times(25.5\,MTD)^{-0.52}\right]} \end{aligned} \qquad (2)$$

where SN, BPN, V, and MTD: are skid numbers, skid numbers calculated by the British Pendulum device, standard speed (40 mile/h $\approx$ 65 km/h), and the mean texture depth of the pavement (mm), respectively.

3. Results and Discussion

To investigate the effect of the grading type and Nominal Maximum Aggregate Size (NMAS) in the coarse texture, the sand distribution test was used the following results were obtained. The variations trend of the SMA coarse texture mixture in terms of NMAS are shown in Figure 4.

It is evident from Figure 4 that Mean Texture Depth (MTD) and the NMAS have a direct relationship. This means that by increasing the value of the NMAS, the value of MTD and as a result of the skid resistance would be increased. Among the SMA samples, the sample with a nominal size of 19 mm and the sample with a nominal size of 9.5 mm have the maximum and the minimum MTD, respectively. The grading with higher MTD uses more sand volume to fill the empty space of its surface. As a

result, with an increase in sand volume on the sample surface, the MTD would increase.

3.1. BPN Result by Changing the Dust Weight
To investigate the effect of the dust content and NMAS on the coarse texture, the British Pendulum test was performed at environment temperature, and the following results were obtained. The variation trend of the coarse texture of the SMA mixture in terms of NMAS and dust content is shown in Figure 5.

As indicated in Figure 5, by increasing the amount of dust content over the sample surface, the skid resistance is decreased. According to the results, when the maximum amount of dust is applied, the skid number is reduced in the range of 9 to 16% for the SMA samples, and 15 to 24% for the Hot Mix Asphalt (HMA). For the dusted surface samples with 19 mm NMAS, the highest and the lowest skid number were observed for the SMA samples, and the HMA samples, respectively, Given that dust, is very small particles with the size of less than 100 μm diameter, these particles could move into the air void spaces on the road surface, and because of their small size, they would fill the pores in the asphalt pavement, which would decrease the wheel-pavement surface contact and consequently, would reduce their skid resistance.

3.2. The Effect of Sample Surface Temperature on the Skid Resistance
The temperature variations of the pavement surface cause a change in the skid resistance of the surface (Liu et al., 2019). Since the asphalt mixtures applied on the pavement surface are viscoelastic material, the temperature affects their measured frictional specifications. The effect of the temperature on the skid resistance could be caused by the changes in the bitumen stiffness. In this research, to investigate the effect of temperature on the skid resistance, the British Pendulum test at 10, 35, and 60 °C were performed on the samples and the

results were recorded. A heater was used to achieve these surface temperatures. To observe the simultaneous effect of temperature and dust content on the skid resistance, 3D plots were used as indicated in Figure 6.
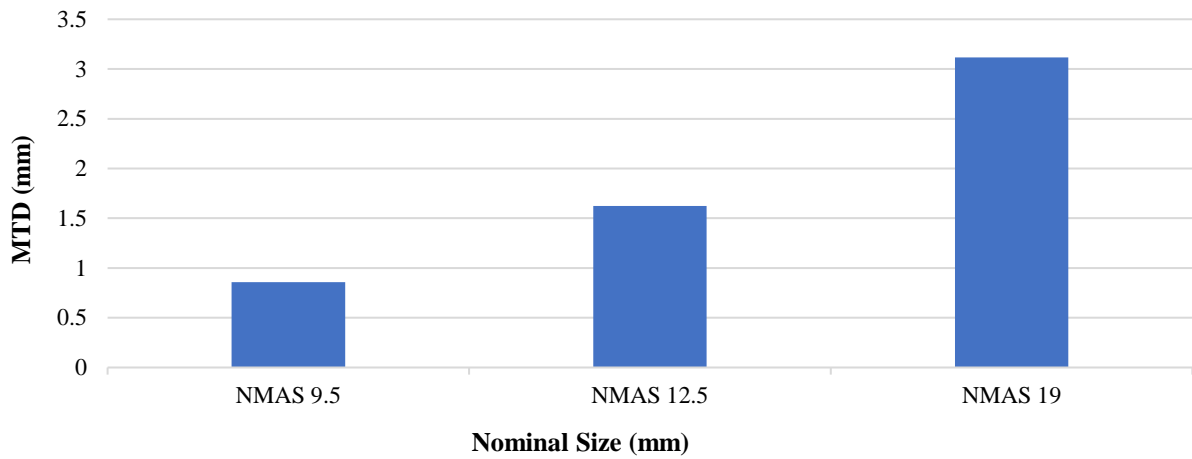
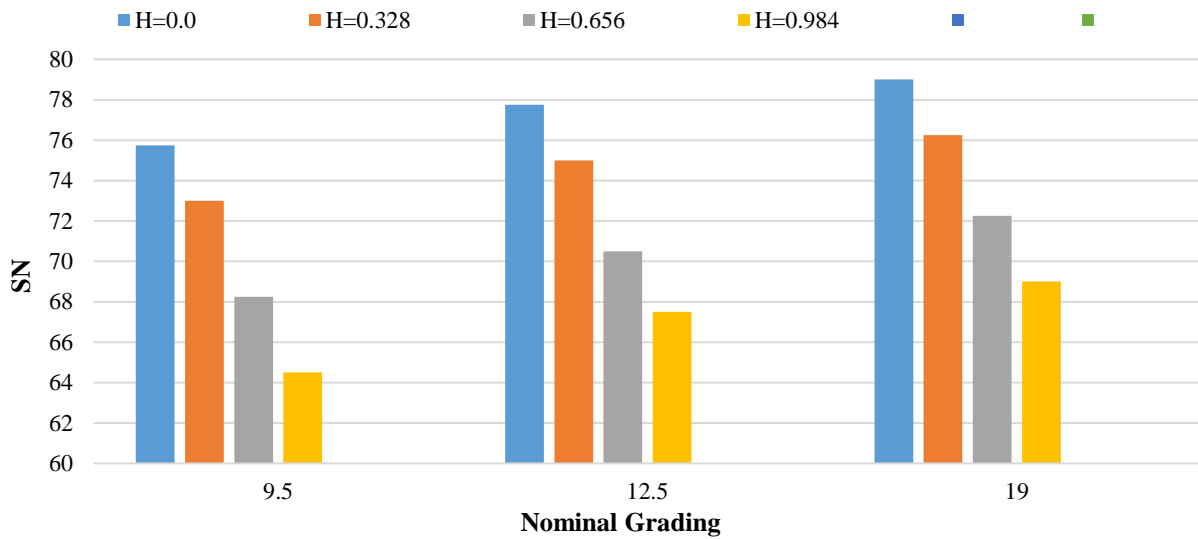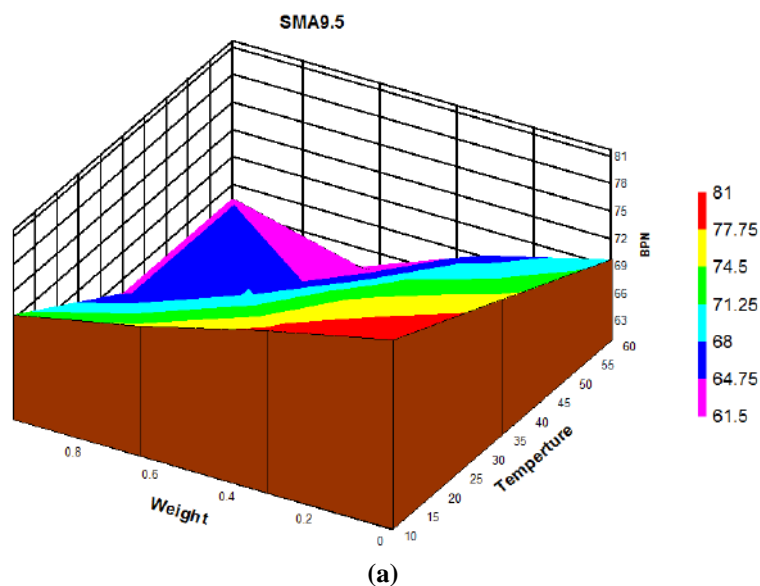**Fig. 4.** The variations trend of the SMA coarse texture mixture concerning the NMAS

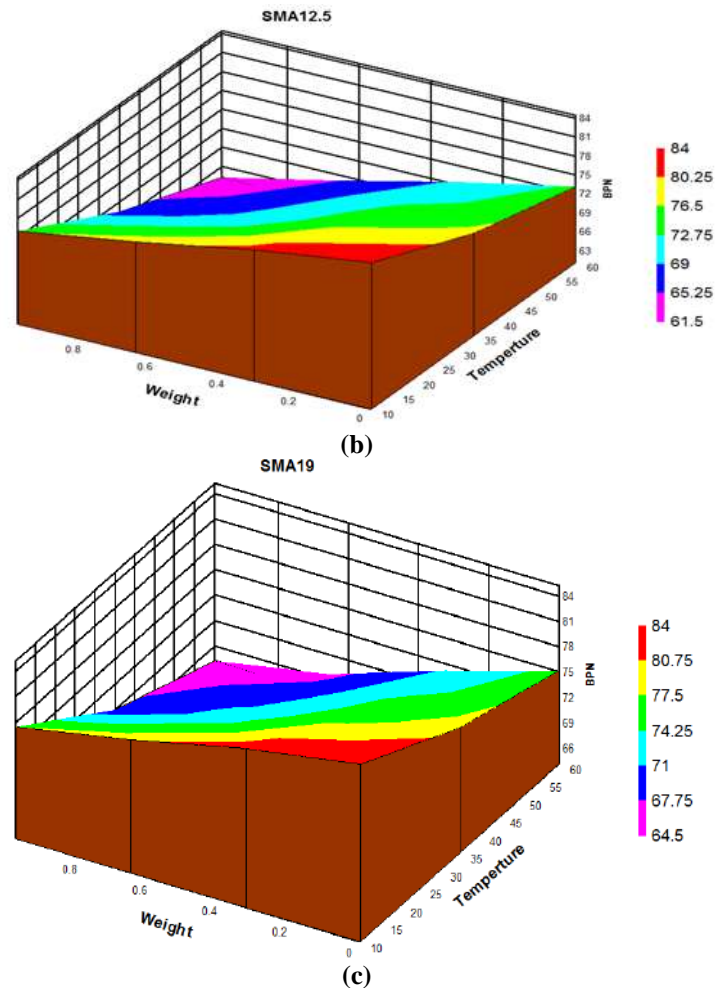**Fig. 5.** The effect of grading and dust content at normal ambient temperature on the sample surface

(a)

(b)

(c)

Fig. 6. 3D plots of the simultaneous effect of temperature and dust content on the skid resistance for SMA asphalt mixture with nominal sizes 9.5 mm to 19 mm

As can be seen from the 3D plots in Figure 6, the simultaneous increase in dust content and temperature would reduce the skid resistance significantly. By increasing the temperature from 10 °C to 60 °C and increasing the dust content from zero to 0.984 gr, the skid resistance of the HMA mixtures was decreased 36-40% and the skid resistance of the SMA mixtures was reduced 25-29%; the minimum decrease in skid resistance (25%) was for SMA with 19 mm NMAS.

As can be seen, the best skid resistance is achieved for SMA samples with 19 mm NMAS. At 10 °C and in the absence of dust, by increasing the nominal size of SMA samples from 9.5 mm to 19 mm, the skid resistance is increased up to 4%.

In the case of zero dust content, increasing the nominal size of SMA to 19 mm would increase the skid resistance by

15% at 10 °C, by 18% at temperature 35 °C and by 23% at temperature 60 °C, which is inconsistent with the results of Elkin et al. (1980). Moreover, by increasing the NMAS in SMA and HMA, the skid resistance would increase, which is inconsistent with the results of Fakhri and Tarikhbakhsh (2014). These results could be explained by the Fowler diagram of these samples, shown in Figure 3. As mentioned earlier, as the grading curve gets closer to the 0.45 power line, the grading density would increase. Given that the samples with higher NMAS are located at a further distance from the Fowler line, they would have lower density and a more open grading which could lead to an increase in their BPN value.

The results indicate that combined effects of the dust on the road surface and high ambient temperatures would lead to a higher reduction in the skid resistance. By

increasing the temperature from 10 °C to 60 °C (in the absence of dust on the sample surface), the skid resistance of the SMA samples decreased in the range of 12-15%, which is inconsistent with the results of Khasawneh and Liang (2012). When 0.984 gr of the dust was spread over the sample surface, an increase in the temperature from 10 °C to 60 °C, resulted in a 14-17% reduction in the skid resistance of the SMA samples The maximum reduction in skid number was observed for the HMA mixture with grading No. 6 in Iranian Road Pavement Design Code (i.e.19 mm NMAS). The latter could be attributed to the higher proportion of fine aggregates and the higher bitumen content of HMA samples in comparison with the SMA samples. Under the same temperatures, the maximum skid number was observed for the SMA mixture with a nominal size of 19 mm.

The SN values are calculated based on the relations defined in the previous section for the experimental samples. SN for other temperatures at different dust contents applied on the sample surface was calculated, and the results are presented in Figure 7. The results indicate that the simultaneous effect of the fine texture (indicated by the British Pendulum skid number) and coarse texture (MTD) at SN number has caused that SMA mixtures demonstrate considerably higher skid resistance at different ambient temperatures and different dust contents. The maximum SN number in all conditions is obtained for the SMA samples with a 19 mm NMAS due to their maximum BPN and MDT.
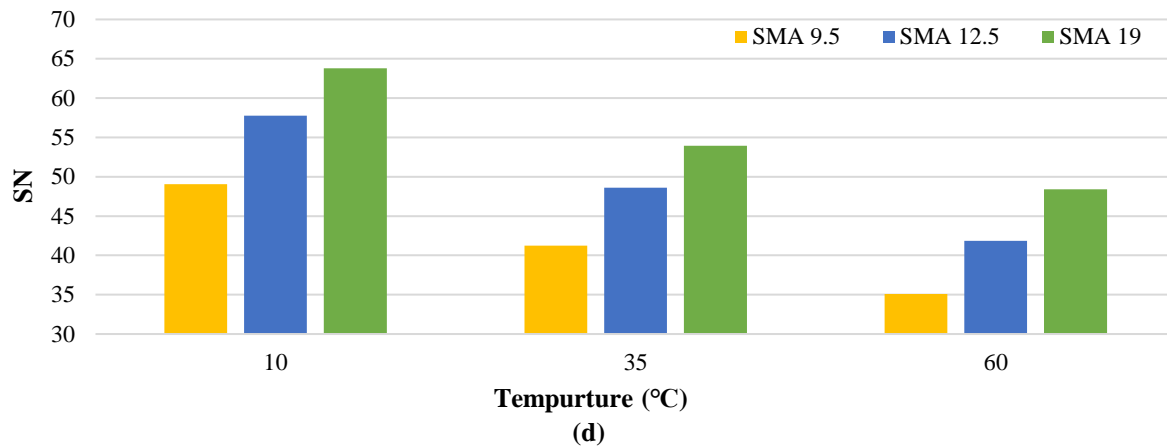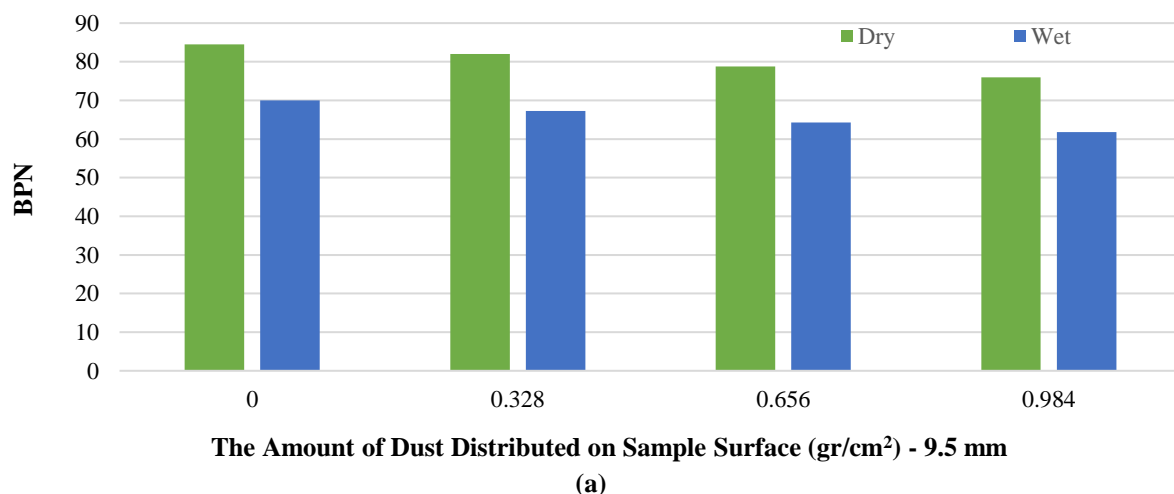

(a)

(b)

(c)

(d)
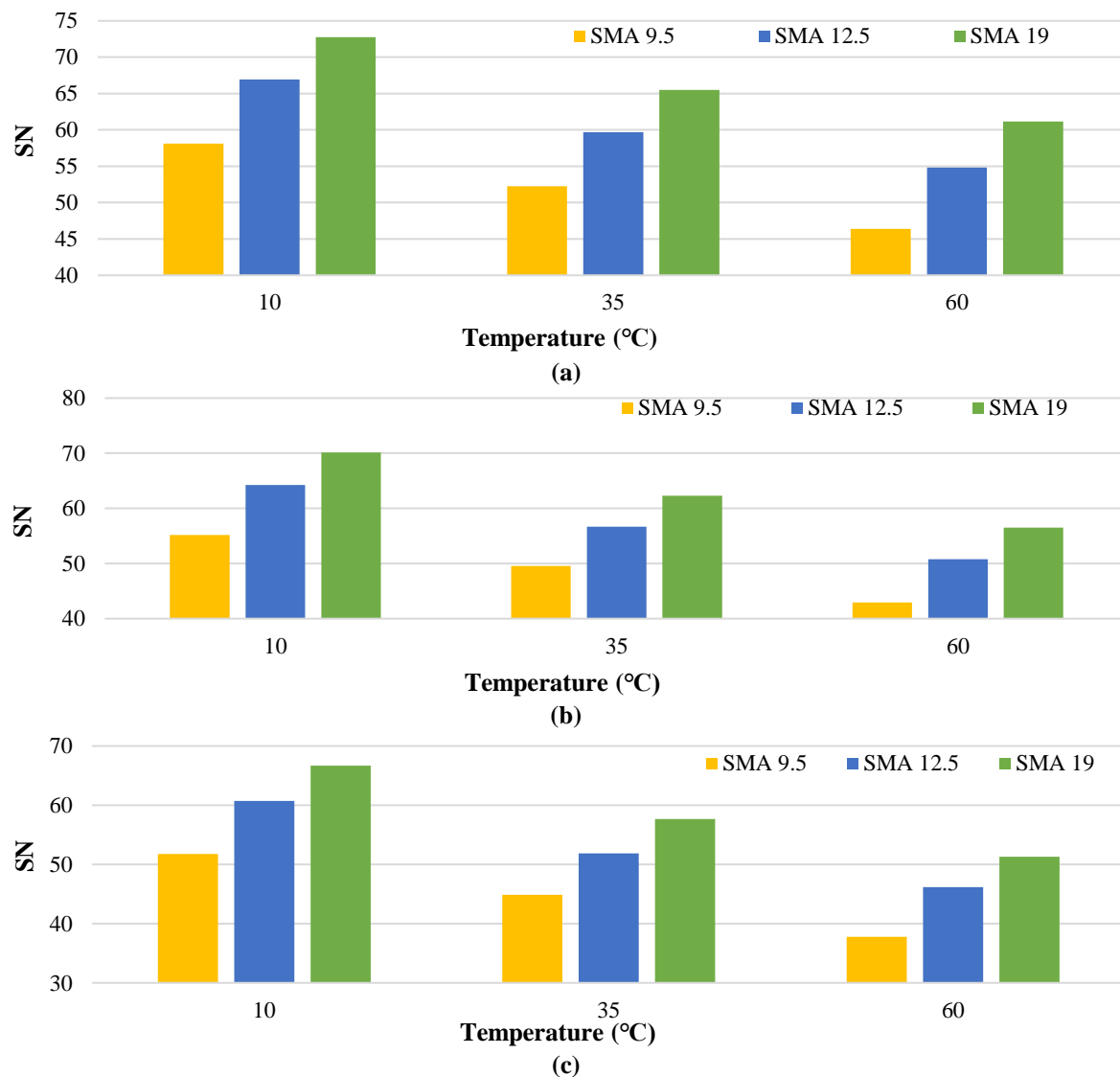
Fig. 7. SN numbers for samples with different values of dust spread over the sample surface with 6 in diameter:
a) 0 gr; b) 0.328 gr; c) 0.656 gr; and d) 0.984 gr

3.3. Results of the BPN Test on the Asphalt Samples in Wet Conditions

The skid resistance of the asphalt samples in the wet and dry conditions at 10 °C under different dust contents was compared with each other as indicated in Figure 8.

The results indicate that the humidity on the surface of the samples in the presence and absence of the dust would lead to a reduction in the skid number. In humid conditions, a thin layer of water is formed between the pavement surface and the rubber surface of the pendulum device and covers the fine texture, which causes a reduction in the surface contact and would significantly reduce the skid resistance. According to the results, the existence of the humidity causes the skid resistance to reduce in the range of 17 to 21% in the samples, which is inconsistent with the results of Henry (1983). It was observed that in the case of zero dust content, the skid resistance would reduce by 17 to 19%. However, in a case where 0.984 gr of the dust was spread over the sample surface, the effect of the humidity on the reduction of skid number was 19 to 21% more than the dry situation with the same dust content. In other words, the existence of 0.984 gr dust on the wet sample surface reduced the skid number in the range of 25-35% in comparison with the dry with zero dust content situations. This reduction in SMA samples was in the range of 25-28%, which is consistent with the results of Tyfore (2009). The main reason for this could be attributed to proper drainage in SMA mixtures, which originates from the wide grading of this mixture. In the same condition in terms of the presence or absence of the dust, the SMA asphalt mixture with 19 mm NMAS created the best skid resistance in wet conditions.
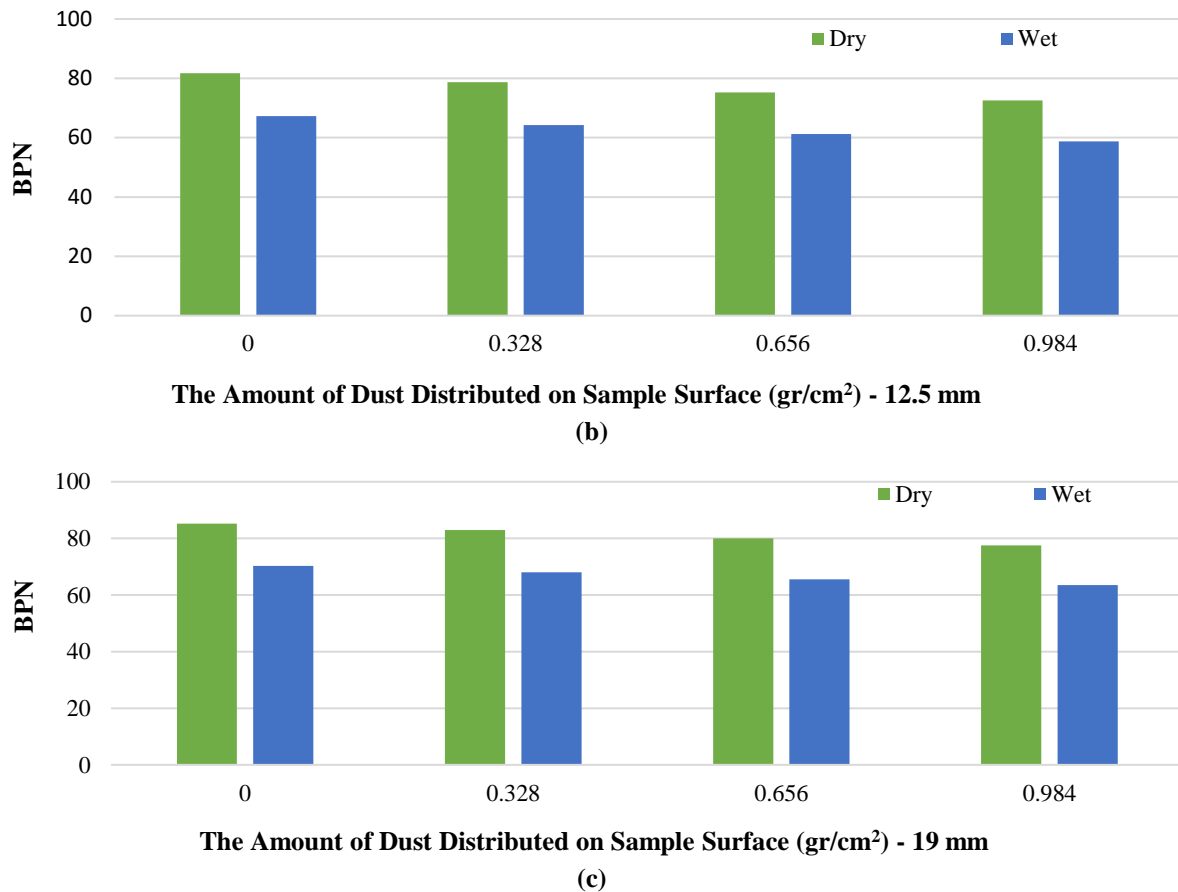

(a)

The Amount of Dust Distributed on Sample Surface (gr/cm²) - 12.5 mm

(b)

The Amount of Dust Distributed on Sample Surface (gr/cm²) - 19 mm

(c)

Fig. 8. The results of the BPN test for SMA asphalt mixture with a nominal size of 9.5 mm to 19 mm in the wet and dry conditions (temperature = 10 °C)

3.4. Analysis Using Taguchi Method

There are different methods to design a test. One of these methods which have been proposed in this field is the factorial method. The main disadvantage of this method is a large number of tests due to a large number of variables which could be time-consuming and costly in many situations. One of the modifications proposed to this method is to use the Taguchi method. This method makes it possible to reach the overall results by a fewer number of tests. Taguchi developed a family of fraction factorial schemes and utilized them in different applications. In this research, the results of the Taguchi method were obtained, and finally, the analysis of the results was performed between the Taguchi results and the factorial results. The related orthogonal arrays for test design with three factors and three levels are indicated in Table 5. Three different factors were considered in this study as follows:

Factor A: Grading type (at three levels: level 1: SMA with nominal size 9.5 mm, Level 2: SMA with nominal size 12.5 mm, and level 3: SMA with nominal size 19 mm).

Factor B: Temperature (at three levels: level 1: 10 °C, level 2: 35 °C, and level 3: 60 °C)

Factor C: Dust content (at three levels: level 1: 0.328 gr of dust content spread over the sample surface, level 2: 0.656 gr of dust content spread over the sample surface; and level 3: 0.984 gr of dust content spread over the sample surface).

The results obtained using the Taguchi method were analyzed using Minitab software and the output results are indicated in Figure 9 from the Minitab software. As it is seen in this figure, by increasing the maximum nominal size of aggregates, the friction also increases which is under the results of other researches (Khasawneh and Alsheyab, 2020).

Table 5. Orthogonal array L9(3^3), and BPN results for defined test conditions

Test condition	Three factors			BPN test results
	A	B	C	
1	1	1	1	78.75
2	1	2	2	68.25
3	1	3	3	58.25
4	2	1	2	78.25
5	2	2	3	67.5
6	2	3	1	65.5
7	3	1	3	77.5
8	3	2	1	76.25
9	3	3	2	66.75
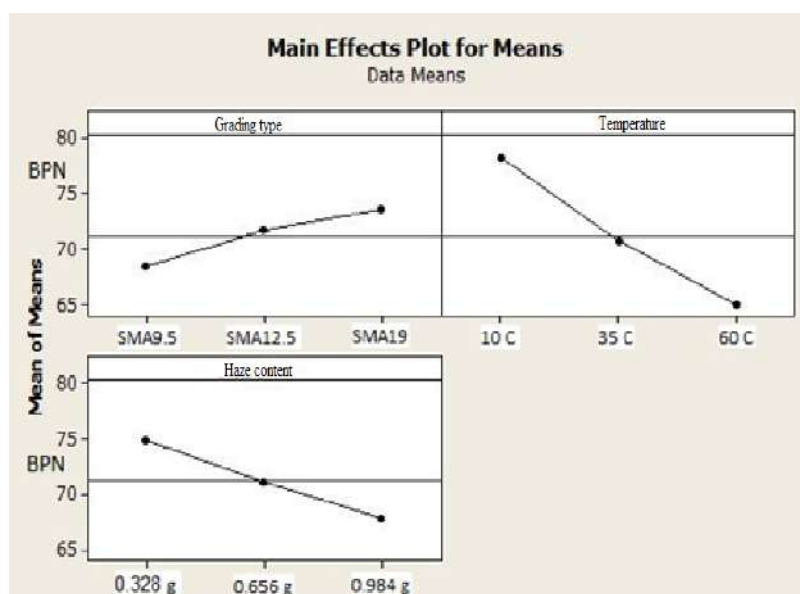
Fig. 9. The output plots of the Minitab software for SMA results

4. Conclusions

In this research, the effect of various dust contents observed in the real world on the skid resistance of the SMA asphalt mixture at different grading and ambient temperatures has been addressed. The results were analyzed using Taguchi and factorial methods and were compared. The following conclusions can be drawn from the tests performed on the samples produced for this purpose:

- When the maximum dust content (0.984 gr) was spread over the pavement surface, the skid number was reduced in the range of 9-16% for SMA samples with different grading. The SMA samples with 19 mm NMAS demonstrated the best skid resistance, irrespective of the dust content value.
- In the presence of different dust contents

on the sample surface, the skid number was reduced by an increase in the sample surface temperature from 10 °C to 60 °C, i.e. the skid resistance of the SMA samples reduced in the range of 12-17%.

- The simultaneous increase in the dust content and surface temperature would decrease the skid resistance significantly. By increasing the temperature from 10 °C to 60 °C and increasing the dust content from zero to 0.984 gr, the skid resistance of the SMA mixtures was decreased in the range of 25-29%.
- The maximum SN values on all cases related to SMA mixtures with 19 mm NMAS could be attributed to the combined effect of the fine texture and MTD on the SN values resulted in to observe.
- The surface humidity of the samples in

the presence and the absence of the dust would reduce the skid resistance. The surface humidity alone caused 17 to 19% reduction in the skid number of the samples. However, when 0.984 gr of dust were spread on the surface of the sample, the effect of the humidity on the reduction of skid number was 19-21% more than the dry surface with the same dust content.

- The presence of 0.984 gr of dust spread over the wet sample surface resulted in a 25 to 28% reduction in the skid resistance compared to clear and dry sample surfaces.

- The SMA asphalt samples with 19 mm NMAS created the highest skid resistance in comparison with the samples produced with another grading, irrespective of having dust on their surface or not.

- By performing fewer tests (9 BPN test) for the SMA samples, via using the Taguchi method, the same results as the factorial method were obtained.

5. Acknowledgment

6. References

AbdullahI, S. (2016). *Investigation of quantitative changes in precipitation dust in Zahedan city,* M.Sc. Thesis, Department of Natural Resources. Yazd University.

ASTM E303-93, (2018). *Standard test method for measuring surface frictional properties using British Pendulum tester*, West Conshohocken, PA, USA.

ASTM E465, (2017). *Standard test method for measuring mean profile depth using sand patch method*, West Conshohocken, PA, USA.

Blake, D.M., Wilson, T.M., Cole, J.W., Deligne, N.I. and Lindsay, J.M. (2017). "Impact of volcanic ash on road and airfield surface skid resistance", *Sustainability*, 9(8), 1389.

Cao, P., Yan, X., Bai, X. and Yuan, C. (2010). "Effects of contaminants on skid resistance of asphalt pavements", In *Traffic and Transportation Studies 2010*, 1341-1351.

Chan, C.Y., Huang, B., Yan, X. and Richards, S. (2010). "Investigating effects of asphalt pavement conditions on traffic accidents in Tennessee based on the pavement management system (PMS)", *Journal of Advanced Transportation*, 44(3), 150-161.

Dan, H.-C., He, L.-H. and Xu, B. (2017). "Experimental investigation on skid resistance of asphalt pavement under various slippery conditions", *International Journal of Pavement Engineering*, 18(6), 485-499.

Do, M.-T., Cerezo, V. and Zahouani, H. (2014). "Laboratory test to evaluate the effect of contaminants on road skid resistance", *Proceedings of the Institution of Mechanical Engineers, Part J: Journal of Engineering Tribology*, 228(11), 1276-1284.

Elkin, B.L., Kercher, K.J. and Gulen, S. (1980). "Seasonal variation in skid resistance of bituminous surfaces in Indiana", *Transportation Research Record*, 777, 50-58.

Fakhri, M. and Taribakhsh, M. (2014). "Studying the effect of gradation and macro texture generating by the method of gravel distribution, on the skid resistance of the concrete pavements", *Journal of Civil and Environmental Engineering*, 43(73), 69-78.

Henry, J.J. (1983). "Comparison of the friction performance of a passenger car tire and the ASTM Standard test tires", In *Frictional Interaction of Tire and Pavement*, ASTM International.

Irfan, M., Ali, Y., Ahmed, S., Iqbal, S. and Wang, H. (2019). "Rutting and fatigue properties of cellulose fiber-added stone mastic asphalt concrete mixtures", *Advances in Materials Science and Engineering*, Hindawi, Article ID 5604197, 8 p.

Jalal-Kamali, M.-H., Hasani, A. and Sodagari, J. (2019). "Introduction and application of rotational abrasion device to determine concrete pavement abrasion", *Civil Engineering Infrastructures Journal*, 52(2), 295-308.

Jalalkamali, R., Dibaee, M.M., Jalal Kamali, M.H. and Hassani, A. (2021). "An investigation of the relationship among skid resistance, mean texture depth and abrasion resistance for different macrotextures of concrete pavements", *Civil Engineering Infrastructures Journal*, 54(2), 301-317.

Kamel, N. and Gartshore, T. (1982). "Ontario's wet pavement accident reduction program", In *Pavement Surface Characteristics and Materials*, ASTM International.

Khasawneh, M.A. and Alsheyab, M.A. (2020). "Effect of nominal maximum aggregate size and aggregate gradation on the surface frictional properties of hot mix asphalt mixtures", *Construction and Building Materials*, 244,

118355.

Khasawneh, M.A. and Liang, R.Y. (2012). "Temperature effect on frictional properties of HMA at different polishing stages", *Jordan Journal of Civil Engineering*, 6(1), 39-53.

Kogbara, R.B., Masad, E.A., Kassem, E., Scarpas, A.T. and Anupam, K. (2016). "A state-of-the-art review of parameters influencing measurement and modeling of skid resistance of asphalt pavements", *Construction and Building Materials*, 114, 602-617.

Liu, Q., Hossain, S.M.K., Tighe, S.L. and Shalaby, A. (2019). "Field assessment of three-dimensional surface texture and frictional properties of experimental Canadian road pavements", In *Pavement and Asset Management,* 73-80, CRC Press.

National Cooperative Highway Research Program (NCHRP). (1999). *Designing stone matrix asphalt mixtures for rut-resistant pavements,* Report 425, Project D9-8 FY'94, Auburn, AL, United States, 88 p.

Raufi, H., Topal, A., Sengoz, B. and Kaya, D. (2020). "Assessment of asphalt binders and Hot Mix asphalt modified with nanomaterials", *Periodica Polytechnica Civil Engineering*, 64(1), 1-13.

Sharafati, A. and Mishmast Nahi, A. (2017). "Analysis of the effect of 120-day storms on the increase of road accidents, Case study: Roads to Zabol city", *Rahvar Scientific Promotional Quarterly*, 14(38), 137-148.

Terrones-Saeta, J.M., Suárez-Macías, J., Iglesias-Godino, F.J. and Corpas-Iglesias, F.A. (2020). "Evaluation of the use of electric arc furnace slag and ladle furnace slag in stone mastic asphalt mixes with discarded cellulose fibers from the papermaking industry", *Metals*, 10(11), 1548.

Tyfour, W.R. (2009). "Tire skid resistance on contaminated wet pavements", *JJMIE*, 3(2).

van Bijsterveld, W. and del Val, M.A. (2016). "Towards quantification of seasonal variations in skid resistance measurements", *Road Materials and Pavement Design*, 17(2), 477-486.

Wallman, C.-G. and Åström, H. (2001). "Friction measurement methods and the correlation between road friction and traffic safety: A literature review", Swedish National Road and Transport Research Institute (VTI) Report, 47 p.

Wang, D., Xie, X., Oeser, M. and Steinauer, B. (2015). "Influence of the gritting material applied during the winter services on the asphalt surface performance", *Cold Regions Science and Technology*, 112, 39-44.

Xiao, J., Kulakowski, B.T. and EI-Gindy, M. (2000). "Prediction of risk of wet-pavement accidents: Fuzzy logic model", *Transportation Research Record*, 1717(1), 28-36.

Zealand, T.N. (2002). "Specification for skid resistance investigation and treatment selection", NZTA T10 Specification, NZ Transport Agency, New Zealand, 21 p.

Zhang, L., Ong, G.P. and Fwa, T.F. (2015). "Numerical study on the influence of aggregate size on skid resistance performance of porous pavements", *Asian Transport Studies*, 3(3), 284-297.

On Compressive Stress-Strain Behavior of Standard Half-Scale Concrete Masonry Prisms

Kahrizi, E.[1] [ID], **Aghayari, R.[2]*** [ID], **Bahrami, M.[3]** [ID] **and Toopchi-Nezhad, H.[2]** [ID]

[1] M.Sc., Department of Civil Engineering, Razi University, Kermanshah, Iran.
[2] Associate Professor, Department of Civil Engineering, Razi University, Kermanshah, Iran.
[3] Ph.D. Candidate, Department of Civil Engineering, Razi University, Kermanshah, Iran.

© University of Tehran 2022

ABSTRACT: Masonry buildings are the most utilized structural system worldwide due to the ease of construction and cost-effectiveness. The effective design of masonry structures has been always an important research subject. Experimental studies are the main component of such research studies. The budget and equipment limitations may challenge the laboratory testing of full-scale masonry specimens and test structures. As such, the use of model-scale specimens may be found as a promising alternative to study the response behavior of this type of structure. In this paper, the stress-strain behavior of half-scale concrete masonry units and prisms (hollow and fully grouted) under compressive loads is evaluated and compared with their full-scale counterparts. The half-scale specimens are standard in that the principles of similitude law have been followed precisely in their aggregate grading, mix-design, physical dimensions, and loading. The stress-strain diagram and failure modes of the half-scale are similar to those of the full-scale. The ratio of half-scale to the full-scale compressive strength of the hollow and grouted masonry prisms on average was found to be 1.07, and 1.08, respectively. The experimentally-evaluated response of the standard half-scale specimens that fully satisfy the requirements of similitude law may be extended with good accuracy to the full-scale masonry.

1. Introduction

Masonry structures comprise a large portion of building inventory worldwide. Masonry buildings incorporate load-bearing walls that perform a variety of other functions in addition to supporting the loads. The load-bearing walls in a masonry building subdivide spaces, provide thermal and acoustic insulation, and provide fire and weather protection. These functions in a framed building have to be accounted for separately (Rai, 2002). Other advantages such as the possibility of using local labor and materials, ease of construction, longevity, being architecturally pleasant, and cost-effectiveness have made this type of structure a suitable choice for many

* Corresponding author E-mail: reza_agh@razi.ac.ir

projects.

Masonry buildings may be constructed with stones, bricks, and concrete blocks. Stones have been frequently employed in the construction of historic buildings. Many old buildings were built with unreinforced brick- or block-masonry. Being unreinforced, the masonry assemblages in such buildings are very susceptible to brittle failure during seismic events.

The engineering design of masonry buildings dates back to the 1950s, where, intensive theoretical and experimental research studies were conducted on various aspects of masonry subassemblies (Rai, 2002). The contemporary masonry structures incorporate steel reinforcement to improve the flexural and shear behavior of the walls under earthquake loads. The design is conducted based on the factors affecting the strength, stability, and hysteretic load-displacement performance of masonry structures. Current masonry code provisions may be divided into two broad categories, namely, empirical design methods, and strength design methods (ACI 530, 2013; CSA Standard A165, 2002; Eurocode 6-1996-1-1, 1996-3, 2006).

The empirical design includes a set of construction criteria that is applied to the buildings of specific constraints. For instance, to achieve an intermediate level of ductility in the unreinforced masonry buildings, the load-bearing masonry walls may be confined with a set of horizontal and vertical reinforced-concrete tie-elements based on empirical guidelines (Standard No. 2800, 2013). The tie-elements which are mainly constructed at the intersection of perpendicular walls and the roof levels, also improve the monolithic performance of the whole building. The design of this structural system is empirical with no engineering calculations to evaluate the demand and capacity of the walls. As such, the mechanical properties of the masonry units and mortar are not directly taken into account during the design process and detailing of the structure. The number of above-ground stories in this system is limited to two stories only (Standard No. 2800, 2013). The tied-masonry buildings performed satisfactorily in the past moderate earthquakes of Iran (Eshghi et al., 2009).

The strength design methods in modern design codes such as ACI 530, CSA A371, and Eurocode 6 are based on the ultimate- or limit-state-design methodologies. The design steps include the loading of structure, structural analysis, and design. The analysis is carried on the structural model of the building which can be created in many commercial software packages. The analysis outputs represent the demands on different structural elements of the masonry building. The load-capacity of the walls including, axial, in-plane and out-of-plane flexural, and shear strength values are determined based on the code-specified expressions, and the nominal mechanical properties of masonry units and prisms. The design objective is to match the capacities with the demands.

As with the other structural systems, the design code regulations for masonry buildings are being developed continuously. This is evidenced by the changes taking place in the masonry codes internationally (Rai, 2002). A significant number of studies on the compressive behavior of hollow, partially-grouted, and fully-grouted concrete masonry assemblages can be found in the literature. These studies investigated the influence of different parameters including block compressive strength, type of mortar and grout, the number of vertical and horizontal mortar joints within the specimen, mix design, and water to cement ratio on the compressive strength and failure modes of full-scale masonry assemblages (Zahra et al., 2021; Hassanli et al., 2015; Mohammad et al., 2010; Andria, 2017; Huang et al., 2017; Oliveira et al., 2014; Gustavo 2019).

Experimental studies are a major prerequisite to code developments. However, the cost of testing on full-scale masonry specimens and systems is prohibitive (Hamid et al., 1985). Working

on model-scale specimens and structures is a rational way of cutting the costs of experimental studies. Hamid et al. (1985) studied the effects of mortar and grout strength, height-to-thickness ratio, number of courses, and bond type on the ¼ scale prism compressive strength. According to the authors, excellent correlations were obtained for the mode of failure and moduli of elasticity of ¼ scale and full-scale prisms. Another study on the ¼ scale concrete masonry prisms showed the relatively higher compressive strength of the full-scale prisms (Camacho et al., 2000). Long et al. (2005) studied the compressive strength and diagonal tension of ½ scale masonry prisms. They concluded that the half-scale masonry could be deemed as a good model of full-scale masonry, particularly for grouted specimens. Another study on ½ scale masonry prisms showed a comparable modulus of elasticity and strain at peak strength to their full-scale counterparts, and some discrepancies in the compressive strength and post-peak behavior (AbdelRahman et al., 2020). Sathiparan et al. (2016) studied the effects of scale on the mechanical properties of concrete blocks and prisms and concluded that while the compressive strength of masonry did not significantly influence by the scale, all of the other tested properties, including water absorption rate, porosity, shear strength, and flexural bond strength significantly influenced by the scale.

Given the disparate results found in the literature on the effects of the scale of the behavior of concrete masonry, this field deserves further investigation. The main objective of this study is to construct standard ½ scale concrete masonry prisms to be the most representative of their full-scale counterparts under compressive loads. This is however conditional on following the principles of true similitude law in the construction of the model-scale masonry units and specimens. The similitude law that is employed in this study is known as the "practical true model" (Harris et al., 1999). This is an appropriate modeling

technique that is used to study the elastic and inelastic behavior and failure modes of masonry structures to static loads under the assumption that there are no significant time-dependent effects that influence the structural behavior. In this similitude model, the material properties are the same in both model and the prototype (i.e., the full-scale model) structure. For complete similarity of the structural behavior, a dimensional analysis will give the scale factors shown in Table 1. The length scale factor, S_l, in a half-scale model is $\frac{1}{2}$. If it is assumed that the stresses caused by the self-weight of the structure are not significant, as is the case for most masonry buildings, the scale factors cited in Table 1 are adequate for modeling masonry structures (Harris et al., 1999).

Table 1. Scale factors in the practical true model (Harris et al., 1999)

Quantity	Dimension	Scale factor
Linear dimension	L	S_l
Area	L^2	S_l^2
Concentrated load	F	S_l^2
Pressure	FL^{-2}	1
Displacements	L	S_l
Stress	FL^{-2}	1
Strain	1	1
Specific weight	FL^{-3}	$1/S_l$

In this study, the principles of similitude law have been followed precisely in the grading of aggregate, mix-design, physical dimensions of the blocks, and loading of the half-scale masonry blocks and prisms and their corresponding full-scale counterparts.

2. Experimental Program

The main purpose of this research is to investigate the relationship between mechanical properties, and the load-deformation behavior of half-scale and full-scale masonry prisms; material and laboratory conditions in both scales are identical and made under ASTM standards.

Therefore, in the first step, the physical and mechanical properties of half-scale and full-scale masonry blocks were evaluated and compared. In the second phase of the study, the hollow and grouted masonry

prisms were constructed in half-scale and full-scale, and then their mechanical properties, as well as their stress-strain diagrams, were evaluated and compared.

2.1. Test Specimens
2.1.1. Dimensions of Concrete Blocks

Figure 1 shows the typical hollow concrete blocks fabricated for this study. As seen, the masonry blocks are Full-Scale (FS) and Half-Scale (HS) splitter units with the physical dimensions outlined in Table 2. The physical dimensions including the thicknesses of face-sell and web of the FS-units satisfy the minimum requirements prescribed by the ASTM C90.

As seen in Table 2, the HS-blocks represent a true half-scale replica of their full-scale counterparts.

2.2. Mix Design for Full-Scale Concrete Blocks

Proportioning the mix components for a Concrete Masonry Unit (CMU) is an important step in producing high-quality units. A well-proportioned mix will result in improved mechanical properties (such as compressive strength, weight, and absorption rate of the masonry unit). As a preliminary step, a well-graded aggregate must be selected for the concrete mix. In this study, the aggregates of the concrete mix were graded based on ASTM C136M, guidelines using sieve analysis. Figure 2 shows the distribution of particles in the granular material (i.e., results of the sieve analysis). The upper and lower bounds prescribed by the ASTM C136 are also shown in the figure.
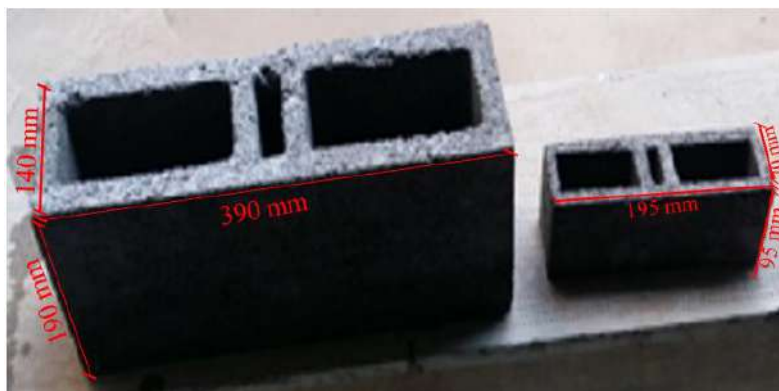
Fig. 1. Typical concrete masonry unit (full-scale and half-scale)
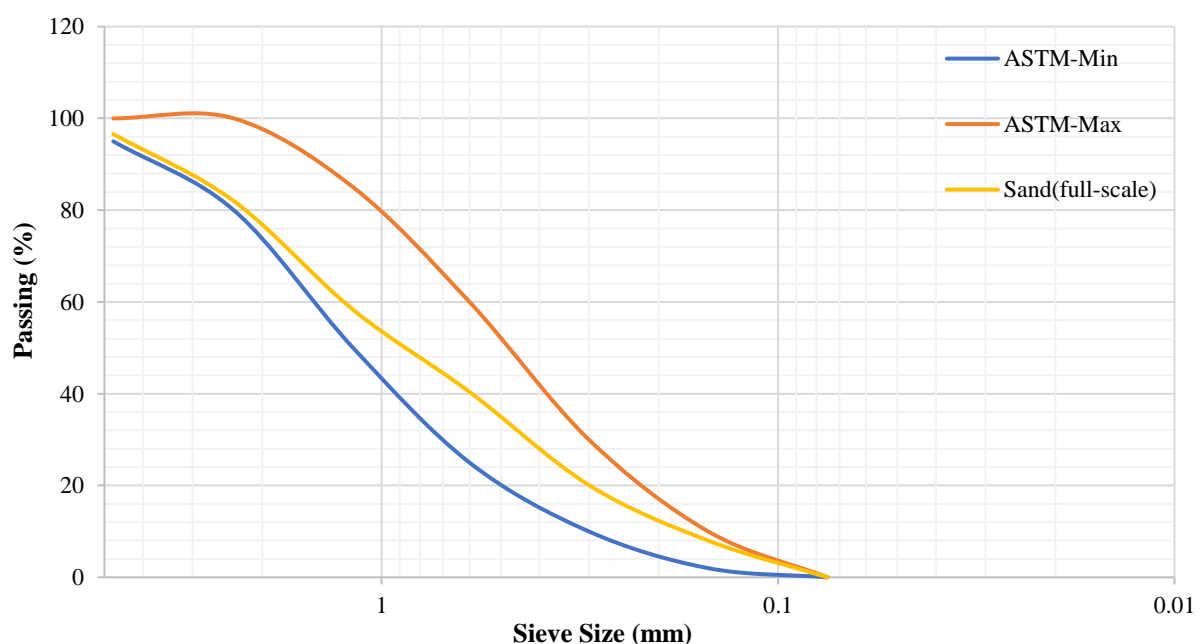
Fig. 2. Grading of aggregates for the full-scale blocks

Table 2. Physical dimensions of concrete masonry units

Scale	Length (mm)	Heigth (mm)	Width (mm)	Face shell thickness (mm)	Web thickness (mm)	Solid (%)
Half	195	95	70	14	11	53.48%
Full	390	190	140	28	22	53.48%

The concrete mix of the masonry units contains both fine-grained and coarse-grained materials (25% gravel and 75% sand). The gravel material of the concrete mix passed Sieve #3/8 and remained on Sieve #4 as prescribed by the ASTM C136. In additional Cement is one of the most extensively used construction material for buildings and infrastructures in Iran (Hosseinijou et al., 2021), in concrete mix of blocks were used cement type II.

The fineness modulus (FM) method is one of the most commonly used techniques to design the concrete mix for masonry units (Jablonsky, 1996). To obtain an optimal-mix design, the concrete blocks of different water, cement, and aggregate weight ratios were fabricated and tested for compressive strength. The compressive strength is determined by dividing the ultimate compressive force by the net area of the concrete block. The net area is calculated by dividing the net volume of the masonry unit by its total height. The net volume is evaluated based on the procedure outlined in the ASTM C140-13. To eliminate any inconsistency in the test results, the top and bottom surfaces of the masonry blocks were capped with a thin layer of high-strength gypsum with an approximately 2 to 3 mm thickness.

A total of eight different mix designs were investigated in this study (see Table 3). According to the ASTM C90, the lower admissible grade for the structural concrete blocks is 13.1 MPa. Accordingly, the mix designs 5 to 8 that comply with this requirement may be deemed acceptable (see Table 3). Given the larger strength of the mix-design 7, it was selected for the fabrication of the concrete blocks of this study.

According to the numbers in the last column of Table 3, Mix design 7 is acceptable and optimal.

2.3. Mix Design for Half-Scale Concrete Blocks

The Half-Scale (HS) blocks are designed and fabricated based on a true replica model in which the material properties of the model remain the same as those of the full-scale model. However, the physical dimensions of the model scale block, as well as its granular aggregates, are scaled by a factor of ½.

To achieve a well-graded half-scale aggregate consistent with the full-scale granular materials, the sieve size of the upper and lower bounds of the ASTM C136 shown in Figure 2 were multiplied by the scale factor of ½.

Thus, the maximum size of the half-scale aggregates was selected to be 2.38 mm that was half of the maximum size of 4.75 mm in the full-scale aggregates. Figure 3 shows the distribution of particles in the granular material (results of sieve analysis) and the upper and lower bounds prescribed by ASTM C136 that were multiplied by the scale factor of ½.

Table 3. Mix design of the concrete blocks

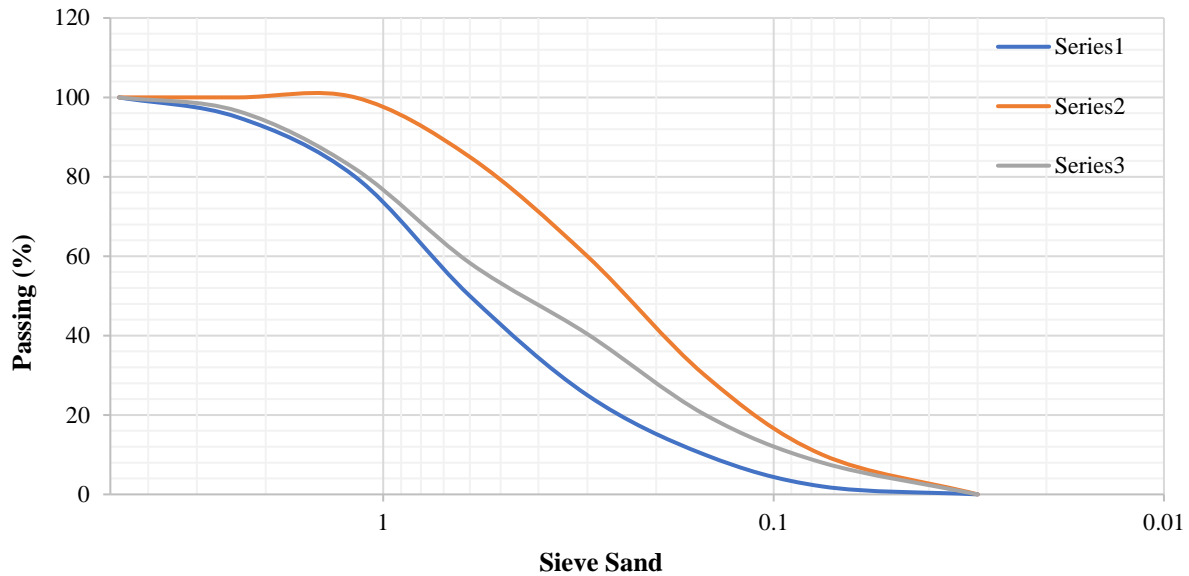| Mix designs	The weight ratio of cement to aggregate	The weight ratio of water to the mixture of cement and aggregate	Water to cement ratio	Average compressive strength of 3 block at 28 says (MPa)
1	1:9	7.5%	0.75	9.4
2	1:8	7%	0.63	9.5
3	1:7	7%	0.56	12.3
4	1:6	7.5%	0.54	10.36
5	1:6	7%	0.49	13.3
6	1:5	8.3%	0.5	17.2
7	1:5	8.1%	0.49	18.1
8	1:4	8.8%	0.44	14.1

Fig. 3. Grading of aggregates for the half-scale blocks

The half-scale aggregates were employed in a mix-design consistent with the mix-design 7 given in Table 3. Three HS-blocks were fabricated and tested in conformance with ASTM C90. The average compressive strength of the said HS-blocks was measured to be 17.9 MPa which was in excellent agreement with the compressive strength of 18.1 MPa obtained for the FS-blocks.

3. Material Properties of the Concrete Blocks

The density, water absorption, and linear shrinkage are the critical material properties that are used, in addition to the compressive strength, to classify the concrete masonry units. Table 4 includes the average values of the said material properties for the full-scale and half-scale concrete blocks. The concrete block density is evaluated based on ASTM C90. The masonry blocks are classified as heavy-, normal-, and light-weight depending on the density of the concrete material. Given the average density evaluated for the masonry blocks of this study, both the FS- and HS-concrete blocks may be classified as normal-weight. The level of water absorption of concrete is evaluated experimentally in conformance with ASTM C140. As seen in Table 4, the absorption values evaluated for the FS- and

HS-blocks satisfied the maximum permissible value outlined by the relevant ASTM standard. The linear shrinkage of the concrete material was evaluated with the aid of ASTM C426.

The mechanical properties of the concrete blocks were determined according to ASTM C90 guidelines. Using Archimedes' law, the volume of the full-scale and half-scale blocks was evaluated to be 0.005538 and 0.000692 m^3, respectively. As such, the effective cross-sectional area of the full-scale and half-scale blocks (determined by dividing the volume by the total height of the block) was evaluated to be 29147.4 and 7284 mm^2, respectively. The ratio of the half-scale to full-scale cross-section areas read 0.25, which is consistent with the square of the scale factor, i.e., $(\frac{1}{2})^2 = 0.25$.

The last column of the table shows the ratio of half-scale to full-scale of the mechanical properties evaluated for the masonry blocks of this study. As seen, an excellent correlation exists between the two. The largest difference is related to the absorption of the blocks. The level of absorption is proportional to the perimeter surface of the block. The perimeter surfaces of the full-scale and half-scale blocks were measured to be 411920 and 102980 mm^2, respectively. The ratio of half-scale to full-scale perimeter two areas is 0.25.

Table 4. Material properties of concrete masonry units (full-scale and half-scale)

Property	Half-scale (Average)	Full-scale (Average)	ASTM-req	(Half-scale/ Full-scale)
Density (kg/m^3)	2020.23	2133.38	Normal weight[1]	0.95
Absorption (kg/m^3)	143.86	168.8	208 kg/m^3	0.85
Compressive strength (MPa)	17.47	17.6	≥ 13.1	1.01
Linear shrinkage	0.19%	0.18%	$\leq 0.065\%$ [4]	1.05

1: According to ASTM C90, as the density of half-scale and full-scale blocks was greater than 2000 kg/m^3, both blocks were classified as normal weight blocks.

2: ASTM C140, the Maximum Absorption averaged three normal weight blocks is 208 kg/m^3

3: ASTM C90, Minimum compressive strength averaged three normal weight blocks is 13.1 MPa

4: ASTM C90 limits its potential drying shrinkage to 0.065%.

4. Mortar and Grout

4.1. Full-Scale Masonry

The sand grading for the preparation of mortar (type S) and grout is based on the ASTM C144 and ASTM C404 requirements, respectively. Figure 4 shows the results of sand grading, as well as the permissible bound recommended by the ASTM standard. As seen, overall, the sand grading satisfies the standard requirements.

According to the ASTM C270 the relative volume of cement, crushed lime, and sand in S mortar are recommended to be 1.5, 0.5, and 4.5, respectively. Besides, the compressive strength of standard samples of $100 \times 100 \times 100$ mm is 12.4 MPa. Table 5 includes the strength values obtained for six mortar specimens. The average strength value is approximately 24 MPa.

Grout for use in concrete masonry construction should comply with ASTM C476. According to this standard relative volume of cement and sand is recommended to be 1 and 3, respectively. Also, the minimum grout compressive strength is 13.79 MPa. The average strength value obtained for six grout specimens is approximately 22.68 MPa.
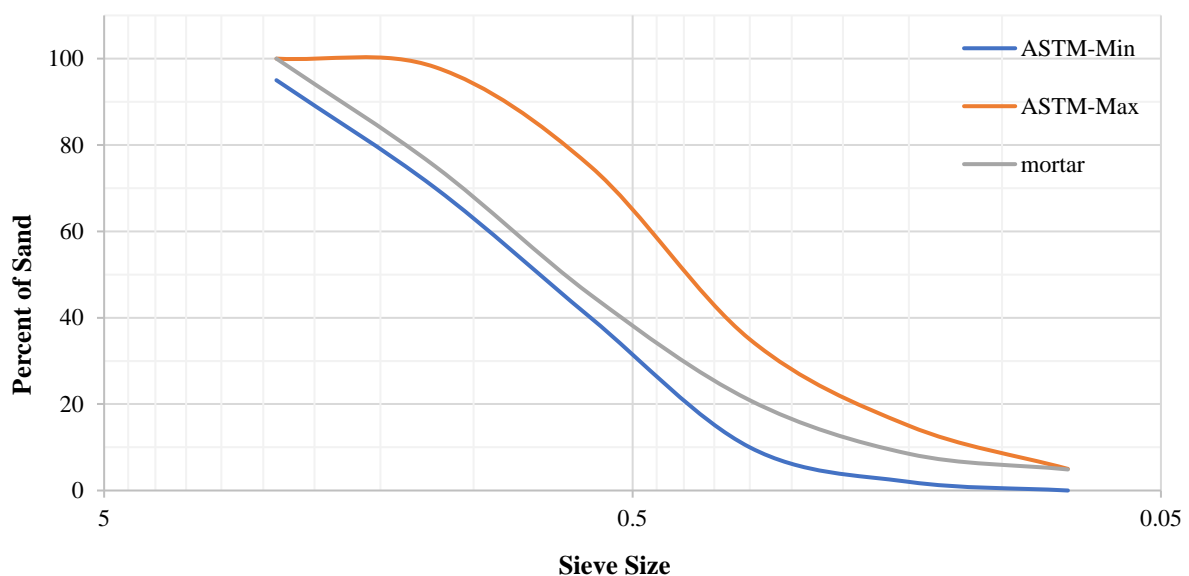
Fig. 4. Sand-grading for the (full-scale) mortar/grout

Table 5. Compressive strength of full-scale mortar specimens

Sample	1	2	3	4	5	6
Compressive strength (MPa)	24.06	27.04	25.43	22.87	21.59	23.45
Ave. strength (MPa)			24.07			

4.2. Half-Scale Masonry

In the construction of the half-scale units, both the physical geometry of the concrete block and the maximum size of its coarse aggregate were multiplied by a scale factor of ½. Consistently, in the mortar mix of the half-scale units, the maximum size of the coarse aggregate must be divided by a factor of 2. For the full-scale units, the sand material passing Sieve #8 was employed in the mortar mix design in conformance with the ASTM Standard. Therefore, to construct a consistent mortar mix for the half-scale units, the sand material passing Sieve #16 was utilized. Table 6 includes the compressive strength values obtained for the half-scale mortar cube specimens tested in conformance with ASTM C270. As with the full-scale specimens, the cubic half-scale mortar specimens were cured in a water pool for 28 days.

The average compressive strength of the full-scale and half-scale mortar specimens of this study were evaluated to be 24.1 MPa and 23.3 MPa, respectively. As such, the ratio of half-scale to the full-scale compressive strength of the mortar specimens was evaluated to be 0.97. The proximity of this ratio to the unity verifies the excellent consistency between the half-scale and full-scale mortar specimens.

As with mortar, half-scale grout specimens, the maximum size of the coarse aggregate and dimensions of samples must be divided by a factor of $^1/_2$, the cubic half-scale grout specimens were cured in a water pool for 28 days.

The average compressive strength of the full-scale and half-scale grout specimens was evaluated to be 22.68 MPa and 22.45 MPa, respectively. As such, the ratio of half-scale to the full-scale compressive strength of the grout specimens was evaluated to be 0.99.

5. Masonry Prisms

One of the main objectives of this research is to compare the compressive stress-strain properties of half-scale and full-scale concrete masonry prisms. As such, a set of hollow and fully grouted masonry prisms were constructed in full- and half-scale arrangements. The compressive strength of the prisms was evaluated experimentally according to the CSA A165. According to this standard, the prism specimens comprise four courses of concrete blocks, three rows of mortar bed joints, and two mortar head joints as seen in Figure 5. Results of such specimens are more representative of a real concrete masonry wall as they include the influence of both the mortar bed joints and head joints in the compressive behavior of the masonry assemblage. The width of mortar joints in the full-scale and half-scale masonry prisms was 10 mm and 5 mm, respectively. To eliminate any inconsistency in the test results as a result of stress concentrations, the top and bottom surfaces of the masonry prisms were capped with a thin layer of 2 to 3 mm thickness of high-strength gypsum (see Figure 5). All of the prisms were tested after 28-days.

5.1. Test Setup

Figure 6 shows an overview of the test setup. As seen in this figure the masonry prism is placed between the rigid upper and lower platens of the test machine.

The compressive load is measured via a load cell secured between the upper platen and the hydraulic ram. The test is performed in a displacement control manner. The outputs of a linear potentiometer that provided the feedback signals to manage the motions of the ram, was utilized as the vertical deformations of the masonry prism.

5.2. Test Results

In this study 20 masonry prisms in two groups were tested. Each group contains 5 grouted and 5 ungrouted masonry prisms. The ultimate compressive load, P, and ultimate strength, f'_m of the prisms of this study are summarized in Table 7. The ultimate strength of masonry prisms was calculated by dividing the ultimate load by the effective cross-section of the prisms.

Table 6. Compressive strength of full-scale mortar specimens

Sample	1	2	3	4	5	6
Compressive strength (MPa)	24.06	27.04	25.43	22.87	21.59	23.45
Ave. strength (MPa)			24.07			
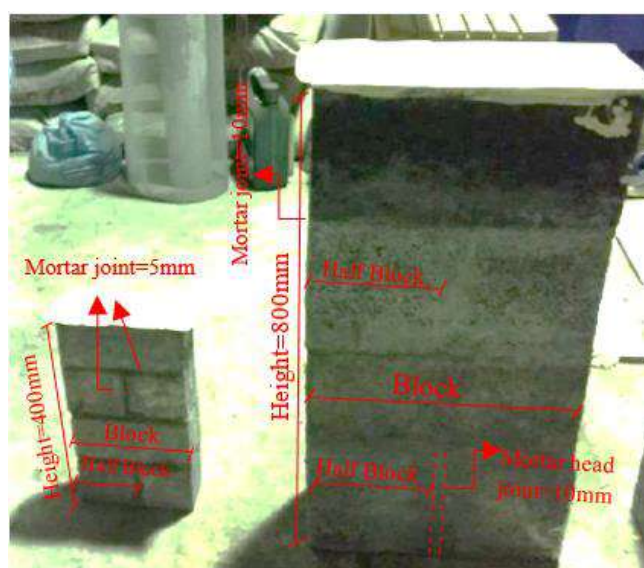
Fig. 5. Typical half-scale and full-scale masonry prisms

Fig. 6. An overview of the compression test setup for the masonry prisms

According to ASTM C1314, the ultimate strength of the masonry prism must be modified to include its slenderness ratio. The correction factor is determined based on the ratio of height, h_p, to thickness (the smallest dimension of the masonry prism), t_p, according to the following table (ASTM C140).

The correction factors shown in Table 7 may be linearly interpolated for the h_p/t_p values are not given directly in the table. However, the correction factors may not be extrapolated for the aspect ratios 1.3 and

5.0. Given the height to thickness ratio of the masonry prisms, 5.6, the correction factor from Table 7 is evaluated to be 1.22. This correction factor was applied to the ultimate compressive strength values given in Table 8. Table 8 also includes the average and standard deviation of the results. The ratio of the standard deviation to the mean (average) of the strength values, f'_m, ranges from 6.8% to 8.4% in different prisms. The relatively low standard deviation values indicate that the results are not widely dispersed about the average values.

Table 7. Height to thickness correction factors for masonry prism compressive strength (ASTM C140)

h_p/t_p	1.3	1.5	2	2.5	3	4	5
Correction factor	0.75	0.86	1	1.04	1.07	1.15	1.22

Table 8. Results of axial compression tests for the full-scale and half-scale prisms

prism	Hollow					Grouted				
	Half-Scale (HS)		Full-Scale (FS)		$\frac{f'_{m,HS}}{f'_{m,FS}}$	Half-Scale (HG)		Full-Scale (FG)		$\frac{f'_{m,HS}}{f'_{m,FS}}$
	P (kN)	$*f'_m$ (MPa)	P (kN)	f'_m (MPa)		P (kN)	f'_m (MPa)	P (kN)	$*f'_m$ (MPa)	
1	81.90	17.08	286.45	14.93	1.14	170.17	15.2	528.89	11.81	1.28
2	90.45	18.86	345.90	18.03	1.05	154.25	13.78	647.82	14.48	0.95
3	75.10	15.66	331.45	17.27	0.90	145.01	12.97	588.59	13.15	0.99
4	87.08	18.16	293.70	15.30	1.18	185.97	16.61	592.75	13.24	1.25
5	96.72	20.17	361.19	18.82	1.07	142.88	12.77	586.7	13.11	0.97
Ave.	**84.33**	**18.06**	**326.89**	**16.87**	**1.07**	**159.66**	**14.26**	**588.95**	**13.16**	**1.08**
St. Dev.	**2.76**	**1.23**	**5.41**	**1.23**	**0.30**	**1.27**	**1.20**	**6.08**	**0.92**	**0.37**

$$*f'_m = \frac{(\text{Correction Factor}(Table6) \times P)}{A_e}$$

In the construction of the masonry prisms of this study, the S-mortar was only applied to the webs (side walls) of the concrete blocks. Therefore, the effective cross-section in the hollow prisms of this study is equivalent to the cross-section of the block webs. The effective cross-section area for the full-scale and half-scale hollow prisms are $2 \times 390 \times 30 = 23400\ mm^2$, and $2 \times 195 \times 15 = 5850\ mm^2$, respectively. The effective cross-section area in the grouted specimens is calculated to be $390 \times 140 = 54600\ mm^2$, and $195 \times 70 = 13650\ mm^2$, for the full-scale and half-scale prisms, respectively.

The ultimate strength of a masonry assemblage is affected by the compressive strength of its masonry units and the type of mortar used in its construction. Given the compressive strength of the concrete blocks of this study, the minimum ultimate compressive strength of a concrete masonry prism constructed with Type S mortar is expected to be 11.5 and 8.8 for hollow and grouted prisms, respectively, based on CSA A165. According to Table 8, the minimum compressive strength of the full-scale for hollow and grouted prisms are 14.93 and 11.81 MPa, respectively. These values are comparable with the strength values prescribed by the CSA A165 standard. The lower compressive strength of the grouted prisms as compared to the hollow prisms is related to the effects of several factors including the water absorption of the concrete masonry units and the grout shrinkage (Drysdale et al., 1994). Although grouting results in reduced compressive strength, the larger effective cross-section area of the grouted masonry prism results in an increased compressive load-bearing capacity as compared to its hollow prism counterpart.

For the hollow and grouted masonry prisms, the ratio of half-scale to full-scale compressive strength values was evaluated to be 1.07, and 1.08, respectively. These indicate the excellent consistency that exists between the half-scale and full-scale prisms of this study. The average stress-strain curves obtained for the hollow and grouted prisms are shown in Figures 7a and 7b, respectively. The following procedure used to obtain the average stress-strain curves shown in Figure 7. First the experimental stress-strain curve of the individual specimens of each group of prisms were evaluated. Next, a polynomial of order 6 was fitted to each curve, and its coefficients were evaluated with a double precision accuracy (This was performed in excel). For each specimen the magnitude of the corresponding stress at any desired strain level could be calculated using the polynomial function evaluated specifically for that specimen in the previous step. The average stress-strain curve was constructed by calculating the average stress values of

specimens at various discrete strain levels.

Figure 7 contains the stress-strain curves of the full-scale and half-scale specimens. Overall, a reasonable correlation exists between the stress-strain relationships of the full-scale and half-scale prisms. The average ultimate strength of the half-scale hollow and grouted prisms to their full-scale counterparts was found to be 107% and 108%, respectively.

Given the nonlinear stress-strain behavior of masonry prisms, the secant modulus of elasticity varies with the magnitude of stress (or strain) values experienced by the material. In this study,

the chord modulus of elasticity as a material property of the prisms was evaluated and compared. The chord modulus of elasticity represents the slope of a line fitted to the stress-strain curve between the stress values ranging from 5% to 33% of the compressive strength of prisms (Drysdale et al., 1994). Table 9 includes the average chord modulus of elasticity of the prisms. The last column of the table indicates the ratio of half-scale to full-scale moduli. As seen an acceptable correlation exists between the model and prototype masonry prism. The fully grouted prisms show better consistency.
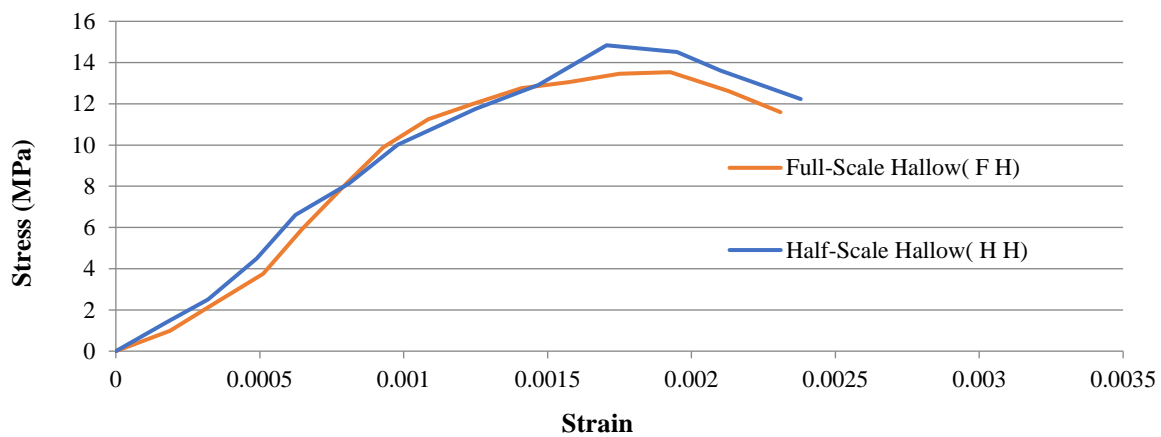
(a) Hollow Prisms
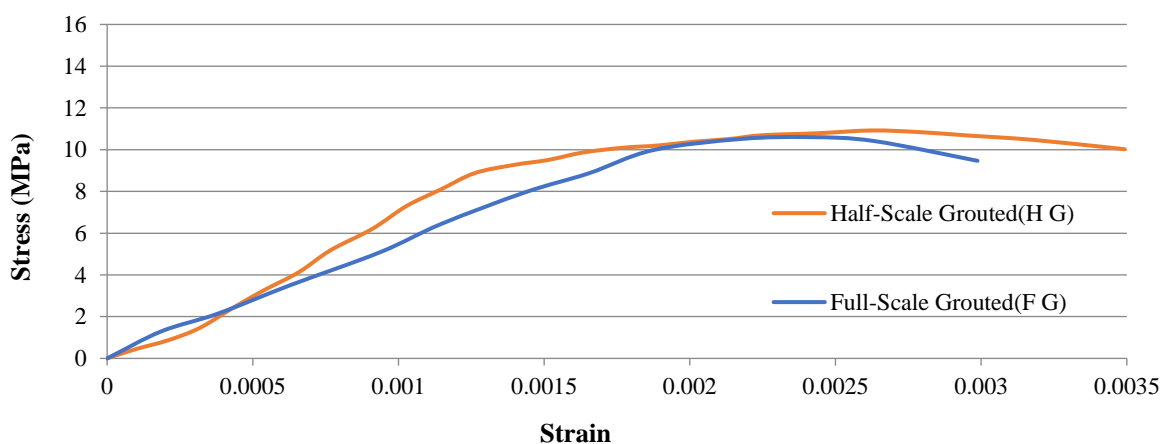
(b) Grouted Prisms
Fig. 7. Stress-strain curves of full-scale and half-scale masonry prisms

Table 9. The chord modulus of elasticity of the masonry prisms

Prism		σ_{Max}	$0.33\sigma_{Max}$	$\varepsilon_{0.33\sigma Max}$	E (MPa)	$\dfrac{E_{Half-Scale}}{E_{Full-Scale}}$
Hollow prism	HH	14.8	4.88	0.00055	8872	1.17
	FH	13.8	4.55	0.0006	7590	
Grouted prism	HG	11.7	3.86	0.0006	6433	1.12
	FG	10.8	3.56	0.00062	5748	

Figure 8a shows the typical failure modes observed in the full-scale hollow prisms (FH) after the completion of testing. The failure pattern includes the formation of significant vertical cracks, (along the axis of compression loading) in the webs of the concrete blocks, as well as in the mortar head joints of the prism. The face shells of the concrete blocks would also experience significant cracks and failure. According to Figure 8b, a relatively similar pattern of failure was observed in the hollow half-scale (HH) prisms.

Figure 9a shows the pattern of failure in the full-scale grouted (FG) prisms. Unlike the hollow prisms, no visible distress was observed in the specimen before the axial load reached its maximum value. When the axial load converged to its ultimate value, the vertical cracks initiated at the sides of the prism. The cracks were expanded and enlarged by increasing axial load. Eventually, the horizontal cracks that led to the splitting of the masonry assemblage were created. The failure pattern of the half-scale grouted (HG) prisms was found to be similar to that of the full-scale specimens (see Figure 9b).

(a) Typical failure modes in the FH
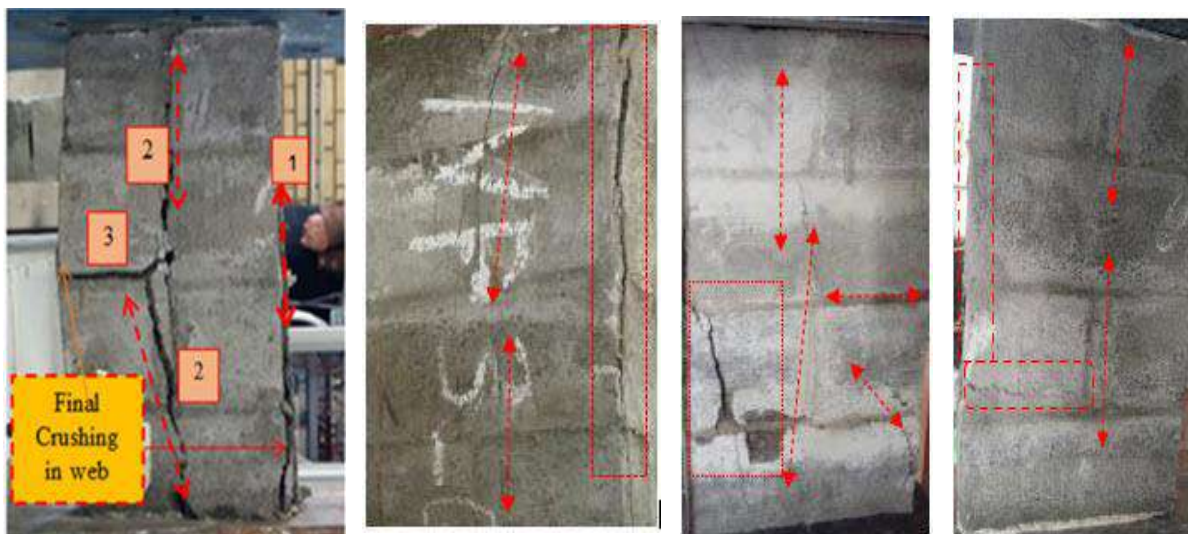
(b) Typical failure modes in the HH
Fig. 8. Typical failure modes in the FH and HH prisms

(a) Typical failure modes in the FG

(b) Typical failure modes in the HG

Fig. 9. Typical failure modes in the FG and HG prisms

6. Conclusions

In this research, the stress-strain behavior of the full-scale and half-scale concrete masonry blocks and prisms were investigated experimentally. The objective was to construct half-scale masonry units and prisms to be a true replica of the conventional full-scale counterparts. To achieve the research objectives, the size of aggregates in the concrete, mortar, and grout mixes, and the physical dimensions of the half-scale masonry assemblages complied with the scale-factor of ½ according to the similitude law. The ultimate strength of the half-scale specimens was evaluated and compared with those of the full-scale configuration. The main outcomes of this study are as follows:

Masonry units: The ratio of half-scale to full-scale mass density, water absorption, and linear shrinkage were measured to be 0.95, 0.85, and 1.05, respectively. The compressive strength of the half-scale unit was found to be on average nearly 1% larger than the full-scale blocks.

Mortar and grout: The ratio of half-scale to the full-scale compressive strength of the grout and mortar specimens was evaluated to be 0.99 and 0.97,

respectively.

Masonry prisms: The ultimate compressive strength of the half-scale hollow masonry prisms was found to be on average 7% larger than their full-scale counterparts. Similarly, the average ultimate strength of the half-scale fully-grouted prisms was +8% off as compared to their corresponding full-scale prisms. The chord modulus of elasticity of half-scale hollow and grouted specimens was found to be on average 17% and 12% larger than their corresponding full-scale specimens, respectively. As such, the half-scale prisms were found to be slightly stronger and stiffer than the full-scale ones under compressive loads due to the scale effects. The failure modes of the two systems were found to be similar.

The results of this study suggest that the standard half-scale units and assemblages that are constructed consistent with the principles of similitude law are to a large extent representative of the response behavior of the full-scale masonry units and assemblages. As such, the response behavior of the half-scale concrete masonry assemblages may be extended to the conventional full-scale masonry specimens. This conclusion is of interest as the application of standard half-scale masonry units in experimental research studies leads to significant ease of work and cost savings.

7. References

AbdelRahman, B. and Galal, K. (2020). "Influence of pre-wetting, non-shrink grout, and scaling on the compressive strength of grouted concrete masonry prisms", *Construction and Building Materials*, 241, 117985.

ACI 530. (2013). *Building code requirements and specification for masonry structures and companion commentaries,* American Concrete Institute.

Alvarenga, R.C.S.S., Nalon, G.H., Fioresi, L.A.F., Pinto, M.C., Pedroti, L.G. and Ribeiro, J.C.L. (2017) "Experimental evaluation of the influence of mortar's mechanical properties on the behavior of clay masonry", In *Characterization of Minerals, Metals, and Materials*, 2017, 671-679, Springer, Cham.

Andria, I., Samira, R., Mark, H., Pedram, K. and Nigel, SH. (2017). "Testing and finite element modeling of concrete block masonry in compression", *13th Canadian Masonry Symposium*, Halifax, Canada.

ASTM C90-16a. (2016). *Standard specification for loadbearing concrete masonry units*, American Society for Testing and Materials, West Conshohocken, Pa.

ASTM C136/C136M-19. (2019). *Standard test method for sieve analysis of fine and coarse aggregate*, American Society for Testing and Materials, West Conshohocken, Pa.

ASTM C140-13a. (2013a). *Standard test methods for sampling and testing concrete masonry units and related units*, American Society for Testing and Materials, West Conshohocken, Pa.

ASTM C144-04. (2018). *Standard specification for aggregate for masonry mortar*, American Society for Testing and Materials, West Conshohocken, Pa.

ASTM C270-19. (2019). *Standard specification for mortar for unit masonry*, American Society for Testing and Materials, West Conshohocken, Pa.

ASTM C426-16. (2016). *Standard test method for linear drying shrinkage of concrete masonry units*, American Society for Testing and Materials, West Conshohocken.

ASTM C404-18. (2018). *Standard specification for aggregates for masonry grout,* American Society for Testing and Materials, West Conshohocken, Pa.

ASTM C476-19. (2019). *Standard specification for grout for masonry*, American Society for Testing and Materials, West Conshohocken, Pa.

ASTM C1314-12. (2012). *Standard test method for compressive strength of masonry prisms*, American Society for Testing and Materials, West Conshohocken, Pa.

Camacho, J.S., Logullo, B.G., Parsekian, G. and Soudias, P.R. (2015). "The Influence of grouting and reinforcement ratio in the concrete block masonry compressive behavior", *Revista IBRACON de Estruturas e Materiais,* 8, 341-364.

Camacho, J.S. and Andolfato, R.P. (2000). "Development of the production techniques of the small scale concrete block", *12th International Brick/Block Masonry Conference,* Madrid-Spain.

CSA Standard A165. (2002). *Concrete materials and methods of concrete construction, methods of test for concrete,* Canadian Standards Association, Toronto.

Drysdale, R.G., Hamid, A.A. and Baker, L.R. (1994). *Masonry structures: Behavior and design,* Prentice-Hall, Englewood Cliffs, N.J.

Eshghi, S. and Pourazin, Kh. (2009). "In-plane behavior of confined masonry walls, with and without opening", *International Journal of Civil*

Engineering, 7(1), 49-60.

Eurocode 6-1996-1-1, 1996-3. (2006). *Design of masonry structures, Part 1-1: Rules for reinforced and unreinforced masonry, Part 3: Simplified calculation methods for unreinforced masonry structures*, European Committee for Standardization, Brussels.

Gustavo, H., Carol. F. and Leonardo, G. (2019). "Strength and failure mechanisms of masonry prisms under compression, flexure and shear: Components' mechanical properties as design constraints", *Journal of Building Engineering*, 28, 101038.

Hamid, A.A., Abboud, B.E. and Harris, H.G. (1985). "Direct modeling of concrete block masonry under axial compression", In *Masonry: Research, Application, and Problems*, ASTM International.

Harris H.G. and Sabnis, G. (1999). *Structural modeling and experimental techniques*, CRC press.

Hassanli, R., ElGawady, M.A. and Mills, J.E. (2015). "Effect of dimensions on the compressive strength of concrete masonry prisms", *Advances in Civil Engineering Materials*, 4(1), 175-201.

Hosseinijou, S.A. and Mansour, S. (2021). "Dynamic material flow analysis of cement in Iran: New insights for sustainability of civil infrastructures", *Civil Engineering Infrastructures Journal,* 54(2), 381-403.

Huang, L., Long, L. and Yan, L. (2014). "Compressive strength of double H concrete block masonry prisms", *Journal of Materials in Civil Engineering,* 26(8), 06014019.

Jablonsky, N. (1996). *Mix design for concrete block, proportioning using the fineness modulus method,* The Aberdeen Group, 1-4.

Long, L., Hamid, A. and Drysdale, R.G. (2005). "Small-scale modeling of concrete masonry using half-scale units: A preliminary study", *10th Canadian Masonry Symposium*, Banff Alberta, June 8-12.

Mohammad, G., Eduardo, R., Almir, B. and Roman, H. (2010). "Influence of vertical joint on the mechanical behavior of concrete block masonry", *Engenharia Estudo*, 10(1), 75-80.

Oliveira, R., Martin, G. and Nalon, G.H. (2018). "Influence of blocks and grout on compressive strength and stiffness of concrete masonry prisims", *Construction and Building Materials,* 182, 233-241.

Rai, D.C. (2002). *Review of design codes for masonry buildings,* Indian Institute of Technology, Kanpur, India.

Sathiparan, N., Anjalee, W.A.V. and Kandage, K.K.S. (2016). "The scale effect on small-scale modelling of cement block masonry", *Materials and Structures*, 49(7), 2935-2946.

Standard No. 2800. (2013). *Iranian code of practice for seismic resistant design of building*, 4th Edition, Ministry of Urban and Road Construction, Tehran.

Zahra, T., Thamboo, J. and Asad, M. (2021). "Compressive strength and deformation characteristics of concrete block masonry made with different mortars, blocks and mortar beddings types", *Journal of Building Engineering*, 38, 102213.

Structural Control of Building with ATMD through AN-IT2FLC under Seismic Excitation

Golnargesi, S.[1][*] ⓘ, Shariatmadar, H.[2] ⓘ and Golnargesi, B.[3] ⓘ

[1] Assistant Professor, Faculty of Civil Engineering and Environment, Khavaran Institute of Higher Education, Mashhad, Iran.
[2] Professor, Faculty of Civil Engineering, Ferdowsi University, Mashhad, Iran.
[3] Ph.D. Candidate, Islamic Azad University, Mashhad Branch, Mashhad, Iran.

© University of Tehran 2022

ABSTRACT: This paper focuses on the design of Adaptive-Neural Interval Type-2 Fuzzy Logic Controller (AN-IT2FLC) in an active tuned mass damper to reduce the response of building under seismic excitation. One of the main shortcomings of Interval Type-2 Fuzzy Logic Controller (IT2FLC) is its need to adjust in any earthquake. This is whilst the AN-IT2FLC can solve this problem using the training process. In this research, four inputs are used for designing and training of AN-IT2FLC as controlled displacement and velocity of roof level with IT2FLC, acceleration of the implemented earthquakes and the control force of IT2FLC. AN-IT2FLC training performed based on the eight earthquake records of El Centro, Hachinohe, Kobe, Northridge, Loma Prieta, Tabas, Morgan Hill and Erizkan with various seismic characteristics. In order to investigate the effectiveness of the proposed controller, an 11-story building with ATMD on its top floor analyzed under another four ground accelerations of Chi-Chi, Kern-county, Coalinga and Coyote-lake records. The results revealed that ATMD with AN-IT2FLC is able to achieve more response reduction with higher speed and accuracy rather than that of the IT2FLC.

Keywords: AN-IT2FLC, ATMD, Earthquake Excitation, Structural Control.

1. Introduction

It is inevitable that natural disasters such as earthquakes cause damage to the structures unpredictably. The earthquake excitations must be damped in some way to minimize possible damages to the building. The use of structural control systems can help the structural designers to achieve this aim. So far, various types of structural control systems and devices have been proposed, which are divided into four general categories according to the type of operation as passive, active, semi-active, and hybrid. Due to their simple application and high reliability, passive control methods are widely used. One of the most effective devices of passive control is the Tuned Mass Damper (TMD), which attracted many researchers' attention (Farshidianfar and Soheili, 2013; Meshkat Razavi and Shariatmadar, 2015; Ying Zhou et al., 2019; Ying Zhou et al., 2020; Love and Haskett, 2019; Anajafi and Medina, 2017; Miguel et al., 2016; Lievens et al., 2016; Zuo et al., 2021; Jin et al., 2020; Huang et al., 2020;

Boccamazzo et al., 2020).

Extensive efforts have been done to increase the capacity of TMD, including setup of an active control force between the building and the TMD. This new control system is called "Active Tuned Mass Damper" (ATMD). By surveying the structural control concepts, it can be found that the ATMD which is used in this study is a hybrid control device.

The role of the hybrid control system is to reduce building vibration under seismic loadings with uncertain characteristics such as strong winds and highly damaging earthquake excitations and consequently to increase comfort of occupants of the building.

A hybrid control system may use active control to supplement and improve the performance of a passive control system and because double control devices are operating in it (e.g. in an ATMD) it can alleviate some of the restrictions and limitations that exist when each system is acting alone. In the other hands, a hybrid control device is typically defined as one that utilizes a combination of passive and active systems where in the passive control may be added to an active control scheme to decrease its energy requirements. For example, the mass damper and actuator are the passive and active devices in an ATMD, respectively.

It should be noted in passing that one of the essential differences between an active and a hybrid control scheme, in many cases, is the amount of external energy used to implement control force which is much less in the hybrid control system. In this regard, a side benefit of hybrid control device is that, in the case of a power failure, the passive component of the control still offers some degree of protection, unlike an active control system. Thus, higher levels of performance may be achievable and the overall reliability and efficiency of the controlled structure is increased.

After reviewing the superiority of hybrid control system over its active and passive, its advantages are compared with semi-active ones, in the following:

- Semi-active devices composed of materials with variable characteristic (such as viscosity) which may change its properties during operation and makes them to be unreliable.
- Practical design of a semi-active system using conventional technologies is under the constraints of weight, size and cost.
- Design of semi-active devices involves many mechanical and electrical components that puts limit on the tuning range of the resonance frequency of the device.

Because of the mentioned comparative disadvantages of semi-active systems, the use of hybrid control devices such as ATMD is recommended for the optimal control objectives.

Finally, in comparison with other control systems, a number of advantages associated with hybrid control systems can be cited as:
- Enhanced effectiveness in response control;
- Relative insensitivity to site conditions and ground excitations;
- Applicability to multi-hazard mitigation situations;
- Control objective selectivity.

For example, in the latter, while the main objective is to increase structural safety during severe earthquakes, human comfort should also be emphasized over other aspects of structural motion during noncritical times (Soong and Reinhorn, 1993; Housner et al., 1997; Spencer and Nagarajaiah, 2003; Bathaei et al., 2017; Wang et al., 2021; Ying Zhou et al., 2020).

This is why several theoretical and laboratory studies have been done to find the optimal actuator force to reduce the response of the buildings. For the first time, Kobori et al. (1991) used an ATMD to reduce the response of a real 10-story building under external forces of earthquake and wind. Theoretical studies have been carried out on the active mass damper in two general fields of mathematical research and artificial intelligence. Among the mathematical

studies, the Linear Quadratic Regulator (LQR) optimize control (Chang and Soong, 1980), the pole assignment and the Bang-Bang (Collins and Basu, 2006) control strategies can be mentioned. Also, numerous studies are conducted in the field of fuzzy systems, neural networks and adaptive-neural fuzzy systems, some of which are referred as below:

Guclu and Yazici (2008) compared fuzzy and Proportional-Derivative (PD) controllers in a 15-story building. Optimization of fuzzy membership functions in an ATMD controller accomplished by Pourzeinali et al. (2007), through using genetic algorithm to optimize fuzzy controller parameters. The results revealed that the fuzzy optimized controller has a much better behavior compared to the LQR controller. In order to reach synthetic artificial accelerograms with response spectrum similar to the target spectrum, combination of neural networks and wavelets used by Bargi et al. (2012). Golnargesi et al. (2014), modeled the interval type 2 FLC in an active tuned mass damper for seismic control of buildings. One of the weak points of the conventional fuzzy systems (FLS) is the lack of consideration of the uncertainty in fuzzy rules. Type 2 fuzzy systems are capable of considering this kind of uncertainty. Their research deduced that the interval type 2 FLC is more effective than the FLC in mitigating the response of the building. Naderpour et al. (2016) used a suitable neural network to estimate the dispersion of far-field earthquake disturbances. The results showed that the trained neural network has an acceptable accuracy compared with the finite element models. Golnargesi et al. (2018) investigated the seismic control of buildings with ATMD using interval type2 FLC, including soil-structure interaction. They analyzed the structural response in two conditions, with and without considering the Soil-Structure Interaction (SSI) effects. Their research results demonstrated that considering soil type effects has a significant impression on

structural responses. Chen et al. (2019) used EB algorithm to optimize the controlling system. They showed that the proposed method is more useful for closed loop control systems. Bakhshinezhad and Mohebbi (2019) developed the fragility curves of buildings with SATMD by considering uncertainties of different parameters. The results included that STMD improves the performance of seismic fragility of nonlinear buildings.

Considering the studies carried out in this field, it can be concluded that there has not been undertaken any similar research on the use of interval type 2 fuzzy systems and neural networks simultaneously to control the structural responses and it is the innovation of this research which will be expressed in the following.

The aim of the present study is to design a new active control system to reduce the seismic response of buildings, called the Adaptive-Neural Interval Type 2 Fuzzy Logic System (AN-IT2FLS). For this purpose, an ATMD with AN-IT2FLC is installed on the top floor of an 11-story shear building and the proposed control system is trained using eight various earthquakes. Therefore, to investigate the efficiency of the proposed control algorithm, the building is analyzed under two far-field earthquakes (Kern-county and Chi-Chi) and two near-field earthquakes (Coalinga and Coyote-lake), where structural responses are obtained in different control cases. The results indicate the high ability, accuracy and speed of processing of AN-IT2FLC in mitigating building response compared to IT2FLC with optimum general parameters in different types of earthquake records.

2. Modeling and Numerical Example

An n-story shear building, along with an ATMD on its roof level, can be considered as a (n+1) degrees of freedom building (Figure 1).

The equation of motion of the above system under seismic excitations is as Eq.

(1), in which M, K and C: are the matrices of mass, stiffness and damping of the building, U: is the horizontal displacement vector of stories toward the ground, E: is the effect vector, a_g: is the ground acceleration, E_f: is the position vector of the control force and F: is the control force.

$$M.\ddot{U}(t) + C.\dot{U}(t) + K.U(t) = -M.E.a_g + E_f.F \tag{1}$$

$$U(t) = \{u_1(t), u_2(t), \ldots, u_n(t), u_d(t)\} \tag{2}$$

$$M = diag[m_1, m_2, \ldots, m_n, m_d] \tag{3}$$

$$K = \begin{bmatrix} K_1 + K_2 & -K_2 & 0 & \ldots & & 0 \\ -K_2 & K_2 + K_3 & & & & \cdot \\ & & & & & \cdot \\ \cdot & & & & & \cdot \\ \cdot & & 0 & \ldots & -K_n & 0 \\ \cdot & & & & & \\ & & & -K_n & K_n + K_d & -K_d \\ & & & \cdot & & \\ 0 & \ldots & 0 & & -K_d & K_d \end{bmatrix} \tag{4}$$

$$C = \begin{bmatrix} C_1 + C_2 & -C_2 & 0 & \ldots & & 0 \\ -C_2 & C_2 + C_3 & & & & \cdot \\ & & & & & \cdot \\ \cdot & & & & & \cdot \\ \cdot & & 0 & \ldots & -C_n & 0 \\ \cdot & & & & & \\ & & & -C_n & C_n + C_d & -C_d \\ & & & \cdot & & \\ 0 & \ldots & 0 & & -C_d & C_d \end{bmatrix} \tag{5}$$

$$E = \{1, 1, \ldots, 1\}^T_{((n+1)\times 1)} \tag{6}$$

$$E_f = \begin{bmatrix} [0]_{(n-1)\times 1} \\ -1 \\ 1 \end{bmatrix} \tag{7}$$

where in the K and C matrices, K_d: is the mass damper stiffness and C_d: is the damping coefficient of the mass damper. Eq. (1) can be written in the form of the space state as follows:

$$\dot{X} = A.X + B_f.F + B_g.a_g \tag{8}$$

where X: is a vector of (n+1) order, and is defined with A, B_f, B_g in the following equations:

$$X = \left\{ \begin{array}{c} \{u\}_{(n+1)\times 1} \\ \{\{\dot{u}\}_{(n+1)\times 1}\} \end{array} \right\} \tag{9}$$

$$A = \begin{bmatrix} [0]_{(n+1)\times(n+1)} & [I]_{(n+1)\times(n+1)} \\ [-M^{-1}.K]_{(n+1)\times(n+1)} & [-M^{-1}.C]_{(n+1)\times(n+1)} \end{bmatrix} \tag{10}$$

$$B_f = \left\{ \begin{array}{c} \{0\}_{(n+1)\times 1} \\ \{-M^{-1}.E_f\}_{(n+1)\times 1} \end{array} \right\} \tag{11}$$

$$B_g = \left\{ \begin{array}{c} \{0\}_{(n+1)\times 1} \\ \{-E\}_{(n+1)\times 1} \end{array} \right\} \tag{12}$$

The used building in this paper is an 11-story shear building (Figure 2) located in Rasht city of Iran with an ATMD on the last floor (Pourzeinali et al., 2007). The structural characteristics of the building (stiffness and mass of stories) are listed in Table 1.

The structural damping matrix is calculated according to the Rayleigh's method. Considering the damping ratio of the building as the 5% of critical damping value for the first and second modes, calculation of damping matrix can be done as follows (Pourzeinali et al., 2007):

$$C = X_1.[M] + X_2.[K] \tag{13}$$

$$X_1 = \xi\left(\frac{2\omega_1.\omega_2}{\omega_1 + \omega_2}\right) \quad, \quad X_2 = \xi\left(\frac{2}{\omega_1 + \omega_2}\right) \tag{14}$$

where, ω_1 and ω_2: are the first two natural frequencies of the uncontrolled structure and calculated as 6.5727 and 19.355 (rad/s), respectively.

3. Adaptive-Neural Interval Type-2 Fuzzy Logic Systems (AN-IT2FLS)

Jang (1993) presented the adaptive neural fuzzy inference system (ANFIS). This system is a simple learning technique uses fuzzy algorithms to convert inputs given to a desired output through the processing of information. ANFIS is a combination of

both fuzzy and neural networks and integrates both into a single method simultaneously. In this method, the parameters of the fuzzy inference system are adjusted using neural networks.

Since different rules cannot share the same output function, and the number of membership functions must be equal to the number of rules, it is possible to use the architecture of a neuro-fuzzy system from two IF-THEN fuzzy rules, based on a first-order model (Eqs. (15) and (16)).

$$Rule_{(1)}: IF\ x\ is\ A_1\ AND\ y\ is\ B_1 \text{، } THEN\ f_1 = p_1 x + q_1 y + r_1 \tag{15}$$

$$Rule_{(2)}: IF\ x\ is\ A_2\ AND\ y\ is\ B_2 \text{، } THEN\ f_2 = p_2 x + q_2 y + r_2 \tag{16}$$

where X and Y: are system input, A_i and B_i: are fuzzy sets, f_i: is fuzzy outputs obtained from fuzzy rule, p_i, q_i and r_i: are design parameters during the training process. The architecture of ANFIS for implementing these two rules is clear in Figure 3.
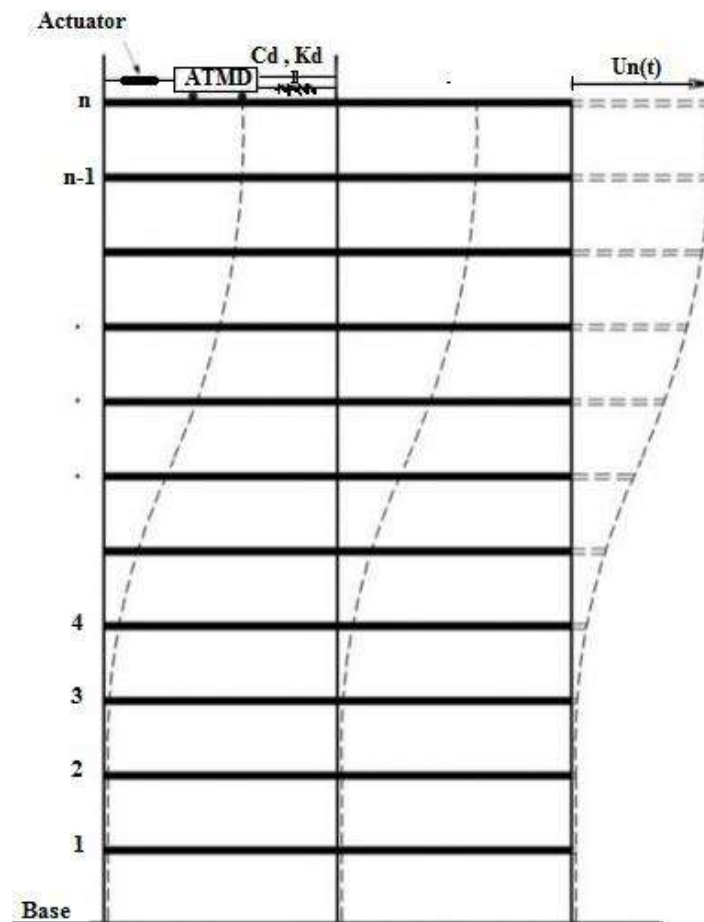
Fig. 1. n-story shear building with ATMD on the top floor

Table 1. Mass and stiffness of building stories

Floor	Stiffness (N/m)	Mass (kg)
1	4.68e8	21537
2	4.76e8	201750
3	4.68e8	201750
4	4.5e8	200930
5	4.5e8	200930
6	4.5e8	200930
7	4.5e8	203180
8	4.37e8	202910
9	4.37e8	202910
10	4.37e8	176100
11	3.12e8	66230
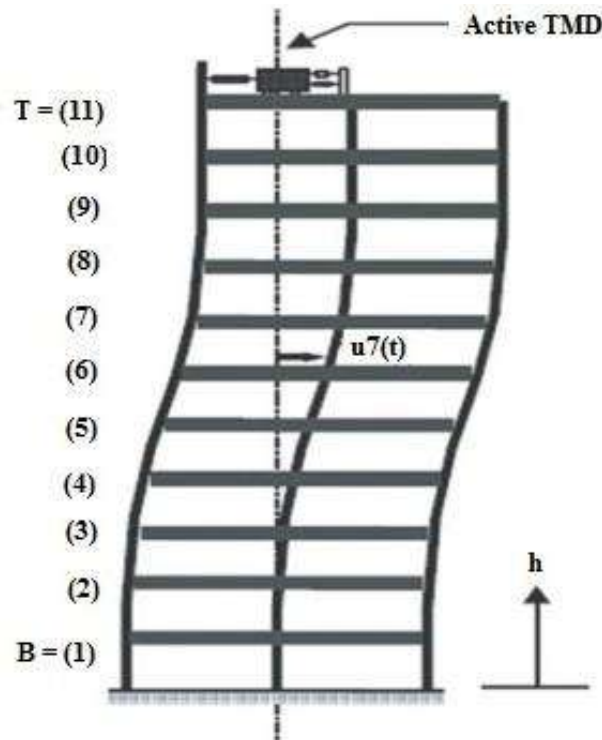
Fig. 2. The 11-story building with ATMD
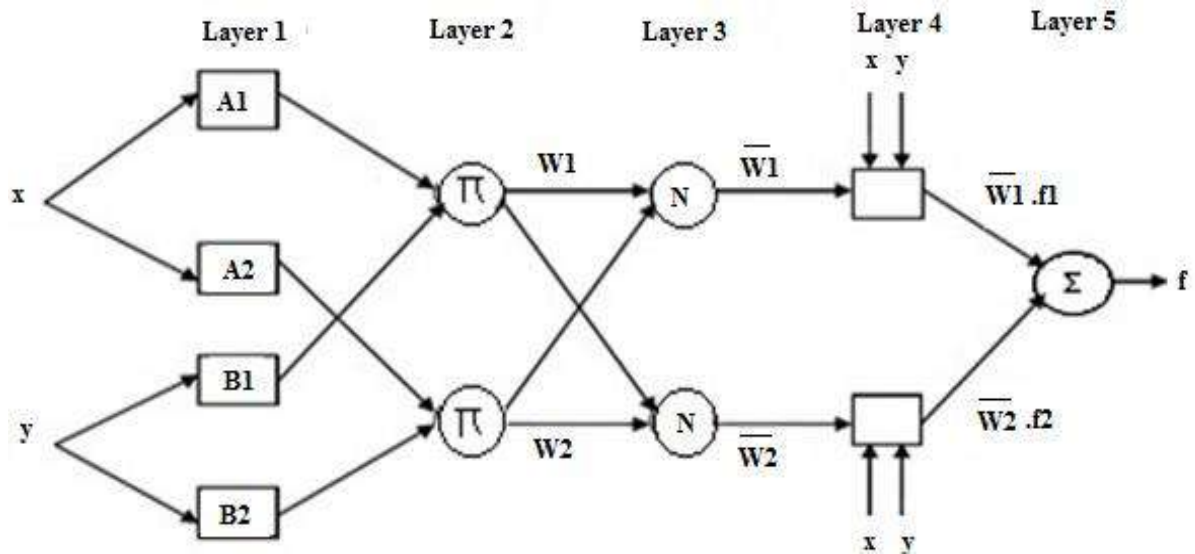
Fig. 3. ANFIS Architecture

According to Figure 3, the circle sign represents a fixed node and the square sign indicates the consistent node. Also from the Figure 2, it can be seen that ANFIS architecture has 5 layers. In Layer 1, all are compatible nodes. The outputs of the Layer 1 are the degrees of membership of the fuzzy inputs, which can be seen in Eqs. (17) and (18):

In this layer, X and Y: are its node inputs, and A_i and B_i: are defined as parameters associated with the $\mu_{Ai}(x)$ and $\mu_{(Bi-2)}(y)$ functions. In Layer 2, nodes are considered to be constant. This layer contains fuzzy operators that are represented by the π parameter and act as a simple coefficient. The output of this layer is represented by Eq. (19):

$$O_{1،i} = \mu_{Ai}(x) ، \quad i = 1،2 \tag{17}$$
$$O_{1،i} = \mu_{Bi-2}(y) ، \quad i = 3،4 \tag{18}$$

$$O_{2،i} = w_i = \mu_{Ai}(x) * \mu_{Bi}(y) ، i = 1،2 \tag{19}$$

in Layer 3, the fixed nodes are shown with the parameter N and play a normalize role rather than the previous layer. The output of this layer can be expressed as Eq. (20):

$$O_{3,i} = \overline{w}_i = \frac{w_i}{w_1 + w_2} \ , \ i = 1, 2 \quad (20)$$

Regarding the Eq. (21), the fourth layer, composed of product of normalized weight of each fuzzy rule and the output of the last part of that rule.

$$O_{4,i} = \overline{w}_i f_i = \overline{w}_i (p_i x + q_i y + r_i), \ i \\ = 1, 2 \quad (21)$$

in such a way that $\overline{w}_i$: is the output of the third layer, and p_i, q_i and r_i: are defined as the corresponding parameters.

In the fifth layer, there is only one fixed node with the sign Σ, which represents the total input signals. The total output of the ANFIS is seen in Eq. (22).

$$O_{5,i} = \sum_i \overline{w} f_i = \frac{\sum_i w_i f_i}{\sum_i w_i} \quad (22)$$

Now, if the Interval Type-2 Fuzzy Inference System (IT2FIS) used in ANFIS introduced in this section, Adaptive-Neural Interval Type-2 Fuzzy Inference System (AN-IT2FIS) will be obtained, which will be followed by its design and how it will be modelled.

4. AN-IT2FLC Training and Design

In this paper, the training Process of AN-IT2FLC, is done by gradient descent algorithm. The main advantages of this

learning algorithm are the fast and well fitness of training data and simplicity of iterative formula for the computation.

In the following, for the learning of fuzzy rules and membership functions of AN-IT2FLC the mentioned algorithm is expressed (Ichihashi, 1991; Kosko, 1992; Yager and Filev, 1994). For a given fuzzy system model with a number of input variables $(x_1, x_2, ..., x_n)$ and one output variable (y), the fuzzy rule base is defined as follows (Ichihashi, 1991; Kosko, 1992):

Rule i: If x_1 is A_{1i} and x_2 is A_{2i} ... and x_n, is A_{ni}, Then y is y_i (i = 1, 2, ..., m) (23)

where A_{ji} (j=1, 2, …, n and i=1, 2, …, m): is a membership function for the input variable x_j which is expressed in Eq. (27), y_i is a real number on the output universe Y, and m: is the number of the fuzzy rules.

$$A_{ji}(x_j) = exp \ (-(x_j-a_{ji})^2/b_{ji}) \\ (j=1,2,...,n \ and \ i=1,2,...,m) \quad (24)$$

where a_{ji}: is the centre of A_{ji} and b_{ji}: is the width of A_{ji}.

In this research, four kinds of vector inputs (each one having lots of data for the time domain of training earthquake records), are used in order to design and train of AN-IT2FLC. The training earthquakes, which are used in this study, are eight arbitrary records of El Centro, Hachinohe, Kobe, Northridge, Loma prieta, Tabas, Morgan Hill and Erizkan records with different seismic properties. The characteristics of these ground accelerations shown in Figure 4 and Table 2.

Table 2. Specifications of earthquakes for training process of AN-IT2FLC

Earthquake	PGA	Duration (Sec)
El Centro	0.342g	50
Kobe	0.328g	69.98
Hachinohe	0.225g	35
Northridge	0.248g	59.98
Loma Prieta	0.112g	39.94
Tabas	0.852g	32.82
Morgan Hill	0.312g	39.97
Erzikan	0.515g	21.31

(a) El Centro

(b) Hachinohe

(C) Kobe

(d) Northridge

(e) Morgan Hill

(f) Erizkan

(g) LomaPrieta

(h) Tabas
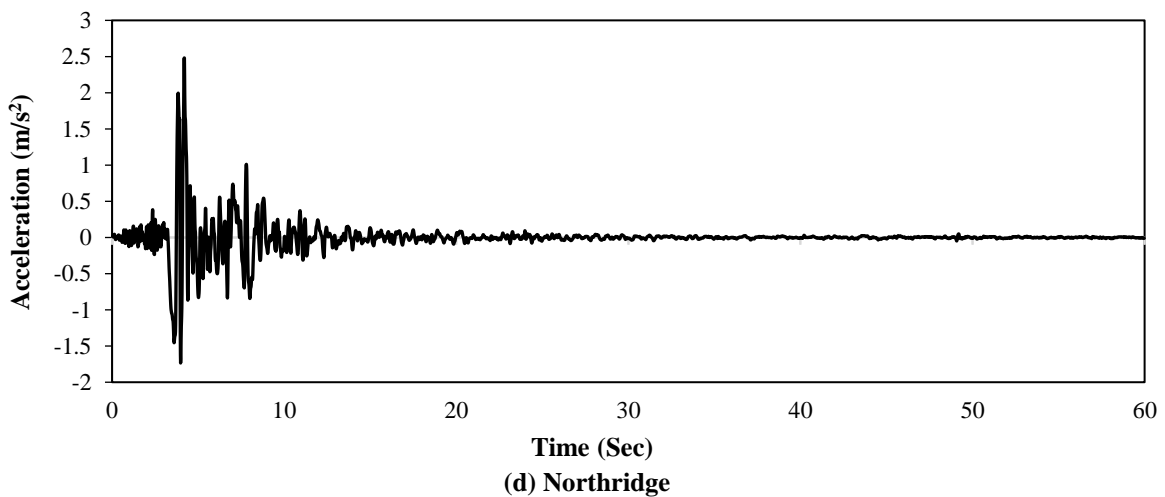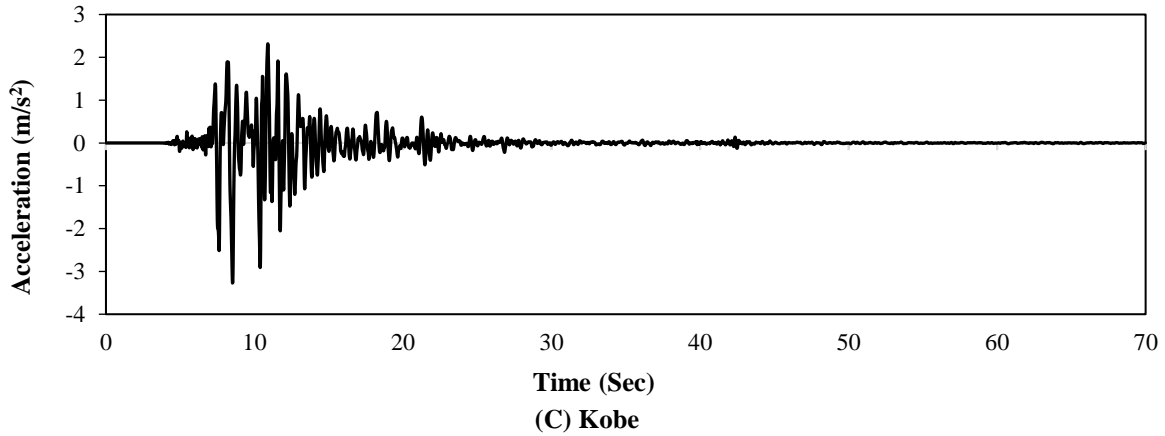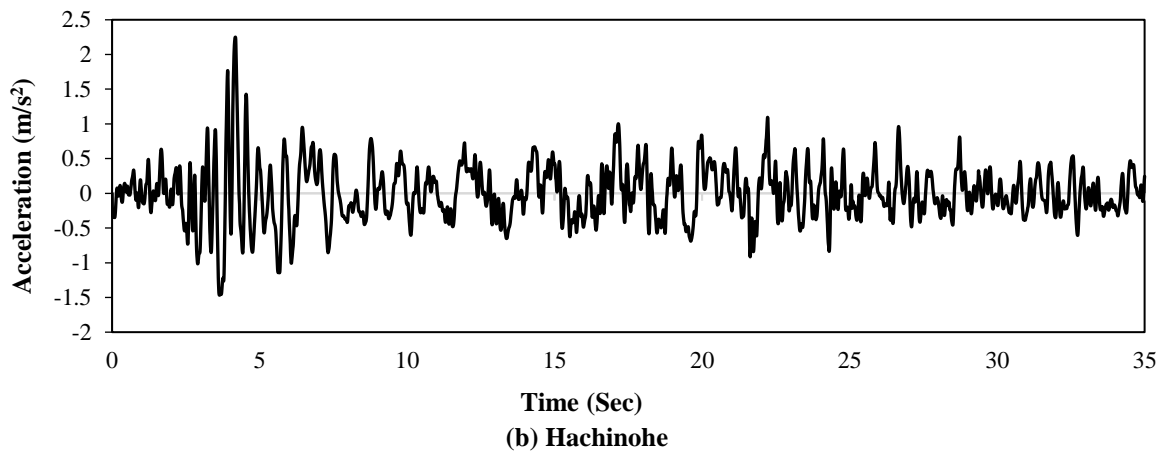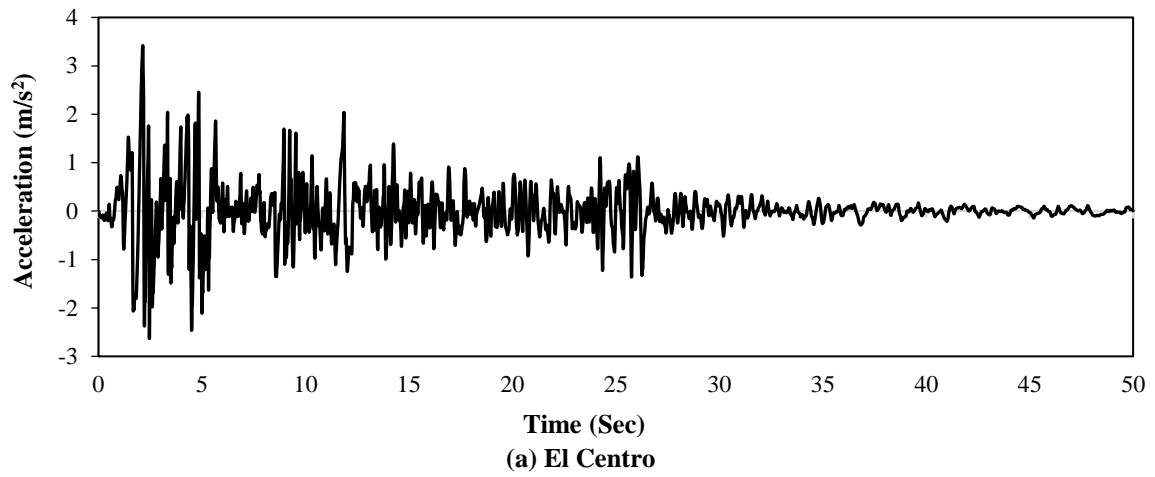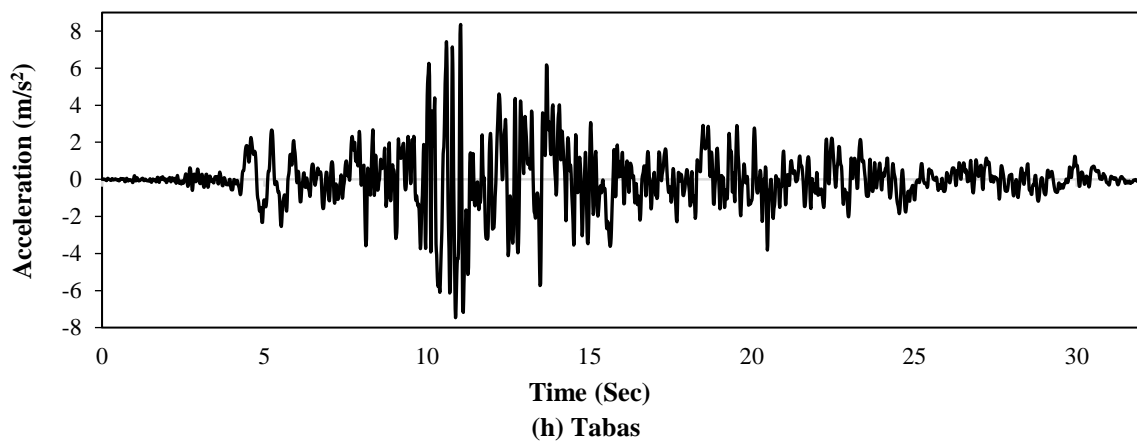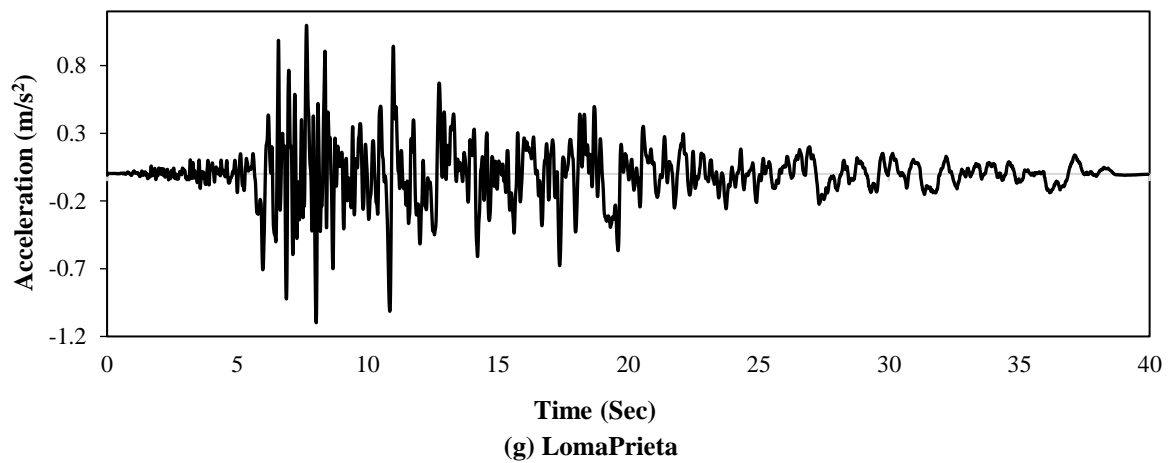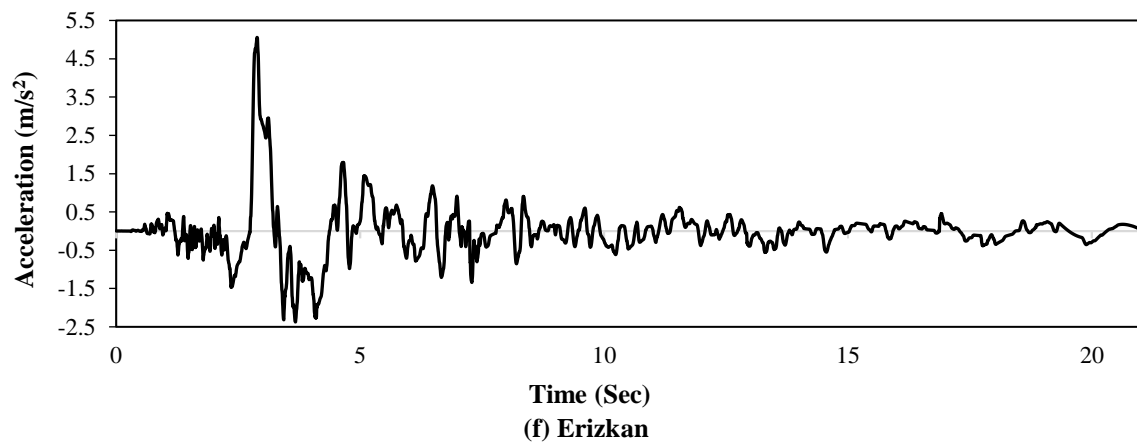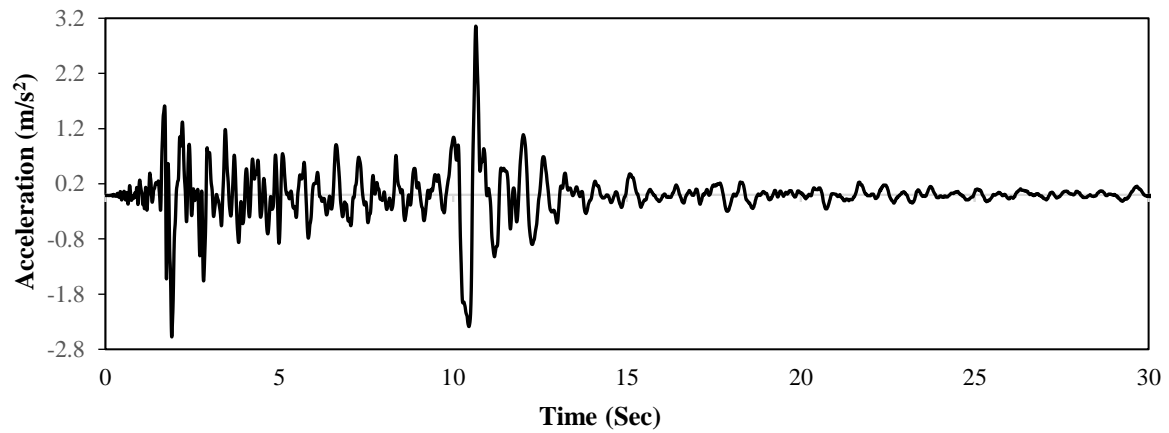
Fig. 4. Time history records of the eight earthquakes for training of AN-IT2FLC

The first two types of inputs are displacement and velocity of the building's top floor, which is controlled with an ATMD through IT2FLC under the seismic excitation. The third input, is the acceleration vector of mentioned earthquakes for the all instances of time domain records. The last input required for training of the proposed controller, is the IT2FLC control force vector of ATMD in the above-mentioned earthquakes. It is noteworthy that the associated data for designing of IT2FLC, such as the type and number of MFs of input and output variables and the fuzzy rule base, have been extracted from the research done by Golnargesi et al. (2014).

When an observation $x_1, x_2, ..., x_n$: is given, according to simplified fuzzy reasoning method (Ichihashi, 1991), a fuzzy inference conclusion y can be obtained as follow:

First, for i=1, 2, ..., m the agreement of i'th antecedent part is calculated using product operator:

$$h_i=$$
$$A_{1i}(x_1)A_{2i}(x_2)...A_{ni}(x_n)=\prod_{j=1}^{n}A_{ji}(x_j)(i=1,2,...,m) \tag{25}$$

Then, a consequence y is calculated using center of gravity method as follows:

$$y=(\sum_{i=1}^{m}h_iy_i)/(\sum_{i=1}^{m}h_i) \tag{26}$$

The only output of mentioned algorithm of this research is the trained AN-IT2FLC control force.

When a training input-output datum $x_1, x_2, ..., x_n$; y^*: is given for the fuzzy system model, it is well known to use the following objective function E for evaluating an error between y^* and y, which can be regarded as an optimum problem:

$$E = (y^* - y)^2/2 \tag{27}$$

where y^*: is a desired output value, and y: is

a fuzzy inference result. In order to minimize the objective function E, a learning algorithm for updating the parameters (a_{ji}, b_{ji}, and y_i) has been proposed based on gradient descent algorithm as follows (Ichihashi, 1991; Kosko, 1992):

$$a_{ji}(t+1) = a_{ji}(t) - \frac{\alpha\partial E}{\partial a_{ji}(t)}$$
$$= a_{ji}(t) - \alpha\left(\frac{\partial E}{\partial y}\right)\left(\frac{\partial y}{\partial h_i}\right)\left(\frac{\partial h_i}{\partial A_{ji}}\right)\left(\frac{\partial A_{ji}}{\partial a_{ji}(t)}\right)$$
$$= a_{ji}(t)$$
$$+ \frac{2\alpha(y^* - y)(y_i - y)h_i(x_j - a_{ji})}{b_{ji}\sum_{i=1}^{m}h_i} \tag{28}$$

$$b_{ji}(t+1) = b_{ji}(t) - \frac{\beta\partial E}{\partial b_{ji}(t)}$$
$$= b_{ji}(t) - \beta\left(\frac{\partial E}{\partial y}\right)\left(\frac{\partial y}{\partial h_i}\right)\left(\frac{\partial h_i}{\partial A_{ji}}\right)\left(\frac{\partial A_{ji}}{\partial b_{ji}(t)}\right)$$
$$= b_{ji}(t) + \frac{\beta(y^* - y)(y_i - y)h_i(x_j - a_{ji})^2}{b_{ji}^2\sum_{i=1}^{m}h_i} \tag{29}$$

$$y_i(t+1) = y_i(t) - \frac{\gamma\partial E}{\partial y_i(t)}$$
$$= y_i(t) - \gamma\left(\frac{\partial E}{\partial y}\right)\left(\frac{\partial y}{\partial y_i(t)}\right)$$
$$= y_i(t) + \frac{\gamma(y^* - y)h_i}{\sum_{i=1}^{m}h_i} \tag{30}$$

where a, β and γ: are the learning rates that are the constants in the learning process, and t: means the learning iteration. Consequently, the process of training and application of AN-IT2FLC is as follows in Figure 5.

According to this figure, when the controller training performed by above-mentioned algorithm in Matlab program (Figure 5a), it can be used for response reduction of structure in any earthquake record as in Figure 5b. The reference values shown in Figure 5b are the top story displacement and velocity of the building with zero quantities.

5. Result and Discussion

In the first part of results interpretation,

accuracy of AN-IT2FLC design will be evaluated. This verification done through comparing the maximum controlled response of stories in the case of using proposed controller with similar values of

uncontrolled, controlled responses with TMD, and controlled responses with ATMD through IT2FLC under the eight mentioned earthquake records. These result, are shown in Figure 6.
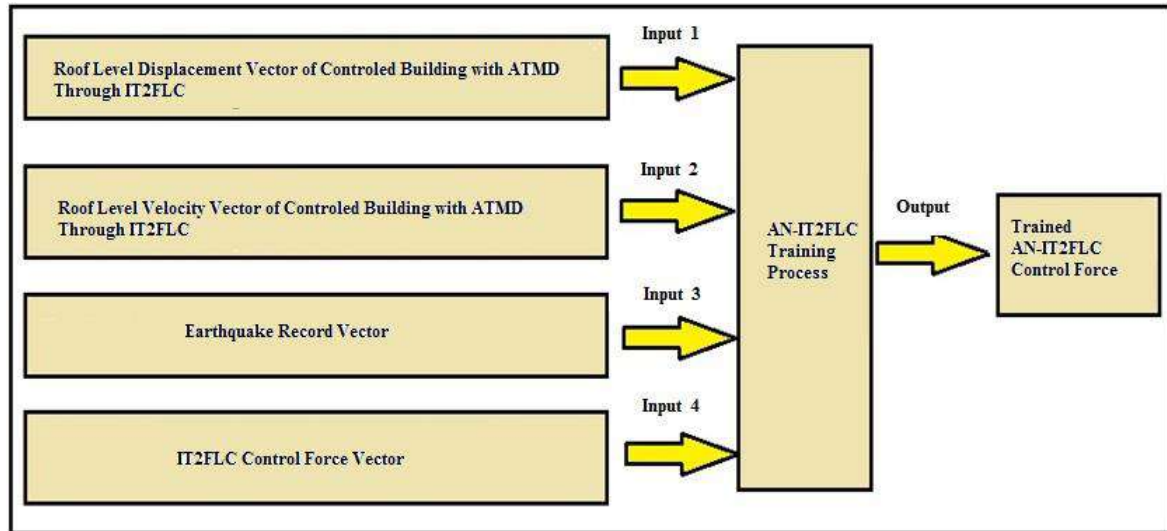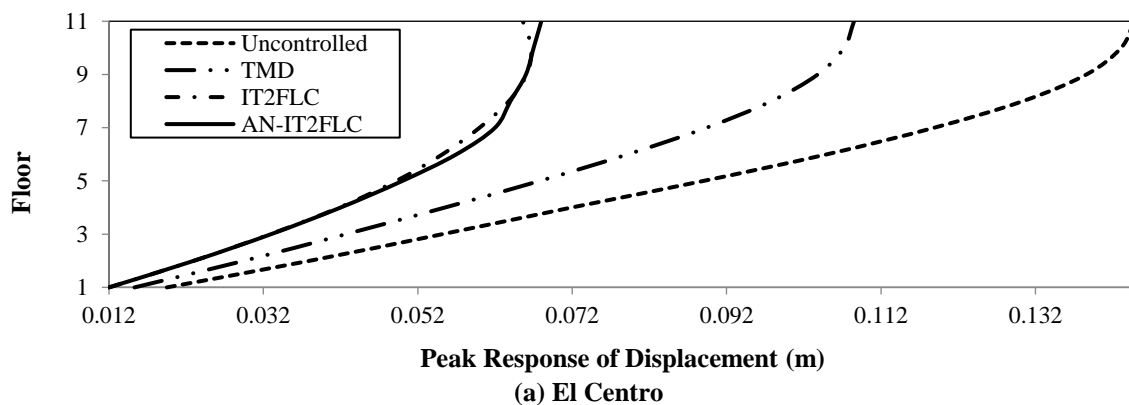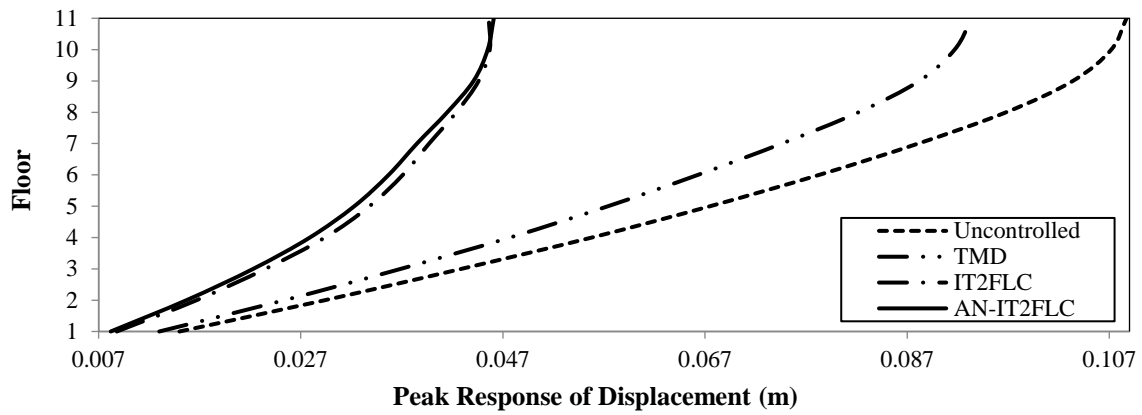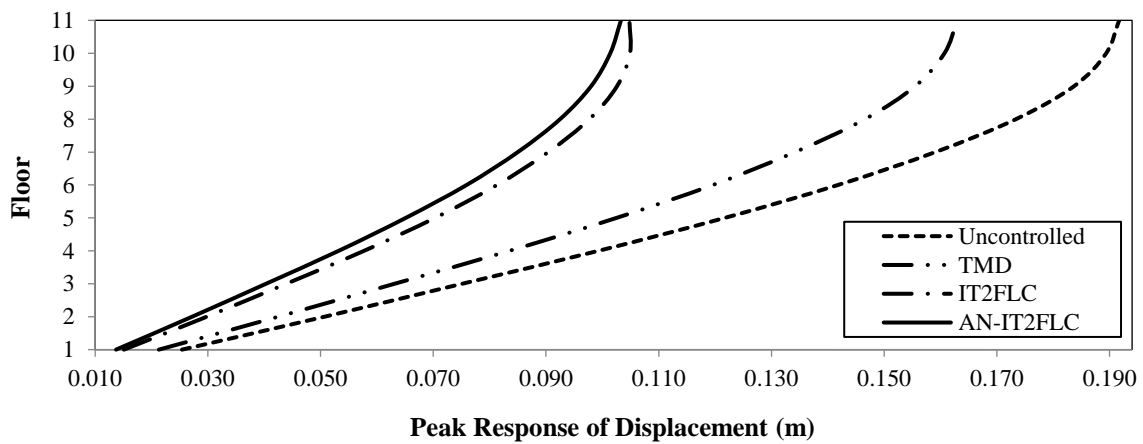

(a) Training
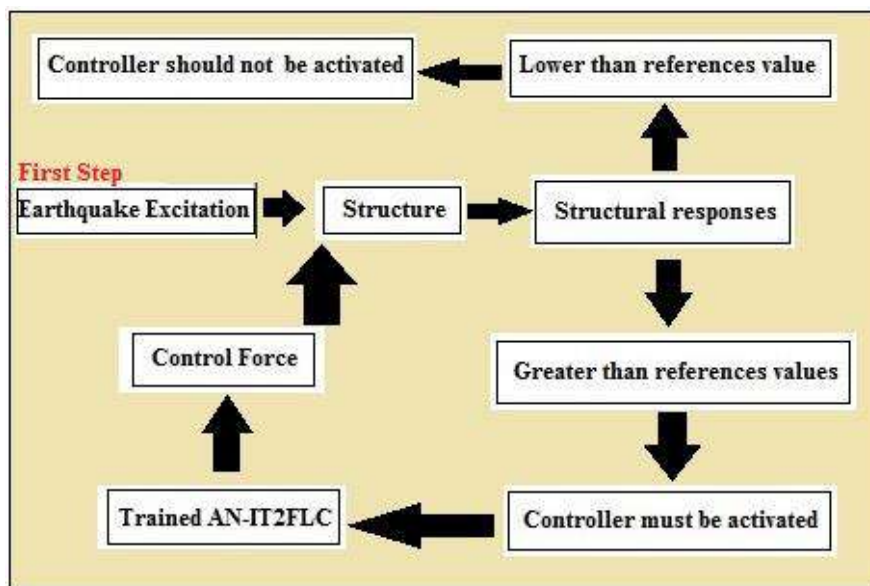
(b) Application
Fig. 5. Flowchart of AN-IT2FLC

Peak Response of Displacement (m)
(a) El Centro

(b) Hachinohe

(C) Kobe

(d) Northridge

(e) MorganHill

(f) Erizkan

(g) Loma Prieta

(h) Tabas
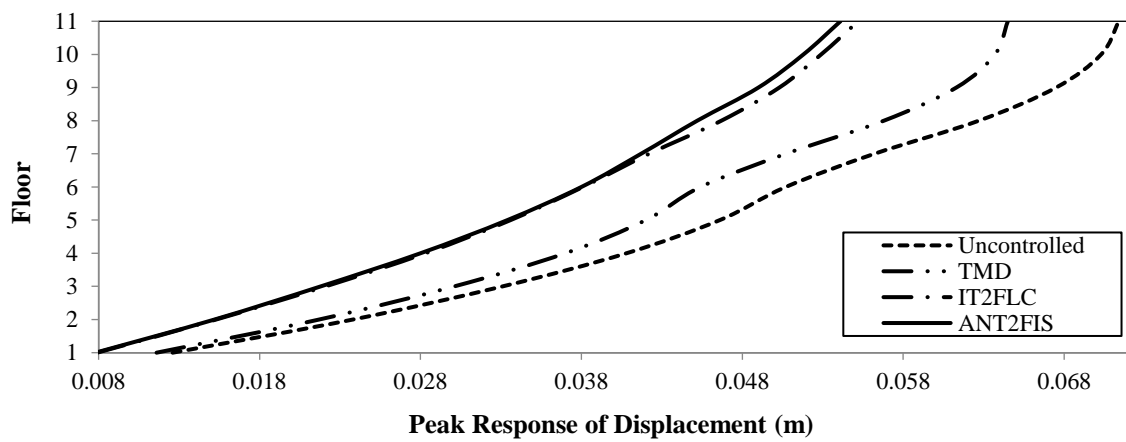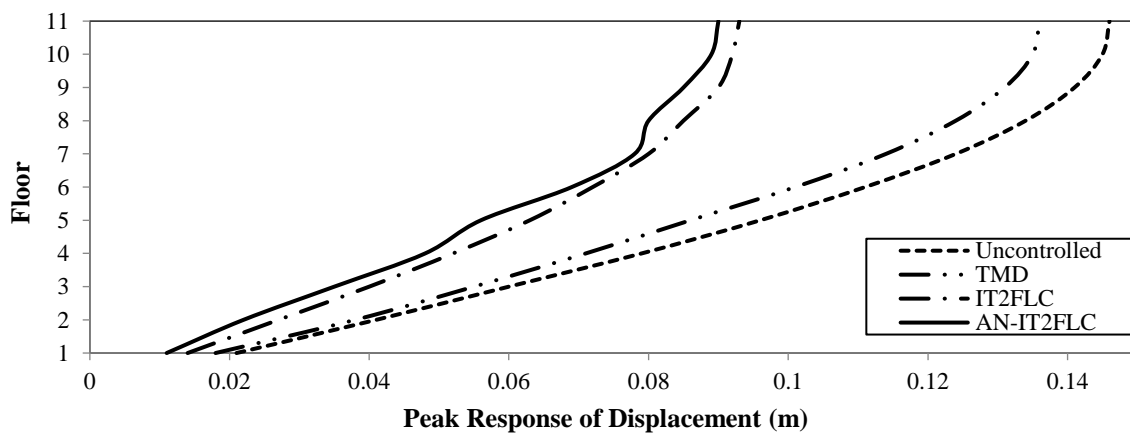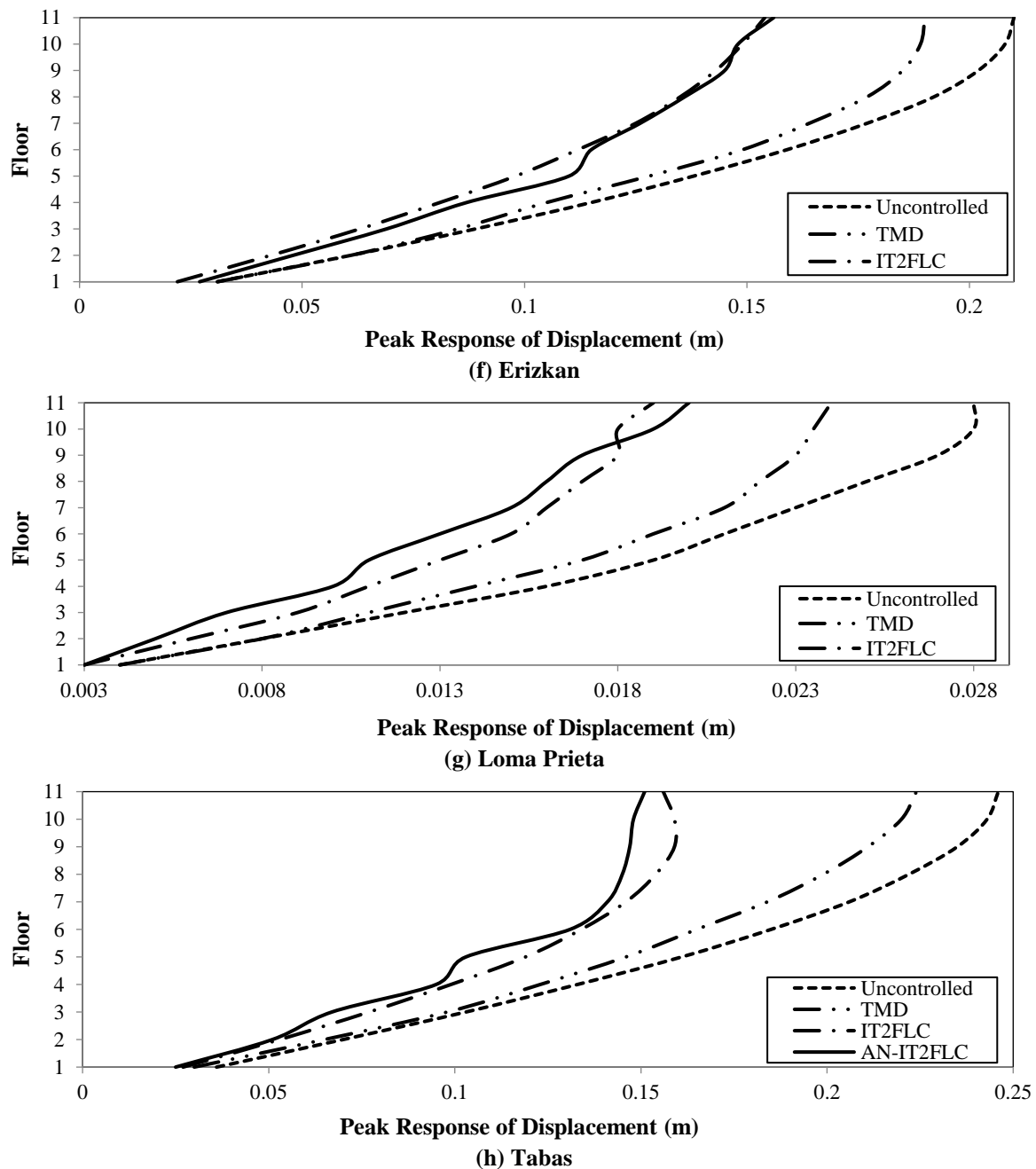
Fig. 6. Maximum displacement response of stories in different control cases for eight various ground accelerations

The results of peak response of displacement controlled with TMD are also presented for comparison. So the optimum parameters of TMD (damping ratio and tuning frequency ratio) are derived using Shuffled Complex Evolution (SCE) algorithm (Meshkat Razavi and Shariatmadar, 2015) in this study.

In the following, the steps for obtaining the optimum TMD parameters for the 11-storey shear building are described:

TMD is firstly designed to control the first modal displacement response of the mentioned building. Given the properties of the first mode that need to be controlled (Table 3) (Golnargesi et al., 2014), the TMD is designed in the same procedure as designing a TMD for a SDOF structure.

The mass ratio is defined as the damper mass to the first-mode modal mass as:

$$\mu = \frac{62.19 \times 10^3}{1057 \times 10^3} = 0.06$$

Table 3. Properties of the first mode of the 11-Story building (Golnargesi et al., 2014)

	Mass (Kg)	Damping ratio (%)
SDOF system	1057×10^3	5
Mass damper	62.19×10^3	7

Having known mass ratio (μ) and damping ratio (ξ) values, the optimum TMD parameters are obtained as (Meshkat Razavi and Shariatmadar, 2015):

$$\xi_{d_{opt}} = 0.1738 \text{ and } f_{OPT} = 0.9005$$

Now, the first-mode displacement response of 11-story building can be controlled by the TMD. This completes the design procedure.

According to Figure 6 results show that the response reduction of AN-IT2FLC is more or the same as the IT2FLC in the eight earthquakes. Therefore, it can be concluded that the design of AN-IT2FLC is convenient.

The IT2FLC which is used in the previous part is designed based on two input variables each one having three upper and three lower Membership Functions (MFs) and one output variable. The main purpose of using two input variables for the IT2FLC is to show the efficiency of the fuzzy approach in the control problem. These input variables help in generating the inference rule base.

In this study, the inference rules have been developed by expert's knowledge and are shown in Table 4 and also the used specifications of IT2FLC have been given in Table 5.

The upper and lower MFs are triangular shaped and have been defined on the common interval [-1,1]. These MFs are shown in the Figure 7 of the manuscript as follows (Golnargesi et al., 2014):

Table 4. Inference rules for the IT2FLC (Golnargesi et al., 2014)

Displacement	Velocity		
	N	Z	P
N	PB	PM	PS
Z	PS	Z	NS
P	NS	NM	NB

Table 5. Specifications of IT2FLC (Golnargesi et al., 2014)

Aggregation	Maximum
Fuzzy Inference	Mamdani type
Type reducer	COS
Defuzzification	Center average
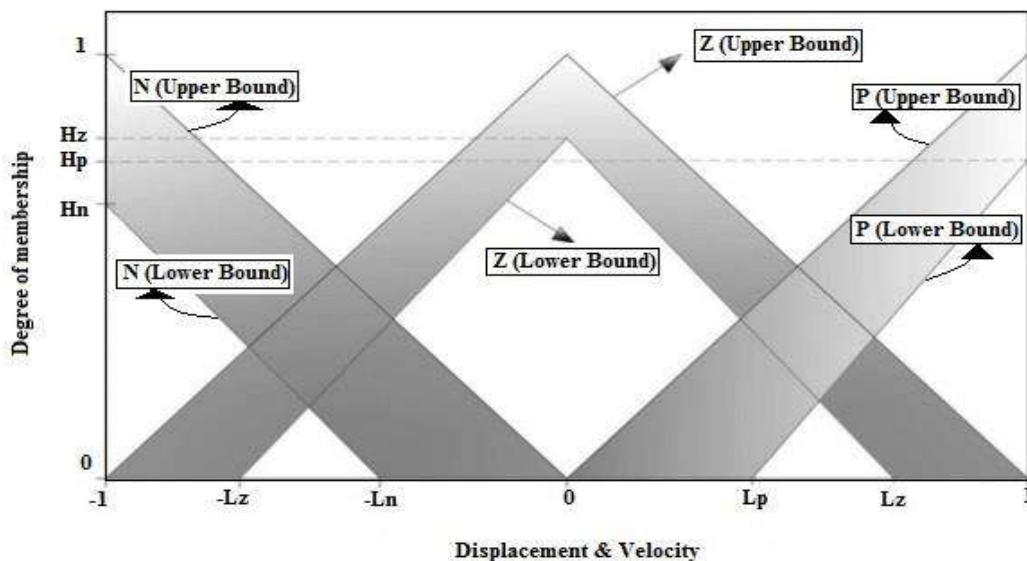
Fig. 7. Membership function of input parameters of IT2FLC (Golnargesi et al., 2014)

According to this figure, H_i and L_i ($i=z, n, p$) are the lower MF parameters. The peak responses of stories controlled with IT2FLC obtained based on adjusting of IT2FLC input parameters. In the other hand, to achieve the maximum response reduction of IT2FLC, the mentioned process must be done in any earthquake records. (Golnargesi et al., 2014).

This is one of the main deficiencies of IT2FLC, which it needs to adjust in any new ground acceleration. To increase the performance of IT2FLC in any new earthquake records, a numerical averaging method is used and general optimum parameters of IT2FLC, obtained based on the eight mentioned ground accelerations of the first part (Table 7).

Although the response reduction of IT2FLC with general parameters (General IT2FLC) is, less than that of the IT2FLC results of the first part, but is more practical in response reduction of structure for the new earthquakes.

So in the second part, in order to evaluate the efficiency of AN-IT2FLC, four other ground accelerations (Figure 8), including two far-field earthquakes (Kern-county and Chi-Chi) and two near-field earthquakes (Coalinga and Coyote-lake) are used and results are compared for different control states including uncontrolled and controlled by IT2FLC with general optimum parameters (Figure 9).

From the results, it can be concluded that ATMD with AN-IT2FLC reduces the peak displacement of building stories more than that of the ATMD through general IT2FLC for the Chi-Chi, Kern-county, Coyote-lake and Coalinga earthquakes. The corresponding response reduction at the roof level is about 18%, 16%, 9% and 7% for the mentioned earthquake records, respectively. In other words, comparing the response reduction of peak displacement of two types of controllers (AN-IT2FLC and general IT2FLC) revealed that the performance of the proposed controller is better than that of the IT2FLC.

Table 6. Adjusted parameters of IT2FLC for eight training earthquakes

Earthquake	IT2FLC input parameters					
	H_z	H_p	H_n	L_z	L_p	L_n
Displacement						
El Centro	0.3	1	1	1	1	1
Hachinohe	0.3	1	1	0.3	1	1
Kobe	0.3	0.8	1	0.3	1	1
Northridge	1	1	0.3	1	1	1
Loma Perieta	1	0.3	1	1	1	1
Tabas	1	0.3	0.3	1	1	1
Erizkan	0.3	1	1	0.3	1	1
Morgan Hill	1	1	1	0.3	1	1
Velocity						
El Centro	1	0.4	1	1	0.4	1
Hachinohe	1	0.4	0.4	1	0.4	0.4
Kobe	1	1	1	1	1	1
Northridge	1	0.3	0.3	1	1	1
Loma Perieta	1	1	1	1	1	1
Tabas	1	0.3	1	1	1	1
Erizkan	0.3	1	1	0.3	1	1
Morgan Hill	1	1	1	0.3	1	1

Table 7. General optimum parameters of IT2FLC

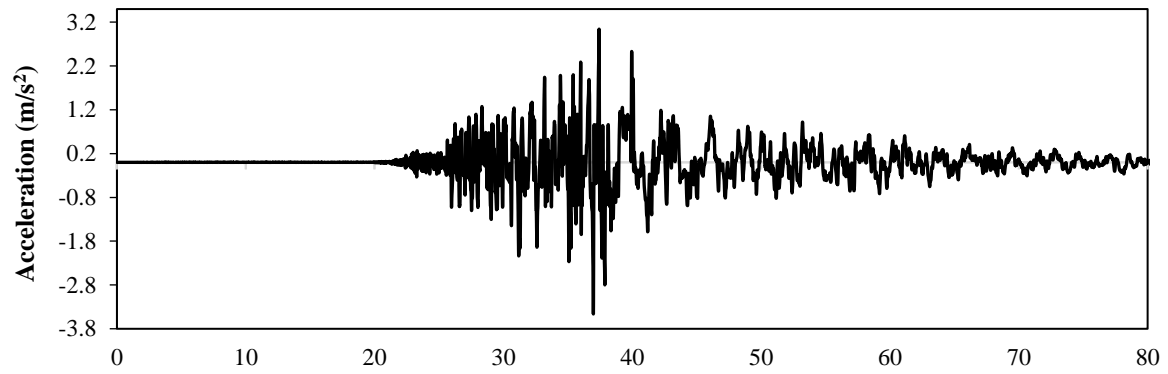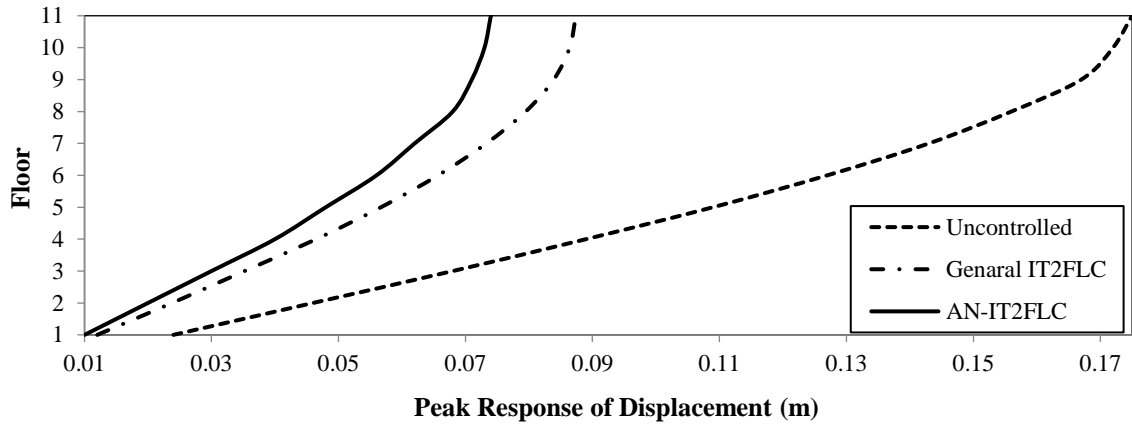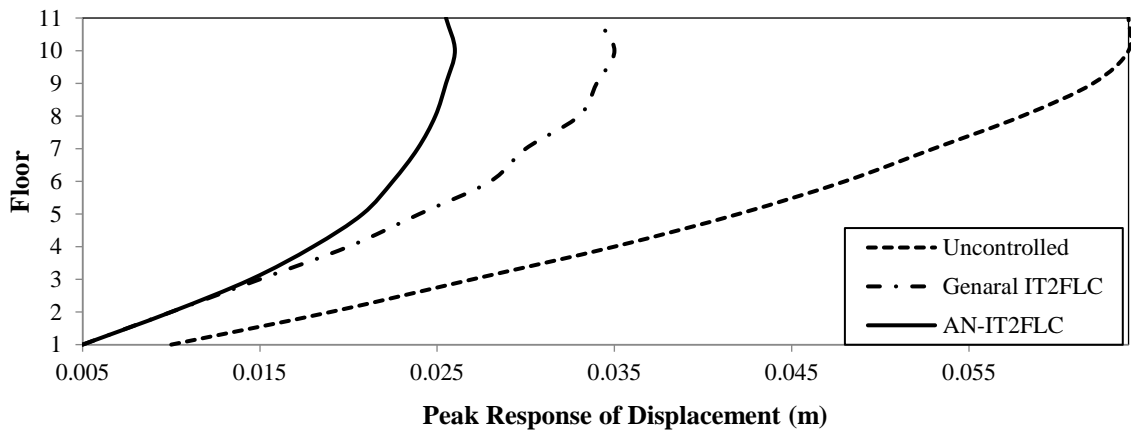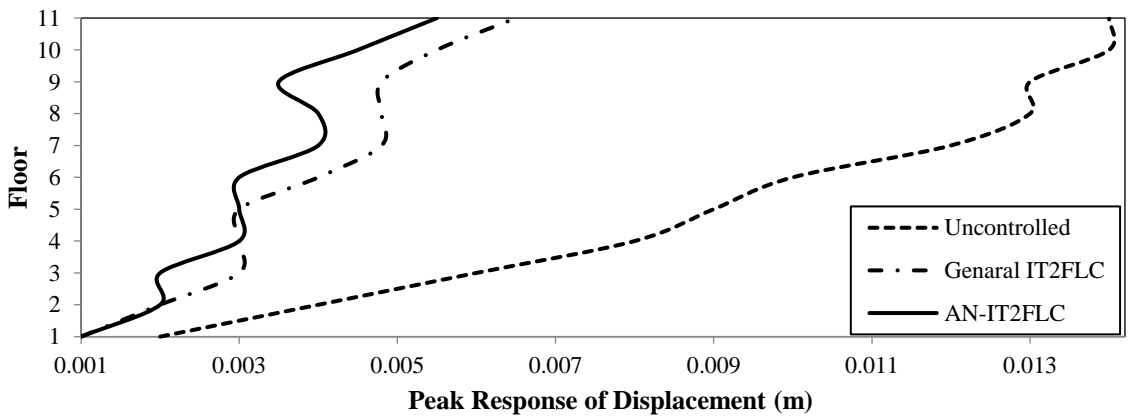| General parameters of IT2FLC					
H_z	H_p	H_n	L_z	L_p	L_n
Displacement					
0.65	0.8	0.85	0.65	1	1
Velocity					
0.9	0.65	0.85	0.85	0.85	0.95
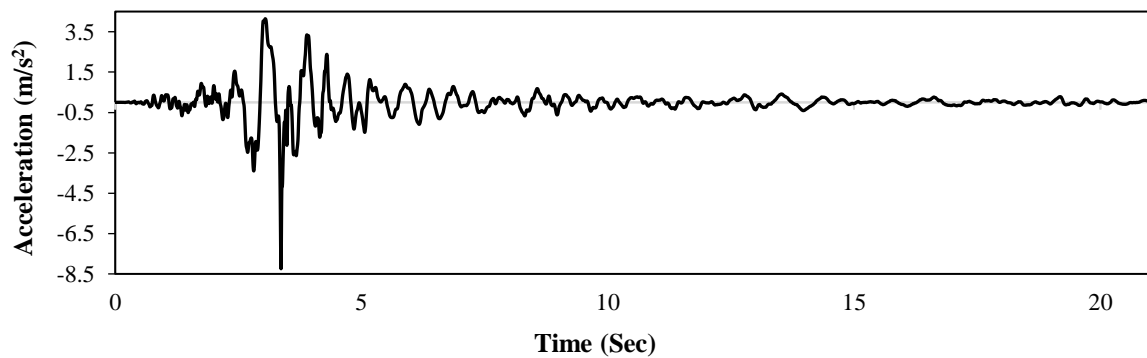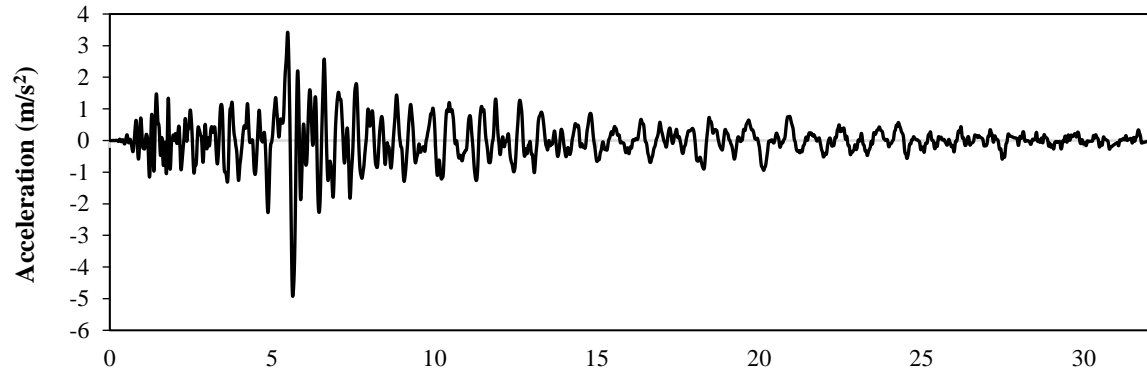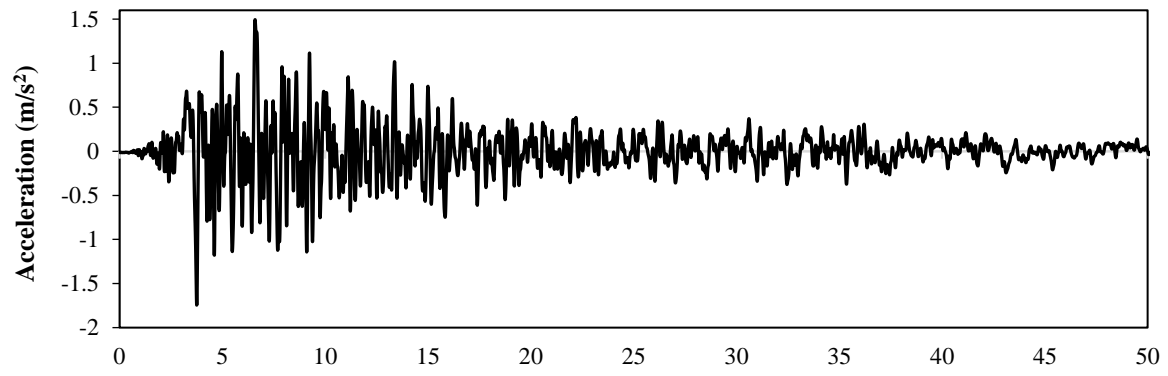
Fig. 8. Near-field and far-field ground acceleration records used in this study to investigate the efficiency of AN-IT2FLC
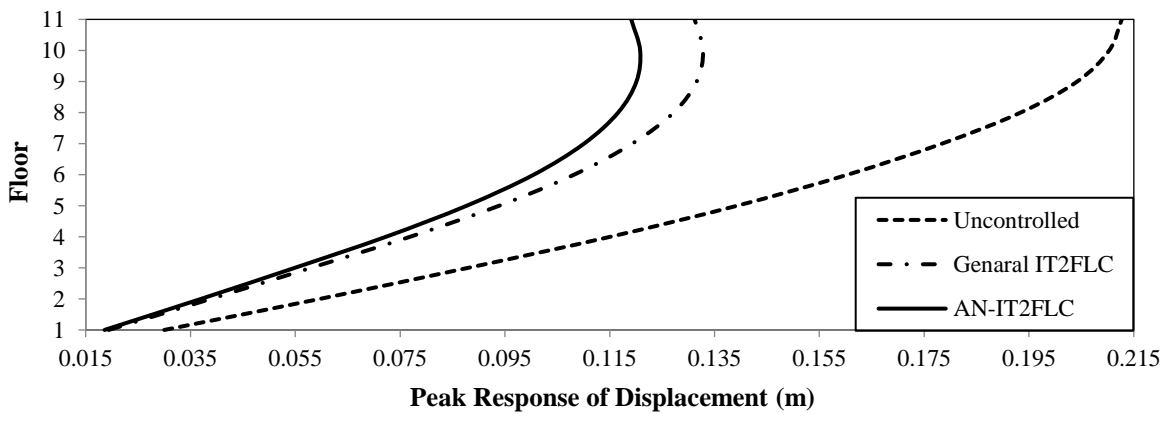
(a) Chi-Chi

(b) Kern-county

(C) Coyote-lake

(d) Coalinga

Fig. 9. Peak displacement response of stories for various control systems and different earthquakes

In fact, one of the main reasons for the superiority of the proposed controller is its compatibility in different seismic conditions. In the other words, the AN-IT2FLC, only once trained for a number of optional earthquakes and then the proposed controller with adjusted parameters can be used to mitigate the structural response in any desired ground accelerations with a much higher speed and more response reduction than those obtained by IT2FLC.

The displacement time response of top floor is also calculated and compared in two modes of controlled with ATMD through general IT2FLC and AN-IT2FLC and different ground accelerations (Figure 10).

By comparing the results of time responses of building' top floor in the case of using two types of controllers, it is concluded that the controlled responses obtained with ATMD through AN-IT2FLC is less than that of the General IT2FLC. The response reduction is more for far field ground accelerations (Chi-Chi and Kern-county records).

Another and more precise criteria for assessing and comparing the performance of both ATMD controllers (AN-IT2FLC and general IT2FLC) in term of time response reduction, is the controlled Integral Square Error (ISE) displacement of top floor (Figure 11).

Comparing the values of controlled displacement ISE of two controllers, revealed that the obtained response reduction of the proposed controller is more than that of the IT2FLC in mentioned earthquake records.

Although a visual comparison of responses in Figures 10 and 11 indicates the superiority of the proposed controller in the time history and ISE displacement responses of top floor, however for a quantitative review, a comparison between the mentioned responses has been done in Tables 8 and 9 in the term of maximum responses of time history and the average ISE response reduction, respectively.

Table 8. Peak response of top floor displacement (m)

General IT2FLC	AN-IT2FLC	General IT2FLC	AN-IT2FLC
Chi-Chi		Kern-county	
0.087	0.071	0.034	0.028
Coyote-lake		Coalinga	
0.0028	0.0025	0.106	0.098

Table 9. Average ISE response reduction of AN-IT2FLC to general IT2FLC at the top floor (%)

Chi-Chi	Coyote-lake	Coalinga	Kern-county
22	11	10	13

(a) Chi-Chi

(b) Kern-county

(C) Coyote-lake
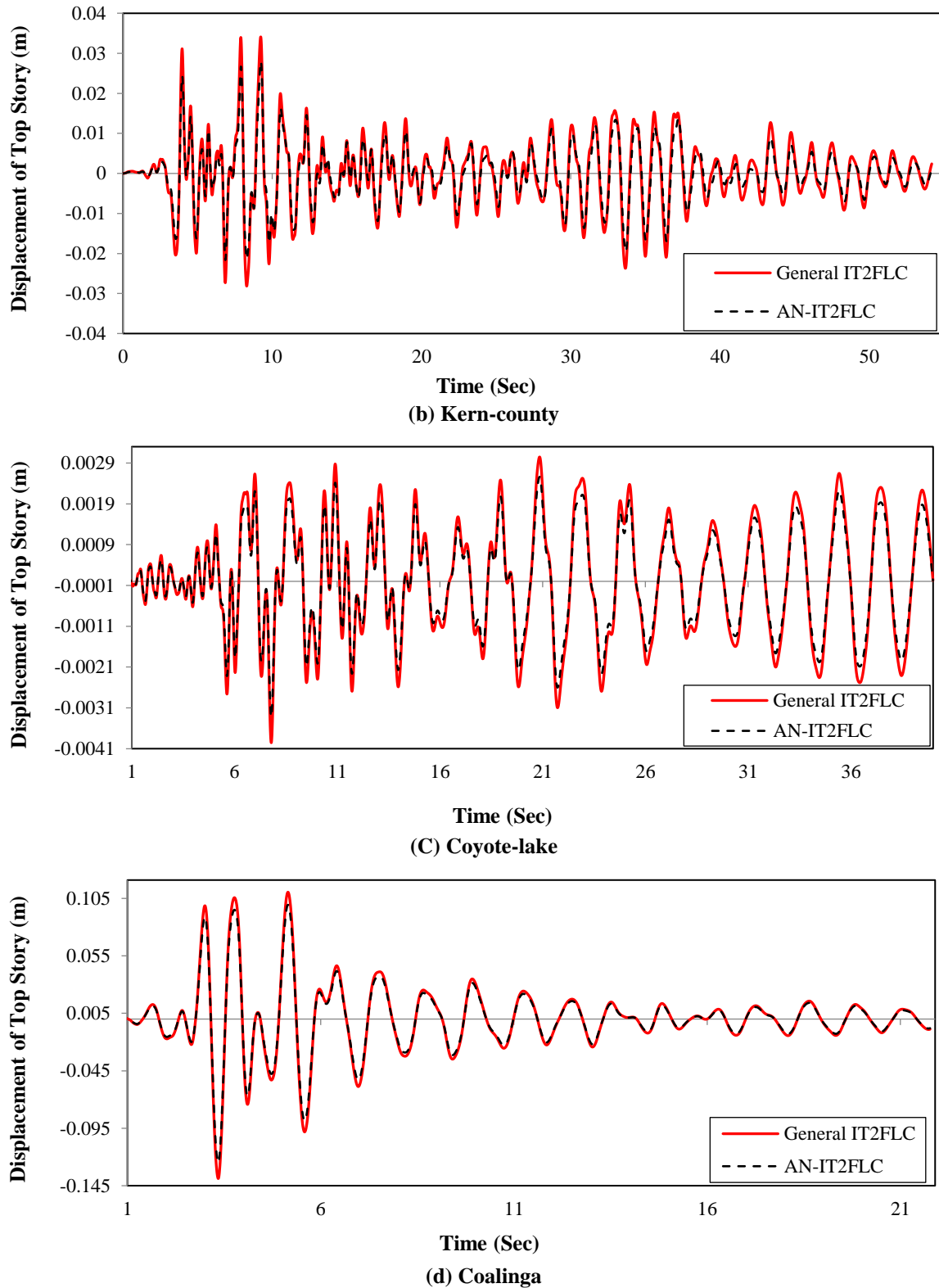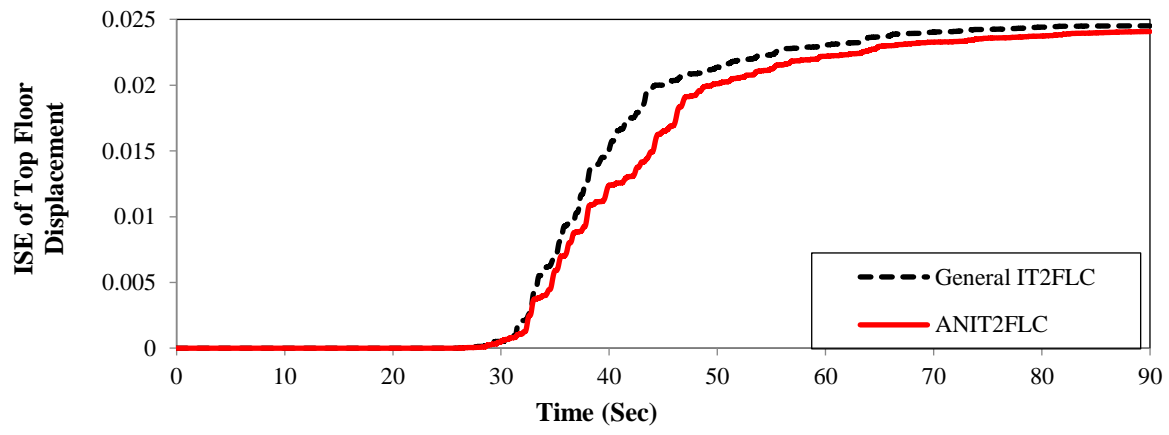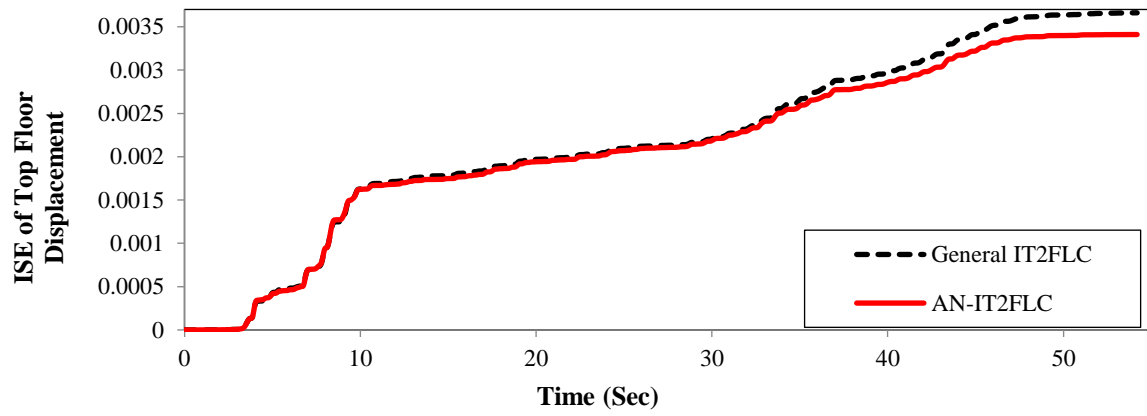

(d) Coalinga
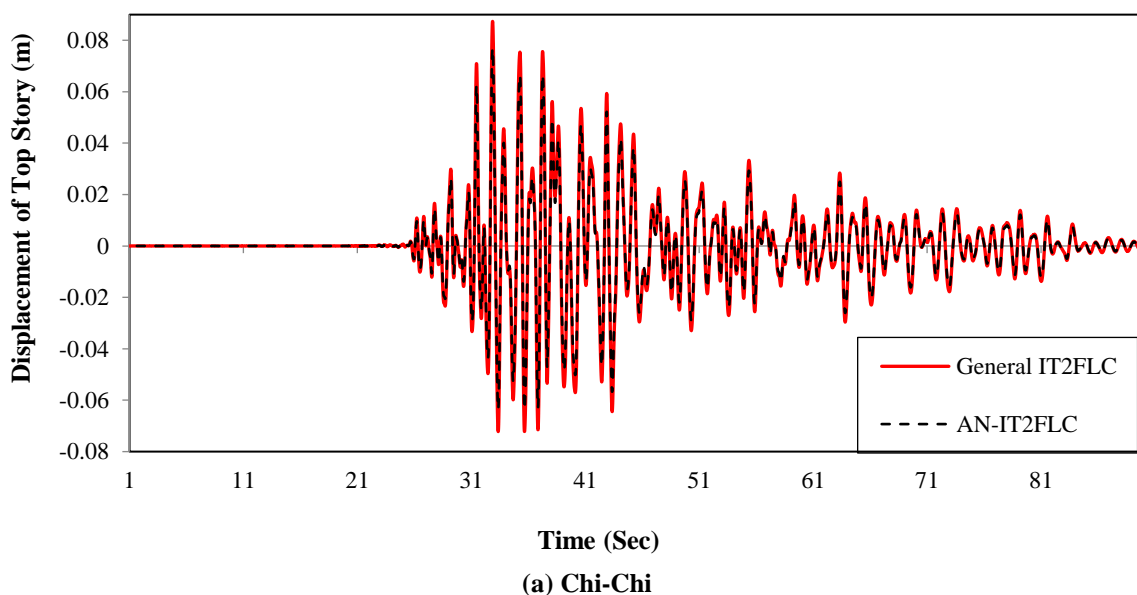
Fig. 10. Comparison of controlled time history response of roof level with ATMD through IT2FLC and AN-IT2FLC for different earthquake

It is seen from the first table that AN-IT2FLC reduces the peak response of top floor more than that of the general IT2FLC and are about 18%, 16%, 9% and 7% for t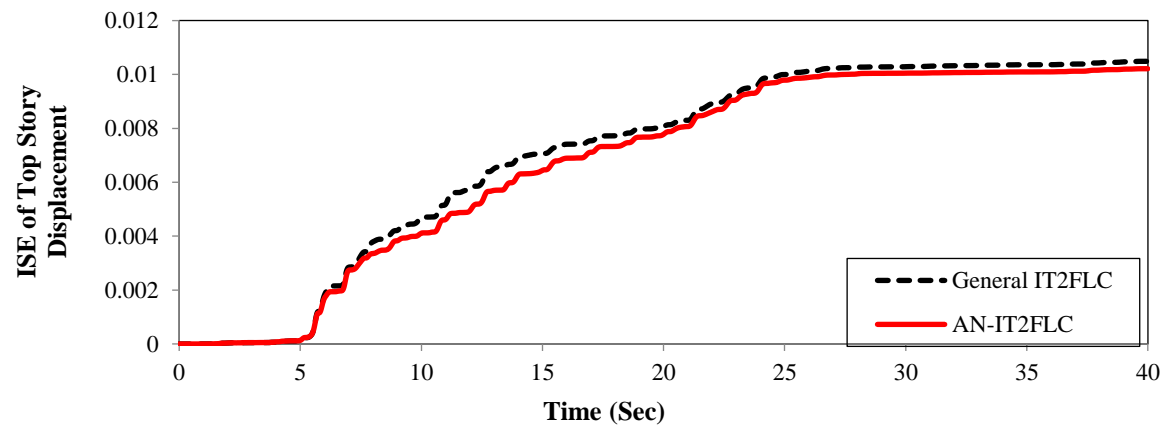he Chi-Chi, Kern-county, Coyote-lake and Coalinga earthquakes. From the results, it can be seen that the most and the least response reductions belong to the Chi-Chi and Coalinga ground accelerations, respectively.
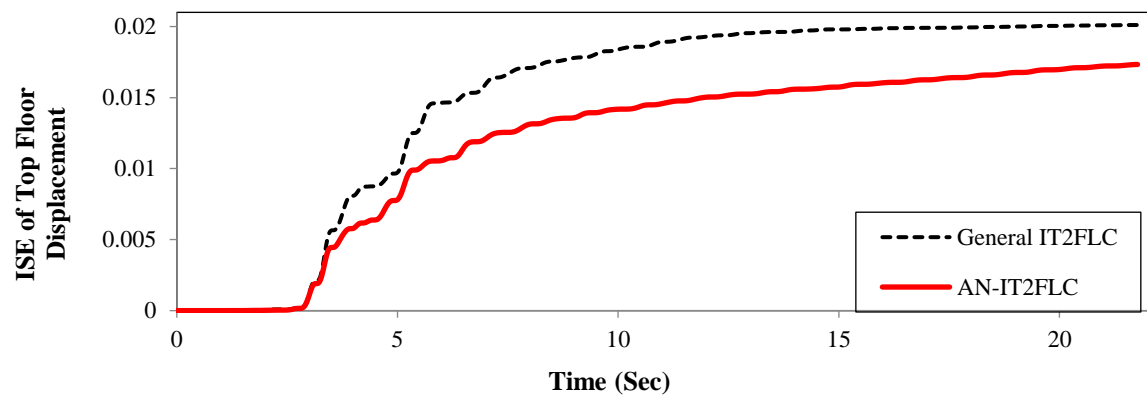
Fig. 11. Comparison of controlled ISE of roof level with ATMD using AN-IT2FLC and IT2FLC for different earthquake

Another criterion for comparison of controlled time history responses is the ISE displacement of the top floor. For a quantitative interpretation of the results which are presented in Figure 11, the percentage of the average ISE response reduction of AN-IT2FLC to general IT2FLC are also calculated and is provided in the last table.

According to Table 9 it can be seen that the most and the least percentage of average response reduction of ISE are 22% and 10% for the Chi-Chi and Coalinga ground earthquakes, respectively. In the last part of results, the corresponding values of maximum control forces are shown in Table 10.

Table 10. Comparison of maximum control force of AN-IT2FLC and General IT2FLC for different earthquakes

Earthquake	Maximum control force (kN)	
	General IT2FLC	AN-IT2FLC
Chi-Chi	390	483
Kern-county	610	641
Coalinga	1120	1250
Coyote-lake	490	520

According to Table 10, it can be realized that the peak value of active control force in AN-IT2FLC is little more than the general IT2FLC in most earthquake records. Furthermore, from the results it can be understood that the highest values of control force in both controllers belongs to Coalinga earthquake record compared to other ground accelerations. This is due to the pulse-like feature of Coalinga record, which the most active actuator mechanism occurs under the influence of this earthquake.

6. Conclusions

This research is one of the first studies conducted on the use of AN-IT2FLC in an ATMD. One of the main disadvantages of the IT2FLC is its dependence on adjust and optimize parameters in each earthquake record, in order to achieve the maximum response reduction. However, this defect

has been addressed in the proposed controller using the neural network training process. In this study, an 11-story shear building with an ATMD on its roof level was used to evaluate the performance of AN-IT2FLC. The proposed controller was initially trained using eight earthquakes with various seismic specifications. Then, the controller efficiency was evaluated using two far-field earthquakes (Chi-Chi and Kern-county) and two near-field earthquakes (Coalinga and Coyote-lake). Various results of this analysis were obtained, which are summarized as following:

- AN-IT2FLC does not need to adjust and optimize the fuzzy MFs parameters, in each earthquake records. In other words, the controller parameters trained only once for a given number of arbitrary earthquakes and the most structural response reduction obtained with much higher speed and accuracy rather than other earthquakes.
- By comparing the maximum response of the stories, it concluded that the proposed controller has a greater response reduction, rather than General IT2FLC. The most response reduction of AN-IT2FLC rather than General IT2FLC occurred in the Chichi earthquake and was about 18%.
- Evaluating the ISE responses indicates that ATMD with AN-IT2FLC reduces the time response of top floor more than that of ATMD through general IT2FLC in most earthquakes.
- Comparison of maximum control force in two types of controllers (AN-IT2FLC and general IT2FLC) indicates that the proposed controller has a little more values, compared to the general IT2FLC.

7. References

Anajafi, H. and Medina, R. (2017). "Comparison of the seismic performance of a partial mass isolation technique with conventional TMD and base-isolation systems under broad-band and narrow-band excitation", *Engineering*

Structures, 158(3),110-123.

Bargi, K., Kave, A., Lucas, C. and Rahami, H. (2012). "Generation of artificial earthquake accelerograms using wavelet and neural networks", *Sharif Journal of Civil Engineering*, 2-28(3), 79-88.

Bakhshinezhad, S. and Mohebbi, M., (2019). "Multiple failure criteria-based fragility curves for structures equipped with Satmds", *Earthquake and Structure*, 17(5), 463-475.

Bathaei, A. Ramezani, M. and Ghorbani, A., (2017). "Type-1 and Type-2 fuzzy logic control algorithms for semi-active seismic vibration control of the College Urban Bridge using MR dampers", *Civil Engineering Infrastructures Journal*, 50(2), 331-351.

Boccamazzo, A., Carboni, B. and Quaranta, G. (2020). "Seismic effectiveness of hysteretic tuned mass dampers for inelastic structures", *Engineering Structures*, 216, 110591.

Chang, J.C.H. and Soong, T.T. (1980). "Structural control using active tuned mass dampers", *Engineering Mechanics Division*, 106(6), 1091-1098.

Collins, R. and Basu, B. (2006). "Control strategy using bang-bang and minimax principle for FRF with ATMDs", *Engineering Structures*, 28(3), 349-356.

Chen, T., Bird, A., Muḥammad, J.M., Cao, S.B., Melvilled, C. and Cheng, C.Y.J., (2019). "Prediction and control of buildings with sensor actuators of fuzzy EB algorithm", *Earthquakes and Structures*, 17(3), 307-315.

Chopra, A.K., (2001). *Dynamics of structures-theory and applications to earthquake engineering*, 2nd Edition, Prentice-Hall, 472-496.

Farshidianfar, A. and Soheili, S. (2013). "Ant colony optimization of tuned mass dampers for earthquake oscillations of high rise structures including soil–structure interaction", *Soil Dynamic and Earthquake Engineering*, 51, 14-22.

Guclu, R. and Yazici, H. (2008). "Vibration control of a structure with ATMD against earthquake using fuzzy logic controllers", *Sound and Vibration*, 318(1-2), 36-49.

Golnargesi, S., Shariatmadar, H., Meshkat Razavi, H. (2018). "Seismic control of building with active tuned mass damper through interval type-2fuzzy logic controller including soil-structure interaction", *Asian Journal of Civil Engineering*, 19(2), 177-188.

Housner, G.W., Bergman, L.A., Caughey, T.K., Chassiakos, A.G., Claus, R.O., Masri, S.F., Skelton, R.E., Soong, T.T., Spencer Jr., B.F. and Yao, T.P. (1997). "Structural control: Past, present, and future", *Journal of Engineering and Mechanics*, ASCE, 123(9), 897-971.

Huang, H., Mosalam, K.M. and Chang, W.S. (2020). "Adaptive tuned mass damper with shape memory alloy for seismic application", *Engineering Structures*, 223, 111171.

Ichihashi, H. (1991). "Iterative fuzzy modeling and a hierarchical network", *Proceedings of the 4th IFSA Congress, Engineering*, Brussels, 49-52.

Jang, J.R. (1993), "Adaptive-network-based fuzzy inference system", *IEEE Transactions on Systems, Man, and Cybernetics*, 23(3), 665-685.

Jin, C., Chung, W.C., Kwon, D.S. and Kim, M.H. (2020). "Optimization of tuned mass damper for seismic control of submerged floating tunnel", *Engineering Structures*, 241, 112460.

Kobori, T., Koshika, N., Yamada, K. and Ikeda, Y. (1991). "Seismic response controlled structure with active mass driver system, Part 1: Design", *Earthquake Engineering and Structure Dynamics*, 20(2), 133-149.

Kosko, B. (1992). *Neural Networks and fuzzy systems*, Prentice Hall, Englewood Cliffs.

Liangkun, W., Weixing, S., Ying, Z. and Quanwu, Z., (2020). "Semi-active eddy current pendulum tuned mass damper with variable frequency and damping", *Smart Structures and Systems*, 25(1), 65-80.

Liangkun,W., Weixing, S. Ying, Z., (2019). "Study on self-adjustable variable pendulum tuned mass damper", *The Structural Design of Tall and Special Buildings*, 28(1), 1561.

Liangkun,W., Weixing, S. Xiaowei, L., Quanwu, Z., Ying, Z., (2019)."An adaptive-passive retuning device for a pendulum tuned mass damper considering mass uncertainty and optimum frequency", *Structural Control and Health Monitoring*, 26(7), e2377.

Liangkun,W., Nagarajaiah, S, Weixing, S, Ying, Z., (2020). "Study on adaptive-passive eddy current pendulum tuned mass damper for wind-induced vibration control", *The Structural Design of Tall and Special Buildings*, 29(15), e1793.

Love, J.S. and Haskett, C. (2019). "Measuring inherent structural damping of structure-TMD systems", *Engineering Structures*, 196(3), 109-300.

Lievens, K., Lombaert, G. and De Roeck, G. (2016). "Robust design of a TMD for the vibration serviceability of a footbridge", *Engineering Structures*, 123, 408-418.

Meshkat R.H. and Shariatmadar, H. (2015). "Optimum parameters for tuned mass damper using Shuffled Complex Evolution (SCE) algorithm", *Civil Engineering Infrastructures Journal*, 48(1), 83-100.

Miguel, L., Lopez, R. and Torii, A. (2016). "Robust design optimization of TMDs in vehicle–bridge coupled vibration problems", *Engineering Structures*, 126, 703-711.

Naderpour.H, Vosughifar,H. and Ghobakhloo, E. (2016). "Evaluation of effective parameters on wave diffraction of far-fault ground motions using artificial neural networks", *Sharif Journal*

of Civil Engineering, 32-2(1), 13-23.

Pourzeynali, S., Lavasani, H.H. and Modarayi, A.H. (2007). "Active control of high rise building structures using fuzzy logic and genetic algorithms", *Engineering Structure*, 29(3), 346-357.

Soong,T.T, Spencer, B.F. (2002). "Supplemental energy dissipation: state-of-the-art and state-of-the-practice", *Engineering Structure*, 24(3), 243-259.

Shariatmadar, H., Golnargesi, S. and Akbarzadeh Totonchi, M.R. (2014). "Vibration control of buildings using ATMD against earthquake excitations through Interval Type-2 Fuzzy Logic Controller", *Asian Journal of Civil Engineering*, 15(3), 321-338.

Spencer Jr, B.F. and Nagarajaiah, S. (2003)." State of the art of structural control", *Journal of Structural Engineering*, ASCE, 129, 845-856.

Wang, L., Nagarajaiah, S., Shi, W. and Zhou, W. (2021). "Semi-active control of walking-induced vibrations in bridges using adaptive tuned mass damper considering human-structure-interaction", *Engineering Structures*, 244, 112743.

Yager, R.R. and Filev, D.P. (1994). "Generation of fuzzy rules by mountain clustering", *International Journal of Intelligent and Fuzzy Systems*, 2(3), 209-219.

Yager, R.R. and Filev, D.P. (1994). *Essentials of fuzzy modeling and control*, John Wiley & Sons.

Zuo, H., Bi, K., Hao, H. and Ma, R. (2021). "Influences of ground motion parameters and structural damping on the optimum design of inerter-based tuned mass dampers", *Engineering Structures*, 227, 111422.

Assessment of Corrosion in Offshore R.C. Piers and Use of Microsilica to Reduce Corrosion Induced Oxidation (A Case Study of Wharves 11 and 12 in Imam Khomeini Port, Iran)

Tangtakabi, A.R.[1] , **Ramesht, M.H.[2]*** , **Golsoorat Pahlaviani, A.[2]** and **Pourrostam, T.[2]**

[1] Ph.D. Candidate, Department of Civil Engineering, Islamic Azad University, Central Tehran Branch, Tehran, Iran.
[2] Assistant Professor, Department of Civil Engineering, Islamic Azad University, Central Tehran Branch, Tehran, Iran.

ABSTRACT: Deterioration due to corrosion is an important issue affecting the durability, strength, and sustainability of buildings and structures. Many cities are located in coastal areas and many reinforced concrete structures in these areas are exposed to chloride aggressive marine environments. Therefore, it is important to provide protection and offer appropriate repair methods of buildings vulnerable to the degrading effects of corrosion. The present study sets out to identify and evaluate the causes and extent of corrosion observed in Piers 11 and 12 in Imam Khomeini port, Iran. The microsilica is used to reduce corrosion. In order to achieve the above-mentioned goals, a number of experimental field tests were performed to determine the level of concrete condition in terms of reinforcement corrosion. Some tests were conducted to determine the conditions of concrete piers in terms of reinforcement corrosion. Then a reinforcement corrosion current density test is performed using a potentiostat involving a placement process; with different water-to-cement ratios and superplasticizers, the microsilica content was 5%, 10%, and 15%. Microsilica can serve as an alternative to cement and was measured according to the ASTM standards. Microsilica was exposed to aggressive conditions at different periods and a concrete compressive strength test was performed. The results showed that the compressive strength and corrosion resistance of the concrete increased for concrete mixture containing 10% microsilica with a water-to-cement ratio of 34% and a superplasticizer ratio of 6%.

1. Introduction

Concrete is one of the common engineering materials that have frequently been used over the last 100 years (Abedini and Zhang, 2021; Zhang et al., 2020). Experts have always considered this material to construct various structures such as buildings, piers, ports, tanks, bridges, and other various structures. Even today concrete is used on a

---

* Corresponding author E-mail: Mhramesht@yahoo.com

wide scale in modern societies, and will most probably be employed in future. The reason is that it shows excellent mechanical performance, has high durability, and is characterized by its low cost and energy consumption (He et al., 2020; Antunes et al., 2021). One of the most common causes of destruction in reinforced concrete structures is the deterioration of offshore concrete ones due to reinforcement corrosion under the influence of chloride ions.

In recent years, extensive researches have been conducted in this field, and corrosion has been dealt with as the most important phenomenon in discussions about the damage threatening concrete structures in an offshore environment. Of course, the existence of unfavorable conditions in these areas reveals the need for repairing the structure and determining their service life. From the point of view of armature corrosion in concrete structures, the conditions determining offshore structures on the margin of the Persian Gulf have turned this area into one of the most aggressive ones in terms of both solutes in seawater and their climatic conditions. So far, the concrete structures in the Persian Gulf have inflicted severe damage and high repair costs on the countries in the regions. This situation has come about through the corrosion of buried reinforcement, which is regarded as a serious economic problem. As a result, increasing attention has been paid to identifying the causes of reinforcement corrosion, preventing it, and tracing factors contributing to the highest strength and durability of concrete structures (Liu et al., 2021).

Parrott (1994) examined carbonation-induced corrosion and introduced the "un-neutralized remainder" measure, which is the difference between the concrete cover and the depth of carbonation. Corrosion was found to increase when the un-neutralized remainder approaches zero and becomes negative. However, corrosion halts, as this value approaches less than -10 mm. Roy et al. (1999) examined the reasons for

corrosion as a product of humidity level. This process can be complex since maximum carbonation is obtained at 75% and 92% humidity. Besides, pore size is an important factor, with larger pores facilitating higher penetration and hence more corrosion. Furthermore, the rate of carbonation was shown to be directly proportional to the strength of concrete.

It is important to mention that the exposure of reinforced concrete structures to chemical and electrochemical damage is attributable to the phenomena of chloride infiltration (Zhang and Abedini, 2021) which is the most important cause of corrosion in this area. The useful life of the offshore concrete structures is significantly reduced due to reinforcement corrosion and concrete cracking. This type of damage is to be seen more in the tidal zone because the intensified penetration of chloride into the concrete in it is due to wetting and drying, and as a result, increases the corrosion current density (Liu et al., 2021). Moreover, concrete repair is one of the important aspects of the maintenance of concrete structures. On the other hand, the maintenance of concrete piers is considered to be one of the most important causes of the life span of concrete structures in the world, to which is allocated large sums of money every year.

Increasing the durability and the life span of these repairs provides an index of the selection of materials. Given that selecting suitable materials for repair has received attention in most parts of the world and, as a result, significant progress has been made in this field. However, this industry still suffers from shortcomings as far as concrete repairs are concerned. In this connection, recent studies of repairs to piers, bridge decks, and other structures have shown that the failure of a repair operation is due to various factors, including an improper selection of repair materials, low execution skills, and insufficient properties of primary concrete. This means that a good repair improves the performance of offshore structures or buildings. By contrast, poor

repair disables structure performance in a relatively short time. The reason is that the suitable choice of repair materials depends on their properties and the behavior of composite parts.

The performance of cement paste has already been investigated by adding microsilica (7% and 10% as cement substitute) to ordinary Portland cement Type 2 under wetting and drying conditions. The results show the excellent performance and higher strength of concrete containing microsilica, as against ordinary concrete, which does not use it. In addition, the results showed that capillary water uptake increased in those parts which were exposed to the tidal zone through using a larger amount of microsilica in the mixtures (Ganjian and Pouya, 2009). Bagheri et al. (2013) conducted a number of experiments and observed that concrete electrical resistivity could increase five times by replacing 12% microsilica with cement.

Pandey and Kumar (2019) performed an evaluation on the water absorption and chloride ion penetration of rice straw ash and microsilica admixed pavement quality concrete. They derived two equations for both initial and secondary rate of water absorption. Moffatt and Thomas (2018) showed that, given the same duration and conditions, the performance of concrete which contained fly ash and microsilica exposed to an offshore environment could

decrease the depth of chloride penetration from 90 to 40 mm, as against all the control samples which had no fly ash or microsilica in them. Also, the results of permeability test indicate a significant increase resistance against chloride ion penetration for concrete containing fly ash and microsilica. In addition, the results of the test indicate a significant increase in resistance to chloride ion penetration in the case of concrete containing fly ash and microsilica. Siddique (2011) pointed out that the use of microsilica in concrete eliminates weak interfacial areas by strengthening the bond between cement paste and aggregates, and by forming structures with less porosity and more homogeneity. This has the effect of increasing the compressive strength of concrete. Based on what discussed above, one of the main objectives of this study is to assess the amount of corrosion seen in concrete piers mentioned above and determine the role of microsilica in increasing their compressive strength and reducing their corrosion.

2. Location of Case Study Offshore

The project site of the western Piers 11 and 12 is located in Imam Khomeini port in the southwest of Khuzestan province, and at the northeastern end of Khoor Mussa in the coastal areas of the Persian Gulf (see Figure 1).

Fig. 1. A satellite image of the wharves 11 and 12 at Imam Khomeini Port

In such areas, water and soil are polluted, and even the regional atmosphere contains elements which are harmful to the Persian Gulf. Moreover, in the areas under discussion, humidity and temperature are so high that they not only set off the process of structural destruction, but increase the speed of damage as well. Wharves 11 and 12 are important and strategic since they play a major role in accelerating the process of exporting and importing goods at the port in question, which has a total mooring length of about 1.5 km. These wharves were planned by the consultants of Iran Compsax in 1970. Having been designed and approved, their construction operations began in 1975 and ended in 1978.

3. Evaluating Offshore Concrete Structures

Appropriately repairing failures to extend the useful life of offshore concrete structures is indeed the best method whereby premature failures can be prevented. This means that such repair and reconstruction of structures entails high costs. Taking preventive measures can reduce, at least to some extent, the costs incurred. Moreover, periodic visits play a significant role in deciding on preventive action before any major damage is done. This has the advantage of reducing repair and reconstruction costs. Decisions can also be made about structural evaluation through occasional observation of faults. A periodic evaluation of structures is performed based on determining the need for maintenance, restoration, and reconstruction. This involves two stages of initial and final visits. The estimated type of fault and the penetration of chloride ions are the main agents of corrosion onset in reinforcement buried in concrete in most offshore structures (Babaee and Castel, 2016). It is, vital to study concrete resistance to chloride ion penetration. Such ions enter concrete both from an external environment by contact with contaminated soil or seawater and from an internal one using calcium

chloride-based accelerated additives or contaminated materials containing ions. It must be emphasized that this is a well-known mechanism whereby chloride ions penetrate into the concrete, thus reducing the useful life of such structures (Babaee and Castel, 2018). Also noteworthy is the fact that the penetration of chloride ions into concrete is determined not by one, but rather by several factors (ionic release, capillary absorption, and suction, permeability, and migration) associated simultaneously with the environment which contains chloride ions (Bagheri et al., 2012). Tests are necessary to determine the exact type and number of faults for designing supplementary tests. After completing the structure evaluation, its service life was determined, and requisite decisions were made regarding the maintenance, repair, or reconstruction of the structure. Figure 2 shows the schematic chart of periodic inspection and evaluation cycle.

4. Evaluation Tests of Concrete Structures

Concrete evaluation tests are generally performed on non-destructive concrete to achieve the following objectives: 1) Preparing a chloride ion profile (chloride ion concentration and the amount of penetration into different depths of internal concrete) to determine the corrosion status in reinforcements; 2) Determining concrete electrical resistivity; 3) Determining the pulse speed and concrete mechanical modulus.

4.1. Preparing the Chloride Ion Penetration Profile

Penetration of chloride ions is the main agent of corrosion onset in reinforcements buried in concrete in most offshore structures. Therefore, it is of particular importance to study the concrete resistance to chloride ion penetration.
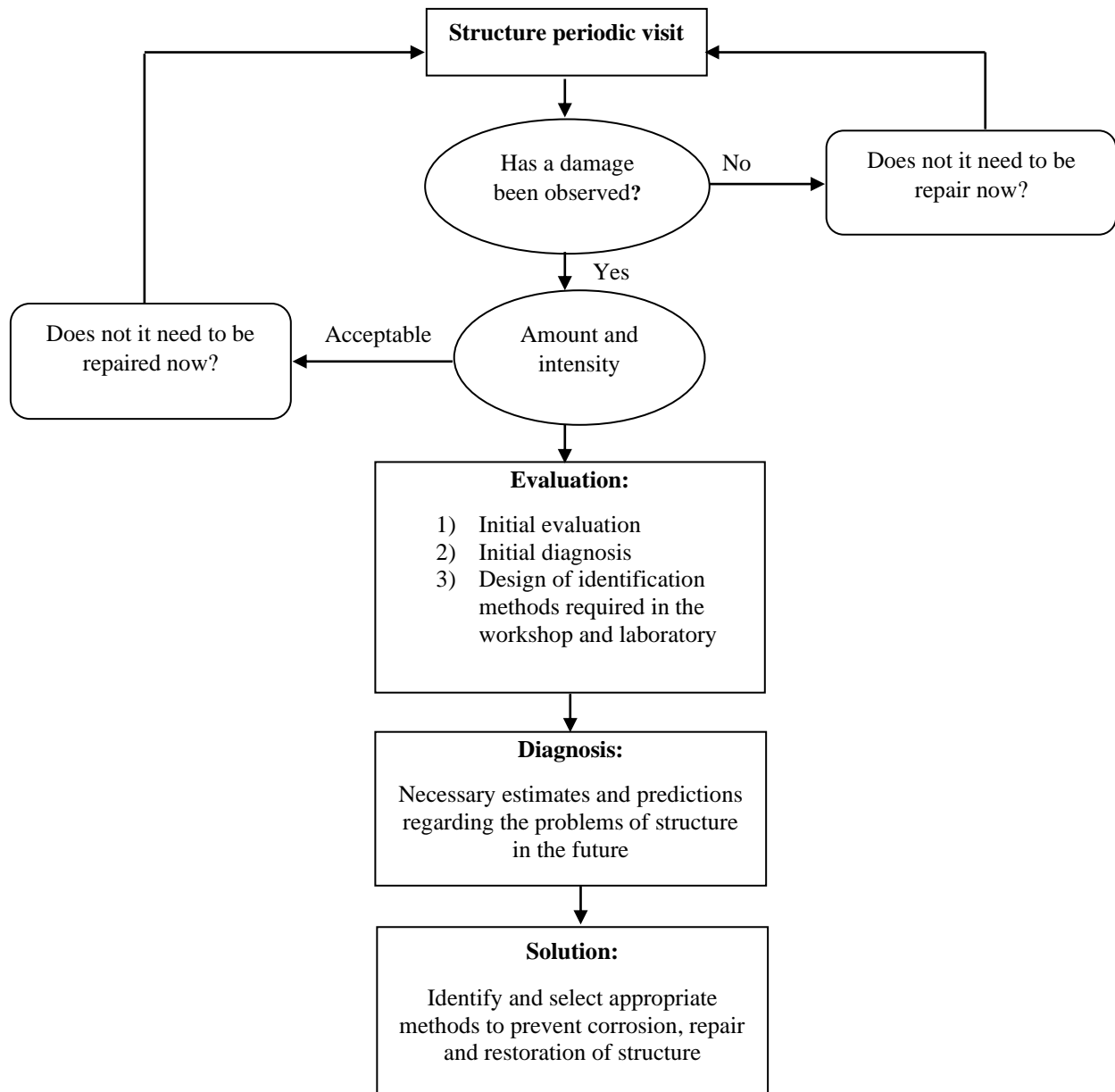
Fig. 2. The cycle of periodic evaluation and offshore concrete structures evaluation

Chloride ions enter into the concrete both from the outside environment, by contact with contaminated soil or seawater, and from the internal environment using calcium chloride-based accelerator additives or by using contaminated materials with chloride ions. It is well-known that the mechanisms of chloride ion penetration into concrete are due to the great importance of chloride ion penetration as an essential factor in reducing the useful life of concrete structures. Effects of corrosion on the properties of materials that result from the penetration of chloride ions include the deterioration of such properties (cover), limited concrete (core), longitudinal and transversal reinforcements, and connection between concrete and steel. The onset time of corrosion and corrosion surface (i.e., structure deterioration relating to the process of reinforcement corrosion) consists of three stages. The first stage is connected with diffusion, a process in which chloride ions disperse on enforcement surfaces. The second stage concerns the development from the onset time of corrosion until concrete begins to crack. The third stage has to do with

deterioration. This paper presents a model of chloride ion corrosion based on Fick's second law in order to simulate the theory and mathematics of the steps mentioned above. The concentration of concrete chloride is a function of depth and time according to Fick's second law and a one-dimensional solution based on developed models (Li and Zheng, 2005).

$$c(x,t) = cs[1 - \mathrm{erf}\left(\frac{x}{2\sqrt{Dc * t}}\right)] \qquad (1)$$

where $C(x,t)$: is the concrete chloride concentration, cs: is the surface chloride concentration, Dc: is the concrete chloride diffusion coefficient, x: is depth of concrete surface, t: is time and erf: is the error function.

When chloride concentration on the surface of the reinforcement reaches a critical level, reinforcement corrosion starts. Various functions have been introduced for critical chloride concentration, based on the existing environmental conditions. The function proposed for this study is connected with a particular region near the Persian Gulf. In this study, the onset time of corrosion has been proposed as a result of laboratory studies (base on the simulated environmental conditions prevailing in the Persian Gulf and the Oman Sea), and experimental studies of the true corrosive environmental conditions in southern regions of Iran have been done. This can be represented as follows:

$$Tcorr = 0.75 \left(\frac{dc}{B1}\right) c1 \qquad (2)$$

where $Tcorr$: is onset time of corrosion (years), and dc: is the thickness of steel bar coat (mm), c_1 and B_1: are fixed coefficients. It must be noted that the coefficients depend on the ratio of cement to water and the percentage of microsilica used in designing the concrete mix.

The diameter of reinforcement decreases over time as a result of corrosion. Eq. (3) is meant to calculate the reduction of the steel rod's corroded diameter based on the calculated corrosion onset. Thus:

$$db = dbi - 1.508\left(1 - \frac{w}{c}\right) - \frac{1.64}{dc}(t - Tcorr)0.71 \qquad (3)$$

where db: is the reduced steel bar diameter, dbi: is the initial diameter of steel bar, and w/c: is the water-cement ratio.

Based on the reduced diameter of the steel bar due to corrosion, the amount of corrosion ($\Delta corr$) in terms of reduction of the reinforcement diameter is defined as follows:

$$\Delta corr = \frac{d2b - d2bi}{d2bi} \times 100 \qquad (4)$$

where $\Delta corr$: is the amount of corrosion, $d2b$: is the reduced steel bar diameter and $d2bi$: is the initial diameter of steel bar.

As can be verified, first the corrosion occurs on the bar, and then, owing to the expansion of the corrosion products, cracking takes place in the cover of concrete piers. Based on the preceding remarks, one of the most important tests for determining the quality of concrete is to prepare a penetration profile of chloride ions in the depth of concrete. For the purposes of this study, our tests were conducted by following the ASTM C1152 standard method, as explained below.

4.1.1. First Stage: Collection of Concrete Powder from the Structure

At least 10 grams of concrete powder taken from different depths of piers were required in order to draw chloride ion profiles. For this purpose, two methods were used (drilling and core extraction based on RILEM TC-178 method) and concrete powder was prepared in the laboratory. In the drilling method, a drill with an adjustable ruler was used to make a number of holes in the desired location according to the diameter of the drill. This involved 5 steps, during each of which a hole with a depth of one centimeter was

dug. The resulting concrete powder was stored and encoded bags to prevent any moisture. As for the core extraction method, first the sample of the cylinder was taken from the concrete held by a clamp. Then, the powder was prepared from the primary surface layer of each member by drilling a hole on the basis of the process described above. Finally, the samples were transferred to the laboratory, where steps were taken to prepare the solution by passing the powder through a 70-point sieve. It should be noted that an on-site drilling method was used at the pier (Figure 3).

4.1.2. Second Stage: Solution of Chloride Ion in Nitric Acid

The solution was prepared according to ASTM C114 (2017), Part 19. For this purpose, first, 10 grams of concrete powder was poured into Erlenmeyer, which passed through a 70-degree sieve. Then 75 ml of distilled water was poured into Erlenmeyer, and immediately afterwards nitric acid was diluted, drop by drop, with distilled water to a volume of 25 ml. This was added to a mixture of concrete and distilled water to dissolve all the chloride ions in acid. In order to ensure the dissolution of total chloride ions in acid, 2 to 3 drops of methyl orange index were poured into the solution. If the index rated the solution as acidic, all chloride ions were dissolved in the acid. Afterwards, the solution was heated to the boiling-point and passed through a filter paper. The volume of this solution, which contained distilled water, reached a level of 250 ml. Figure 4 illustrates all the steps involved.

4.1.3. Third Step: Determination of Chloride Ions Concentration in the Solution

To measure the amount of chloride ions in the solution, which used a tetrapetometric device because it was only needed to pour a certain amount of this solution into this device and specify its amount. The amount of chloride ions was determined in the solution, to divide the ions by 10 grams to

measure their quantity, and to obtain their percentage. The solution was measured 3 times, and in different volumes, by the device. Then the weighted average was taken from the results in order to measure the amount of chloride ion in the solution. This was done to make the measurement as accurate as possible. The results were given as input to Excel software, which determined the average depth, and plotted the profile of chloride ion penetration.

4.2. Electrical Resistivity of Concrete

Determining concrete electrical resistivity is a suitable indicator whereby one can evaluate concrete permeability and its resistance to penetration of chloride ions and also concrete resistance to the passage of electric currents. In this connection, two anodic and cathodic regions are formed in the process of re-bar corrosion that are potentially different. This means that the transfer of hydroxyl ions from the cathode to the anode takes place under the influence of concrete electrical resistivity. For the higher electrical resistivity of the concrete lower's corrosion current density. What distinguishes this method is that it is quite non-destructive, and its simplicity, speed, and economy make it more efficient. Note that the ions which have penetrated into the concrete move through its pores, and that the concrete has electrical conductivity cause by the movement of ions. Of course, the amount of concrete electrical resistivity depends directly on its permeability and environmental conditions (the moisture of the concrete and the number of ions which have penetrated into it). There is no doubt that if concrete permeability is higher, ions can enter the concrete environment easily and quickly, and that if the number of penetrating ions is higher, concrete electrical resistivity will be less. Therefore, concretes with a high electrical resistivity will show better performance against penetration of chloride ion and the onset of corrosion. It is usually the case that chemical additives do not reduce the

electrical resistivity of concrete, but the effect of pozzolanic materials such as

microsilica is significant since it increases such resistance.

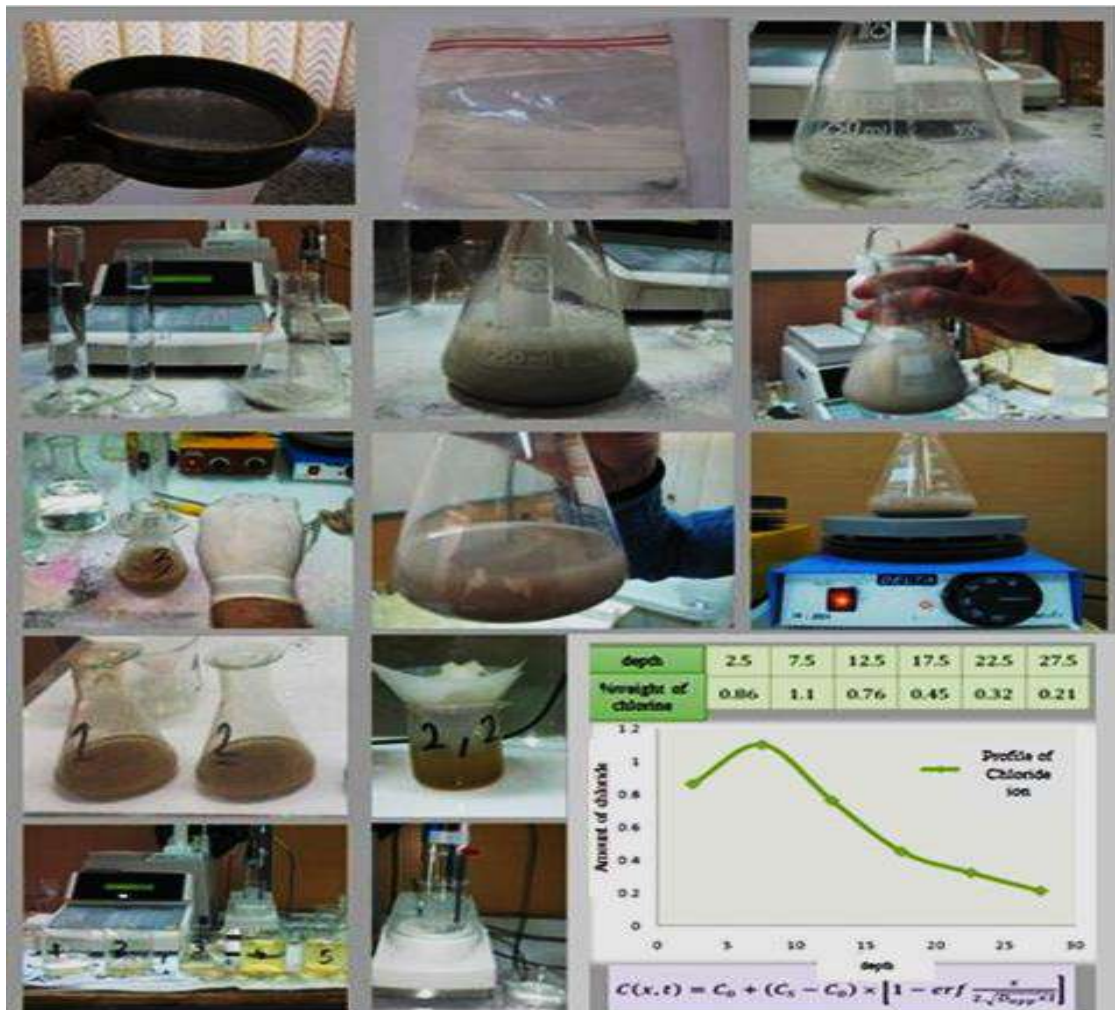**Fig. 3.** Concrete drilling to get concrete powder

Fig. 4. A view of all the steps for preparing solutions according to ASTM C114 Standard (2017) and obtaining a chloride ion profile

Fig. 5. Measuring device electrical resistivity

The probable corrosion rate of concrete was determined on the basis of the electrical resistivity specified in Table 1, and in accordance with the recommendations of ACI 222 Standard (2001). It should be noted that the model of the device used in this test was Resipod Proceq, which also suggested the figures whereby the possible corrosion rate could be interpreted.

The standard method for performing the test in question is based on FM 5-578 FDOT (Ryan, 2011). Moreover, most electrical resistivity was performed together with half-cell potential tests in order to predict the possibility of corrosion. To perform this experiment according to the standard method, and also to eliminate the effect of reinforcement on the results, reading was performed in three directions at one point: horizontal, vertical and oblique. Considering the fact that the minimum cover in the members of the structure was not less than 30 mm, the effect of the armature on the test results is insignificant according to the explanations provided in the device catalog. As a result, the lowest number was reported as being the electrical resistivity. Similarly, information can be obtained about the concrete strength when it confronts aggressive factors from concrete electrical resistivity.

A concrete electrical resistivity test was performed at 23 points on the concrete Piers 11 and 12. The results are shown in Table 2. An outline of the results obtained by summarizing an electrical resistivity test for different elements of structure is shown in Table 3.

Table 1. Possible corrosion rates vs. Wenner test

Possible corrosion potential	Results of Wenner test (KΩ-cm)
Very high	5 >
High	5 - 10
Medium to low	10 - 20
Insignificant	20 <

Fig. 6. A view of the concrete superficial electrical resistivity test performed by using the Wener method on the concrete pier

Fig. 7. Concrete electrical resistivity test on Piles docks 11 and 12

Table 2. Test results for determination of concrete electrical resistivity

No	Test position	Test code	Moisture content	Vertical (kΩ/cm)	Horizontal (kΩ/cm)	Diagonal (kΩ/cm)
1	Wharf 11th Part 1.S	SR-P-01		65	62	67
2	Wharf 11th Part 1. A	SR-P-02		18	16	17
3	Wharf 11th Part 2. S	SR-P-03		33	34	39
4	Wharf 11th Part 2. A	SR-P-04		84	95	84
5	Wharf 31th Part 1.S	SR-P-05		97	150	167
6	Wharf 31th Part 1.A	SR-P-06	88%	307	327	300
7	Wharf 12th Part 5.S	SR-P-07		53	70	84
8	Wharf 12th Part 5.A	SR-P-08		66	94	98
9	Wharf 12th Part 6.N	SR-P-09		25	25	22
10	Wharf 12th Part 7.AN	SR-P-10		39	46	45
11	Wharf 12th Part 7.AS	SR-P-11		164	180	160

Table 3. Test results based on determining concrete electrical resistivity in the structure members

No	Structure element	Repair status	Minimum number read (KΩ-cm)	Maximum number read (KΩ-cm)	Possible corrosion rate (KΩ-cm)
1	Concrete piles	Repaired	13	73	Normal
2	Concrete piles	Non-repair	-	-	-
3	Structure concrete beams	Repaired	8	80	High
4	Structure Concrete beams	Non-repair section	15	88	Normal
5	Concrete slab under the pier	Repaired	23	38	Low
6	Concrete slab under the pier	Non-repair section	9	47	High
7	Forehead pier	Repaired	12	57	Normal
8	Forehead pier	Non-repair section	11	26	High

4.3. Pulse Velocity and Concrete Mechanical Modulus (Ultrasonic)

The ultrasonic pulse velocity technique performance was investigated (as a non-destructive test for concrete) to estimate the mechanical properties of concrete. The standard method used for this test was according to ASTM C597 (2002) and was performed to determine the pulse velocity of the concrete mechanical modulus, and it was non-destructive. This test is also known as ultrasonic pulse wave velocity, and is applied on the basis of determining the speed of these waves passing through the concrete. By the way, the most famous device used for this test is called Pundit. This device, which emits vibrations at its ordinary frequency, generates ultrasonic pulses by applying a sudden change of potential from an exciter transmitter to a piezoelectric transducer crystal. The transmitter transducer is in contact with the two sides of the concrete, and the vibrations caused in this way are received by it after passing through the concrete. In this test, it is possible to transmit generators in three

ways: direct, semi-direct and superficial. Of these three options, the first one is the most suitable for transmitting waves. Therefore, the variability of velocity along different paths in the structure is a sign of change in concrete quality. It is interesting to point out that pulse speed measurement can be used to control quality. It is also possible to establish an experimental relationship between pulse velocity and static and dynamic elasticity modulus and concrete strength. However, these relationships are influenced by factors such as the type and amount of cement, additives, aggregates, processing conditions and concrete age, as explained below:

$$V = \sqrt{\frac{(1-\mho)E_d}{p(1+\mho)(1-2\mho)}} \qquad (5)$$

where V: is the pulse rate (m/s), v: is the

Poisson's ratio, p: is the concrete density (kg/m^3), and Ed: is the mechanical modulus of elasticity concrete (MN/m^2).

A concrete ultrasonic test was performed by using a Pundit Lap + device on different members of the structures at Piers 11 and 12. This experiment was performed to determine shear wave velocity in concrete, and to determine concrete mechanical elasticity modulus. Here, a concrete ultrasonic test was performed at 15 points of Piers 11 and 12. The results are shown in Figure 8 and Table 4.

A concrete qualitative classification using pulse velocity is shown in Table 5 (Maierhofer, 2010). The average quality of concrete in the beams is as follows: poor in piles, deck slabs, and pier forehead. The results of the concrete shear wave velocity test in different structure members are summarized in Table 6.

Table 4. Results of an ultrasonic concrete test (pulse velocity) on different members of Piers 11 and 12

Row	Test position	Test code	Test method	Shear wave velocity (m/s)	Quality category
1	Wharf 11th, south side of the pile on the axis B-31	UT-P-265	Indirect	2622	Weak
2	Wharf 11th, north side of the pile head on axis B-31	UT-CP-266	Indirect	2471	Weak
3	Wharf 11th, the lower side of the slab on axis 30th and 31th -A and B	UT-S-267	Indirect	2358	Weak
4	Wharf 11th, South face of the pile on axis B-11	UT-P-268	Indirect	2421	Weak
5	Wharf 11th, north side of the pile head on axis B-11	UT-CP-269	Indirect	2113	Weak
6	Wharf 11th - lower side of the slab on axis A and B-12 and 13	UT-S-270	Indirect	3318	Medium
7	Wharf 11th, west side of the beam on axis B and C-1	UT-B-271	Indirect	3563	Good
8	Wharf 11th, lower face of the slab on axis B and C-1 and 2	UT-P-272	Indirect	4518	Great
9	Wharf 12th, west side of the beam on axis B and C-1	UT-B-273	Indirect	2620	Weak
10	Wharf 12th, lower side of the slab on axis B and C-1 and 2	UT-S-274	Indirect	2439	Weak
11	Wharf 12th, south face of the pile head on axis B-1	UT-CP-275	Indirect	3764	Good
12	Wharf 12th, south side of the pile on axis B-2	UT-P-276	Indirect	2182	Weak
13	Wharf 12th, south face of the pile on axis B-11	UT-P-277	Indirect	2254	Weak

Table 5. Concrete quality classification based on pulse velocity

Concrete quality	Pulse speed	
	ft/s	m/s
Great	< 15	4500 >
Good	12 - 15	3500 - 4500
Medium	10 - 12	3000 - 3500
Weak	7 - 10	2000 - 3000
Very weak	7 <	2000 <

Fig. 8. Concrete ultrasonic test on piles, slabs and forehead at Piers 11th and 12th

Table 6. A summary of ultrasonic test results in the structure of different structure members of Piers 11 and 12

No.	Structure element	Average shear wave velocity (m/s)	Quality category
1	Concrete piles	2655	weak
2	Concrete structure beams	3707	good
3	Concrete slab under pier	2610	weak
4	Pier forehead	2695	weak

5. Materials and Methods

In this study, Portland cement was used to make specimens. In addition, a mixture of river-type sand and crushed-type gravel was prepared (with a specific weight of 2560 kg/m^3 2650 kg/m^3, respectively). A suitable aggregate was also prepared.

5.1. Mixing Ratios

Three super plasticizers within the range of 2%, 4% and 6% were used separately by considering three types of microsilica (5%, 10% and 15% with a grade of 400), and by selecting three water-to-cement ratios (34%, 40% and 45%). The objective was to achieve a suitable slump in different designs in conformity with the aim of this study, i.e. the application of microsilica in order to improve mechanical properties, to increase durability, and to reinforce concrete compressive strength in offshore piers. This was followed by making a control sample made and tested from a cement of a mixed grade. The number of concrete mixtures studied was referred to as M*S*W*, where M: indicates microsilica, S: represents superplasticizer, and W: stands for water-to-cement ratio. As can be seen from Tables 7-9, based on the granulations of three types of Shootar materials, the most suitable mixing design which agrees well with the specifications was selected. The design had the following ingredients: 1) Crushed gravel (12-25) mm, 30% by weight; 2) Broken gravel (5-19) mm, 30% by weight; 3) Natural washed sand (0-8), 40 mm by weight; 4) the mixing plan is done according to the specifications shown in Table 7; 5) Consumable cement is considered Type 2 from Tehran Cement Factory having a 400 kg per cubic meter grade; 6) The water cement ratio 0.34%, 0.40%, and 45% obtained with an average slump of 65 mm from Mahshahr Iran water. It must be pointed out that the mixing plan was drawn up on the basis of specifications seen in Table 7.

5.2. Cement Type

Durability of cement-based materials is an indication of their service life under a certain environmental conditions. Environmental conditions are the main factors in durability. According to ACI 201 (2008), durability of cement-based materials is their ability to withstand weathering, chemical attack, wear or any process which leads to damage (Tajdini et al., 2021). The consumable cement was considered to be of Type 2, Tehran Cement Factory, with a content of 400 kg per cubic meter. The cement chemical characteristics are given in Table 10.

Table 7. Concrete mix proportions

Mixing scheme number	W/C	SF (%)	Water (Kg/m³)	Microsilica (Kg/m³)	Cement (Kg/m³)	Coarse-grained (Kg/m³)	Fine-grained (Kg/m³)
1		0		0	400		
2	0.34	5		20	380		
3		10	136	40	360	1118.4	745.6
4		15		60	340		
5		0		0	400		
6	0.4	5	160	20	380		
7		10		40	360	1104	736
8		15		60	340		
9		0		0	400		
10	0.45	5	180	20	380		
11		10		40	360	1092	728
12		15		60	340		

Table 8. Results of specific weight, dry volume unit weight and materials water absorption

Description	Appearance specific weight (gr/cm³)	Real specific weight (gr/cm³)	Dry volume unit weight (gr/cm³)	Water absorption (%)
Gravel 12-25	2.710	2.645	1.39	0.86
Gravel 5-19	2.722	2.66	1.5	1.04
Sand 0-8	2.712	2.604	1.59	1.53

Table 9. Results of abrasion percentage using the Los Angeles and sand equivalence method

Description of specimens	Cycle drop	Abrasion weighing	Permissible limits of abrasion	Sand equivalence	Permissible limits of sand equivalence
Gravel 12-25 mm	500	17.6	40	--	--
Gravel 5-19 mm	500	21	40	--	--
Sand 0-8 mm	--	--	--	0.16	75

Table 10. Chemical characteristics of consumable cement

Chemical composition	SiO_2	Al_2O_3	SO_3	Fe_2O_3	CaO	MgO	C_3S	C_2S	C_3A
Percentage	21.97	4.26	1.65	3.55	64.56	2.33	50.68	24.76	3.65

5.3. Superplasticizer Additive

A concrete superplasticizer is a type of chemical additive with a water-reducing function. This reduction in water content will cause concrete strength and durability to increase. For purposes of this research, MECRET TB 101F was used, which is a delayed superplasticizer whose combined base includes naphthalene and melamine, and which is resistant to corrosion. As a result, it is suitable for offshore structures and corrosive environments.

Table 11. Chemical characteristics of consumable cement

Characteristic	Description
Appearance	Powder – brown
Volumetric weight	5507 gr/lit
PH of 20% solution	Approximately between 8 to 11

5.4. Microsilica

In this study, microsilica with a particle density of 2200 kg/m³ was used. Table 12

presents the results of the chemical analysis of this microsilica.

5.5. Selection Criteria

Two standards, ASTM and ASTM C33 were used to make laboratory specimens and select materials. Based on the criteria of regulation, maximum grain size was used to make laboratory specimens (ASTM, 2021).

6. Results and Discussion

Cubic specimens in three dimensions (15 × 15 × 15 cm) were made to evaluate the compressive strength of concrete, and to conduct an analysis of each specimen with a view to measuring compressive strength and corrosion current density. The specimens were submerged to the sea water in order to test them for corrosion. The results of the compressive strength experiment are shown in Table 14.

Table 12. Chemical properties of microsilica

Chemical composition	SiO$_2$	Al$_2$O$_3$	Fe$_2$O$_3$	CaO	MgO	SO$_3$
Percentage	95.1	1.32	0.87	0.49	0.97	0.1

Table 13. Determining the percentage of ingredients in concrete laboratory specimens

Sample code	W/C	Type of cement	Microsilica (%)	Superplasticizer (%)
M0S6w34:1			0	
M5S6w34:2	34%		5	0.6
M10S6w34:3			10	
M15S6w34:4			15	
M0S2w40:5			0	
M5S2w40:6	40%	2	5	0.4
M10S2w40:7			10	
M15S2w40:8			15	
M0S2w45:9			0	
M5S2w45:10	45%		5	0.2
M10S2w45:11			10	

Table 14. The results of compressive strength tests on concrete specimens for 28 days

Specimen code	Length (cm)	Width (cm)	Height (cm)	Maximum force (kg)	Compressive strength (kg/cm^2)
M0S6w34:1	15.1	15.1	15	126800	383
M5S6w34:2	15.1	15	15	152160	579
M10S6w34:3	15.2	15.2	15.3	158500	603
M15S6w34:4	15.1	15.1	15.1	164840	627
M0S2w40:5	15.1	15.1	15.1	121600	365
M5S2w40:6	15.1	15	15	148300	534
M10S2w40:7	15.2	15.1	15.1	153400	581
M15S2w40:8	15.1	15	15	157600	590
M0S2w45:9	15.1	15.1	15	111500	321
M5S2w45:10	15.1	15	15	124820	484
M10S2w45:11	15.3	15.1	15.1	134700	505
M15S2w45:12	15.1	15	15	148800	558
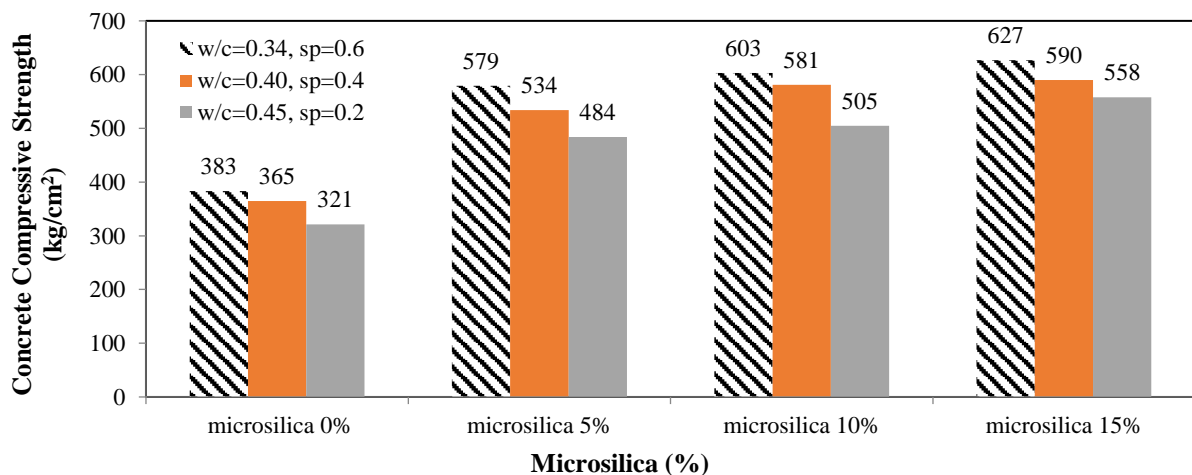
Fig. 9. The effect of microsilica on concrete compressive strength for 28 days

Table 15. Ranges of corrosion current density and their interpretation (Gu et al., 2000)

Extent of corrosion	Corrosion current density (μA/cm^2)
Passive condition	$i_{corr} < 0.1$
Low to moderate corrosion	$0.1 < i_{corr} < 0.5$
Moderate to high corrosion	$0.5 < i_{corr} < 1$
High corrosion	$i_{corr} > 1$

In this study, concrete specimens were kept in a laboratory in the Persian Gulf environment for 18 months. Corrosion tests were then conducted on the laboratory samples 80 times for 4.5 months, and the test results were compared with each other.

The results are shown in Figures 10-12. In Figure 10, the effect of microsilica on the compressive strength of concrete for 28 days, with three water-to- cement ratios and 3% superplasticizer are shown. It can be seen from the figure that the average compressive strength increases by 30%, compared with the control specimen without microsilica, thus reducing the ratio of water to cement, as well as the use of microsilica. In these figures, the corrosion current density is presented, in terms of the age of concrete (i.e., corrosion duration), for specimens containing microsilica 15%, 10%, and 5% (weight of cement), and for those without microsilica. This involves Type 2 cement. After 18 months, the corrosion current density within the range of 5%,10%, and15% was less than that of the specimen without microsilica (see Figures 11 and 12). The fineness of the microsilica grains, compared with the round grains of cement, can be said to be the reason for this decrease. First, they fill very fine spaces of glaze when they are placed next to the cement glaze. Secondly, they combine with calcium hydroxide [$(OH)_2$] resulting from the dewatering of the cement and convert it into hydrated calcium silicate because they are chemically active. In this way, voids are reduced in the cement glaze, the calcium hydroxide changes into a more solid body (similar to other cement paste silicates), the cement paste texture becomes more uniform, and the concrete properties are improved. In all three figures, the corrosion current density is shown on the basis of the age of concrete with three water-to-cement ratios (0.34%, 40%, and 45%) and by considering 3 percentages of different microsilica. These figures show that the corrosion current density within the range of 10% and 15% is much lower than that of samples without microsilica and the instances of corrosion intensities are very close to each other. It can be observed that the difference between the corrosion current density of mixtures containing 10% microsilica, and that of mixtures containing 15% microsilica, arises from an increase in calcium hydroxide, which itself results from the hydration of cement and water in higher grade mixtures. As a result, when there are higher amounts of microsilica, they increase the gel and neutralize the negative effect of the excess mixture. Although the ratio of microsilica is 15% lower than the other two ratios of it, because of the trend of severe corrosion in shapes, it can be seen from these figures that the two ratios of microsilica (i.e., 10% and 15%) are very close to each other and the important factor at this stage is the economics of microsilica consumption, as indicated by its large volume in this project.
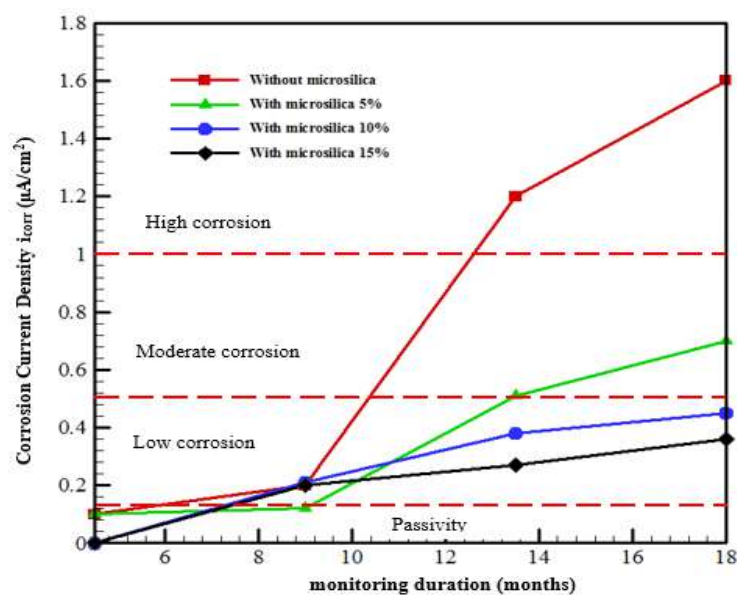
Fig. 10. Corrosion rate of concrete specimens at different times (SP = 0.6, w/c = 0.34)
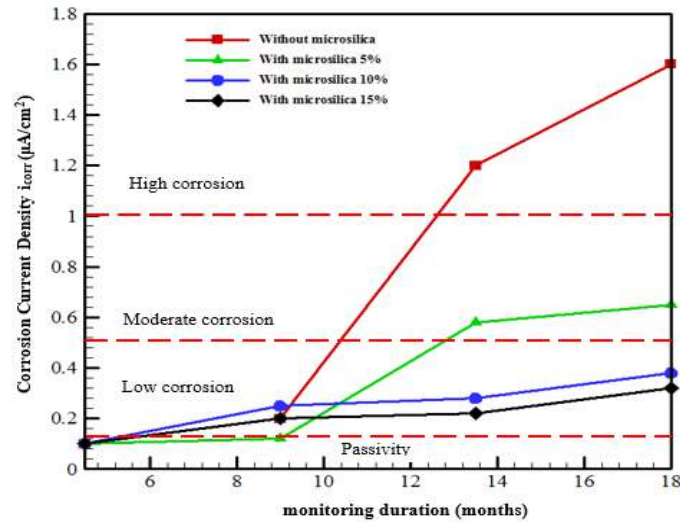
Fig. 11. Corrosion rate of concrete specimens at different times (SP = 0.4, w/c = 0.40)
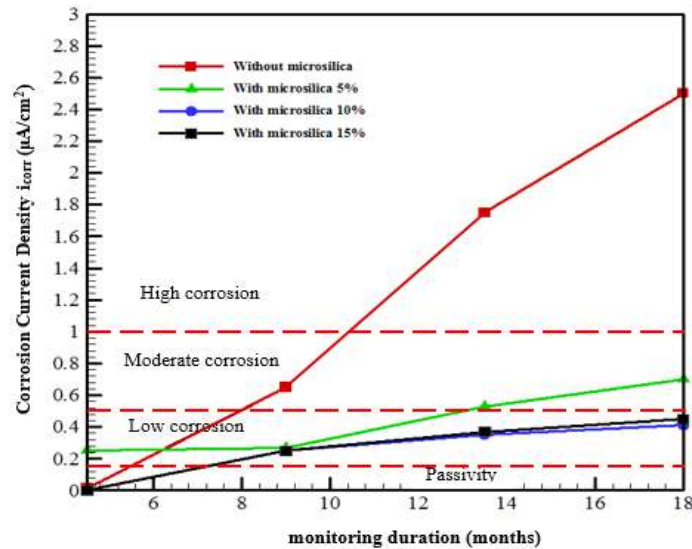
Fig. 12. Corrosion rate of concrete specimens at different times (SP = 0.2, w/c = 0.45)

7. Conclusions

The results demonstrated that the number of invasive salts in the Persian Gulf water is significantly higher than the average quantity determined for open seas. This high concentration in seawater results mostly from high evaporation of water, low rainfall, and the presence of polluting petrochemical industries in the region. From the results, it is indicated that over time, concrete piles have suffered the most damage because of chloride penetration and reinforcement corrosion and, therefore, must be repaired by using appropriate materials. The tidal zone is an area subject to changes at water level and constantly becomes wet and dry so that most destruction of the concrete takes place. Given that the corrosion of rebar's is one of the main factors in destroying reinforced concrete structures, concrete permeability is the most important cause of the increasing rate of this destruction. In this connection, the use of pozzolanic materials such as microsilica plays a significant role to have a dense concrete and increasing electrical resistivity at concrete and reducing the permeability of concrete. On the basis of the results obtained from this study it is suggested that the microsilica used in concrete should be about 10%. Because of the reduction of concrete permeability, it is suggested that the water-to-cement ratio and superplasticizer should be 34% and 6%, respectively.

8. Acknowledgement

9. References

Abedini, M. and Zhang, C. (2021). "Dynamic vulnerability assessment and damage prediction of RC columns subjected to severe impulsive loading", *Structural Engineering and Mechanics*, 77(4), 441.

ACI 201. (2008). *Guide to durable concrete*, American Concrete Institute.

ACI 222 Standard. (2001). *Protection of metals in concrete against corrosion*, American Concrete Institute.

Antunes, D., Martins, R., Carmo, R., Costa, H. and Júlio, E. (2021). "A solution with low-cement light weight concrete and high durability for applications in prefabrication", *Construction and Building Materials*, 275, 122153.

ASTM C597. (2002). *Standard test method for pulse velocity through concrete*, ASTM International.

ASTM C114. (2017). *Chemical Analysis of Hydraulic Cement*, ASTM International.

ASTM. (2021). *Standard specification for concrete aggregates, Annual Book of ASTM Standards*, 04.02, USA.

Babaee, M. and Castel, A. (2016). "Chloride-induced corrosion of reinforcement in low-calcium fly ash-based geopolymer concrete", *Cement and Concrete Research*, 88, 96-107.

Babaee, M. and Castel, A. (2018). "Chloride diffusivity, chloride threshold, and corrosion initiation in reinforced alkali-activated mortars: Role of calcium, alkali, and silicate content", *Cement and Concrete Research*, 111, 56-71.

Bagheri, A., Zanganeh, H., Alizadeh, H., Shakerinia, M. and Marian, M.A.S. (2013). "Comparing the performance of fine fly ash and silica fume in enhancing the properties of concretes containing fly ash", *Construction and Building Materials*, 47, 1402-1408.

Baqheri, A.R., Zanganeh, H., Samadzad, H. and Kiani, A.L.A.H. (2012). "Assessing the durability of binary and ternary concretes using rapid chloride resistance test and the accelerarted rebar corrosion test", *The International Congress on Durability of Concrete*, Tehran, Iran.

Ganjian, E. and Pouya, H.S. (2009). "The effect of Persian Gulf tidal zone exposure on durability of mixes containing silica fume and blast furnace slag", *Construction and Building Materials*, 23(2), 644-652.

Gu, P., Beaudoin, J., Zhang, M.H. and Malhotra, V. (2000). "Performance of reinforcing steel in concrete containing silica fume and blast-furnace slag ponded with sodium-chloride solution", *Materials Journal*, 97(3), 254-262.

He, B., Gao, Y., Qu, L., Duan, K., Zhou, W. and Pei, G. (2019)."Characteristics analysis of self-luminescent cement-based composite materials with self-cleaning effect", *Journal of Cleaner Production*, 225, 1169-1183.

He, X., Zheng, Z., Yang, J., Su, Y., Wang, T. and Strnadel, B. (2020). "Feasibility of incorporating autoclaved aerated concrete waste for cement replacement in sustainable building materials", *Journal of Cleaner Production*, 250, 119455.

Liu, J., Huang, H., Ma, Z.J. and Chen, J. (2021). "Effect of shear reinforcement corrosion on interface shear transfer between concretes cast at different times", *Engineering Structures*, 232, 111872.

Li, C.Q. and Zheng, J.J. (2005). "Propagation of reinforcement corrosion in concrete and its effects on structural deterioration", *Magazine of Concrete Research*, 57(5), 261-271.

Parrott, L. (1994). "A study of carbonation-induced corrosion", *Magazine of Concrete Research*, 46(166), 23-28.

Moffatt, E. and Thomas, M. (2018). "Performance of 25-year-old silica fume and fly ash lightweight concrete blocks in a harsh marine environment", *Cement and Concrete Research*, 113, 65-73.

Maierhofer, C., Reinhardt, H.W. and Dobmann, G. (2010). *Non-destructive evaluation of reinforced concrete structures: Non-destructive testing methods*, Woodhead Publishing.

Poston, R.W., Kesner, K., McDonald, J.E., Vaysburd, A.M. and Emmons, P.H. (2001). "Concrete repair material performance, Laboratory study", *Materials Journal*, 98(2), 137-147.

Pandey, A. and Kumar, B. (2019). "Evaluation of water absorption and chloride ion penetration of rice straw ash and microsilica admixed pavement quality concrete", *Heliyon*, 5(8), e02258.

Roy, S., Poh, K. and Northwood, D. (1999). "Durability of concrete accelerated carbonation and weathering studies", *Building and Environment,* 34 (5), 597-606.

Ryan, E.W. (2011). "Comparison of two methods for the assessment of chloride ion penetration in concrete: A field study", M.Sc. Thesis, University of Tennessee.

Siddique, R. (2011). "Utilization of silica fume in concrete: Review of hardened properties", *Resources, Conservation and Recycling*, 55(11), 923-932.

Tajdini, M., Bargi, M.M. and Rasouli Ghahroudi, O. (2021). "An investigation on the effects of adding nano-sio_2 particles and silica Ffume with different specific surface areas on the physical and mechanical parameters of soil-cement materials", *Civil Engineering Infrastructures*

Journal, 54(1), 93-109.

Zhang, C., Abedini, M. and Mehrmashhadi, J. (2020). "Development of pressure-impulse models and residual capacity assessment of RC columns using high fidelity Arbitrary Lagrangian-Eulerian simulation", *Engineering Structures*, 224, 111219.

Zhang, C. and Abedini, M. (2021), "Time-history blast response and failure mechanism of RC columns using Lagrangian formulation", *Structures*, Elsevier, 34, 3087-3098.

Behavioural Study of Incorporation of Recycled Concrete Aggregates and Mineral Admixtures in Pavement Quality Concrete

Jindal, A.[1]* and G.D. Ransinchung, R.N.[2]

[1] Assistant Professor, Department of Civil Engineering, School of Engineering and Technology, Central University of Haryana, India.
[2] Professor, Department of Civil Engineering Indian Institute of Technology, Roorkee, India.

ABSTRACT: The following is an in-depth study discussing various aspects of a sustainable Pavement Quality Concrete (PQC) mix with inclusion of Recycled Concrete Aggregates (RCA) and mineral admixtures. In addition to investigation of basic mechanical properties; compositional, morphological and interspatial aspects of hardened concretes were analysed to understand the macro and micro level effects of incorporating fine particulate fly ash, rice husk ash or bagasse ash in concrete mix having recycled concrete aggregates using state of the art techniques such as X-Ray Diffraction (XRD), Scanning Electron Microscopy (SEM) and Mercury Intrusion Porosimetry (MIP). The study of PQC mixes prepared with assimilation of RCA and mineral admixtures show that addition of particulate mineral admixtures significantly enhanced the compressive and flexural strength of the mix incorporating RCA to the order of 15% and 25%, respectively. The study concluded that admixing mineral admixtures at 15% dosage refined the pore structure by reducing the average pore size by up to a few microns and also reducing the total pore volume which indicates towards the concrete mix being less permeable. This refinement in pore structure of concrete mix resulted in reduced water absorption and higher density values thus indicating improvement in durability of concrete.

Keywords: Concrete, Mercury Induced Porosimetry, Mineral Admixtures, Recycled Concrete Aggregate.

1. Introduction

In today's scenario, the construction industry plays a major role in helping developing countries to move at a steady pace towards urbanization and industrialization. Developing countries are going through a rapid infrastructural transformation phase wherein more urban areas are being developed. For a developing country like India, wherein the population count is growing profoundly every day from around 1210 million in 2011 (Census of India, 2011) to a projected count of over 1.64 billion by 2050 (UN DESA, 2018) stress on construction is the need of the hour. This has led to rapid growth in new construction activities as well as demolition

* Corresponding author E-mail: ajindal@cuh.ac.in

of old structures resulting in generation of construction waste in huge quantities. In order to get an idea of future construction activities for a country like India, according to a study it is estimated that almost 70% of the buildings supposed to exist by 2030 are yet to be constructed (Sankhe et al., 2010).

Such activities demand large quantities of materials from depleting natural sources, forcing us to look beyond conventional sources for alternatives. Countries all over the world have come up with creative techniques for utilization of different recycled construction wastes. Hongkong has introduced a construction waste charge for developers as well as tax concession benefits for recycling centers (CSE, 2014). Singapore legislature brought in tightened rules and regulations with penalties due to which it is able to recycle nearly 98% of its Construction and Demolition (C & D) waste (Nagapan et al., 2012). Malaysia is also one such country which is trying to handle C & D waste with aggressive rules and policies (Wahi et al., 2015). Many countries like USA, UK, Australia, Germany, Portugal, Korea, Hongkong, France, China, Japan, European Union etc. have already established specifications for incorporating recycled materials in fresh construction activities (CCANZ, 2013; Tam and Lu, 2016; Jain et al., 2019; Tam, 2008; Zega and Di Maio, 2011; Lennon, 2005). According to a report by the Technology Information Forecasting and Assessment Council (TIFAC), an approximate 40-60 kg/m^2 of waste is generated from new construction activities while an approximate 300-500 kg/m^2 of construction waste is generated out of demolished buildings (TIFAC, 2001).

Considering the scenario for a rapidly developing country like India, no codal standards or specifications are generally established for using concrete waste for new applications. Such a country produces a large quantity of waste; just to get an idea approximately 150 million tons of annual construction and demolition waste was estimated by BMTPC in 2020 (Centre for Science and Environment, 2020). This

waste is generally dumped openly along the roadsides due to weak government laws or their implementations; or is transported to a site outside the city for disposal as landfill. Considering the pace at which developing countries are urbanizing, this waste is bound to increase profoundly which has already started to pose an environmental threat.

Around 25% of total C & D waste in India is contributed by concrete alone which amounts up to around 2.40 to 3.67 million tons per year (TIFAC, 2001). Concrete today is undoubtedly the most widely used construction material (Gagg, 2014). Aggregates in concrete, of all constituents generally contributes towards 60%-70% of the concrete volume (Arredondo-Rea et al., 2019), thus making them one basic amenity for all sorts of concrete constructions. Utilizing this waste as recycled highway materials in pavement construction is therefore an effort to preserve the natural environment by reducing waste and providing a cost-effective material for constructing highways. In fact, the primary objective is to encourage the use of recycled materials in the construction of highways to the maximum economical and practical extent possible with improved or equal performance.

As recycling has become the focus of researchers, a lot of research has been carried out with the inclusion of different recycled/waste materials. However, the majority of the past research concentrates on the mechanical and durability aspects from a macroscopic level; very few studies could be found discussing the microscopic and interstitial properties of pavement quality concrete mix incorporating RCA and mineral admixtures. This study thus concentrates on investigating the effect on concrete mix (PQC mix) at both macro level and microscopic levels owing to the inclusions of RCA as partial substitution for natural coarse aggregates. Thus, determining the suitability of incorporating

RCA for construction of concrete pavements in Indian conditions. The morphological aspects of hardened concrete were analyzed in detail in order to understand the micro level effects of incorporating fly ash, rice husk ash or bagasse ash in concrete mix having RCA. While fly ash and rice husk ash have been in use as mineral admixtures for quite some time, use of bagasse ash is not popular. Also, the literature available for micro analysis of PQC mix using SEM, XRD and Mercury Intrusion Porosimetry (MIP) techniques together is very scanty. This study is thus an effort to discuss the morphological and porosity behaviour of concrete admixed with RCA and mineral admixtures in order to establish a sustainable and durable concrete pavement mix with the incorporation of locally available materials.

2. Literature Review

Re-using waste or recycled materials for new construction applications is not a new concept, in fact it dates back to the Romans who often reused stones from broken roads to construct newer ones. Over the course of time, different materials have been studied by researchers which could be used alongside and or for part replacement of conventional construction materials. Recycled concrete aggregate obtained from processing of demolished concrete waste, has been one such material of interest to researchers globally for quite some time.

Recycled concrete aggregates are aggregates coated with circumferential adhered mortar from old concrete. Researchers such as Rao et al. (2007), Etxeberria et al. (2004), de Oliveira and Vazquez (1996), Kenai et al. (2005), Crentsil et al. (2001) and many more have discussed that recycled concrete aggregates when used without surface treatment in newer concrete applications result in concrete with inferior properties. This has been attributed to weak and porous circumferential mortar surrounding the recycled concrete aggregate particle. Further it has been reported by several researchers such as Xiao et al. (2005), Yong and Teo (2009), Rao et al. (2007), Akbari et al. (2011) and Martínez-Lage et al. (2005) that the inferiority in concrete is reflected both in mechanical and durability properties and was found to be increasing with increase in content of recycled concrete aggregates. Meddah et al. (2020) further discussed that inclusion of recycled concrete aggregates more than 30% as replacement of natural aggregates results in inferior mechanical properties of concrete. Hatungimana et al. (2020) also discussed the effects of incorporating recycled concrete aggregates on the mechanical and durability behavior of concrete. Saravanakumar et al. (2021) discussed that the incorporation of recycled concrete aggregates in addition to slag results in better durability properties and improves the characteristics of concrete in all aspects substantially.

With time and further research various methods / processes / techniques known as beneficiation methods were proposed to help in removal of adhered mortar from recycled concrete aggregates. A few of the beneficiation techniques include acid soaking technique by Tam et al. (2007), thermal-mechanical beneficiation technique by Shima et al. (2005), chemical-mechanical beneficiation technique by Abbas et al. (2007) and microwave assisted beneficiation technique by Akbarnezhad et al. (2011). In addition to the above techniques for removal of adhered mortar, certain methods have also been proposed to improve the performance of recycled concrete aggregates without removing adhered mortar. These studies include treatment of recycled concrete aggregates by oil and silane type surface improvement agents by Tsujino et al. (2007), treatment of recycled concrete aggregates by soaking in pozzolanic slurry by Shaban et al. (2019), treatment of recycled concrete aggregates using calcium carbonate bio-deposition by Grabiec et al. (2012). Kehan et al. (2021)

also discussed various ways of improving the quality of recycled concrete aggregates either by coating them by polymer emulsions or using pozzolanic solutions which tends to fill in the voids with in recycled concrete aggregates thereby lowering its porosity.

Mineral admixtures owing to their pozzolanic properties help in improving the properties of concrete upon their incorporation as evident from the literature. Various researchers have reported improvements in concrete properties with the inclusion of different mineral admixtures in their studies. Some of the studies included use of blast furnace slag with recycled concrete aggregates by Berndt (2009), use of fly ash with recycled concrete aggregates by Kou and Poon (2002), use of high fine fly ash with recycled concrete aggregates by Tangchirapat et al. (2010), use of ground bagasse ash with recycled concrete aggregates by Somna et al. (2012), use of silica fume with recycled concrete aggregates by Wagih et al. (2013), use of ground granulated blast furnace slag with recycled concrete aggregates by Maier and Durham (2012), use of silica fume and ground granulated blast furnace slag with recycled concrete aggregates by Cakir (2014) and many more. Padhi et al (2018) also concluded improvement in properties of concrete containing recycled concrete aggregates with inclusions of rice husk ash with a recommendation of using 100% recycled concrete aggregates with 10-15% rice husk ash for practical applications. Javed et al. (2021) reported an increase in compressive strength of concrete with 100% recycled concrete aggregates with inclusion of bagasse ash up to the order of 20%.

3. Experimental Part

The experimental program for the study included investigations pertaining to properties and behaviour of pavement quality concrete consisting of recycled concrete aggregates and different mineral admixtures both at macro and micro level. The morphological aspects of hardened concrete were analyzed in detail in order to understand the micro level effects of incorporating fly ash, rice husk ash or bagasse ash in concrete mix having recycled concrete aggregates. Among the morphological studies, small hardened concrete specimens were investigated using Scanning Electron Microscopy (SEM) technique for understanding visible morphological variations and powdered concrete specimens were studied using X-Ray Diffraction (XRD) technique for ascertaining the variations in compound compositions. Porosity behaviour and pore structure was studied using Mercury Intrusion Porosimetry (MIP) on hardened concrete specimens. In addition, mechanical and durability properties of concrete mixes were also investigated to correlate the macro level variations in concrete with variations at micro level.

Conventional PQC mixes with and without recycled concrete aggregates and mineral admixtures were prepared as referral mixes for understanding the inclusion effects of recycled concrete aggregates and mineral admixtures. Inclusion of recycled concrete aggregates was carried out by substituting coarse aggregates at a replacement level of 30%. The three mineral admixtures were included at levels of 5%, 10% and 15% as addition to cement.

3.1. Materials Used in Study
3.1.1. Cement

The binder, i.e. cement used for the study was investigated for its physical properties in accordance with IS: 8112 (1989). Table 1 summarizes the properties of Ordinary Portland Cement (OPC), 43 grade used in study.

3.1.2. Aggregates

Coarse Aggregates: Natural and recycled concrete aggregates were used as coarse aggregates in the study both in sizes

of 20 mm and 10 mm. Recycled concrete aggregates were obtained from demolished concrete waste locally procured while crushed granite was used as natural coarse aggregate.

Recycled concrete aggregates obtained from concrete waste after screening, mechanical and manual crushing had adhered mortar which is responsible for inferior properties in comparison to their natural counterparts. Recycled concrete aggregates were processed for surface treatment by soaking them in 0.1 Molar H_2SO_4 solution for a duration of 24 hours and thereafter abrading the dried aggregates in order to remove the adhered mortar. As per studies carried out by Tam et al. (2007) soaking recycled concrete aggregates in H_2SO_4 makes the adhered mortar brittle which helps in better removal of mortar.

Figures 1a and 1b show demolished concrete waste and recycled concrete aggregates obtained after processing.

All the coarse aggregates used in study were investigated for their physical and mechanical properties to check their suitability in accordance with IS: 2386 Part I to VI (1997). Properties discussed in Table 2 show variation in parameters for natural and recycled aggregates, however, the recorded parameters were found to be under acceptable limits for recycled concrete aggregates after surface treatment.

Gradation: Aggregates used in the study were also checked for their gradation as per IS: 383 (1999) and MoRTH (2013). The combined gradation of coarse natural and recycled concrete aggregates are given in Table 3.

Table 1. Cement Properties

	Specific gravity	Fineness percent (%)	Soundness (mm)	Initial setting time (min)	Final wetting time (min)	Consistency (%)
Obtained values	3.15	1.5	2	63	161	28

(a)   **(b)**

Fig. 1. a and b) Recycled concrete aggregates processed from demolished concrete waste

Table 2. Aggregate properties

Type of aggregate	Specific gravity	Water absorption (%)	Aggregate impact value (%)	Crushing value (%)
Acceptable limits	2.5-3.0	0.1-2%	30%	30%
Natural aggregate	2.677	0.274	13.88	17.775
Untreated RCA	2.417	3.18	22.23	19.42
Treated RCA	2.660	1.88	15.67	17.91

Table 3. Combined gradation of coarse aggregates

IS sieve (mm)	Upper limit	Lower limit	Combined gradation for conventional aggregates	Combined gradation for recycled aggregates
40	100	100	100	100
20	100	95	94.41	92
10	55	25	37.47	37
4.75	10	0	1.85	0

Figure 2 represents the graphical plots for combined gradation of coarse natural as well as recycled concrete aggregates. Efforts were made to achieve gradation of recycled aggregates similar to those of natural ones. The gradation of recycled concrete aggregates closely follows the gradation of natural aggregates plot, while for both aggregate types the gradation fits perfectly between the specified limits.

Fine Aggregates: Riverbed sand procured from a local river was used as fine aggregate in this study. The fine aggregates used were found to be belonging to Zone II grade with a fineness modulus of 2.76.

3.1.3. Water

In order to prepare concrete mix and for moist curing of concrete specimens, potable water conforming to IS: 456 (2001) was used.

3.1.4. Mineral Admixture

In order to promote the use of locally available materials efforts were made to incorporate mineral admixtures procured locally or from nearby sources. Fly ash, rice husk ash and bagasse ash were included as mineral admixtures in this study. All the mineral admixtures were assimilated as part additions to binder in concrete mixes. The physical properties and composition of these mineral admixtures are discussed below.

Class F Fly ash procured from the nearest thermal power plant having a specific gravity of 2.24 was used in the study. Rice husk ash used in study was obtained by incinerating locally procured rice husk. Similarly, Bagasse ash was obtained from a local jaggery-manufacturing unit. The specific gravity of Rice husk ash and bagasse ash were reported as 1.81 and 2.38 respectively. Further, Table 4 gives the chemical compositions of all three mineral admixtures determined in laboratory.

3.2. Concrete Mixtures

The concrete mixes under study were designed in accordance with specifications discussed in (Indian Road Congress) IRC 15 (2011) citing the incorporations from IRC 44 (2017) to be intended for concrete pavements. In order to determine mechanical and microscopic properties, investigations on pavement quality concrete mix incorporating recycled concrete aggregates and mineral admixtures were carried out in this study.

In the previous part of study recycled concrete aggregates were incorporated at different levels ranging from 10% to 50% where it was established that mixes with RCA content up to 30% had test values within the specified limits, thus suggesting their potential use for pavement quality concrete (Jindal et al., 2017). Therefore, in this part of study recycled concrete aggregates were included at an optimized level of 30%.

Three different mineral admixtures were used in different proportions (5%, 10%, 15%) along with recycled concrete aggregates as part substitution of coarse aggregates (30% substitution level) in the study. Accordingly, a total of 11 concrete mixes were prepared and investigated for desired properties as presented in Table 5. Amongst 11 concrete mix, one concrete mix designated as NAC was prepared as a base mix (no recycled concrete aggregates and no mineral admixtures) and one concrete mix designated as RAC was prepared with inclusions of recycled concrete aggregates only (no mineral admixtures). A total of 9 concrete mixes containing substituted RCA and mineral admixture are defined by code RAC-Z-n, where the part RAC represents recycled aggregate concrete, Z stands for individual mineral admixture type (F for fly ash, RA for rice husk ash and BA for bagasse ash) and finally 'n' defines the incorporation level of mineral admixture (1 for 5%, 2 for 10% and 3 for 15%). Thus RAC-F-3 represent PQC mix incorporating RCA and 15% fly ash, RAC-RA-1 represent PQC mix incorporating RCA and 5% rice husk ash and RAC-BA-2 represent mix RCA and 10% bagasse ash.
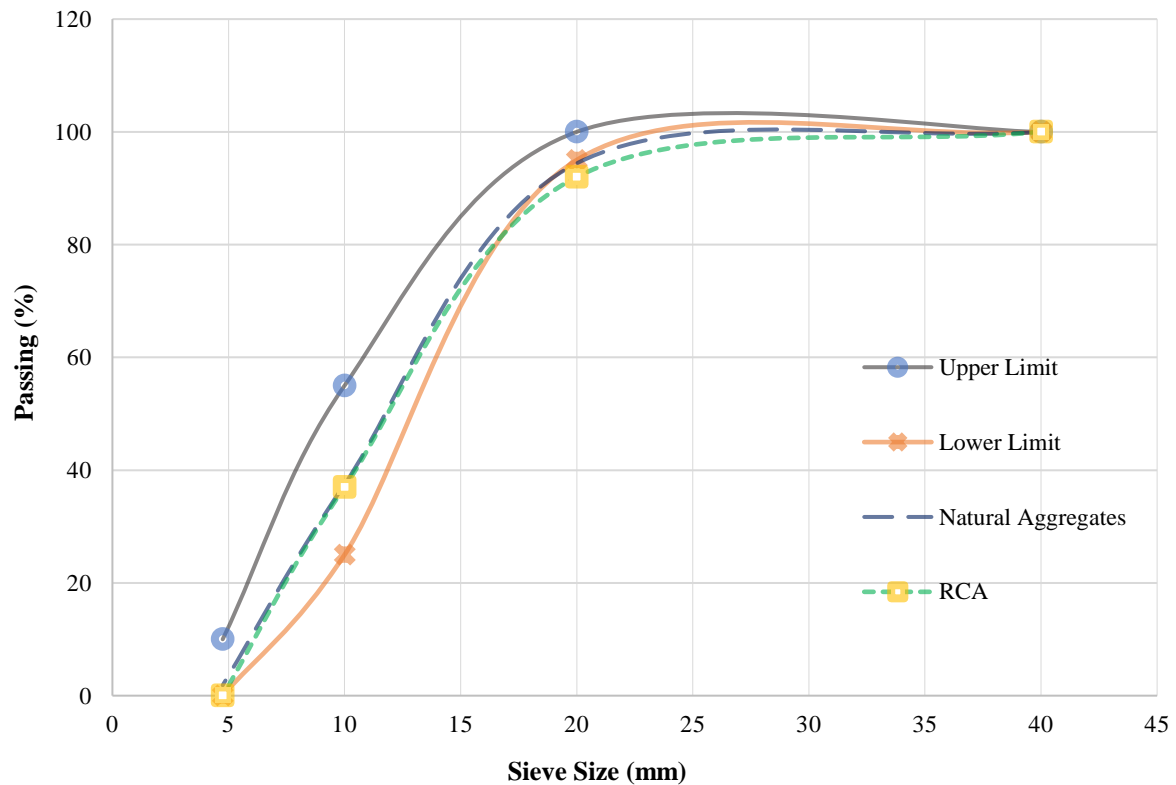
Fig. 1. (a & b): Recycled concrete aggregates processed from demolished concrete waste

Table 4. Chemical composition of mineral admixtures

Mineral admixture	SiO$_2$	Fe$_2$O$_3$	Al$_2$O$_3$	CaO	MgO
Fly ash	58.78	9.31	26.92	1.77	0.68
Rice husk ash	62.75	24.18	2.4	2.76	5.12
Bagasse ash	65.27	2.1	3.11	11.16	1.27

Table 5. Proportions of concrete mixes

Mix	Cement (Kg/m³)	Water (lit)	Fine aggregate (Kg/m³)	Coarse aggregate (Kg/m³)	Recycled aggregate (Kg)	Mineral admixture (Kg)
NAC	400	173	660.22	1180	0	0
RAC	400	173	660.22	826	354	0
RAC-F-1	400	173	660.22	826	354	20
RAC-F-2	400	173	660.22	826	354	40
RAC-F-3	400	173	660.22	826	354	60
RAC-RA-1	400	173	660.22	826	354	20
RAC-RA-2	400	173	660.22	826	354	40
RAC-RA-3	400	173	660.22	826	354	60
RAC-BA-1	400	173	660.22	826	354	20
RAC-BA-2	400	173	660.22	826	354	40
RAC-BA-3	400	173	660.22	826	354	60

4. Study on Hardened Concrete

Behaviour of hardened concrete was studied using destructive testing techniques for the different concrete mixes under study. Representative specimens were investigated for their strength parameters in accordance with IS: 516 (1959) and IS: 5816 (1999). In addition to mechanical properties, efforts were carried out to determine density and water absorption values. Strength parameters recorded at 3, 7 and 28 days of moist curing at room temperature in accordance with IS 456 (2001) and IRC 84 (1983) and density and water absorption parameters observed at 28 days are summarized in Table 6.

Table 6. Strength, density and water absorption values for concrete mixes under study

Mix	Compressive strength (MPa)			Flexural strength (MPa)			Split tensile strength (MPa)			Hardened density (gm/cc)	Water absorption (%)
	3 days	7 days	28 days	3 days	7 days	28 days	3 days	7 days	28 days	28 days	28 days
NAC	18.16	27.17	39.57	2.19	3.68	6.09	1.83	2.12	3.53	2.51	2.117
RAC	16.24	23.77	35.59	2.25	3.41	4.92	2.12	2.54	2.96	2.50	2.3114
RAC-F-1	19.34	25.54	37.06	2.47	3.92	5.40	1.98	2.82	3.10	2.52	2.295
RAC-F-2	20.38	25.99	38.10	2.45	3.43	5.16	1.98	2.40	2.96	2.50	2.204
RAC-F-3	18.46	27.46	41.34	2.41	3.88	6.27	2.12	2.54	3.81	2.49	2.15
RAC-RA-1	17.13	23.77	37.06	2.23	3.62	5.28	1.69	2.40	3.24	2.48	2.31
RAC-RA-2	16.83	23.03	39.13	2.37	3.31	5.52	1.69	2.33	3.53	2.45	2.295
RAC-RA-3	17.42	23.77	40.46	2.39	3.56	6.31	1.98	2.54	3.67	2.45	2.25
RAC-BA-1	17.87	25.10	37.06	2.33	4.24	5.12	1.69	1.98	2.82	2.50	2.35
RAC-BA-2	17.28	24.07	38.54	3.29	4.18	5.87	1.69	2.40	2.96	2.49	2.295
RAC-BA-3	18.31	24.36	40.60	2.35	3.90	6.05	1.83	2.54	3.67	2.49	2.21

4.1. Compressive, Flexural and Splitting Tensile Strength

Hardened concrete specimens representative of different mixes were tested destructively for their compressive, flexural and splitting tensile strength. Efforts were made to establish relationships between the compressive, flexural and split tensile strength values for concrete mix with RCA and mineral admixtures using the experimental data obtained during study. Figure 3 presents compressive, flexural and split tensile strength parameters developed for mixes RAC-F, RAC-RA and RAC-BA respectively.

Incorporating RCA as part replacement of coarse aggregates did lead to reduction in strength in comparison to mix with natural aggregates as discussed by Jindal and Ransinchung (2018). This behaviour of mix with recycled concrete aggregates was found to be similar to studies discussed by Xiao et al. (2005), Limbachiya et al. (2004), Akbari et al. (2011), etc. An increase in strength to the order of 15% for compressive strength and 24% for flexural strength for fly ash admixed mix i.e. RAC-F-3 mix were recorded from Figures 2-4 while the strength gain for rice husk ash admixed mix i.e. RAC-RA-3 mix were to the order of 12% for compressive strength and 25% for flexural strength in comparison to RAC mix. Similar increase in strength values were recorded for mix with bagasse ash i.e. RAC-BA-3 mix to the order of 13% for compressive strength and 20% for

flexural strength. This increase in strength upon inclusion of fly ash, rice husk ash or bagasse ash is in accordance with results discussed by Kou (2012) and Tangchirapat (2010) for fly ash additions in recycled aggregate concretes.

Improvement in strength parameters could be attributed to the incorporation of fine particulate mineral admixtures which owing to their pozzolanic properties helped in better strength development for the mix thereby bringing them on par with that of the mix with natural aggregates only and greater than that for the mix with incorporation of recycled concrete aggregates and no mineral admixtures.

4.2. Hardened Density and Water Absorption

Hardened specimens of concrete mix under study were studied for density and water absorption properties in order to understand the benefits of including recycled concrete aggregates and mineral admixtures on the concrete matrix. Recycled concrete aggregates used in study themselves were found to be having inferior density and water absorption values in comparison to their natural counterparts. This inferiority was thus reflected profoundly in parameters recorded for RAC mix in comparison to NAC mix as discussed in past studies carried out by Joseph et al. (2015), Peng et al. (2013) and many more.

Incorporating fine particulate mineral

admixtures resulted in improving the density and water absorption parameters for different concrete mixes as visible from Figures 4 and 5, respectively. The density values recorded for mix RAC-F-3, RAC-RA-3 and RAC-BA-3 were found to be comparable to that for the NAC mix while similar trends were observed for water absorption parameters. This betterment in density and water absorption behaviour could be credited to ultrafine particulate mineral admixtures which have improved the mix thus making it less permeable.

⌗ Split Tensile Strength (MPa)   **Ⅲ Flexural Strength (MPa)**   **■ Compressive Strength (MPa)**
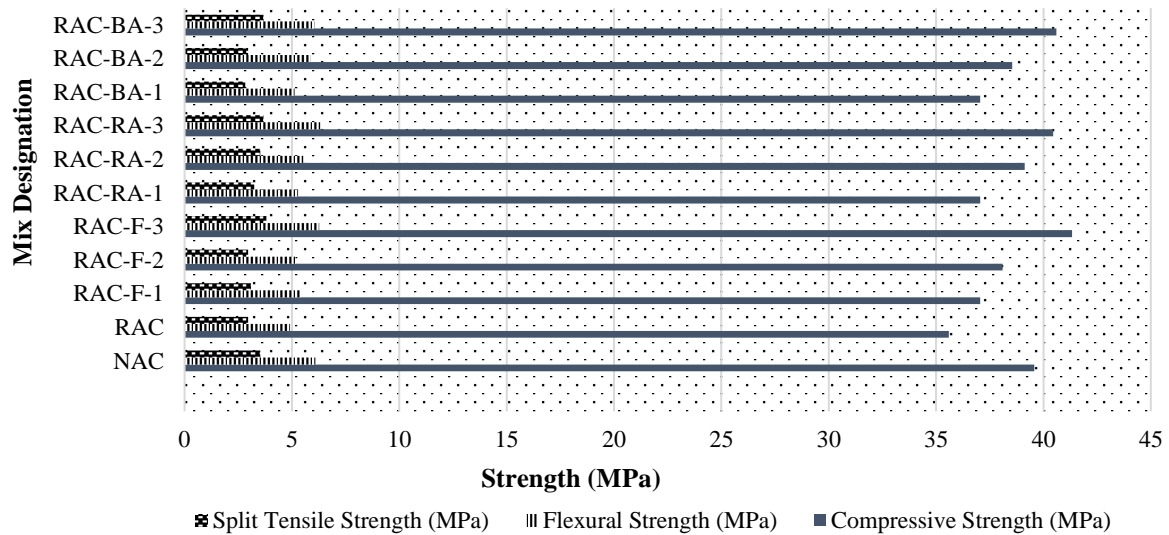
Fig. 3. Compressive Strength, Flexural Strength and Tensile Strength plots for different concrete mix under study
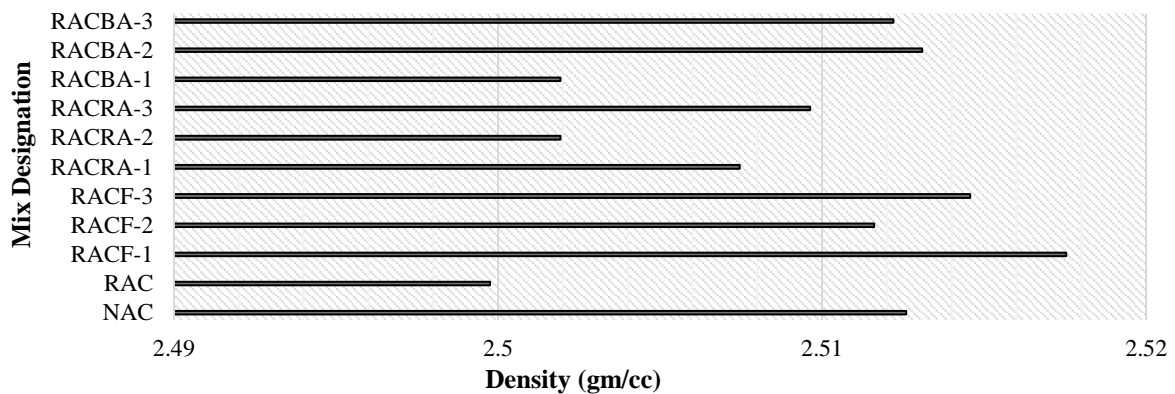
Fig. 4. Hardened density trends
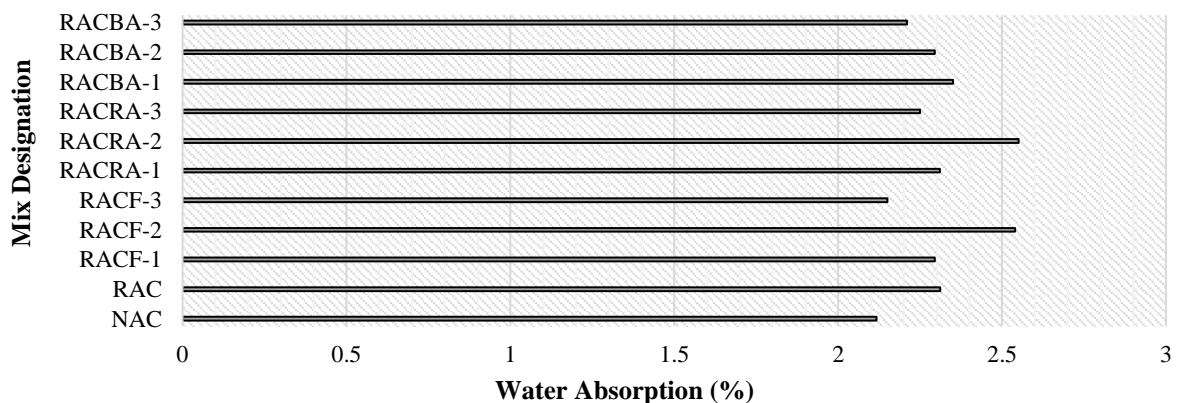
Fig. 5. Water absorption trends

5. Inter-Spatial and Compositional Study

5.1. SEM and EDS Analysis

Incorporation of micro sized particles influences the morphology of concrete in different ways, thus it becomes imperative to understand microscopic changes occurring in concrete with the inclusion of mineral admixtures and recycled concrete aggregates. The Scanning Electron Microscope (SEM) is an instrument, which is used very widely due to its versatility for examination and analysis of microstructural characteristics of solid objects. The microscope generates high-resolution images of shapes of objects which show spatial variations in chemical composition and surface morphology. Energy Dispersive Spectroscopy (EDS) measures the energy and intensity distribution of X-ray signals generated by the electron beam striking the surface of the specimen to help perform elemental analysis of surfaces in SEM. The specimens of concrete mix under study were observed for their SEM images at a curing age of 28 days in order to get a better idea about changes in hydration behaviour upon inclusion of fine particulate mineral admixtures.

The images developed from the SEM were analysed for identification of different hydration products present in the representative samples of different concrete mixes previously discussed by Jindal and Ransinchung (2018). SEM images obtained for different concrete mixes under study are presented in Appendix I.

It was found that hydrated matrix for natural aggregate concrete mix (NAC) had presence of calcium silicate hydrates (C-S-H) in abundance along with other hydration products such as hydroxides and ettringites identifiable as hexagonal prismatic and needle shaped components. On the other hand, the SEM image for RAC mix shows abundance of hydroxides and ettringites thereby suggesting improper hydration which might have led to less bonding and the same was visible from strength parameters discussed above.

Fly ash incorporated as a supplementary cementitious material is responsible for additional hydration products and filler effect when incorporated in concrete mix as discussed by Panesar (2019). SEM images for concrete mixes with recycled concrete aggregates and fly ash (RAC-F mixes) show profound presence of CSH gels and other hydrated products. This is also reflected as increase in strength of concrete mixes upon incorporation of fly ash. Similar trends for concrete with recycled concrete aggregates and fly ash were reported in studies carried out by Shi et al. (2013) and Singh and Singh (2016) depicting more hydration products.

SEM images for concrete mix prepared with inclusions of rice husk ash highlighted the presence of increased quantity of products of hydration and less voids. This has led to gain in strength which has been discussed by other researchers such as Jongpradist et al. (2018) and Zareei et al. (2017) and attributed to the pozzolanic behaviour of rice husk ash.

SEM images obtained for concrete mix specimens prepared upon the addition of bagasse ash as mineral admixture also show increased hydration products in comparison to SEM images for NAC and RAC mix. These variations are similar to those visible for RAC-F and RAC-RA mix. Reduction in voids and profound increase of prismatic components confirms the presence of more hydration products. Studies carried out by Amin (2019) also concluded that concrete containing rice husk ash reported better pozzolanic activity in comparison to natural counterpart.

The concrete mix incorporating recycled concrete aggregate showed more voids and less hydration products in comparison to reference or conventional concrete mix. This could be explained as improper hydration due to recycled concrete aggregates which absorb water from the mix resulting in reduction of strength. Using mineral admixtures however, led to reduction in voids due to additional hydration products owing to their

pozzolanic properties. This reduction of voids is supported by reduced values of water absorption and increase in hardened density parameters indicating better durability and increased strength values.

5.2. XRD Analysis

Incorporation of micro-sized mineral admixtures resulted in variations in properties of pavement quality concrete containing RCA. These variations observed on a macro scale by investigating concrete properties are incurred due to variations at micro levels in concrete. The variations concerning morphological changes were studied with the help of SEM while the variations in hydration products were analysed by studying XRD patterns of different mixes.

The crystallographic data obtained after phase analysis for powdered samples of concrete mixes incorporating different types and proportions of mineral admixtures were needed to be further analyzed. Xpert High Score Plus a tool competent for analyzing the crystallographic data was used for analyzing the XRD data. XRD patterns obtained for different mixes under study after analysis are presented in Appendix II.

Interpretations made from the XRD study are discussed below:

i) Influence of Fly ash

The inclusion of fly ash in concrete mix tends to improve the chemical rate of reactions during hydration. More ettringite and C3A was observed for mixes containing fly ash than those for NAC and RAC mixes. Visible improvements in formation of C-S-H gels with the increase in incorporation level of fly ash falls in conformity with strength improvements observed during investigations of mechanical properties. This could be attributed to the presence of silica in fly ash which reacts with free calcium hydroxide to produce calcium silicate hydrate which adds up to the hydration products resulting in improved mechanical and durability of concrete

mix.

ii) Influence of Rice husk ash

The crystallographic examination of concrete mixes incorporating RCA and rice husk ash showed variations in compound compositions in comparison to RAC mix. The increased presence of C-S-H gels and ettringite as hydration products shows similar composition as those of NAC mix. This is attributed to pozollanic properties of rice husk ash due to which the amorphous silica in rice husk ash reacts with calcium hydroxide to produce excess calcium silicate hydrates which results in better strength and durability of concrete.

iii) Influence of Bagasse ash

The hydration products identified for concrete mixes incorporating RCA and bagasse ash were observed to be similar to those of RAC-F and RCA-RA mixes with minor variations. The presence of silica leading to formation of excess C-S-H gels was observed as in the case of mixes with fly ash or rice husk ash, however a few peaks of calcium aluminum iron oxide were also identified for mixes with bagasse ash. This may be attributed to reaction between calcium oxide, alumina and a part of iron oxide present in RCA thus producing calcium aluminum iron oxide. The presence of ettringite, tri calcium aluminate and reductions in portlandite indicates improved hydration which is reflected as improvement in concrete properties.

Finally, it was established that the mineral admixtures used in this study were siliceous in nature, this resulted in formation of more hydration products which is visible from XRD analysis. Formation of additional CSH resulted in improved strength and durability of concrete.

5.3. Porosity Studies

Durability of concrete is a very important factor while assessing its performance. Determination of pore structure including pore size, pore

distribution and cumulative surface area gives an idea about the permeability of a concrete specimen under study which in turn leads to assessment of its durability. Including micro sized mineral admixtures contributes in the hydration process thereby altering the pore structure of concrete, thus the pore structure of concrete specimens incorporating different mineral admixtures was investigated using the mercury intrusion technique which provides information on relative contribution of different sized pores. Figure 6 presents the Mercury Porosimeter used for porosity studies as well as the representative specimens of concrete mix under study.

The concrete mixes containing RCA and different mineral admixtures were investigated for average pore diameter, total pore volume, total mercury intrusion and cumulative surface area. In order to determine the variations, concrete specimens prepared without RCA and mineral admixture, and one mix containing RCA and no mineral admixtures were also investigated for similar properties. The specimens were tested in pressure ranging from atmospheric pressure to 34.5 Mpa. The results obtained from porosity investigations are summarized in Table 7.

The size of pores for the NAC mix specimen were observed to be varying from a few microns to around 100 microns. The total volume of mercury intruded in the concrete specimen was found to be 0.0287 cc/g while the average pore diameter was observed to be 0.1297 microns. It was also observed that pressurized mercury could achieve contact with micro pores sized up to 1 micron which contributed towards the cumulative contact surface area.

(a)   **(b)**

Fig. 6. a) Mercury Porosimeter; and b) Concrete specimens

Table 7. Porosity data for concrete mix under study

| Mix | Total intrusion volume (cc/g) | Total surface area (m²/g) | Median pore diameter (microns) | | Average pore diameter (microns) |
			Based on volume	Based on surface area	
NAC	0.029	0.886	0.162	0.076	0.130
RAC	0.034	0.271	0.592	0.174	0.355
RAC-F-1	0.046	1.249	0.186	0.077	0.147
RAC-F-2	0.035	0.271	0.158	0.062	0.121
RAC-F-3	0.024	0.194	0.093	0.043	0.050
RAC-RA-1	0.133	5.153	0.109	0.063	0.103
RAC-RA-2	0.090	3.585	0.103	0.065	0.100
RAC-RA-3	0.030	1.073	0.108	0.071	0.111
RAC-BA-1	0.051	1.777	0.134	0.070	0.115
RAC-BA-2	0.014	0.098	1.562	0.215	0.553
RAC-BA-3	0.038	1.268	0.123	0.075	0.119

The pore structure of the concrete specimen from RAC mix was observed to be different from that of NAC mix. The average size of pores was found to be 0.3547 microns which was much higher in comparison to 0.1297 microns for NAC mix. This increase in pore size was previously anticipated due to porous adhered mortar surrounding aggregate particle and is supported by increased water absorption values for RAC mix. It was found that around 99% of the total volume of pores was constituted by pores sized up to 3 microns which also increased the total contact surface between mercury and specimen pores. It could be easily interpreted that the RAC mix has higher and bigger sized pores in the specimen in comparison to NAC mix which increased the porosity of the mix and was reflected in corresponding water absorption values.

It was observed for the specimen of RAC mix that inclusions of RCA led to increase in total pore volume along with increase in pore diameter. Mix RAC-F-1 incorporated 5% fly ash along with RCA due to which the micro fine particles of fly ash participated in the hydration process thereby contributing to hydrated products. This led to slight reduction in total pore volume along with visible reductions in pore size. Around 99% of total pore volume for this specimen was found to be consisting of pores sized around 3 microns. Also the pores contributing to cumulative surface area were found to be smaller in size in comparison to those in RAC mix. The minimum size of pores contributing towards cumulative surface area was observed to be around 1 micron.

The pore structure of RAC-F-2 mix was observed to be very similar to the pore behaviour of RAC-F-1 mix with minor alterations. The average pore diameter for the RAC-F-2 specimen was observed to be 0.1214 microns compared to 0.1469 microns for RAC-F-1 mix. The total intrusion volume of mercury was also observed to be reduced from 0.0459 cc/g for RAC-F-1 mix to 0.0347 cc/g for RAC-F-2

mix. This shows that increasing the content of fly ash in concrete with RCA altered the pore structure of concrete by reducing the pore volume along with the size of pores.

Among the specimens tested for concrete mix containing RCA and fly ash, RAC-F-3 showed significant variations in pore structure in comparison to NAC and RAC mix. The average pore diameter for RAC-F-3 mix was found to be 0.0502 microns which was even smaller than 0.1297 microns for NAC mix. Also the total volume of mercury penetrated into the specimen was observed as 0.0244 cc/g for RAC-F-3 mix which is silently less than 0.0287 cc/g for NAC mix.

Reductions observed in parameters of pore diameter and intrusion volume indicate improved pore structure attributed to fly ash incorporation in mix. Calcium rich minerals present in fine particulate fly ash tend to react with free lime during hydration which increases the products of hydration, leading to refinement in pore structure thus making the concrete mix more durable.

Subsuming rice husk ash in the mix along with RCA led to variations in pore behaviour of concrete. The average size of pores was observed to be reduced from 0.3547 microns for RAC mix to 0.1029 microns for RAC-RA-1 mix which was also less than 0.1297 microns for NAC mix . The total volume of intrusion of mercury into the specimen is an indication of the volume of pores present in the sample which could be intruded by mercury under pressure. Around 80% of total pore volume in the tested specimen was observed to be constituted by pores with size less than 1 micron while RAC mix showed a majority pore volume consisting of pores sized less than 3 microns. This shows that incorporation of rice husk ash helped in reducing the pore size of concrete. Rice husk ash has pozzolanic properties due to presence of silica, alumina and calcium oxide which adds to the hydration process thereby resulting in less pores and thus less permeable concrete.

Pore parameters for mix RAC-RA-2

showed that increasing the content of rice husk ash from 5% in RAC-RA-1 to 10% in RAC-RA-2 led to marginal variations in porosity parameters and pore structure. The average pore size was observed to be 0.0999 microns which was that of both NAC and RAC mix however when compared with RAC-RA-1, the reduction was marginal for average pore size. For RAC-RA-2, around 83% of total pore volume was found to be consisting of pores sized less than 1 micron while for RAC-RA-1 this quantity was around 80% indicating a slight decrease in pore size on increasing the content of rice husk ash.

The reduction in pore volume was visible for concrete with increase in proportions of rice husk ash. This is in accordance with reduced values of water absorption and increased hydration products visible in SEM images for the respective mixes. Similar behaviour was observed for all the mixes with rice husk ash showing improved pore structures which will enhance the durability of concrete. Mix RAC-RA-3 showed average pore size around 0.1113 microns with a total intrusion volume of mercury as 0.0298 cc/g approximately. These parameters show improvement in pore structure in comparison to RAC mix which will correct the deficiencies incurred due to usage of RCA in concrete.

Adding bagasse ash to concrete containing recycled concrete aggregates showed similar effects on concrete with reductions in quantity of pores and also the pore size. Mix RAC-BA-1 recorded an average pore size to be 0.1151 microns which was smaller than those for RAC mix and marginally smaller than the pore size of NAC mix. The total volume of mercury penetrated in the specimen was also found to be lowered in comparison to parameters recorded for RAC mix. This indicates improvement in pore structure of recycled aggregate concrete thereby reducing the volume and size of pores due to enhanced hydration filling up micro pores.

For mix RAC-BA-2 increasing the quantity of bagasse ash from 5% to 10% led to reduction of total mercury volume from 0.0511 cc/g for RAC-BA-1 to 0.0136 cc/g. The maximum size of pores contributing towards cumulative surface area of contact between mercury and pores was found to be around 3 microns. The porosity associated parameters for mix RAC-BA-3 show visible reductions in pores and their size in comparison to RAC mix. The specimen tested for mix RAC-BA-3 recorded an average pore size of 0.1189 microns which was less than the average pore size for both NAC and RAC mix, thus showing appreciable pore variation corresponding to reference natural aggregate concrete mix and mix incorporating recycled concrete aggregates.

Mix with 5% fly ash i.e. RAC-F-1 showed pore behaviour quite similar to that of RAC; however, increasing the proportions of fly ash to 15% led to pore structure refinement of concrete observed with reductions in average pore size and total intrusion volume. Incorporation of rice husk ash also tends to modify the pore structure of concrete thereby improving its mechanical and durability properties. Specimens representing mix RAC-RA-1 and RAC-RA-2 reflected minor variations in porosity parameters, however much improvement was observed for the mix with 15% rice husk ash i.e. RAC-RA-3. Concrete mixes containing bagasse ash were also observed to have improved pore structure with reduction in total pore volume as well as the average size of pores.

This shows that the volume of pores for concrete mix incorporating higher dosage of mineral admixtures i.e. 15% are amounting a few microns which indicates the concrete mix being less permeable thus indicating concrete being more durable. This modification in pore structure of concrete mix is attributed to the pozollanic properties of mineral admixtures which participate in the hydration process thereby filling the micro pores which is reflected as improvement in mechanical and durability properties of concrete thereby rendering

concrete mix more durable and strong and bringing it to par with that of natural aggregate concrete.

6. Conclusions

The following conclusions were drawn from the above study:

i) Inducing 15% mineral admixtures in PQC mix having recycled concrete aggregate resulted in improved mechanical properties. An increase in compressive strength in the order of 4%, 2% and 2.5% was observed for mix admixed with fly ash, rice husk ash and bagasse ash respectively, in comparison to NAC mix.

ii) The improvement trends obtained for flexural strength parameters were similar to those of compressive strength. When compared with RAC mix, the increase in flexural strength was found to be more pronounced for mixes with 15% mineral admixture. In comparison to RAC mix, an increase of about 24% for RAC-F-3 mix, 25% for RAC-RA-3 mix and 20% for RAC-BA-3 mix was recorded. This gain in flexural strength was also higher than NAC mix to the order of 3.5 % for RAC-RA-3 mix and 3% for RAC-F-3 mix.

iii) The split tensile strength of concrete mix with RCA improves with increase in percentage of mineral admixtures. Using 15% fly ash, rice husk ash or bagasse ash as an addition to cement in PQC mix consisting 30% RCA provides similar split tensile strength as that of NAC mix.

iv) Using fine particulate mineral admixtures as an addition to binder reduces the water absorption of PQC mix with RCA significantly. Addition of 15% fly ash, rice husk ash and bagasse ash results in reduction of water absorption of concrete mix by 7.2%, 2.69% and 4.5% respectively.

v) An SEM study helped in understanding the improved strength behaviour of PQC mix with different mineral admixtures. The pozzolanic behaviour of mineral

admixtures resulted in increased quantity of hydration products and thus less voids were observed.

vi) The mineral admixtures used in this study were siliceous in nature, this resulted in formation of more hydration products which is visible from XRD analysis. Formation of additional CSH resulted in improved strength and durability of concrete.

vii) Introduction of mineral admixtures led to refinement of pore structure of concrete. The ultra-fine particles of fly ash, rice husk ash or bagasse ash reduced the average pore size and cumulative pore volume of concretes. PQC mix with 15% mineral admixtures observed average pore size amounting to a few microns which indicates reduced permeability.

7. Acknowledgement

8. References

Abbas, A., Fathifazl, G., Burkan Isgor, O., Razaqpur, A.G., Fournier, B. and Foo, S. (2007). "Proposed method for determining the residual mortar content of recycled concrete aggregates", *Journal of ASTM International*, 5(1), 1-12.

Akbarnezhad, A., Ong, K.C.G., Zhang, M.H., Tam, C.T. and Foo, T.W.J. (2011). "Microwave-assisted beneficiation of recycled concrete aggregates", *Construction and Building Materials*, 25(8), 3469-3479.

Akbari, Y.V., Arora, N.K. and Vakil, M.D. (2011). "Effect of recycled aggregate on concrete properties", *International Journal of Earth Science and Engineering*, 4(6), 924-928.

Amin, M.N., Hissan, S., Shahzada, K., Khan, K. and Bibi, T. (2019). "Pozzolanic reactivity and the influence of rice husk ash on early-age autogenous shrinkage of concrete", *Frontiers in Materials*, 6, 150.

Arredondo-Rea, S.P., Corral-Higuera, R., Gómez-Soberón, J.M., Gámez-García, D.C., Bernal-Camacho, J.M., Rosas-Casarez, C.A. and Ungsson-Nieblas, M.J. (2019). "Durability parameters of reinforced recycled aggregate concrete: Case study", *Applied Sciences*, 9, 617.

Berndt, M.L. (2009). "Properties of sustainable concrete containing fly ash, slag and recycled concrete aggregate", *Construction and Building Materials*, 23(7), 2606-2613.

Çakır, Ö. (2014). "Experimental analysis of properties of Recycled Coarse Aggregate (RCA) concrete with mineral additives", *Construction and Building Materials*, 68, 17-25.

Cement and Concrete Association of New Zealand (CCANZ). (2013). *Best practice guide for the use of recycled aggregates in new concrete*, Technical Report, TR14.

Census of India. (2011). "Provisional population totals, census of India 2011: Urban agglomerations and cities", Retrieved from http://www. censusindia.gov.in/.

Centre for Science and Environment. (2020). India manages to recover and recycle only about 1 per cent of its construction and demolition (C&D) waste, says new CSE analysis, August 25, 2020, New Delhi.

Chen, K., Zhu, Z., Xue, T., Zhang, H., Wang, A., He, R., Yang, H. and Wang, Y. (2021). "Enhancement treatment of recycled concrete aggregates", *Frontiers in Built Environment*, 7, 739148.

CSE. (2014). Construction and Demolition Waste. Centre for Science and Engineering. Retrieved from http://cdn.cseindia.org/userfiles/Construction-and%20-demolition-waste.pdf.

de Oliveira, M.B. and Vazquez, E. (1996). "The influence of retained moisture in aggregate from recycling on the properties of new hardened concrete", *Waste Management*, 16, 113-117.

Etxeberria, M., Vazquez, E., Mari, A., Hendriks, C.F. and van Maasakkers, M.H.J. (2004). "Role and influence of recycled aggregate in recycled aggregate concrete", In: *Conference on Use of Recycled Materials in Buildings and Structures*, Barcelona.

Gagg, C.R. (2014). "Cement and concrete as an engineering material: An historic appraisal and case study analysis", *Engineering Failure Analysis*, 40, 114-140.

Grabiec, A.M., Klama, J., Zawal, D. and Krupa, D. (2012). "Modification of recycled concrete aggregate by calcium carbonate bio-deposition", *Construction and Building Materials*, 34, 145-150.

Hatungimana, D., Yazıcı, Ş. and Mardani-Aghabaglou, A. (2020). "Effect of recycled concrete aggregate quality on properties of concrete", *Journal of Green Building*, 15(2), 57-69.

Martínez-Lage, I., Martínez-Abella, F., Vázquez-Herrero, C. and Pérez-Ordóñez, J.L. (2005). "Properties of plain concrete made with mixed recycled coarse aggregate", *Construction and Building Materials*, 37, 171-176

IRC: 15. (2011). "Standard specifications and code of practice for construction of concrete roads", *Indian Road Congress*, New Delhi, India.

IRC: 44. (2017). "Guidelines for cement concrete mix design for pavements", *Indian Road Congress*, New Delhi, India.

IS 383. (1999). *Specification for coarse and fine aggregates from natural aggregates sources for concrete*, Bureau of Indian Standards.

IS 516. (1959). *Methods of test for strength of concrete*, Bureau of Indian Standards.

IS: 2386 Part I to VI. (1997). *Methods of test for aggregates for concrete*, Bureau of Indian Standards.

IS: 456. (2001). *Plain and reinforced concrete - code of practice,* Bureau of Indian Standards.

IS: 5816. (1999). *Methods of test for splitting tensile strength of concrete*, Bureau of Indian Standards.

IRC: 84. (1983). Code of practice for curing of cement concrete pavements, *Indian Road Congress*, New Delhi, India.

IS: 8112. (1989). *43 Grade ordinary Portland cement - specification*, Bureau of Indian Standards.

Javed, M.F., Durrani, A.A., Kashif Ur Rehman, S., Aslam, F., Alabduljabbar, H. and Mosavi, A. (2021). "Effect of recycled coarse aggregate and Bagasse ash on two-stage concrete", *Crystals*, 11(5), 556.

Jindal, A., Ransinchung RN, G.D. and Kumar, P. (2017). "Study of pavement quality concrete mix incorporating beneficiated recycled concrete aggregates", *Road Materials and Pavement Design*, 18(5), 1159-1189.

Jindal, A. and Ransinchung, G.D. (2018). "Behavioural study of pavement quality concrete containing construction, industrial and agricultural wastes", *International Journal of Pavement Research and Technology*, 11(5), 488-501.

Jongpradist, P., Homtragoon, W., Sukkarak, R., Kongkitkul, W. and Jamsawang, P. (2018). "Efficiency of rice husk ash as cementitious material in high-strength cement-admixed clay", *Advances in Civil Engineering*, Article ID 8346319, 11 p.

Joseph, M., Boehme, L., Sierens, Z. and Vandewalle, L. (2015). "Water absorption variability of recycled concrete aggregates", *Magazine of Concrete Research*, 67(11), 592-597.

Kenai, S., Debieb, F. and Azzouz, L. (2005). "Performance of concrete made with recycled concrete and brick aggregate", In: *Inter American Conference on Non-Conventional Materials and Technologies in Ecological and Sustainable Construction*, *IAC-NOCMAT 2005*, Rio, Rio de Janeiro, Brazil, November.

Kou, S.C. and Poon, C.S. (2012). "Enhancing the durability properties of concrete prepared with

coarse recycled aggregate", *Construction and Building Materials*, 35, 69-76.

Lennon, M. (2005). *Recycling construction and demolition wastes: A guide for architects and contractors*, Boston, MA, USA: Commonwealth of Massachusetts, Department of Environmental Protection.

Limbachiya, M.C., Koulouris, A., Roberts, J.J. and Fried, A.N. (2004). "Performance of recycled aggregate concrete", *RILEM International Symposium on Environment - Conscious Materials and Systems for Sustainable Developments*, 127-136, Japan.

Maier, P.L. and Durham, S.A. (2012). "Beneficial use of recycled materials in concrete mixtures, *Construction and Building Materials*, 29, 428-437.

Meddah, M.S., Al-Harthy, A. and A. Ismail, M. (2020). "Recycled concrete aggregates and their influences on performances of low and normal strength concretes", *Buildings*, 10(9), 167.

MoRTH. (2013). "Specifications for road and bridge work", *Indian Road Congress*, Government of India, Ministry of Road Transport and Highways, New Delhi, India.

Nagapan, S., Rahman, I.A., Asmi, A., Memon, A.H. and Latif, I. (2012). "Issues on construction waste: The need for sustainable waste management", *IEEE Colloquium on Humanities, Science and Engineering Research (CHUSER 2012)*, Kota Kinabalu, Sabah, Malaysia, 329-334.

Padhi, R.S., Patra, R.K., Mukharjee, B.B. and Dey, T. (2018). "Influence of incorporation of rice husk ash and coarse recycled concrete aggregates on properties of concrete", *Construction and Building Materials*, 173, 289-297.

Panesar, D.K. (2019). "Supplementary cementing materials", *Developments in the Formulation and Reinforcement of Concrete*, 55-85.

Peng, G.-F., Huang, Y.-Z., Wang, H.-S., Zhang, J.-F. and Liu, Q.-B. (2013). "Mechanical properties of recycled aggregate concrete at low and high water/binder ratios", *Advances in Materials Science and Engineering*, 1-6.

Poon, C.S., Kou, S.C. and Lam, L. (2002). "Use of recycled aggregates in molded concrete bricks and blocks", *Construction and Building Materials*, 16(5), 281-289.

Rao, A., Jha, K.N. and Misra, S. (2007). "Use of aggregates from recycled construction and demolition waste in concrete", *Resources, Conservation and Recycling*, 50(1), 71-81

Sankhe S., Vittal I., Dobbs R., Mohan A., Gulati A., Ablett J., Gupta S., Kim A., Paul S., Sanghvi A. and Sethy G. (2010). *India's urban awakening: Building inclusive cities, sustaining economic growth*, McKinsey Global Institute.

Saravanakumar, P., Manoj, D. and Jagan, S. (2021). "Properties of concrete having treated recycled coarse aggregate and slag", *Revista de la Construcción*, 20(2), 249-258.

Shaban, W.M., Yang, J., Su, H., Liu, Q., Tsang, D. C. W., Wang, L., Xie J. and Li, L. (2019). "Properties of recycled concrete aggregates strengthened by different types of pozzolan slurry", *Construction and Building Materials*, 216, 632-647.

Shi, X.S., Wand, Q. Y., Li, L. and Long, T. (2013). "Properties of environmental friendly concrete containing recycled coarse aggregate and fly ash", *Applied Mechanics and Materials*, 368, 957-962.

Shima, H., Tateyashiki, H., Matsuhashi, R. and Yoshida, Y. (2005). "An advanced concrete recycling technology and its applicability assessment through input-output analysis", *Journal of Advanced Concrete Technology*, 3(1), 53-67.

Singh, N., and Singh, S.P. (2016). "Carbonation resistance and microstructural analysis of low and high volume fly ash self-compacting concrete containing recycled concrete aggregates", *Construction and Building Materials*, 127, 828-842.

Somna, R., Jaturapitakkul, C., and Amde, A.M. (2012). "Effect of ground fly ash and ground bagasse ash on the durability of recycled aggregate concrete", *Cement and Concrete Composites*, 34 (7), 848-854.

Jain, S., Singhal, S. and Jain, N.K. (2019). "Construction and demolition waste generation in cities in India: An integrated approach", *International Journal of Sustainable Engineering*, 12(5), 333-340.

Tam, V.W.Y., Tam, C.M. and Le, K.N. (2007). "Removal of cement mortar remains from recycled aggregate using pre-soaking approaches", *Resources, Conservation and Recycling*, 50(1), 82-101.

Tam, V.W. (2008). "Economic comparison of concrete recycling: A case study approach", *Resources, Conservation and Recycling*, 52, 821-828.

Tam, V.W.Y. and Lu, W. (2016). "Construction waste management profiles, practices, and performance: A cross-jurisdictional analysis in four countries", *Sustainability*, 8, 190.

Tangchirapat, W., Buranasing, R. and Jaturapitakkul, C. (2010). "Use of high fineness of fly ash to improve properties of recycled aggregate concrete", *Journal of Materials in Civil Engineering*, 22(6), 565-571.

TIFAC, E. (2001). *Utilisation of waste from construction industry*, New Delhi.

Tsujino, M., Noguchi, T., Tamura, M., Kanematsu, M. and Maruyama, I. (2007). "Application of conventionally recycled coarse aggregate to concrete structure by surface modification treatment", *Journal of Advanced Concrete*

Technology, 5(1), 13-25.

UN DESA. (2018). *World urbanization prospects: The 2018 revision*. New York: United Nations Department of Economic and Social Affairs, Population Division.

Wahi, N., Joseph, C., Tawie, R. and Ikau, R. (2015). "Critical review on construction waste control practices: Legislative and waste management perspective", *6^(th) International Research Symposium in Service Management (IRSSM-6 2015)*, UiTM Sarawak, Kuching, Malaysia, 276-283.

Wagih, A.M., El-Karmoty, H.Z., Ebid, M. and Okba, S.H. (2013). "Recycled construction and demolition concrete waste as aggregate for structural concrete", *HBRC Journal*, 9(3), 193-200.

Xiao, J., Li, J. and Zhang, C. (2005). "Mechanical properties of recycled aggregate concrete under uniaxial loading", *Cement and Concrete Research*, 35(6), 1187-1194.

Yong, P.C. and Teo, D.C.L. (2009). "Utilisation of recycled aggregate as coarse aggregate in concrete", *Journal of Civil Engineering, Science and Technology*, 1(1), 1-6

Zareei, S.A., Ameri, F., Dorostkar, F. and Ahmadi, M. (2017). "Rice husk ash as a partial replacement of cement in high strength concrete containing micro silica: Evaluating durability and mechanical properties", *Case Studies in Construction Materials*, 7, 73-81.

Zega, C.J. and Di Maio, A.A. (2011). "Recycled concretes made with waste ready-mix concrete as coarse aggregate", *Journal of Materials in Civil Engineering*, ASCE, 23(3), 281-286.
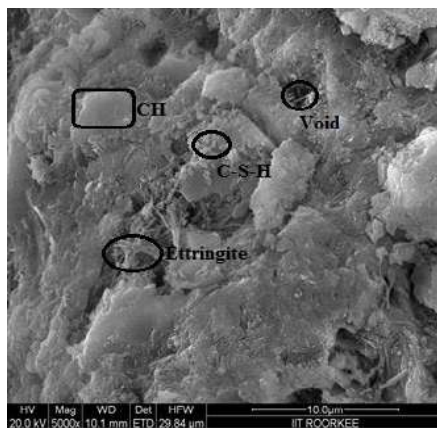
8. APPENDIX – I

Fig. 1. SEM image for NAC mix
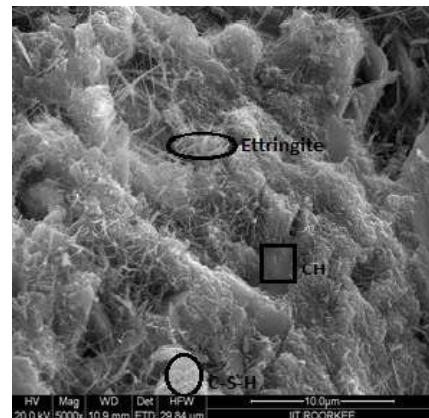
Fig. 2. SEM image for RAC mix
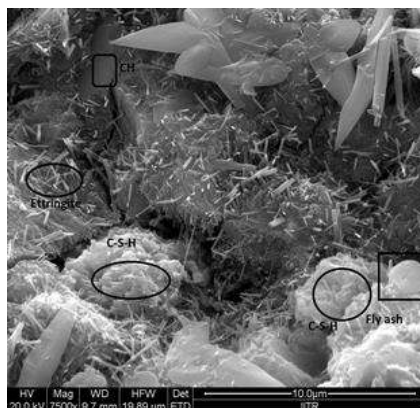
(a)
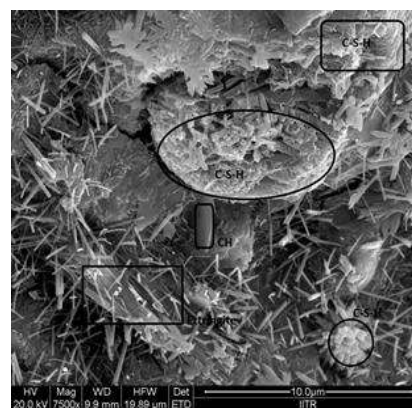
(b)
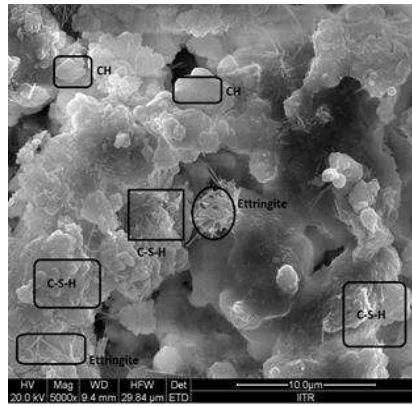
(c)

Fig. 3. SEM images for RAC-F: a) RAC-F-1; b) RAC-F-2; and c) RAC-F-3
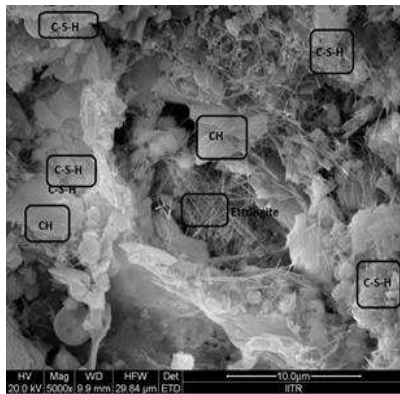
(a)
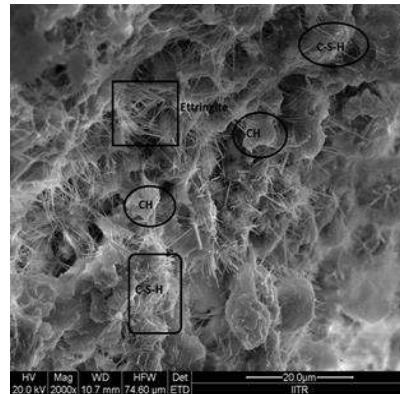
(b)
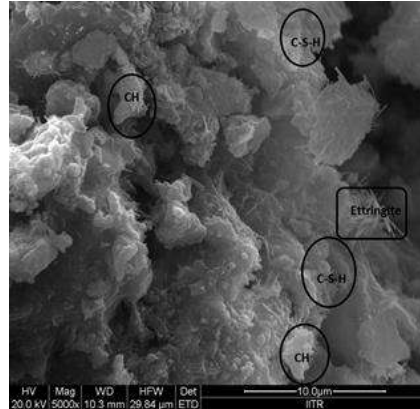
(c)

Fig. 4. SEM images for RAC-RA: a) RAC-RA-1; b) RAC-RA-2; c) RAC-RA-3
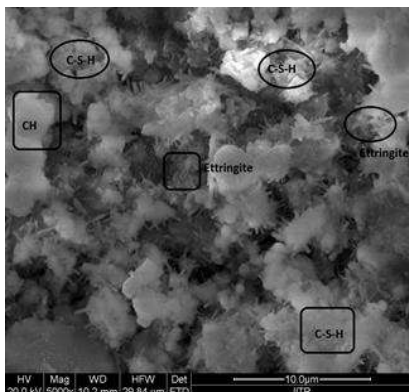
(a)
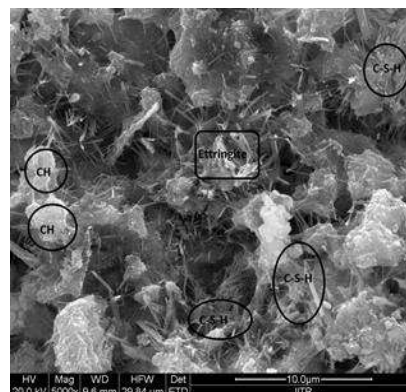
(b)
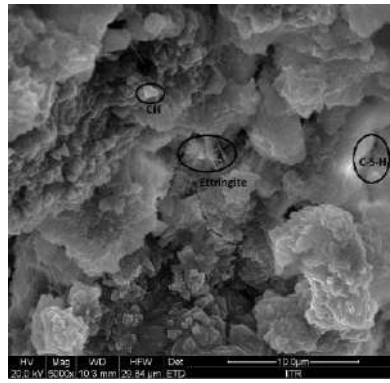
(c)

Fig. 5. SEM images for RAC-BA: a) RAC-BA-1; b) RAC-BA-2; and c) RAC-BA-3

8. APPENDIX – II

(a)

(b)
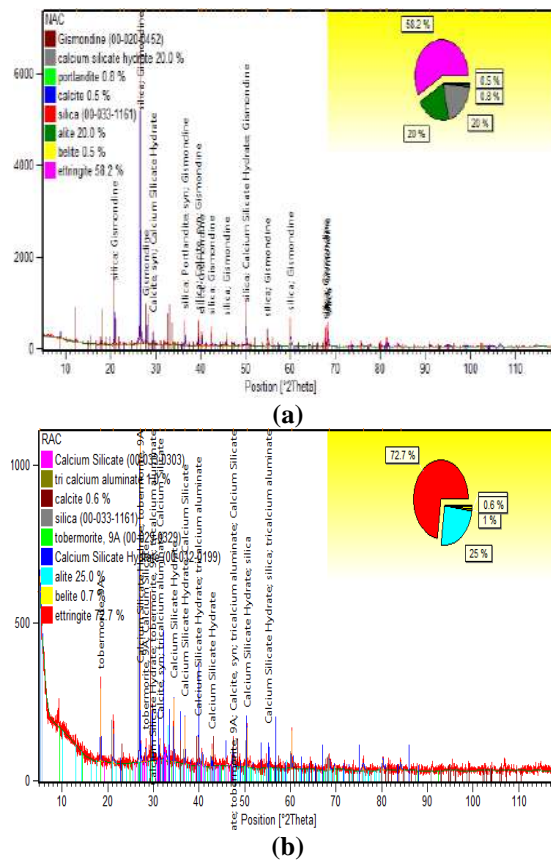
Fig. 1. XRD patterns: a) NAC mix; and b) RAC mix
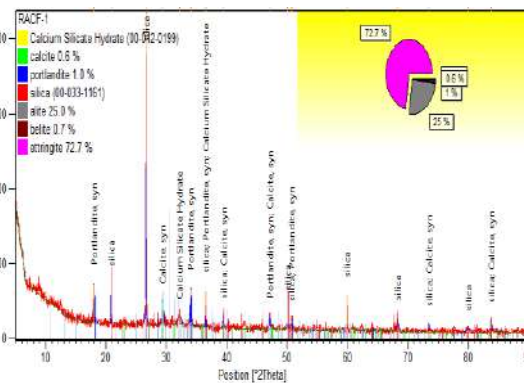
Fig. 2. XRD patterns for RAC-F-1 mix
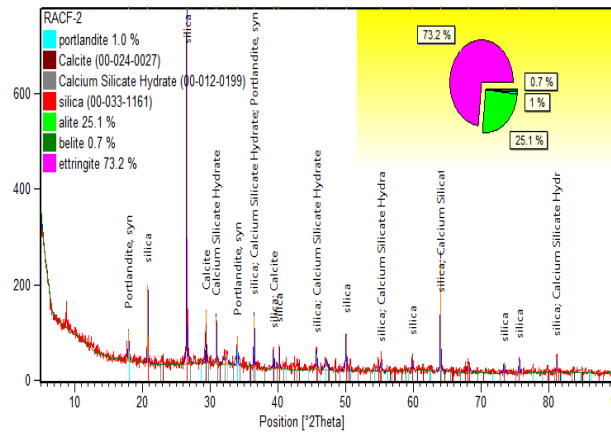
Fig. 3. XRD patterns for RAC-F-2 mix
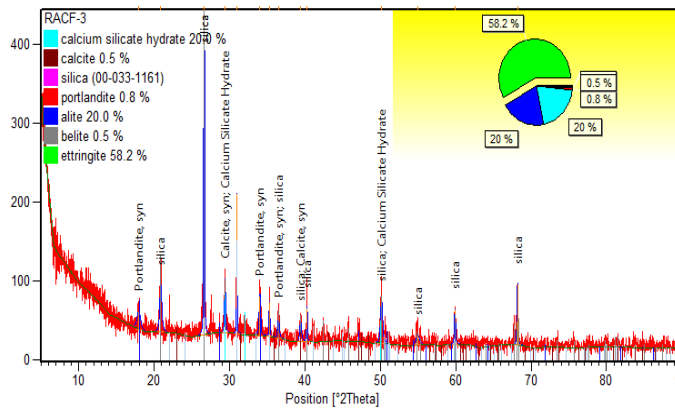
Fig. 4. XRD patterns for RAC-F-3 mix
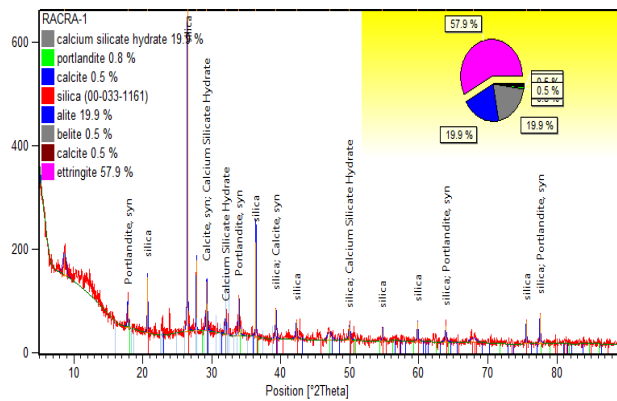
Fig. 5. XRD patterns for RAC-RA-1 mix
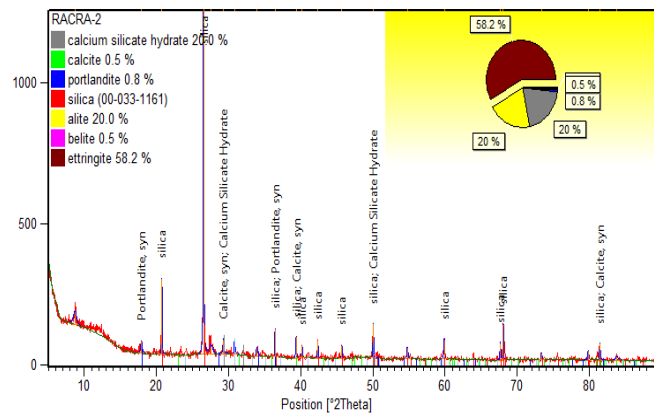
Fig. 6. XRD patterns for RAC-RA-2 mix
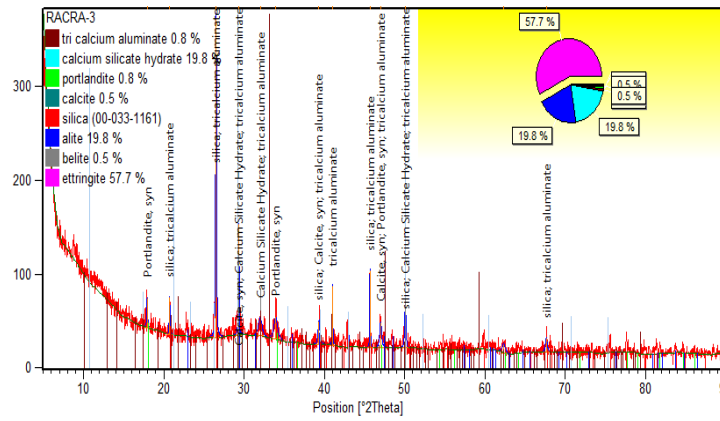
Fig. 7. XRD patterns for RAC-RA-3 mix
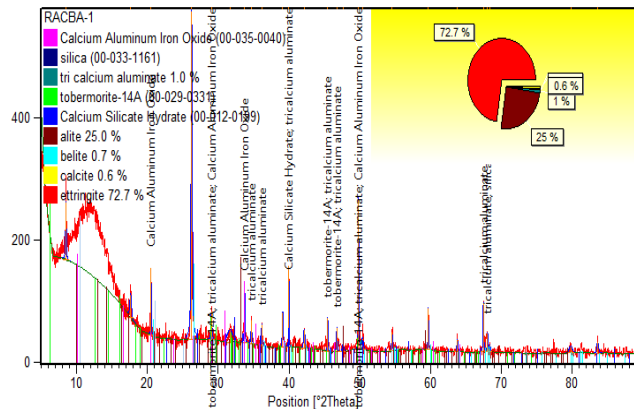
Fig. 8. XRD patterns for RAC-BA-1 mix
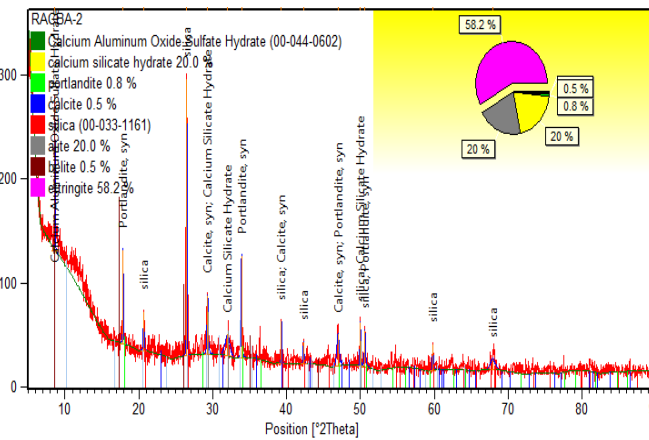
Fig. 9. XRD patterns for RAC-BA-2 mix
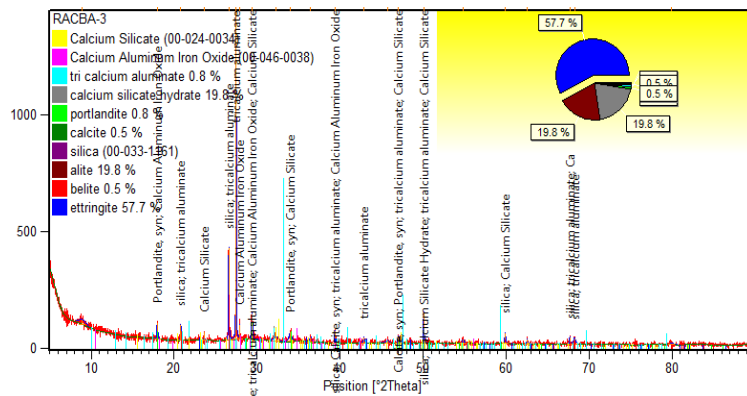
Fig. 10. XRD patterns for RAC-BA-3 mix

DEM Study of Shear Band Formation in Granular Materials under True Triaxial Test Conditions

Hadi, A.H.[1] and Mirghasemi, A.A.[2*]

[1] M.Sc. Student, School of Civil Engineering, College of Engineering, University of Tehran, Tehran, Iran, (Currently Ph.D. Candidate, Department of Maritime and Transport Technology, Faculty of 3ME, Delft University of Technology, Delft, the Netherlands).
[2] Professor, School of Civil Engineering, College of Engineering, University of Tehran, Tehran, Iran.

© University of Tehran 2022

ABSTRACT: Subjected to external loads, granular materials experience severe deformation in a narrow zone before their failure. This phenomenon, which is called strain localisation or shear band, is of vital importance in assessing the stability of the geotechnical structure, studying the stress-strain behaviour of soil and rock materials, and analysing the interaction of soil and structure. The present study is aimed to investigate the effect of various factors on the pattern and inclination of shear band in a general three-dimensional condition of stress using the Discrete Element Method (DEM). Several tests were simulated using a developed version of the TRUBAL program called GRANULE. The GRANULE code was further developed to add the capability of carrying out simulations with different intermediate principal stresses and modelling specimens containing non-spherical particles. The shear band was detected by tracking the motion of the particles and plotting the rotation distribution of particles within the sample. The results prove that the shear band inclination and its pattern, are greatly affected by intermediate principal stress, particle shape, and confining stress. Moreover, it was observed that the change in the b value plays a key role in the alteration of the 3D configuration of the shear band.

Keywords: Discrete Element Method, Granular Materials, Shear Band, Strain Localisation, True Triaxial Test.

1. Introduction

A shear band is defined as the localisation of shear deformations in a set of narrow zones. In other words, a shear band is a thin layer along which two rigid blocks move at different velocities (i.e., strain rates). This phenomenon frequently occurs in granular materials and is considered one of the failure mechanisms in granular media. For instance, localised failure of granular soils in the form of shear bands may lead to several known geotechnical failures. Thus, the deformation and strength properties of the geotechnical structures are controlled by the soil behaviours inside the shear band

---

* Corresponding author E-mail: aghasemi@ut.ac.ir

(Desrues and Viggiani, 2004). This indicates the great importance of accurate estimation of the shear band formation in geotechnical problems. In recent years, a great number of theoretical, experimental, and numerical studies have been conducted to estimate the occurrence of the shear band and investigate its fundamental mechanisms.

Two distinctive failure mechanisms have been observed in the geomaterials, namely diffusive and localised instabilities. Diffusive instability may occur before the localised one and are mostly observable in undrained conditions (Mukherjee et al., 2017; Alipour and Lashkari, 2018; Lashkari et al., 2019). From a theoretical standpoint, localised failure can be considered as instability caused by the bifurcation of the uniform deformation of a soil structure (Rudnicki and Rice, 1975). Put differently, shear band initiation highly depends on the pre-localisation characteristics of homogeneous deformation. Mathematically, the shear band initiation occurs due to the non-uniqueness of equilibrium equations in a particular constitutive model (Gu et al., 2014). Such theories have accurately forecasted shear band occurrence based on Cosserat continuum theory (Vardoulakis, 1989) and elasto-plastic constitutive models (Bardet and Proubet, 1991). However, Desrues and Viggiani (2004) indicated that the theoretical and numerical approach based on continuum mechanics has inherent limitations for studying the mechanical behaviour of granular soils.

In addition to the theoretical studies regarding the investigation of shear band in granular materials, several laboratory experiments have been carried out using advanced equipment like stereophotogrammetry (Desrues and Viggiani, 2004), X-ray Computed Tomography (Andrade et al., 2012), and Particle Image Velocimetry (PIV) (Lashkari and Jamali, 2021). According to these extensive experimental works, the shear band formation and its characteristics are influenced by many factors such as the density, inherent and stress-induced anisotropy of the material, the confining stress, shape of the material, and the particle size.

Nevertheless, these experimental methods cannot provide all the important details of the shear band such as particle rotation, void ratio, and contact force. Additionally, the fundamental mechanism explaining the shear band formation, and the way the characteristics of the shear band are affected is not well understood yet. From the micromechanics point of view, granular media are composed of particles and the macroscale behaviour of the assembly is the result of microscale particle interactions through contacts. Therefore, the contact-based microstructure of the granular materials, such as contact force, contact number, and particle distributions, may play a critical role in determining macroscopic behaviour. The Discrete Element Method (DEM), initially introduced by Cundall and Strack (1979), is a powerful alternative employed by numerous researchers to investigate the micro-, meso-, and macroscale behaviour of granular media in various fields (Yan et al., 2015; Kildashti et al., 2018; Mohajeri et al., 2018; Hajiazizi and Nasiri, 2019; Nadimi et al., 2019; Ghassemi and Shahebrahimi, 2020; Salimi and Lashkari, 2020; Bayesteh and Hoseini, 2021; Fransen et al., 2021). Although DEM is mainly utilised to study particulate assemblies, it has also been used to investigate the microscale properties of clays (Jaradat and Abdelaziz, 2019; Khabazian et al., 2020). Needless to say, shear banding, a common phenomenon in granular media, has been extensively studied using DEM (Garcia and Bray, 2019; Tang et al., 2019; Yu et al., 2021). For instance, Bardet and Proubet (1991) performed DEM simulations to study the structure of the shear band. Their results showed that as the axial strain increases progressively, the thickness of the shear band declines from 9 to 7.5 times the mean particle diameter. Also, they showed the

importance of particle rotation in the shear band. However, they performed their simulation on circular particles that have no rolling resistance at contacts. Iwashita and Oda (1998) used rolling resistance at contact in the DEM and identified that the shear bands' development can be effectively simulated only when incorporating the rolling resistance at contacts in the DEM. Jiang et al. (2010) carried out some 2D numerical simulations on circular disks and realised that the thickness of the shear band is 10-14 times the average particle diameter. Also, contrary to the results by Bardet and Proubet (1991), they realised that this thickness rises as the axial strain increases. Another noteworthy result of this study is that shear band inclination decreases in the range of 54° to 50° with increasing axial strain which can be predicted using the Mohr-Coulomb theory. More recently, Tian et al. (2020) have conducted some biaxial simulations to investigate the effect of particle shape on the shear band properties using the aspect ratio (AR). They concluded that the decrease in the AR leads to more inclination of the shear band.

As can be seen in the literature, few researchers have addressed the issue of shear banding in the general three-dimensional conditions of stress, and there is still a need for thorough investigations of how shear band characteristics are affected by various factors. More specifically, there is no past research capturing the 3D configuration of shear band in true triaxial test conditions and addressing how shear band characteristics are influenced by 3D particle shape indices, i.e., angularity and sphericity. In the current study, the effect of particle shape, intermediate principal stress, and confining stress on shear banding in true triaxial test conditions was investigated. To this end, a macroscopic investigation was conducted to understand and explain the deformation process and shear bands' evolution in granular materials. This approach integrates the results of microscopic numerical models

with macroscopic expression in a three-dimensional space. In this regard, the mechanical behaviour of granular materials in the true triaxial test is examined and shear band failure modes are extracted.

2. DEM Modelling

The Discrete Element Method (DEM) is a numerical method intensively employed by researchers to simulate granular materials because of its unique feature of considering interactions between individual particles (O'Sullivan, 2011). In this study, ASTON version of the TRUBAL program called GRANULE (derived from Cundall's DEM code, Trubal Version 1.51: 9, May 1989) which is an open-source code was used to investigate the shear band and the effect of intermediate principal stress as well as the shape of the particles. The most important advantage of GRANULE over the traditional TRUBAL code is its capability to simulate specimens with rigid boundaries. Rigid boundaries are adopted in this study since the experimental work by Lade and Wang (2001) and Ochiai and Lade (1983) were used as benchmarks, and both studies used the true triaxial apparatus developed by Lade (1978) which is equipped with rigid boundaries. Moreover, as stated by O'Sullivan (2011), simulated specimens with rigid boundaries better represent the real physical test compared to periodic boundaries. Cubical samples were simulated to represent the true triaxial apparatus, which is suitable to investigate the effect of the intermediate principal stress on the granular materials. However, the original code was limited to model spherical particles and also, was not capable of performing tests with different b values ($b = (\sigma_2 - \sigma_3)/(\sigma_1 - \sigma_3)$, where $\sigma_1, \sigma_2, \sigma_3$ are principal stresses). Thus the code was further developed to fit our purposes.

2.1. Particle Shape Considerations

In recent years, there have been considerable advances in modelling particles with real shape (Angelidakis et al., 2021a; 2021b; Zhao and Zhao, 2021).

However, for the purpose of simplicity, the multi-sphere method was adopted in this study to generate irregularly shaped particles. In order to quantitatively investigate the effect of particle shape on the mechanical behaviour of the assemblies, the Angularity Index (AI) as introduced by Sukumaran and Ashmawy (2001) and the sphericity index (SPH) proposed by Krumbein (1941) were used. The Angularity Index (AI) for a 3D particle is calculated based on the weighted average of 2D angularities as:

$$AI = \frac{\sum_{k=1}^{3}(Ang_k . Area_k)}{\sum_{k=1}^{3} Area_k} \tag{1}$$

where AI: is the 3D angularity of the irregularly shaped particle in degree, k: corresponds to different 2D views (i.e., front, top and side views), $Area$: is the area of the 2D projected views, and Ang: is the angularity of the 2D views of the particle which is defined as:

$$Ang = \frac{\sum_{i=1}^{N}(\beta_{i.particle} - 180)^2 - \left(\frac{360}{N}\right)^2}{3 \times 180^2 - \left(\frac{360^2}{N}\right)} \tag{2}$$

where N: is the number of sharp corners of the 2D image and β_i: is shown in Figure 1.
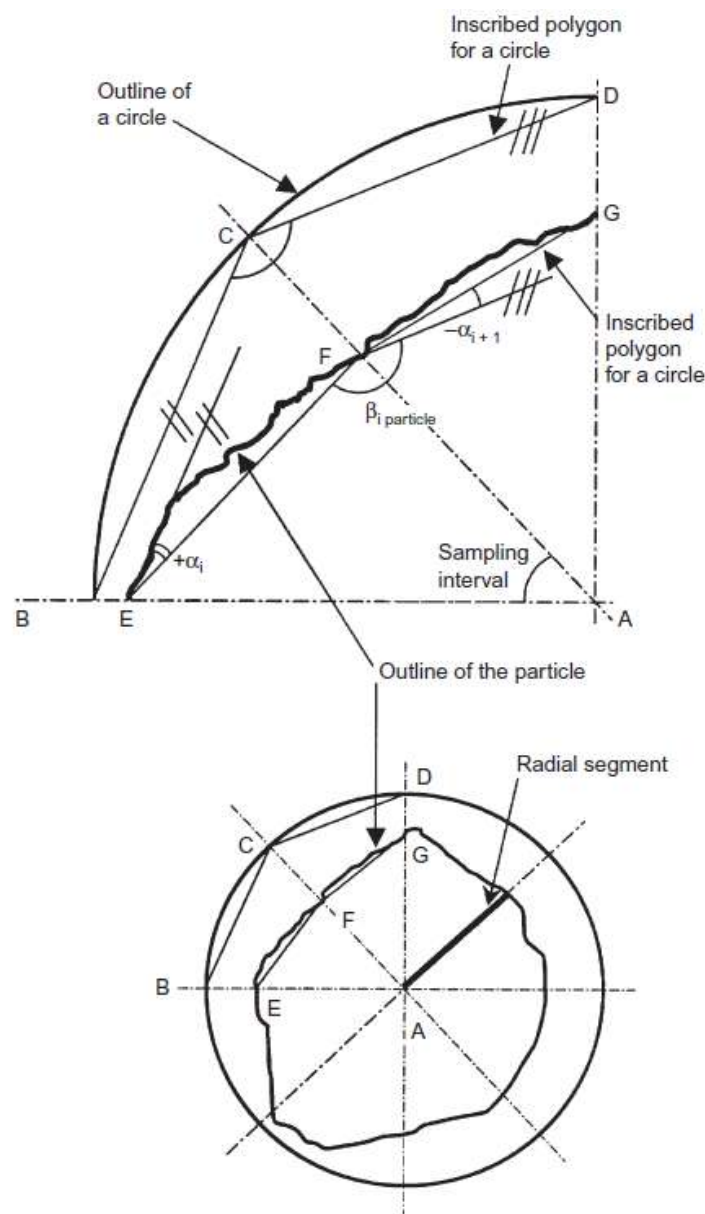
Fig. 1. Parameters used for calculation of 2D angularity (Sukumaran and Ashmawy, 2001)

The sphericity index is also calculated as:

$$\psi = \sqrt[3]{\frac{b.c}{a^2}} \qquad (3)$$

where the amount of *a, b* and *c* is measured as shown in Figure 2. To this end, the longest dimension of the particle (*a* in Figure 2) is measured first. Then, the greatest dimensions in two perpendicularly projected planes (*b* and *c* in Figure 2) are found afterwards.

The angularity and the sphericity of the particles used in the current study are according to Table 1.

2.2. Contact Detection Algorithm for Irregular Particles

The non-spherical particles used in this study are composed of 4 sub-spheres as illustrated in Table 1. When considering modelling irregularly shaped particles in a DEM code, the central problem of contact

detection arises. A two-step algorithm for detecting contacts between the non-spherical particles. In summary, the first step involves detecting contact between the imaginary bounding spheres containing the whole volume of the irregularly-shaped particles and if any contact was detected, the program would search for the potential contacts between the sub-spheres (Figure 3a). For detailed information about this algorithm, the readers are referred to (Shamsi and Mirghasemi, 2012).

2.3. Calculation of Contact Force and Moment

After completion of the contact detection process, forces and moments of all contacts are calculated. For this purpose, the linear contact law was used in this study. A simple formulation could be presented as follows (O'Sullivan, 2011):

$$dF_n = K_n.dv_n.\Delta t \qquad (4)$$
$$dF_s = min\{K_s.dv_s.\Delta t, \mu.dF_n\} \qquad (5)$$
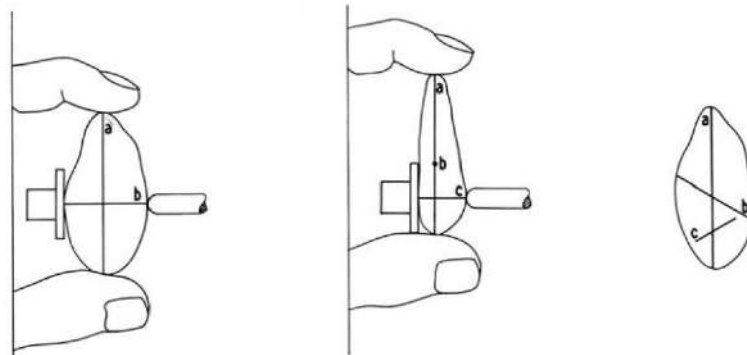
Fig. 2. Definition of the parameters for the calculation of SPH (Krumbein, 1941)

Table 1. Characteristics of particles used in simulations

Particle shape	Particle ID	Sphericity	Angularity (degree)
	P1	100%	0
	P2	93%	8
	P3	70%	15

where, dF_n and dF_s: are the incremental normal and shear force for each cycle, K_n and K_s: are coefficients of normal and shear contact stiffness, dv_n and dv_s: are the normal and tangential components of the relative velocity of particles at the contact point, respectively. μ: is also the coefficient of friction and Δt: is the time step and is computed as:

$$\Delta t = frac \sqrt{\frac{m_{min}}{K_{max}}} \qquad (6)$$

where K_{max}: is the maximum of K_n and K_s, m_{min}: is the smallest mass among particles, and $frac$: is a coefficient between zero and one and should be small enough to ensure the numerical stability in the computations. In the simulation, the value of $frac$ was set to 0.33 based on a trial and error procedure.

As the normal and shear forces for each contact are determined, the accumulative force and moment for each sub-sphere (e.g., sphere A in Figure 3) will be determined as:

$$F_{i.sphA} = F_n n_i + \varepsilon_{ijk} F_s \qquad i = 1,3 \qquad (7)$$
$$n_i = \frac{u_i^B - u_i^A}{d} \qquad (8)$$
$$M_{sphA} = R_{sphA} . F_{si} \qquad (9)$$

where, F_i: is the resultant force transmitted to the centre of each sub-sphere, u_i: is the centre coordinates of the sub-spheres involved in the contact, d: is the distance between the centre of two sub-spheres, and R: is the radius of the sub-sphere. Once the calculation of force and moment of all the sub-spheres is done, these forces and moments are transferred to the centre of mass of the irregular particle. The total amount of force and moment of a particle is determined using the following equations:

$$\left(F_{i.particle}\right) = \sum_{j=1}^{nsph} \left(F_{ij}\right) \qquad i = 1,3 \qquad (10)$$

$$\left(M_{i.particle}\right) = \sum_{j=1}^{nsph} \left(M_{ij}\right)$$
$$- \sum_{j=1}^{nsph} \left(F_{ij}\right).r_{ij} \qquad i \qquad (11)$$
$$= 1,3$$

where F_{ij} and M_{ij}: are the total force and moment of each sphere, respectively, $nsph$: is the number of spheres making up the particle, and r_j: is the distance between the centre of the sphere and the centre of mass of the irregularly shaped particle.

(a)   (b)
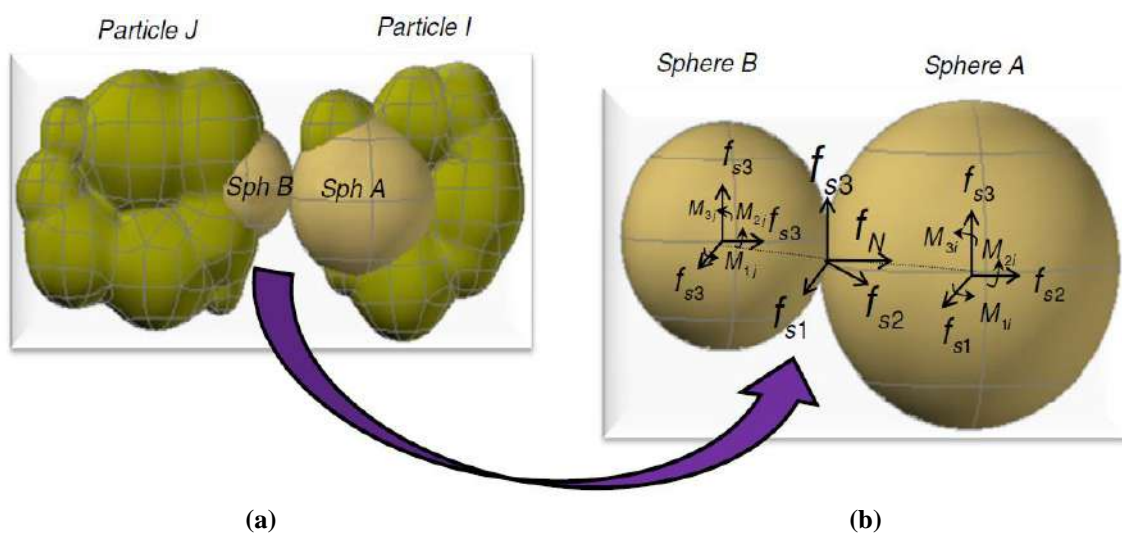
Fig. 3. a) Two sub-spheres in contact; and b) calculation and transfer of forces and moments between two sub-spheres in contact (Shamsi and Mirghasemi, 2012)

2.4. Assembly Properties

The number of particles in a real (and even small) granular assembly is very large. For instance, there are about 4 million particles in a cylindrical sample of sand with a height of 60 mm and a diameter of 30 mm. Simulation of tests using the discrete element method with this number of particles would be extremely time-consuming. Therefore, a much smaller number of particles should be considered. Chantawarangul (1994) compared the results of simulations on samples containing 300, 1000, 3000, and 10000 spherical particles, and concluded that the increase in the number of particles only reduces the oscillation of the curves while the general trend remained unchanged. Taking the time constraint and limited computing power into account, polydisperse assemblies of 2300 clumped particles with the same grain distribution as in Figure 4 were used in the present study.

In order to capture the energy dissipation of a real granular system, three types of damping systems, namely frictional damping, global damping and contact damping were used in this study. Frictional damping prohibits the tangential force from exceeding the frictional strength at the contact between two particles or between particles and walls. Global damping can be imagined as a damper that fixes the particle to a fixed point, and contact damping works based on the relative velocity of two particles in contact.

The value of parameters used in the current study is listed in Table 2. These values were initially chosen based on what was successfully calibrated against experimental results in the previous study by Danesh et al. (2020) employing the same code, i.e., the GRANULE program. Then, final values were fixed adopting the unbalanced force index (I_{uf}), introduced by Ng (2006), as the main criterion. I_{uf}: is defined as:

$$I_{uf} = \sqrt{\dfrac{\sum_1^{N_b}(unbalanced\ forces)^2 \big/ N_b}{\sum_1^{N_c}(contact\ forces)^2 \big/ N_c}} \quad (12)$$

where N_b and N_c: are the number of particles and the number of contacts, respectively. This index should be small enough, i.e., lower than 0.01 in this study, to ensure the numerical stability of the simulation in the sample shearing. Figure 5 shows an example of the unbalanced force index measured at different axial strains with the parameter of Table 2, where I_{uf} was satisfactorily obtained lower than 0.01. In order to better compare the results, all the parameter values are kept unchanged for all simulations.
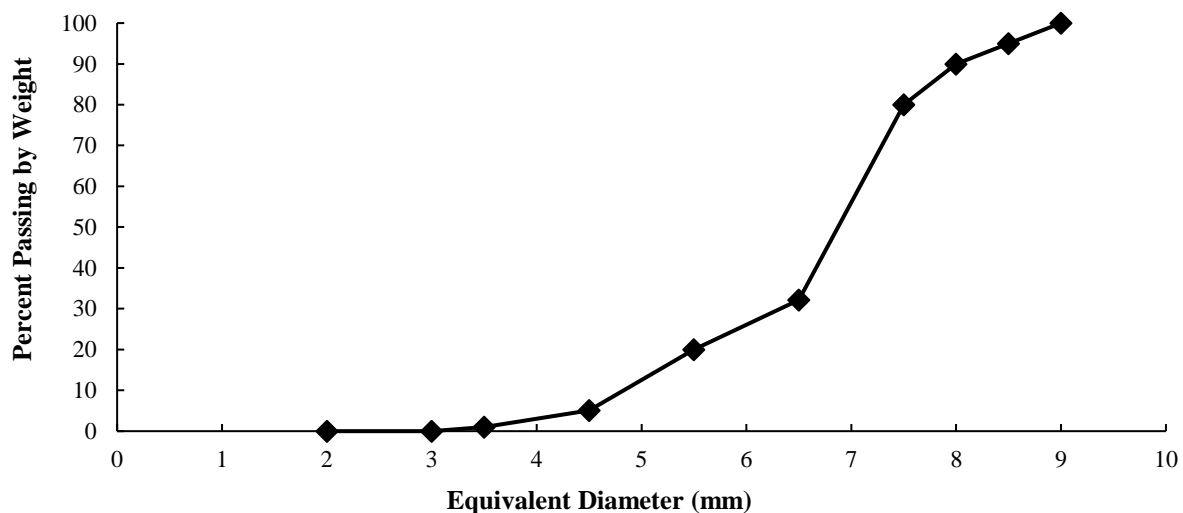
Fig. 4. Grain size distribution used in all simulations

In this research, the diagrams of internal friction angle and volumetric strain against the axial strain are used in order to investigate the mechanical behaviour of the granular assemblies. The sine of mobilised internal friction angle is calculated by:

$$\sin \varphi_{mobilized} = \frac{\sigma_1 - \sigma_3}{\sigma_1 + \sigma_3} \tag{13}$$

where σ_1 and σ_3: are the major and minor principal stresses, respectively. Also, the volumetric strain of the sample is measured by:

$$\varepsilon_v = \frac{V - V_0}{V_0} \tag{14}$$

where V: is the volume of the cubic cell at a given axial strain, and V_0: is the initial volume of the sample at the beginning of the sample shearing (i.e., the axial strain of 0.0).

2.5. Different Stages of True Triaxial Test Simulations

A complete simulation of a true triaxial test using the GRANULE program is composed of four main stages as follows:

2.5.1. Sample Compaction

Since the fundamental approach of the GRANULE is to prohibit the overlap between the particles during the generation process, the initially generated assembly of particles has very high porosity. To reduce the porosity of the specimen and to achieve the desired confining stress, after the initial generation of particles, the rigid boundaries (walls) move towards each other at a strain rate of 5.0×10^{-4}. By doing this, the walls come in contact with the particles and make the granular assembly denser, and at the same time, the stress increases throughout the specimen. This stage continues until the average stress in the specimen slightly exceeds the desired confining stress and the void ratio is between 0.65 and 0.75, the range which was used by Wang and Lade (2001) in their experimental work. Figures 6a and 6b show an example of the sample before and after the compaction, respectively (walls are not shown in these figures).
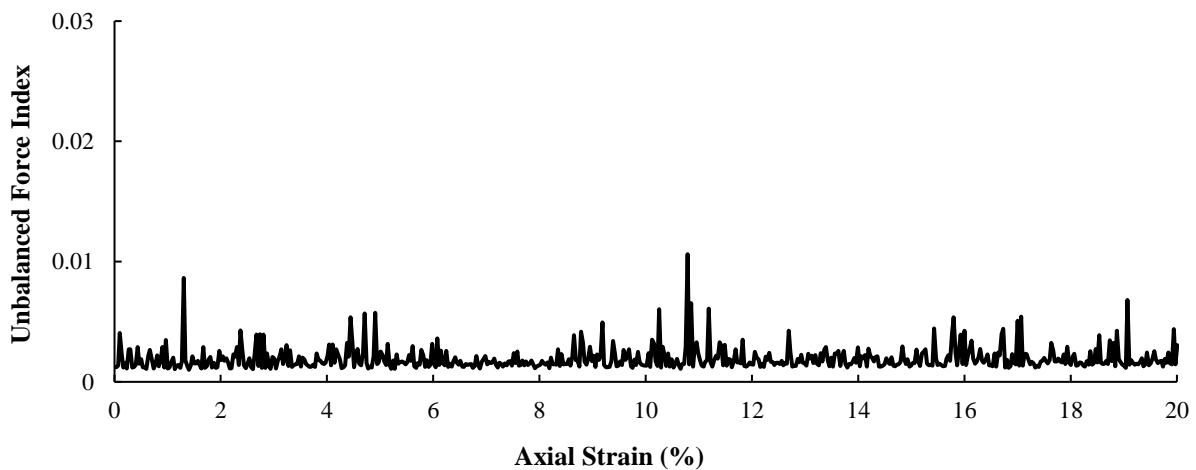
Fig. 5. I_{uf} versus axial strain (ε_a)

Table 2. Values of parameters used in simulations

Parameter	Value
Normal stiffness (N/m)	2.0×10^{10}
Tangential stiffness (N/m)	1.3×10^{10}
Density of particles (N/m³)	2.65×10^{4}
Cohesion	0.0
Coefficient of friction between particles	0.5
Coefficient of friction between particles and walls	0.5
Contact damping coefficient	0.1
Global damping coefficient	1.0
Gravity	0.0

2.5.2. Sample Relaxation

At this phase of the test, the velocity of the walls is set to zero. However, particles are not motionless due to the existing contact forces that remained from the compaction stage. This stage continues until the overlap between the particles is minimised. The more cycles are allocated for this phase, the more homogeneity of the sample is reached, leading to a more actual amount of stress within the specimen. At this stage, the porosity of the sample is constant because of the stationary walls, but the stress within the specimen decreases.

2.5.3. Applying the Desired Confining Stress

Once the equilibrium conditions are established, the desired confining stress should be applied to the specimen. This is achieved by a pre-defined servo control in the program. In this process, the required confining stress is compared to the existing stress within the sample. If the existing stress is greater than the desired stress, the walls move away from particles and vice versa. This procedure is repeated for all walls until the existing confining stress is equal to the required stress.

2.5.4. Sample Shearing

After the above-mentioned three phases, the specimen is ready to be tested under the specific requirements of each simulation. For instance, to simulate a triaxial compression test, the stress must be kept constant in two directions (four walls) using the approach explained in the previous phase, and one of (or both) the other two walls move towards the particles at the desired pace (deviatoric strain) in the third direction. This phase continues until the required axial strain (20% in this study) is reached. In the meanwhile, as the wall approaches the particles, the stress increases within the sample as well as in the other two directions. Thus the four walls of those two directions must move away to keep the stress constant and equal to the desired confining stress. This procedure is slightly different for triaxial tests with a different coefficient (b). Figures 6b and 6c show examples of an assembly of particles under the triaxial compression test at the beginning and the end of the sample shearing, respectively.

3. Results and Discussion

In this section, the results of simulated tests on granular assemblies under general and three-dimensional stress conditions are presented. The purpose of the simulations is to investigate the effect of various factors on the mechanical behaviour of the granular assemblies as well as the shear band characteristics.

In a discrete granular assembly, the interactions between particles occur at the inter-particle contacts, which resist system deformation and maintain stability. Therefore, the macro deformations of the granular assembly are produced because of deformations (or failures) of the initial inter-particle contacts. These contact deformations are considered micro deformations of the system. The normal and tangential deformations, sliding, rolling, and twisting (as well as the combination of them) between two particles at the contact area are thought of collectively as contact deformations and are usually presented in the form of relative displacement increments (Cundall, 1989). In the general 3D case, the mutual configuration of two particles has six degrees of freedom just like a beam in 3D space. In the current analysis, three potential modes of contact displacement: pure rolling, pure sliding, and simultaneous rolling and sliding are considered. Bardet and Proubet (1991) have shown in their study that the particles inside the shear band experience a high degree of rotation and the gradient of particle movement changes near the shear bands. Similarly, in the current study, shear bands are detected employing particle rotation distribution and tracking particle positions throughout the sample shearing.
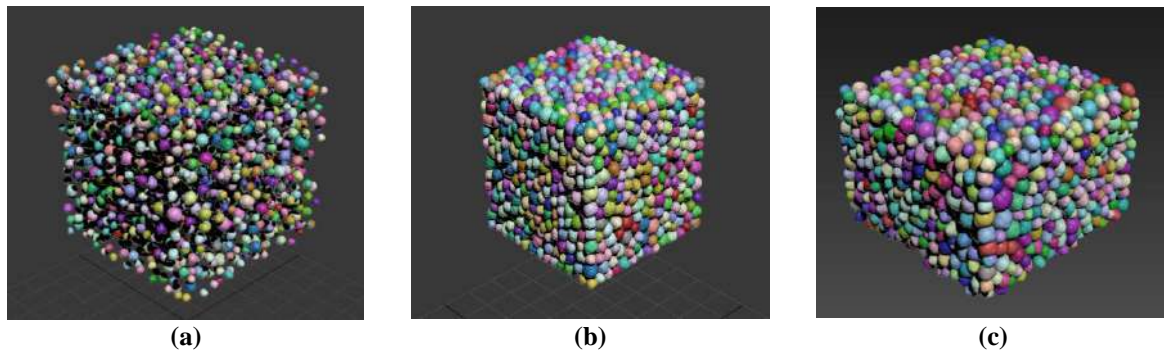
Fig. 6. The assembly of particles: a) Before the compaction; b) After the compaction; and c) At the end of the sample shearing

Due to the complexity of displaying in the 3D environment, the particle rotation distribution is plotted in a set of 2D views (i.e., the X_1- X_2, X_1- X_3, and X_2- X_3 views). In all simulations, the direction in which the increasing axial strain as well as the major principal stress (σ_1) were applied, is called X_1, the one regarding the minor principal stress (σ_3) is X_3 and the other direction would be X_2. An example of particles rotation distribution and particles displacement plot can be seen in Figures 7a and 7b, respectively, in which the coordinates of the centre of circles represent the initial coordinates of the centre mass of the respective particles and the diameter is a function of the amount of rotation in the direction perpendicular to the proposed view. Therefore, to detect the shear band, an average line passing through the circles with relatively large diameters (distinguished with pink colour) was drawn. The angle of this line with the direction of the minor principal stress (horizontal line)

was considered as the shear band orientation.

3.1. Evaluating the Effect of Intermediate Principal Stress (Coefficient b)

To evaluate the effect of the intermediate principal stress, the b value is used. To this end, five tests with b values of 0.0, 0.25, 0.5, 0.75, and 1.0 with the same initial conditions and confining stress (100 kPa) were simulated. The diagram of the mobilised internal friction angle versus axial strain for the conducted tests is shown in Figure 8a. To better observe and compare the trend of changes in the maximum mobilised internal friction angle against b values, Figure 9 is plotted. As can be seen in this diagram, the maximum mobilised internal friction angle increases as the b value goes from zero to about 0.5 and then decreases for b values between 0.5 and 1.0, which is qualitatively in good agreement with the experimental results obtained by Ochiai and Lade (1983).
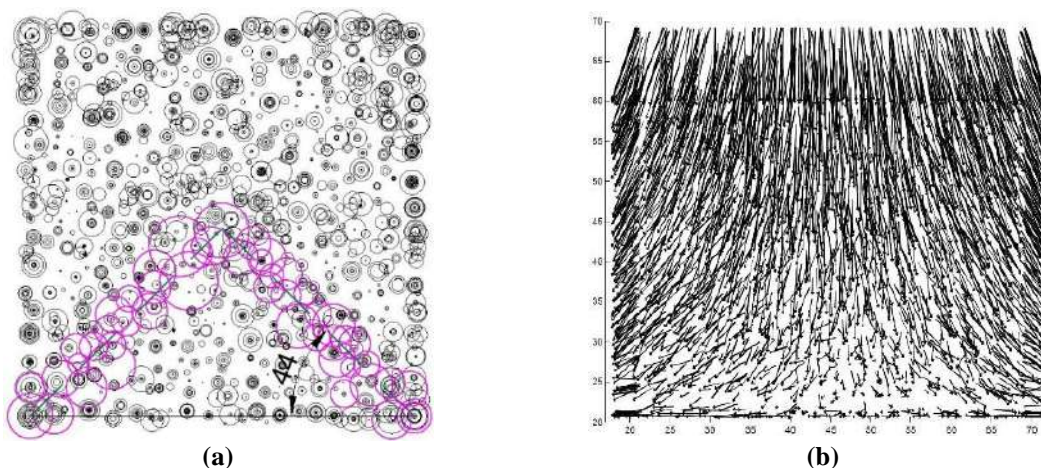
Fig. 7. a) Particles rotation distribution plot; and b) particle displacement plot (X1-X3 view)
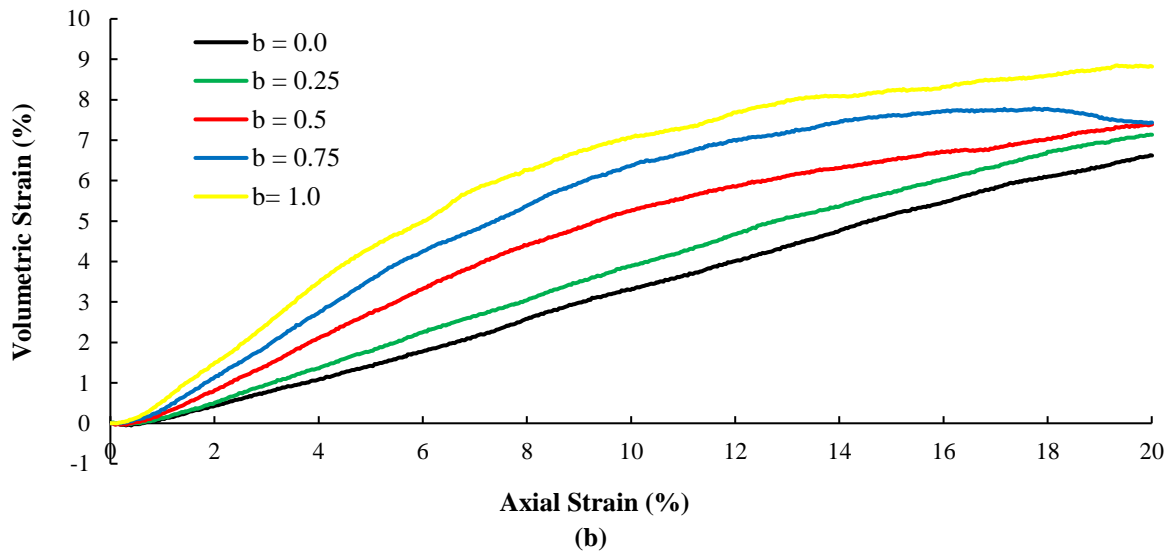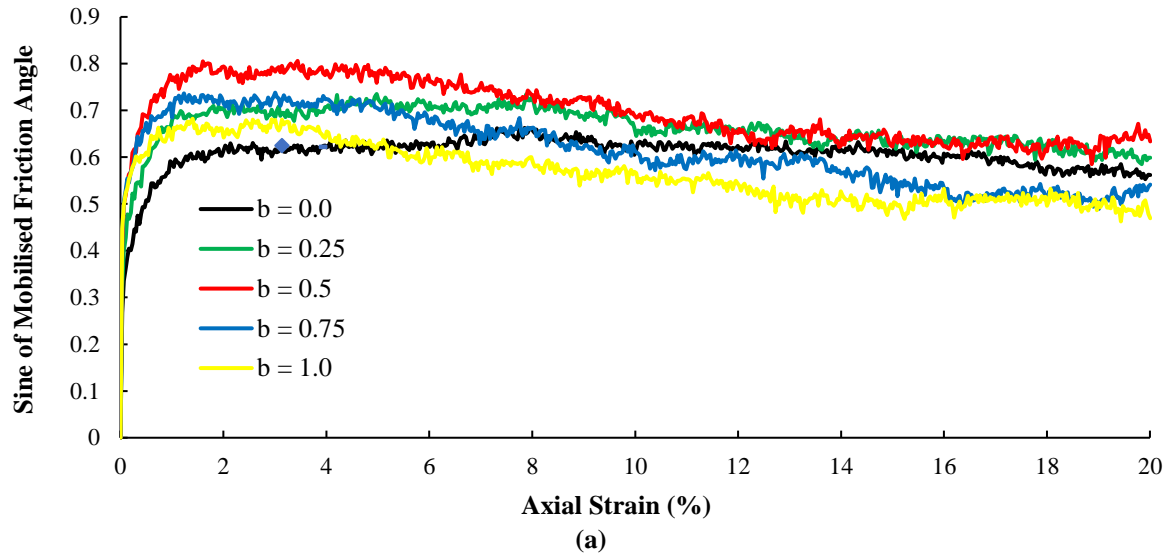
Fig. 8. a) Sin $\varphi_{mobilized}$ versus axial strain (ε_a); and b) volumetric strain (ε_v) versus axial strain (ε_a) for different b values
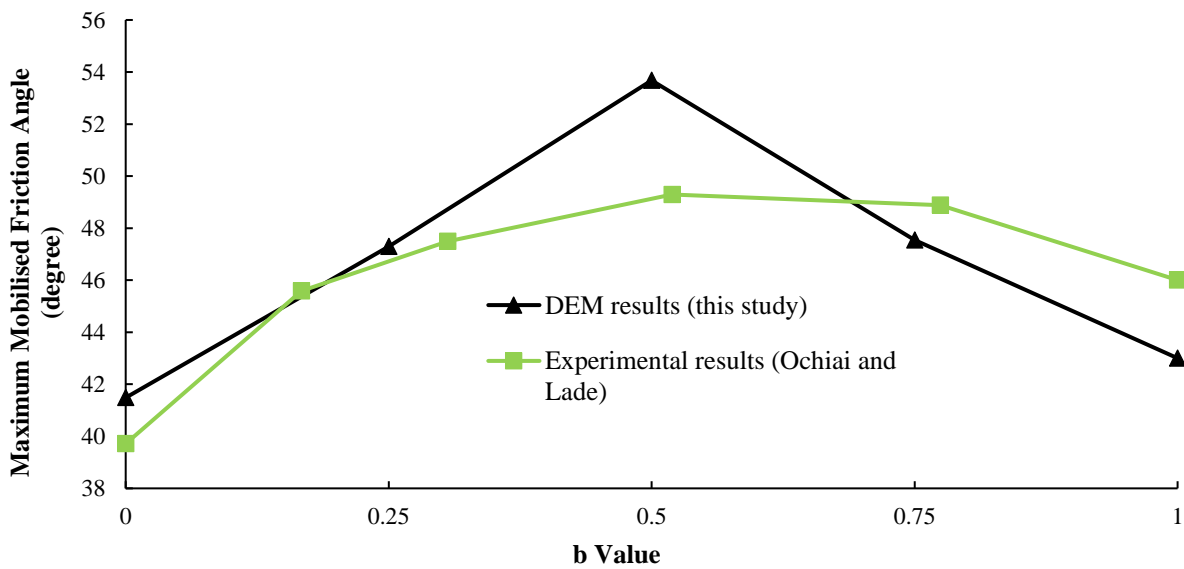
Fig. 9. Comparison of Maximum $\varphi_{mobilized}$ obtained for different b values between experimental results (Ochiai and Lade, 1983) and DEM results (present study)

As indicated in Figure 8b, The more the b value is the more dilation of the sample will be, which is in complete agreement with the similar experimental observations by past researchers such as Rodriguez and Lade (2013). The particle displacement plots in three views for different b values are shown in Figure 10. In order to truncate the process of comparison and evaluation of shear bands, only the results regarding the b value of 0.0, 0.5, and 1.0 are presented. As can be seen in these plots, for b value of 0.0, it seems that the shear band is formed and detectable in both X_1- X_3 and X_2- X_3 views (, and possibly with the same formation due to the symmetry in the loading condition and the geometry), while for other b values, the shear band is observed only in the X_1- X_3 view. Thus, the 3D configuration of the shear band could be considered as a pyramidal shape for b=0.0 and a prism-like shape for other b values as illustrated in Figures 11a and 11b, respectively. This transition from pyramidal shape to prism-like shape configuration is mainly because when b increases, the symmetry in loading condition in both X_1 and X_2 directions is no longer the case and as a result, one pair of walls move away from the particles faster.

In order to determine the inclination of the shear band, the rotation distribution of the X_1- X_3 view as in Figure 12 was used. The measured orientations for all tests with different b values are summarised in Figure 13. It can be seen that the orientation of shear bands generally increases as the b value increases from 0.0 to 1.0, which is consistent with the experimental results acquired by Lade and Wang (2001).
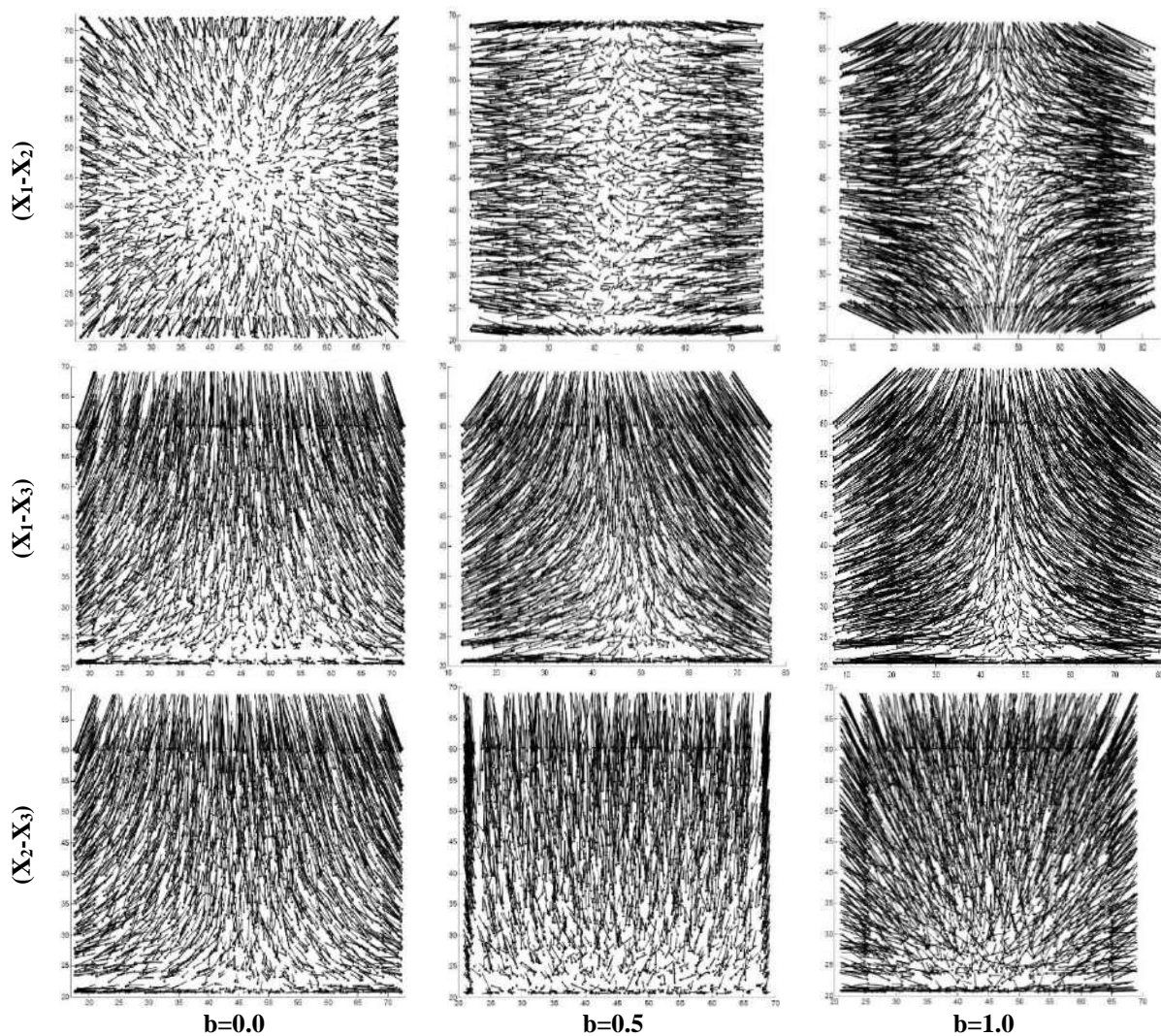
Fig. 10. Particle displacement plot for different b values in three 2D views ($\varepsilon_a = 20\%$)

(a)   **(b)**
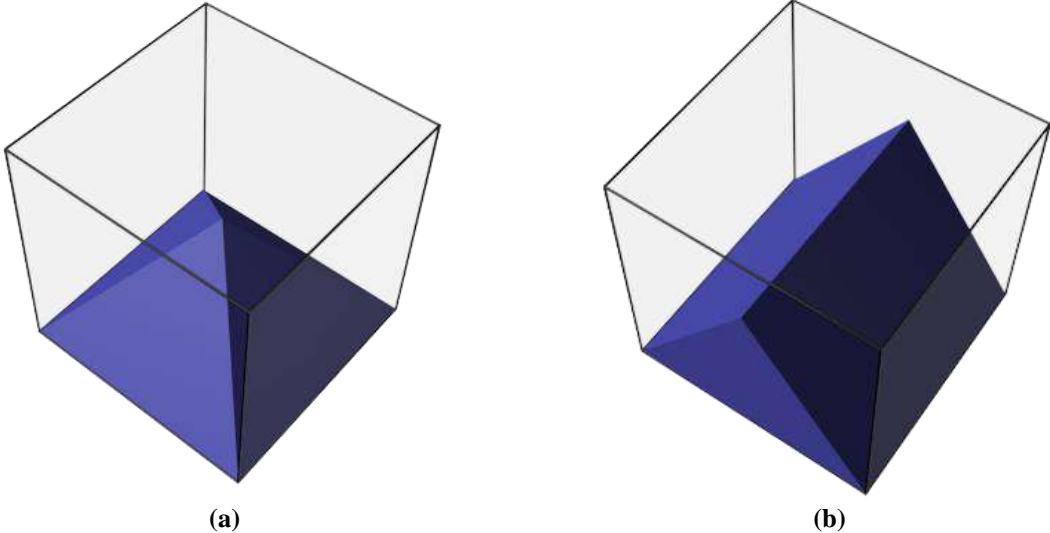
Fig. 11. 3D configuration of the shear bands; a) For b value of 0.0; and b) For other b values

(a)   **(b)**

(c)
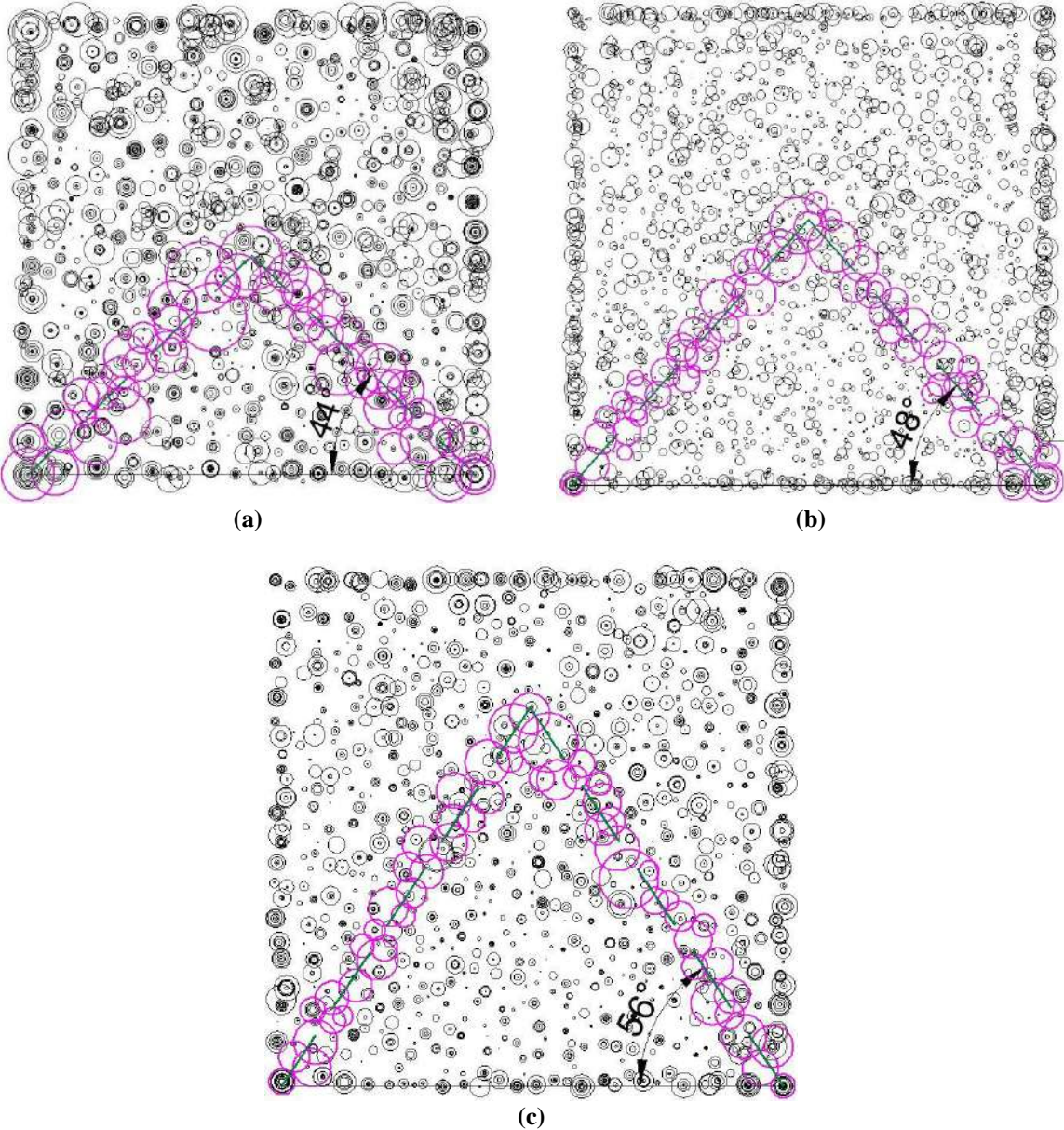
Fig. 12. Particle rotation distribution and shear band inclination: a) b=0.0; b) b=0.5; and c) b=1.0 ($\varepsilon_a = 20\%$)
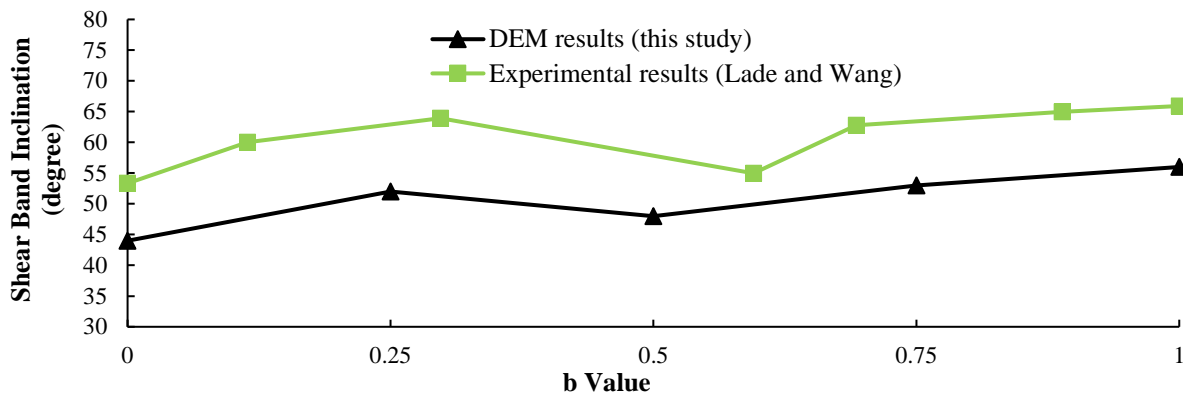
Fig. 13. Comparison of shear band inclination measured for different b values between DEM results (present study) and Experimental results (Lade and Wang, 2001)

3.2. Comparing Plane Strain (PSC) with Compression Triaxial Condition (CTC)

There are some studies regarding the investigation of the shear band in a plane strain condition like what Wang et al. (2019) have carried out. However, most of these studies are in the biaxial condition using 2D simulations. In the current study, a 3D plane strain (PSC) simulation is conducted, and the results regarding the shear band and the mechanical behaviour of the granular assembly was compared to that of Compression Triaxial Condition (CTC). Both simulations were carried out on the samples containing P2-type particles with the same initial arrangements including a confining pressure of 100 kPa and an initial void ratio of 0.643. As can be seen in Figures 14a and 14b, both the internal friction angle and the volumetric strain of the PSC test are considerably higher than that of the CTC test. The increase in the internal friction angle and the dilation can be attributed to the b value of the

simulations. The b value of the PSC simulation was continuously extracted throughout the sample shearing and was plotted as in Figure 15. As can be seen in this figure, the b value of the PSC test is mostly around 0.3. Therefore, the behaviour of the PSC sample is expected to be close to the sample with b = 0.25. Thus, based on what was concluded in the simulations with different b values, it is reasonable that the internal friction angle and the dilation of the PSC test are higher than that of the CTC simulation (b = 0.0).

As can be seen in Figure 16, the shear band in the PSC test is observable only in the X_1-X_3 view while in the CTC test is observed both in X_1-X_3 and X_2-X_3 views. Therefore, for the PSC simulation, a prism-like shear band could be perceived in a 3D view (Figure 11b). Also, as can be seen in Figure 17, the inclination of the shear band regarding the PSC test is slightly higher than that of the CTC test.
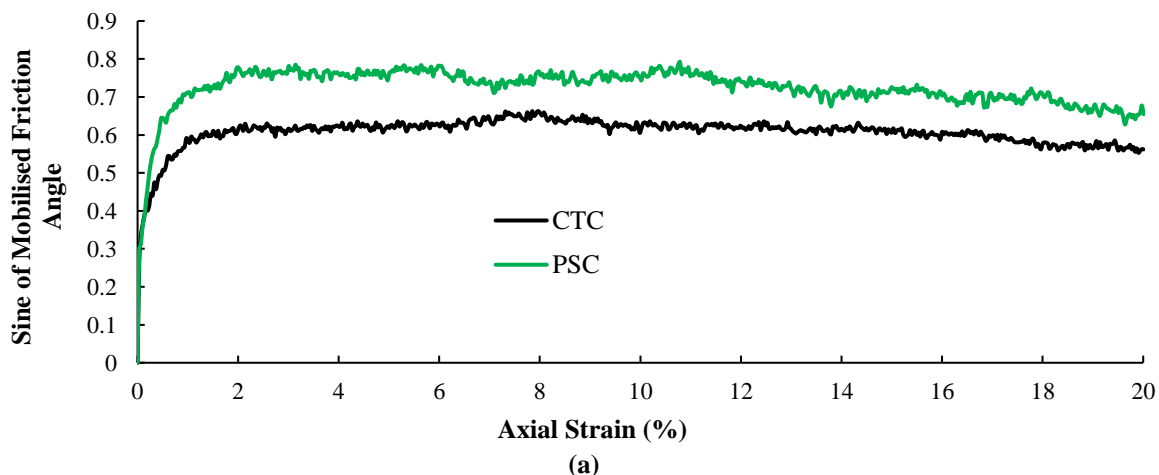
(a)
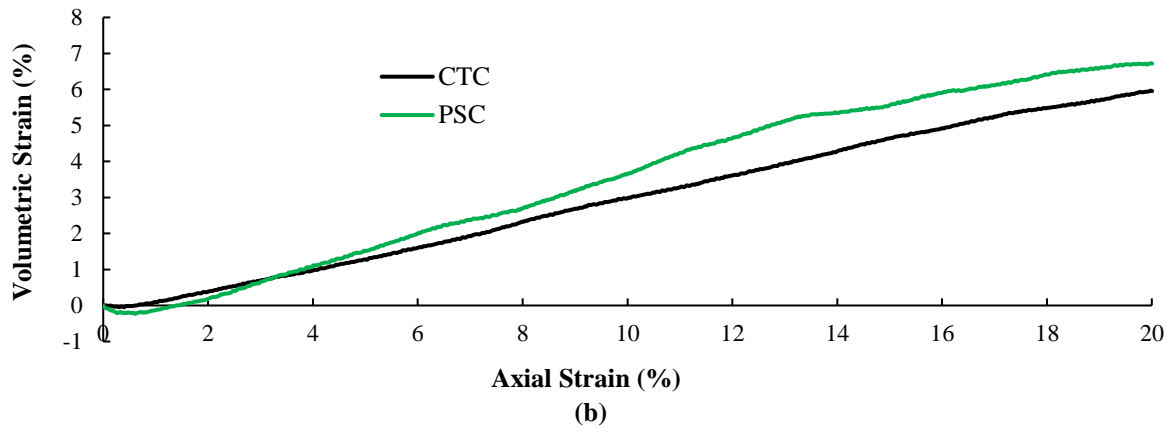
Fig. 14. a) Sin $\varphi_{mobilized}$ versus axial strain (ε_a); and b) Volumetric strain (ε_v) versus axial strain (ε_a) for CTC and PSC tests
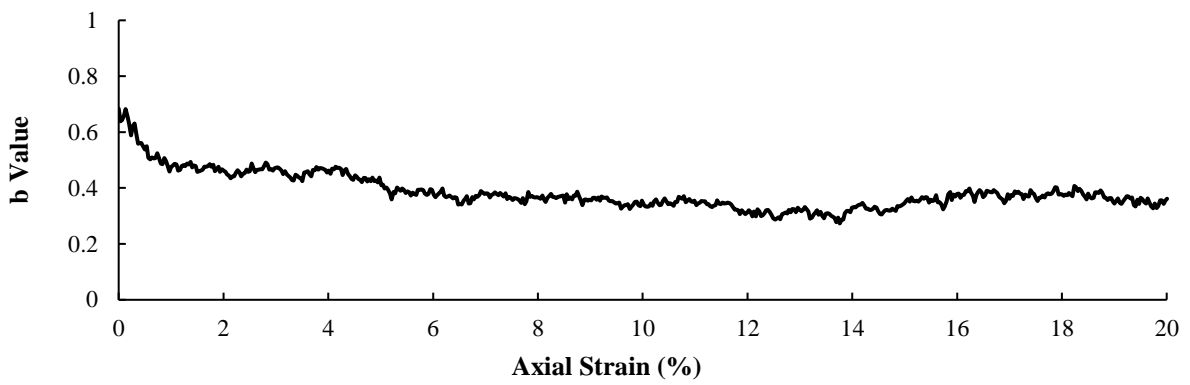
Fig. 15. Measured b value versus axial strain (ε_a) for PSC test
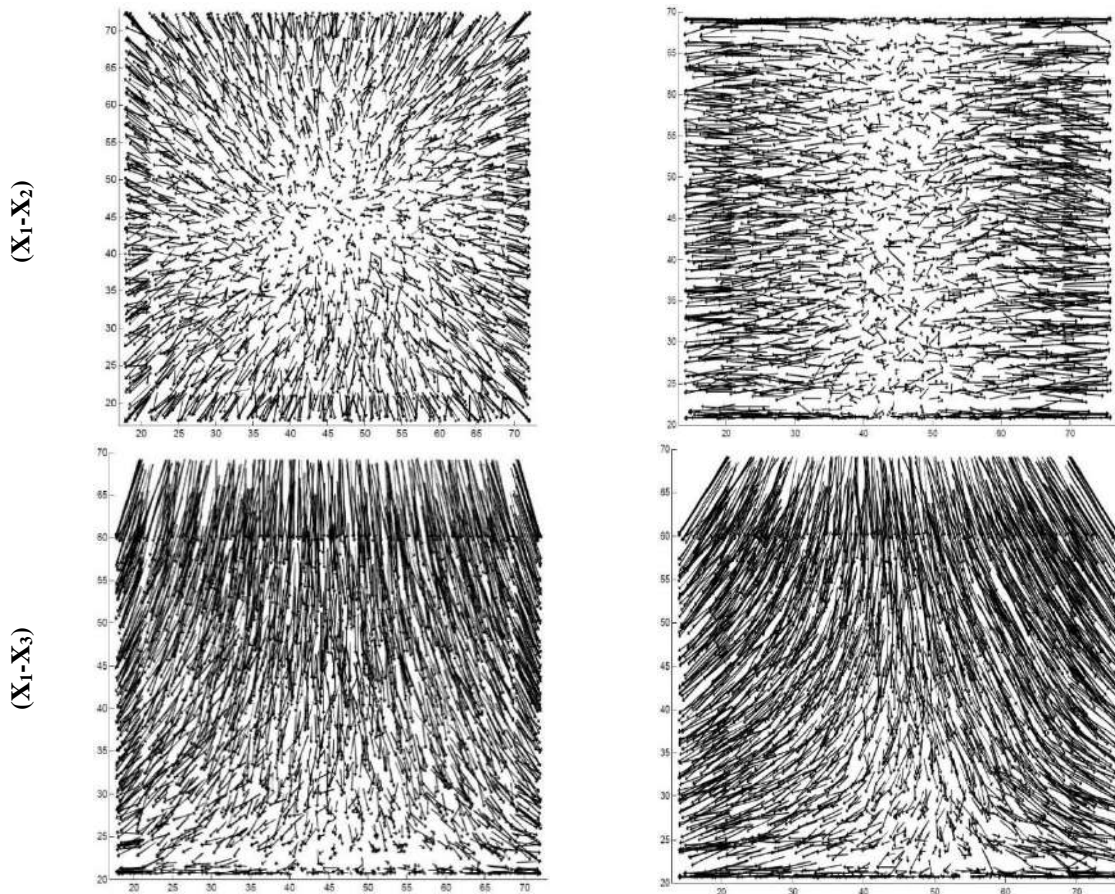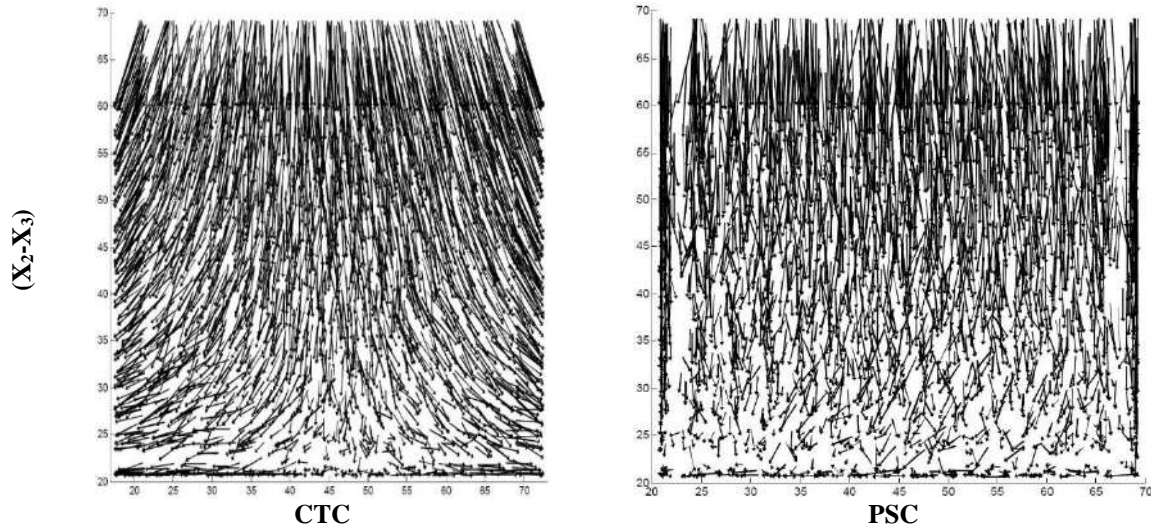
Fig. 16. Particle displacement plot for PSC and CTC tests in three 2D views ($\varepsilon_a = 20\%$)

(a)   **(b)**
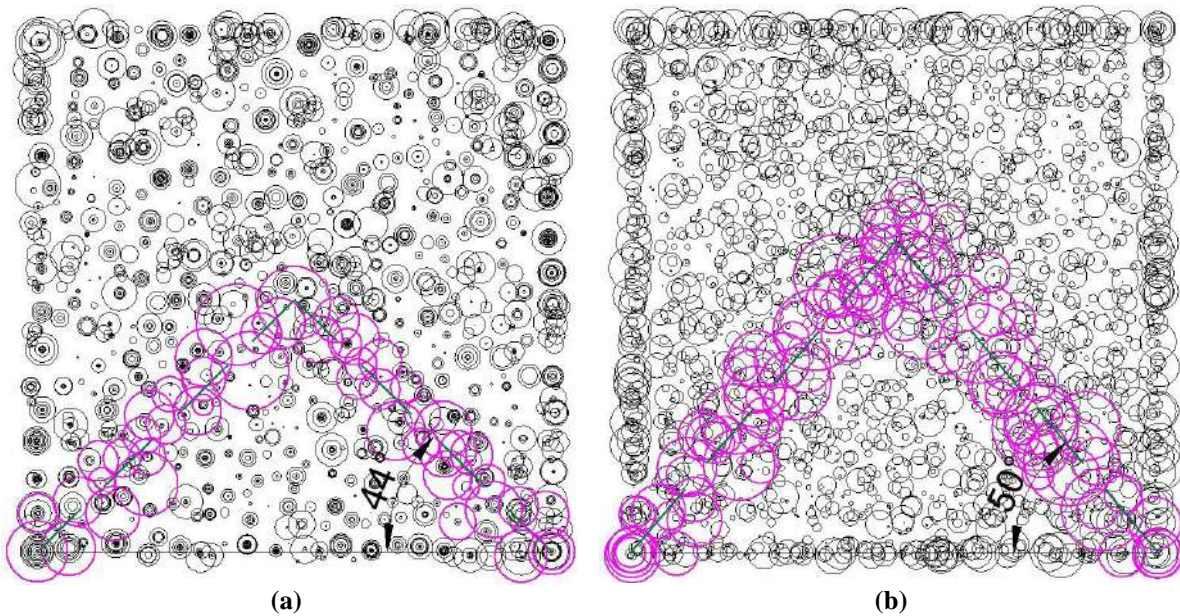
Fig. 17. Particle rotation distribution and shear band inclination: a) CTC test; and b) PSC test ($\varepsilon_a = 20\%$)

3.3. Investigation of the Effect of Particle Shape

To examine the effect of particle shape on the shear band and the mechanical behaviour of the granular assembly, three types of particles, as indicated in Table 1, were used. A set of true triaxial simulations with the same initial arrangements. i.e., b = 0.5, and an initial porosity ratio of 0.64 was carried out. As can be seen in Figure 18a, the higher internal friction angle is achieved as the angularity (AI) increases and the sphericity (SPH) decreases. Moreover, the sample containing particles with higher AI and lower SPH shows more dilative behaviour, as shown in Figure 18b. This is

because the interlocking of particles increases substantially when the angularity increases and the sphericity decreases, resulting in more rolling resistance. Additionally, the increase in the maximum internal friction angle can be attributed to the increase in the coordination number. The coordination number is defined as the number of contacts per particle for a set of particles. There are several relationships for the coordination number. In this study the equation proposed by Thornton (2000), which is called the mechanical coordination number was used as follows:

$$Z_m = 2 \frac{N_c - N_p^1}{N_p - (N_p^1 - N_p^0)} \qquad (15)$$

where, N_p and N_c: are the total number of particles and contacts, and N_p^0 and N_p^1: are the number of particles with zero and one contact, respectively. As can be seen in Figure 19, the mechanical coordination number for the assemblies with non-spherical particles is considerably higher than for the spherical package, leading to a higher number of contacts and following that, achieving a higher level of stress in the sample. This increase in stress results in a higher internal friction angle.

As mentioned earlier, for the b value of 0.5, the shear band is only observed in the X_1- X_3 view. Therefore, the rotation distribution of the X_1- X_3 view was plotted for these three simulations. It is apparent from Figure 20 that as the angularity increases and sphericity decreases, shear bands with higher inclination are observed.

3.4. Evaluation of the Effect of Confining Stress

To do this, three compression triaxial tests (b = 0.0) with confining stresses of 100, 500, and 1000 kPa were performed. The P2-type particle was used and all other parameters of these tests were considered the same. It can be seen from Figures 21a and 21b that as the confining stress of the samples increases, the mobilised internal friction angle and the dilation of the sample decreases. These observations are qualitatively in good agreement with the typical laboratory results using the compression triaxial device (Kolymbas and Wu, 1990). As mentioned above, in the case of b = 0.0, the shear band is formed in both X_1- X_3 and X_2- X_3 views, possibly with the same pattern and a 3D pyramidal shape like Figure 11a. Thus the X_1- X_3 view of the rotation distribution is used to examine the effect of confining stress on the shear band angle. Figure 22 indicates that the increase in the confining stress of the samples results in the decrease of the shear band orientation which is qualitatively consistent with the observed trend in experiments by Han and Drescher (1993) and in DEM simulations by Gu et al. (2014).
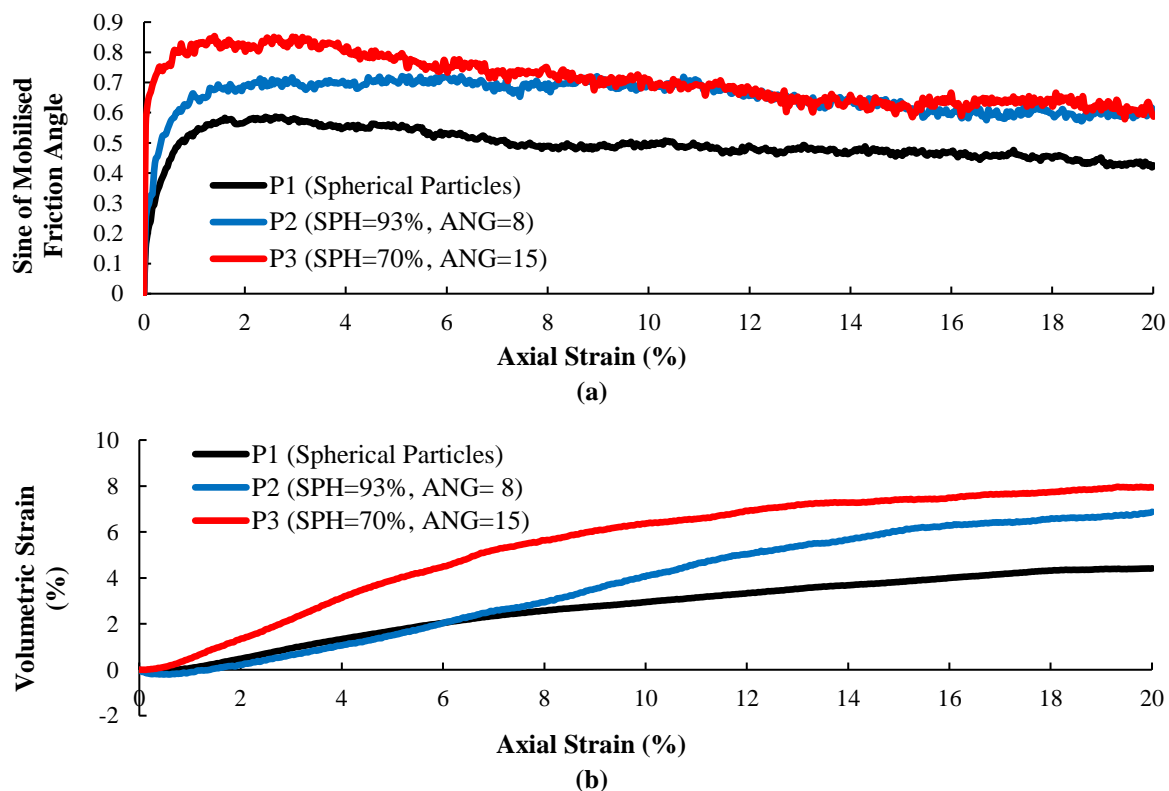
(a)

(b)

Fig. 18. a) Sin $\varphi_{mobilized}$ versus axial strain (ε_a); and b) Volumetric strain (ε_v) versus axial strain (ε_a) for different particle shapes (b = 0.5)
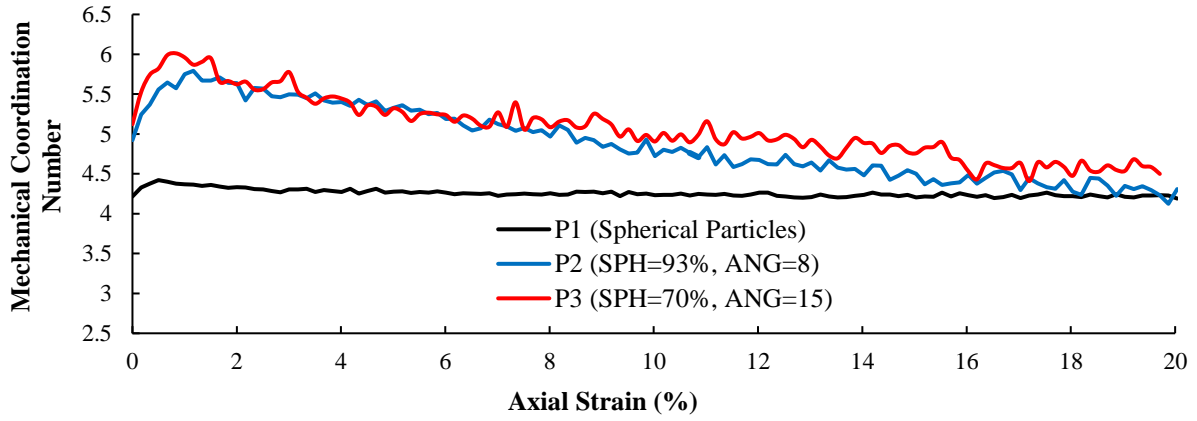
Fig. 19. Mechanical coordination number (Z_m) versus axial strain (ε_a) for different particle shapes (b = 0.5)
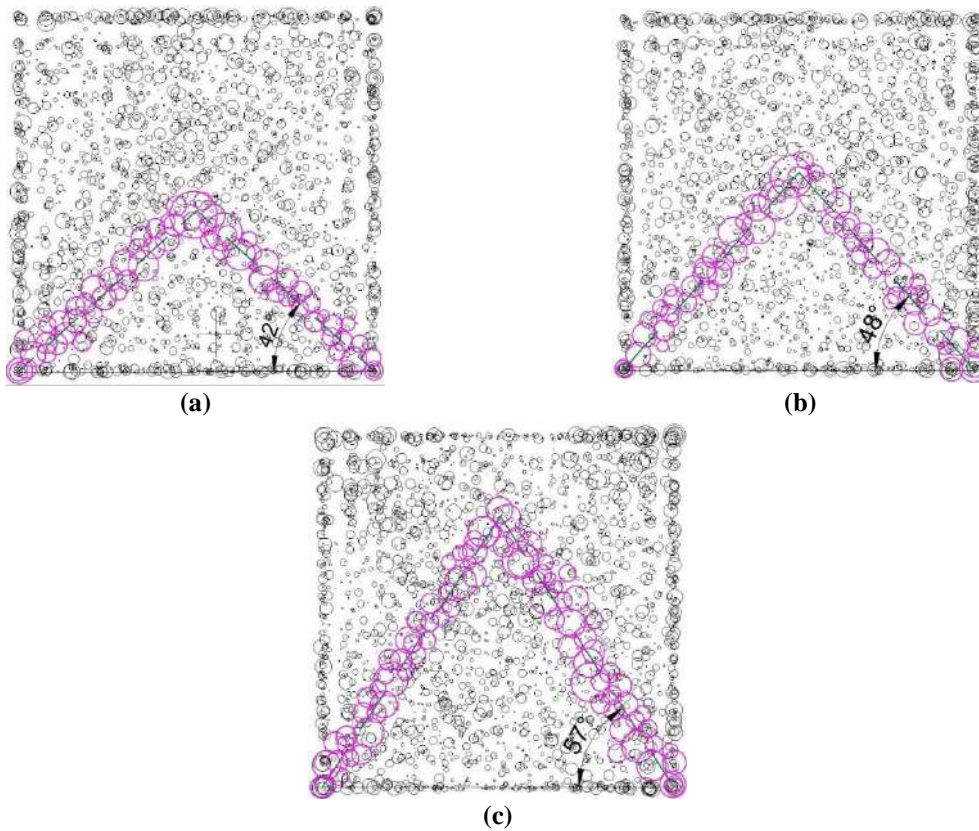
Fig. 20. Particle rotation distribution and shear band inclination in samples with b = 0.5 and: a) Spherical particles; b) Particles with AI = 8 and SPH = 93%; and c) Particles with AI = 15 and SPH = 70% ($\varepsilon_a = 20\%$)
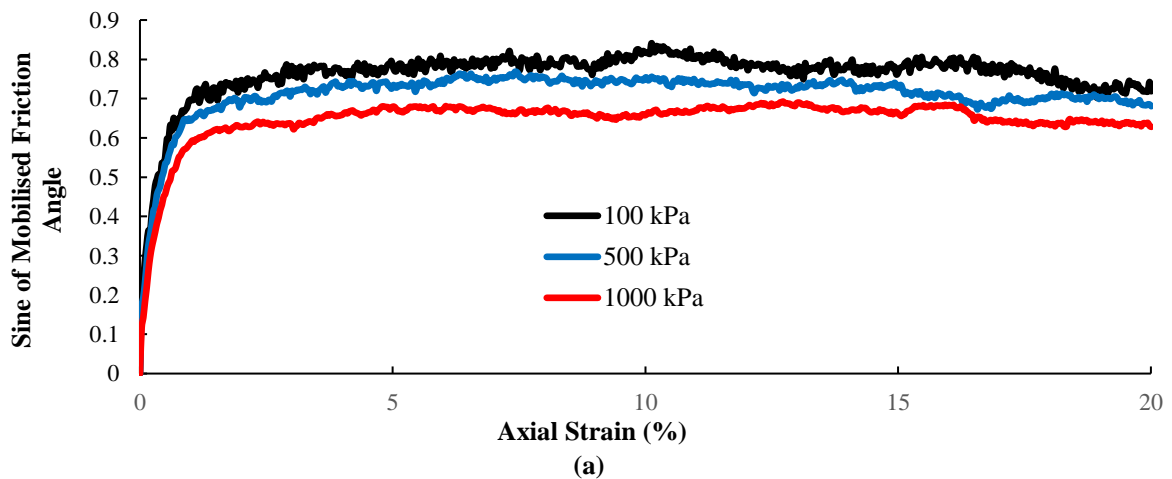
(a)
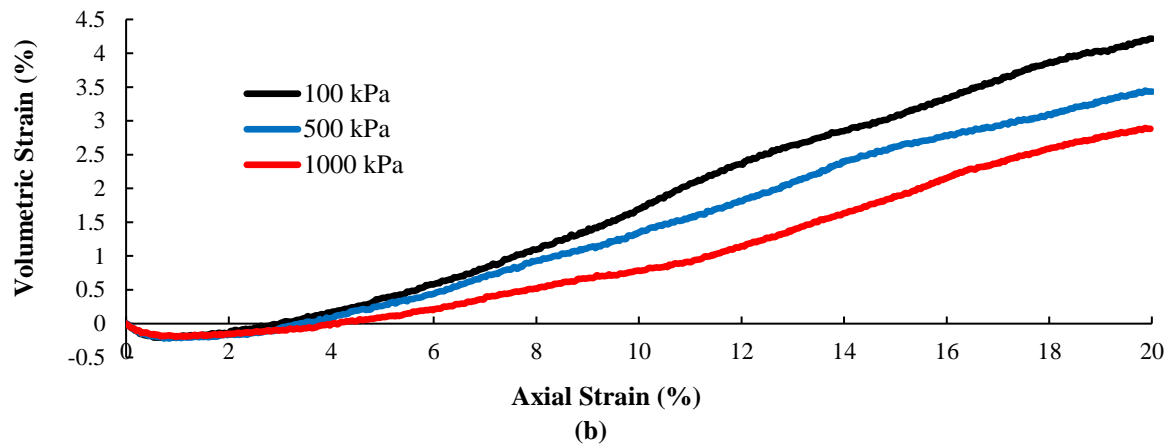
(b)

Fig. 21. a) Sin $\varphi_{mobilized}$ versus axial strain (ε_a); and b) Volumetric strain (ε_v) versus axial strain (ε_a) for different confining stresses (b = 0)

(a)

(b)

(c)
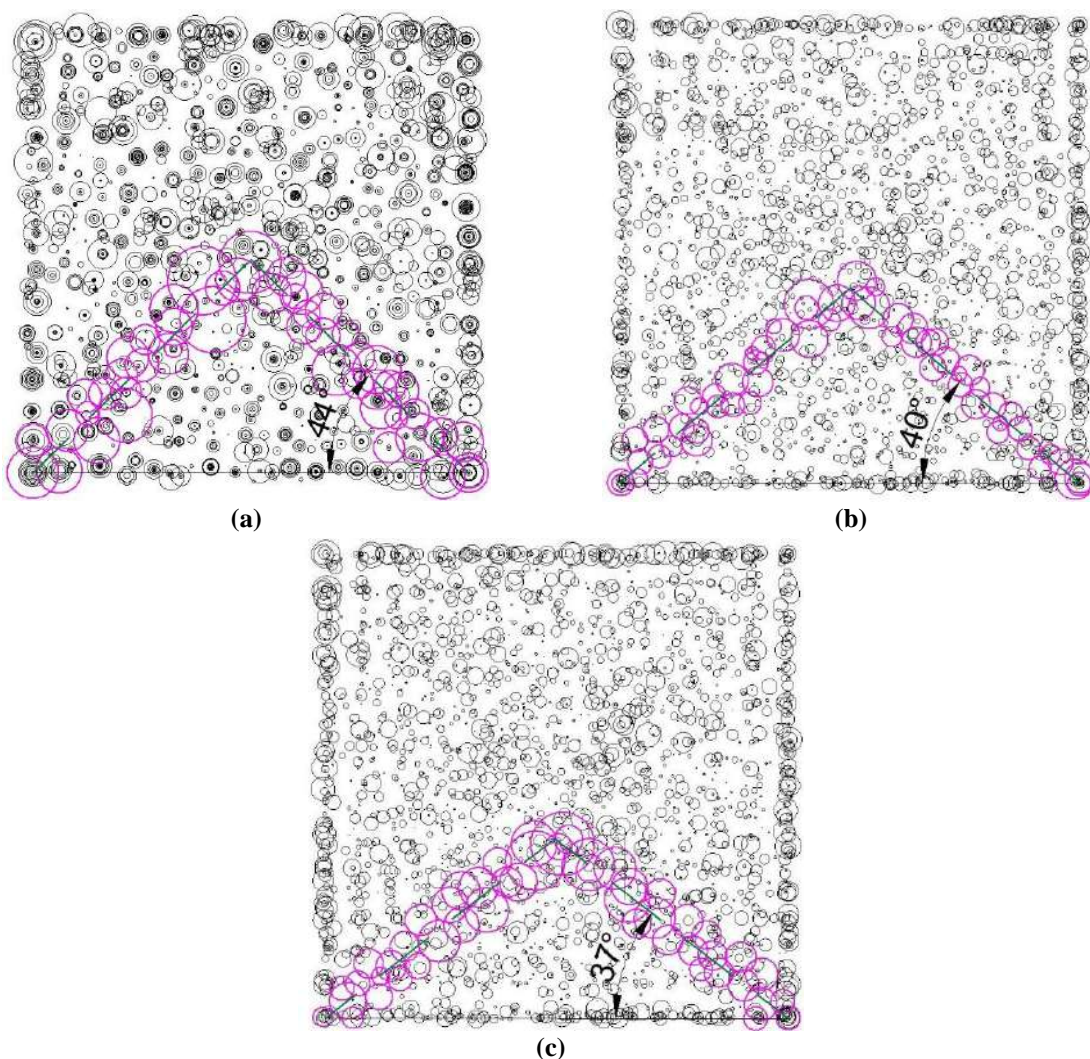
Fig. 22. Particle rotation distribution and shear band inclination in samples with b=0 the confining stress of: a) 100 kPa; b) 500 kPa; and c) 1000 kPa ($\varepsilon_a = 20\%$)

4. Conclusions

In this research, the mechanical behaviour of granular materials with emphasis on the pattern and angle of the shear band was investigated. For this purpose, a three-dimensional discrete element method called GRANULE was used and further developed to include irregularly shaped particles and to simulate tests with different b values.

Then, some systematic simulations were conducted to evaluate the effect of some factors on the mechanical behaviour of the granular assembly and the shear band pattern and orientation. Some acquired results were compared to the past experimental results in order to prove the accuracy and validity of our numerical simulations. The most important results are:

- By increasing the b value from 0.0 to about 0.5, the maximum internal friction angle increases and then decreases for the b value between 0.5 and 1.0 to a value. Moreover, the continuous rise in the b value results in more dilative behaviour of the sample.

- The more the b value is, the more inclination of the shear band will be. However, the shear band angle of the b = 0.5 was obtained slightly lower than that of b = 0.25.

- The amount of internal friction angle, as well as the dilation of the granular assembly, increases under Plane Strain Condition (PSC) compared to Compressive Triaxial Conditions (CTC).

- The shear band in the PSC test was inclined at a greater angle in comparison to the CTC test.

- It was shown that by reducing the sphericity (SPH) and increasing the angularity (AI) the shear band orientation will rise.

- Considering all the simulations with different conditions, it was concluded that the 3D shape and formation of the shear band is affected only by the change in the b value. In other words, for the simulation with b = 0.0 (compression triaxial test), a shear band was observed in both X_1- X_3 and X_2- X_3 views with a similar pattern due to the symmetry of the geometry and loading condition, making a pyramidal shape of the 3D shear band. In the case of other b values (and also the PSC test), the shear band is detectable only in the 2D view which is perpendicular to the mean principal

stress (X_1- X_3 in this study) and a 3D prism-like shear band can be perceived.

5. Disclosure Statement

The authors declare that they have no conflict of interest.

6. References

Alipour, M.J. and Lashkari, A. (2018). "Sand instability under constant shear drained stress path", *International Journal of Solids and Structures*, 150, 66-82.

Andrade, J.E., Chen, Q., Le, P.H., Avila, C.F. and Evans, T.M. (2012). "On the rheology of dilative granular media: Bridging solid-and fluid-like behavior", *Journal of the Mechanics and Physics of Solids*, 60(6), 1122-1136.

Angelidakis, V., Nadimi, S., Otsubo, M. and Utili, S. (2021a). "CLUMP: A Code Library to generate Universal Multi-sphere Particles", *SoftwareX*, 15, 100735.

Angelidakis, V., Nadimi, S. and Utili, S. (2021b). "SHape Analyser for Particle Engineering (SHAPE): Seamless characterisation and simplification of particle morphology from imaging data", *Computer Physics Communications*, 265, 107983.

Bardet, J.-P. and Proubet, J. (1991). "A numerical investigation of the structure of persistent shear bands in granular media", *Geotechnique*, 41(4), 599-613.

Bayesteh, H. and Hoseini, A. (2021). "Effect of mechanical and electro-chemical contacts on the particle orientation of clay minerals during swelling and sedimentation: A DEM simulation", *Computers and Geotechnics*, 130, 103913.

Chantawarangul, K. (1994). "Numerical simulations of three-dimensional granular assemblies*"*, PhD Thesis, University of Waterloo.

Cundall, P.A. (1989). "Evolution of elastic moduli in a deforming granular assembly", *S ELECTE*, 59.

Cundall, P.A. and Strack, O.D.L. (1979). "A discrete numerical model for granular assemblies", *Geotechnique*, 29(1), 47-65.

Danesh, A., Mirghasemi, A. A. and Palassi, M. (2020). "Evaluation of particle shape on direct shear mechanical behavior of ballast assembly using discrete element method (DEM)", *Transportation Geotechnics*, 100357.

Desrues, J. and Viggiani, G. (2004). "Strain localization in sand: an overview of the experimental results obtained in Grenoble using stereophotogrammetry", *International Journal for Numerical and Analytical Methods in Geomechanics*, 28(4), 279-321.

Fransen, M.P., Langelaar, M. and Schott, D.L.

(2021). "Application of DEM-based metamodels in bulk handling equipment design: Methodology and DEM case study", *Powder Technology*, 393, 205-218.

Garcia, F.E. and Bray, J.D. (2019). "Modeling the shear response of granular materials with discrete element assemblages of sphere-clusters", *Computers and Geotechnics*, 106, 99-107.

Ghassemi, A. and Shahebrahimi, S.S. (2020). "Discrete Element Modeling of Dynamic Compaction with Different Tamping Condition", *Civil Engineering Infrastructures Journal*, 53(1), 173-188.

Gu, X., Huang, M. and Qian, J. (2014). "Discrete element modeling of shear band in granular materials", *Theoretical and Applied Fracture Mechanics*, 72, 37-49.

Hajiazizi, M. and Nasiri, M. (2019). "Experimental and numerical investigation of reinforced sand slope using geogird encased stone column", *Civil Engineering Infrastructures Journal*, 52(1), 85-100.

Han, C. and Drescher, A. (1993). "Shear bands in biaxial tests on dry coarse sand", *Soils and Foundations*, 33(1), 118-132.

Iwashita, K. and Oda, M. (1998). "Rolling resistance at contacts in simulation of shear band development by DEM", *Journal of Engineering Mechanics*, 124(3), 285-292.

Jaradat, K.A. and Abdelaziz, S.L. (2019). "On the use of discrete element method for multi-scale assessment of clay behavior", *Computers and Geotechnics*, 112, 329-341.

Jiang, M., Zhu, H. and Li, X. (2010). "Strain localization analyses of idealized sands in biaxial tests by distinct element method", *Frontiers of Architecture and Civil Engineering in China*, 4(2), 208-222.

Khabazian, M., Mirghasemi, A.A. and Bayesteh, H. (2020). "Discrete-element simulation of drying effect on the volume and equivalent effective stress of kaolinite", *Géotechnique*, 1-13.

Kildashti, K., Dong, K., Samali, B., Zheng, Q. and Yu, A. (2018). "Evaluation of contact force models for discrete modelling of ellipsoidal particles", *Chemical Engineering Science*, 177, 1-17.

Kolymbas, D. and Wu, W. (1990). "Recent results of triaxial tests with granular materials", *Powder Technology*, 60(2), 99-119.

Krumbein, W.C. (1941). "Measurement and geological significance of shape and roundness of sedimentary particles", *Journal of Sedimentary Research*, 11(2), 64-72.

Lade, P.V (1978). "Cubical triaxial apparatus for soil testing", *Geotechnical Testing Journal*, 1(2), 93-101.

Lade, P.V and Wang, Q. (2001). "Analysis of shear banding in true triaxial tests on sand", *Journal of engineering mechanics*, 127(8), 762-768.

Lashkari, A., Khodadadi, M., Binesh, S.M. and Rahman. M. M. (2019). "Instability of particulate assemblies under constant shear drained stress path: DEM approach", *International Journal of Geomechanics*, 19(6), 4019049.

Lashkari, A. and Jamali, V. (2021). "Global and local sand–geosynthetic interface behaviour", *Géotechnique*, 71(4), 346-367.

Mohajeri, M., van Rhee, C. and Schott, D.L. (2018). "Penetration resistance of cohesive iron ore: A DEM study", In *9th International Conference on Conveying and Handling of Particulate Solids*, London.

Mukherjee, M., Gupta, A. and Prashant, A. (2017). "Instability analysis of sand under undrained biaxial loading with rigid and flexible boundary", *International Journal of Geomechanics*, 17(1), 4016042.

Nadimi, S., Ghanbarzadeh, A., Neville, A. and Ghadiri, M. (2019). "Effect of particle roughness on the bulk deformation using coupled boundary element and discrete element methods", *Computational Particle Mechanics*, 1-11.

Ng, T.-T. (2006). "Input parameters of discrete element methods", *Journal of Engineering Mechanics*, 132(7), 723-729.

O'Sullivan, C. (2011). *Particulate discrete element modelling: A geomechanics perspective,* CRC Press, London.

Ochiai, H. and Lade, P.V (1983). "Three-dimensional behavior of sand with anisotropic fabric", *Journal of Geotechnical Engineering*, 109(10), 1313-1328.

Rodriguez, N.M. and Lade, P.V (2013). "True triaxial tests on cross-anisotropic deposits of fine Nevada sand", *International Journal of Geomechanics*, 13(6), 779-793.

Rudnicki, J.W. and Rice, J.R. (1975). "Conditions for the localization of deformation in pressure-sensitive dilatant materials", *Journal of the Mechanics and Physics of Solids*, 23(6), 371-394.

Salimi, M.J. and Lashkari, A. (2020). "Undrained true triaxial response of initially anisotropic particulate assemblies using CFM-DEM", *Computers and Geotechnics*, 124, 103509.

Shamsi, M.M.M. and Mirghasemi, A.A. (2012). "Numerical simulation of 3D semi-real-shaped granular particle assembly", *Powder Technology*, 221, 431-446.

Sukumaran, B. and Ashmawy, A.K. (2001). "Quantitative characterisation of the geometry of discret particles", *Geotechnique*, 51(7), 619-627.

Tang, H., Dong, Y., Wang, T. and Dong, Y. (2019). "Simulation of strain localization with discrete element-Cosserat continuum finite element two scale method for granular materials", *Journal of the Mechanics and Physics of Solids*, 122, 450-471.

Thornton, C. (2000). "Numerical simulations of deviatoric shear deformation of granular media", *Géotechnique*, 50(1), 43-53.

Tian, J., Liu, E. and He, C. (2020). "Shear band analysis of granular materials considering effects of particle shape", *Acta Mechanica*, 231(11), 4445-4461.

Vardoulakis, I. (1989). "Shear-banding and liquefaction in granular materials on the basis of a Cosserat continuum theory", *Ingenieur-Archiv*, 59(2), 106-113.

Wang, P., Sang, Y., Shao, L. and Guo, X. (2019). "Measurement of the deformation of sand in a plane strain compression experiment using incremental digital image correlation", *Acta Geotechnica*, 14(2), 547-557.

Wang, Q. and Lade, P.V (2001). "Shear banding in true triaxial tests and its effect on failure in sand", *Journal of Engineering Mechanics*, 127(8), 754-761.

Yan, Y., Zhao, J. and Ji, S. (2015). "Discrete element analysis of breakage of irregularly shaped railway ballast", *Geomechanics and Geoengineering*, 10(1), 1-9.

Yu, J., Jia, C., Xu, W., Zhang, Q. and Wu, C.J. (2021). "Granular discrete element simulation of the evolution characteristics of the shear band in soil–rock mixture based on particle rotation analysis", *Environmental Earth Sciences*, 80(6), 1-14.

Zhao, S. and Zhao, J. (2021). "SudoDEM: Unleashing the predictive power of the discrete element method on simulation for non-spherical granular particles", *Computer Physics Communications*, 259, 107670.

Investigating the Effect of Compaction Level and Aggregate Grading of Stone Materials in Base Layer on Bitumen Penetration Rate

Goli, A.[1*] , Hooshangi, H.[2] and Kazemi, M.[3]

[1] Assistant Professor, Department of Civil and Transportation Engineering, University of Isfahan, Isfahan, Iran.
[2] M.Sc., Graduate Research Assistant, Eskan Deh Road Construction Company, Isfahan, Iran.
[3] Ph.D. Student, Civil Engineering, Arizona State University, Tempe, USA.

ABSTRACT: One of the layers that is applied on the base layer in asphalt pavements and increases the cohesion between the two layers, is the prime coat layer. Due to the fact that there are usually problems with the prime coat penetration into the base layer and penetration is not usually done well, there is a need to identify the factors affecting the penetration into the base layer. In this study, the penetration rate of prime coat coatings made of emulsified bitumen CSS-1h on the grain base level with different aggregate grading (aggregation close to the lower, middle and upper limits in two different types of aggregate grading) and different compaction levels were examined. Optimum water content, density, California Bearing Ratio (CBR) and the permeability of the samples were also examined. According to the results, the compressive strength of stone materials samples increases with approaching the upper limit (fine grain) and increasing the compaction. Also, increasing the grain size and decreasing compaction, increases the prime coat penetration rate, so that the 90% compacted sample with aggregate grading Type 3 has the highest penetration rate. The effect of moisture is obvious on the prime coat penetration, so that prime coat penetration rate is greatly reduced in saturation mode, but moisture in the base layer can help the prime coat to penetrate into the base layer.

Keywords: Aggregate Grading, Base Layer, Compaction, Emulsified Bitumen, Penetration, Prime Coat.

1. Introduction

Iran, like many other countries, uses asphalt pavement. Due to the scarcity of oil resources and environmental protection, the preservation of asphalt layers reduces environmental and economic concerns. One of the approaches to increase the life of asphalt pavements is to improve their engineering performance. (Taherkhani, 2016). In general, The structure of asphalt pavement is a multilayer system (Zhang et al., 2017) and the stress-strain division of the pavement is related to the property of the bonding interface. (Bastidas-Martínez et al., 2020; Hu et al., 2017). Asphalt mixtures

---

* Corresponding author E-mail: a.goli@trn.ui.ac.ir

are usually used in the upper layers of flexible pavements and the protection of the underlying layers against traffic loads and environmental conditions as well as creating a quality surface is one of the most important tasks of asphalt mixtures. (Taherkhani and Afroozi, 2017). Among the pavement layers, the base layer plays an important role in the expression of pavement performance. This layer has a significant role in the distribution of the applied load from the surface to the subgrade layer, so that the transferred stress to the sub-base and subgrade layer reduces (Huang, 2004). Therefore, this layer must have high resistance. Materials aggregate grading is one of the most important factors that affects its resistance and compressive strength (Chhorn and Lee, 2018; Šernas et al., 2020; Xu et al., 2018), and for this reason, different standard aggregate grading are defined in pavement standards regulations for different types of base layers. These aggregate grading are determined by several factors, such as the type of pavement, the type and location of the desired layer in the pavement system, the thickness of the layer and the size of the maximum aggregate diameter (AASHTO, 2013).

To prepare and spread the asphalt layer on the base layer, a layer of bitumen with low viscosity is distributed on the base surface, which is called prime coat (Cross et al., 2005). Distributed bitumen penetrates into the pores of stone materials, and it will facilitate the cohesion of the asphalt layer to the materials under, as well as integrating and consolidating the materials. It also isolates the base layer and binds loose aggregates to each other, providing a uniform surface so that its status does not change during asphalt paving (Chun et al., 2017; Ouyang et al., 2020). Due to the environmental harms of cut-back bitumen, emulsified bitumen is usually used to apply this layer (Slaughter, 2004). Emulsified asphalt is selected with different de-emulsification speed, different viscosity and different asphalt content according to

different types of base (Wang et al., 2017). Due to the importance of the aggregate grading in the base layer and the role of the prime coat in the proper performance of the pavement layer, there is a need for research on the factors affecting the penetration and diffusion of the prime coat layer.

Research and publications in the field of the prime coat has been summarized to a limited number of researches, most of which express its methods and practical points. In these researches, little investigations have been done on the factors affecting the penetration of the prime coat. In this context, the instructions provided by Cross and Shrestha (2005) for single coat and prime coat layers investigated how and when to use these bitumen layers, especially when you need to use prime coat layer, and expressed the types and extent of used materials. One of the significant results has been the importance of proper penetration of the prime coat in creating high performance (Cross et al., 2005). Mohan et al. investigated the penetration rate and cohesion resistance of different types of prime coats on the grain basis. In this research, broken limestone materials were used to construct the base layer, afterwards bitumen was added to the layer in two fashions of spraying and mixing to evaluate the effect of bitumen distribution type. After the experiments, they stated that the best prime coat among the used prime coats were Terra Prime and MC-30 (Mohan et al., 2013). The National Institute for Transport and Road Research (NITRR) states that due to the importance of the prime coat penetration, the prime coat must be able to wet and penetrate the soil layer on the grain basis and create a layer with high cohesion on the basis. Also, the penetration depth depends on the base layer compaction, and the higher the compaction, the lower the penetration rate (Freeman et al., 2010). Furthermore, according to Vignarajah et al. (2007)'s research, prime coat penetration into the base layer depends on various factors such as the prime coat implementation method, bitumen type, base

layer materials, construction method, base layer implementation and base layer permeability. Also, Mantilla and Button (1994) examined the permeability of two types of MC-30 soluble bitumen and two types of emulsified bitumen in different water contents, which showed the penetration rate to be higher than 5 mm in all cases and the two soluble bitumen had the highest penetration rate. Furthermore, Ishai and Livneh (1984) noted less penetration of emulsified bitumen comparing to soluble bitumen, however, the penetration rate of emulsified bitumen was satisfactory. Kucharek et al. (2008) conducted some researches on solvent-free emulsified bitumen and their permeability into grain materials. After making several samples of solvent-free emulsified bitumen, they conducted some experiments such as modified sand penetration tests to evaluate the duration and depth of emulsified bitumen penetration into grain materials with different aggregate grading, compaction levels and moisture values. Finally, the best formulation for making emulsions was reported according to their permeability.

Ouyang et al. (2020) made solvent-free emulsified bitumen, using changes in emulsified bitumen components (such as emulsifiers, bitumen and wetting agents) that affect the particle size of emulsified bitumen and its viscosity, and examined their penetration into the base layer. The results of their experiments have shown that adding wetting agents to the emulsified bitumen can greatly increase the penetration depth of bitumen, and adding emulsifiers will reduce the particle size, which can improve the permeability of the emulsified bitumen.

In this study, which was conducted to investigate the effect of aggregate grading and compaction of the base layer on the emulsified bitumen penetration, firstly, by conducting various experiments, rock mixtures characteristics (optimum water percentage, density, California Bearing Ratio (CBR), and permeability) prepared by two types of aggregate grading as stated in AASHTO Guidance (Transportation Officials, 1993) for stone base layers (aggregate grading Types 3 and 4) is obtained in three aggregate grading limits (lower, middle, upper) and finally the emulsified bitumen absorption rate is investigated in samples made.

2. Materials and Methods

2.1. Materials

The aggregates used to make the base layer samples were limestone aggregates, which are commonly used in pavement layers construction (Behbahani et al., 2020; Motamedi et al., 2021). The bitumen used for the prime coat was slow setting emulsified bitumen CSS-1h, the characteristics of which are given in Table 1. The samples required for the experiments were made according to the aggregate grading shown in Table 2 and Figures 1 and 2.

Table 1. Characteristics of the emulsified Bitumen used for prime coat

No.	Tests title		Standard range		Result	Tests method
			Min	Max		
1	Say bolt viscosity at 25°C, (s)		20	100	**20**	ASTM D88/ISIRI20644
2	Say bolt viscosity at 50°C, (s)		20	100		ASTM D88/ISIRI20644
3	Storage stability		--	0.1	**0.05**	ASTM D6930/ISIRI 20637
4	Sieve test		--	0.1	**0.03**	ASTM D6933/ISIRI20638
5	Cement mixing of emulsified bitumen (%)		--	2	**1**	ASTM D244 /ISIRI 13581
6	Residue by distillation (%)		57	--	**62**	ASTM D6997/ISIRI13580
7	Particle charge		Cationic/Anionic		**Cationic**	ASTM D244/ISIRI3580
8		Penetration, 0.1 mm, @25 °C	100	250	**120**	ASTM D5/ISIRI 2950
9	Test on residue	Ductility, cm, @25 °C	40	--	**110**	ASTM D113/ISIRI 3866
10	after TFOT	Solubility in TCE wt (%)	97.5	--	**98.7**	ASTM D2042/ISIRI 2953

Table 2. Standard limit for base layer for aggregate curve

Sieve size	Passing (%)	
(mm)	Type III	Type IV
50	100	--
37.5	--	100
25	75-95	70-100
19	--	60-90
9.5	40-75	45-75
4.75 (#4)	30-60	30-60
2 (#10)	20-45	20-50
0.425 (#40)	15-30	10-30
0.075 (#200)	2-8	2-8
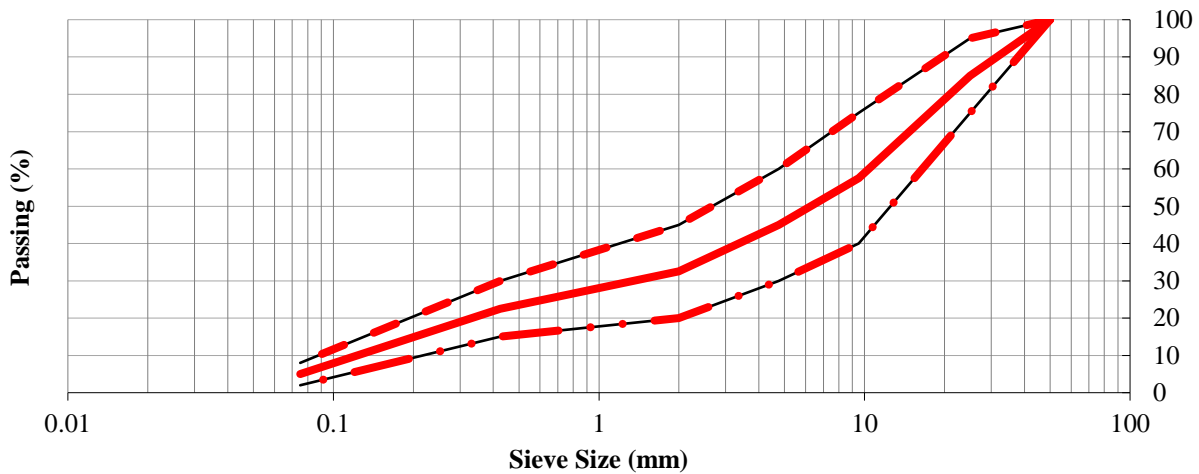
Fig. 1. Aggregation diagram Type 3 (lower, middle, upper limits)
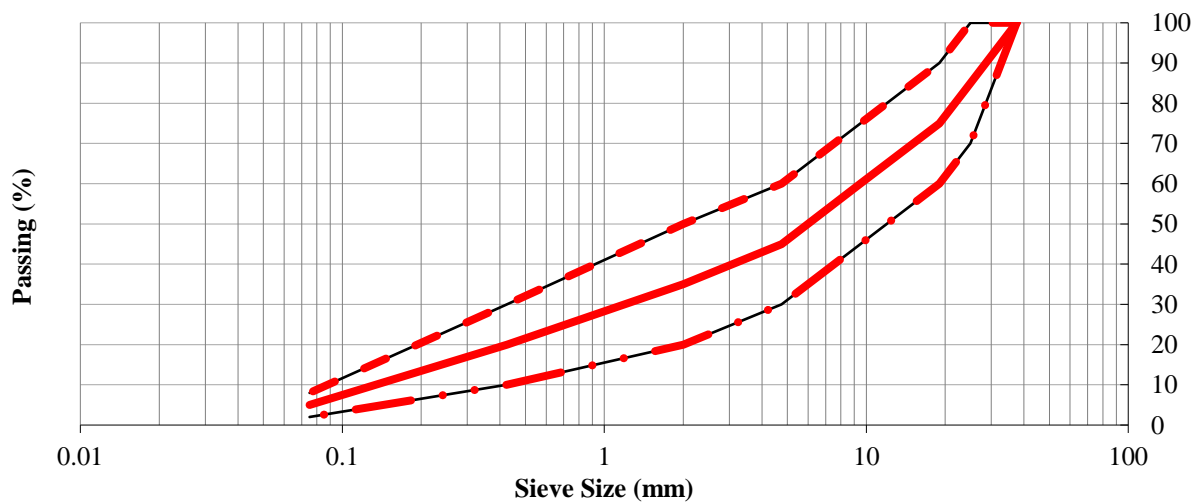
Fig. 2. Aggregation diagram Type 4 (lower, middle, upper limits)

2.2. Compaction and Density Test

In this experiment, which is based on the AASHTO-T265 (Standard AASHTO, 2009), the samples were compacted by 56 hammer blows weighing 4.54 kg from a 457 mm height. After compaction, the mold and compacted wet soil are weighed with an accuracy of 5 g and then, the sample is extracted from the mold and cut vertically from the middle. After which dry density and water content are obtained by Eqs. (1) and (2).

$$W = \frac{W_1}{\omega + 100} \times 100 \tag{1}$$

$$\omega = \frac{A - B}{B - C} \times 100 \tag{2}$$

where ω: is the sample water content, A and B: are the weight of wet and dry soil with mold, respectively, C: is the weight of the mold, and W and W_1: are dry and wet compacted soil (kg/m^3), respectively.

2.3. CBR Test

In this experiment, which is based on the ASTM D 1883-16 (ASTM, 2016), the samples were first compacted by the modified compression method (ASTM D, 2000) and then were loaded. Finally, the CBR rate of each sample was obtained by Eq. (3).

$$CBR = \frac{P_{0.1}}{P} \times 100 \qquad (3)$$

where $P_{0.1}$: is the corrective pressure and P: is the standard pressure.

2.4. Optimum Water Content Test

The maximum laboratory specific gravity of a rock mixture depends on the material, water content and compaction test method. This experiment is conducted according to the AASHTO T99-10 Standard (2015), so that first, a sample of the desired stone materials in different water contents is pounded and compacted in the laboratory, then the maximum dry specific gravity is obtained by drawing the compaction curve of the stone materials. The water content in which the dry specific gravity of the stone materials is maximal is called optimum water content.

2.5. Permeability Test

Permeability is the ability of water to flow through saturated soil. The parameter that expresses the permeability rate of soil is called permeability coefficient or hydraulic conductivity coefficient. In this study, the permeability rate was assessed by performing a falling head test. In this test, the water level in a small diameter pipe drops (from the initial value h_0 to the final value h_f) and the time it takes for the water to reach h_f height from h_0 height is measured. The permeability coefficient is calculated using Eq. (4).

$$K = 2.3 \frac{a \times L}{A \times t} log \frac{h_0}{h_f} \qquad (4)$$

where K: is the permeability coefficient (cm/s), A: is a pipe inside the cross-sectional area (cm^2), L: is the sample length (cm), h_0 and h_f: are the initial and final height of water in the pipe (cm), respectively, and t: is the recorded time to reach the water height from h_0 to h_f.

2.6. Prime Coat Penetration Test

To prepare the samples, the stone materials were compacted according to aggregate grading Types 3 and 4 of the base layer at 90%, 95% and 100% compaction levels in upper, middle and lower limits and kept in laboratory conditions for 72 hours. After 72 hours of making the samples, the samples are prepared in two modes of dry and wet due to the need to investigate the effect of moisture on the surface of the samples and to compare the bitumen penetration rate in two modes of dry and wet. To make the dry samples, the samples were placed in the open air to dry completely. To make the wet samples, the surface of the samples was saturated with a sprinkler and the additional water was collected by a sponge.

In the existing standards, the amount of bitumen for penetration coating is considered to be between 1600 to 2000 gr/m^2 according to the aggregation conditions. Due to the fact that different types of aggregate grading and compaction levels were investigated in this study and the surface of each sample had different absorption and penetration, the bitumen amount of each sample was calculated and distributed 35 gr according to the diameter of the molds. Finally, after spreading the emulsified bitumen on the surface, the prepared samples were kept in the laboratory for 92 hours to investigate the absorption and penetration of the emulsified bitumen. After the required time, the samples are taken out of the mold by a lifting jack and cut from the middle. Finally,

the amount of bitumen penetration into the samples with different aggregate grading and compaction levels were measured.

3. Results and Discussion

3.1. Density

Dry density values of the base layer with aggregate grading Types 3 and 4 for different types of compaction levels and corresponding to the upper, middle and lower limits can be seen in Figure 2. As shown in Figure 2, the maximum dry density of the samples (γ_{dmax}) decreased with decreasing compaction in all the samples. It is quite natural that the compaction of the samples will decrease due to the lower density. Also, in all samples, the aggregation curve of the upper limit has a higher dry density. Because the upper part of the aggregation curve has finer materials. As a result, the void space in stone materials decreases during the compaction and the dry density of the samples (γ_{dmax}) increases.

3.2. The Effect of Aggregate Grading

and Compaction Level on CBR

According to ASTM D1883-16 (ASTM, 2016), the CBR value of the compacted base layer should not be less than 80%. According to Figure 5, all samples with aggregate grading Type 3 had higher values than the specified minimum CBR and had a good compressive strength. It can be concluded that the higher the grain size and compaction, the higher the CBR.

In samples with aggregate grading Type 4, only samples with 100% compaction in all the aggregation limits have the minimum CBR, and in other cases, only the middle and upper limits of 95% compaction and the upper limit of 90% compaction pass the minimum standard. The trend of CBR rate changes in this type of aggregate grading, just as aggregate grading type 3, increases with an increase in compaction and moving of the aggregation towards a smaller size. Comparing the two types of aggregate grading, it can be seen that the samples with aggregate grading Type 3 have a higher compressive strength in all studied cases.

(a)

(b)

(c)
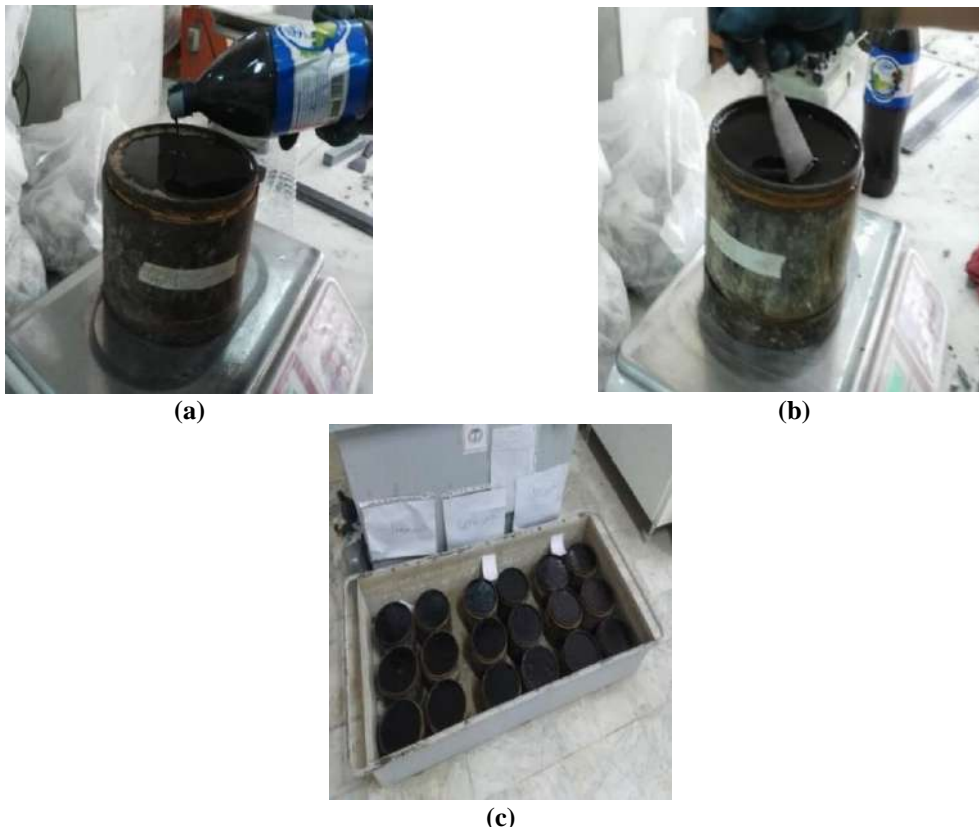
Fig. 3. Bitumen penetration test: a) Spraying bitumen on the surface to the standard level; b) Bitumen distribution; and c) Placement on the surface of the sample for prime coat penetration
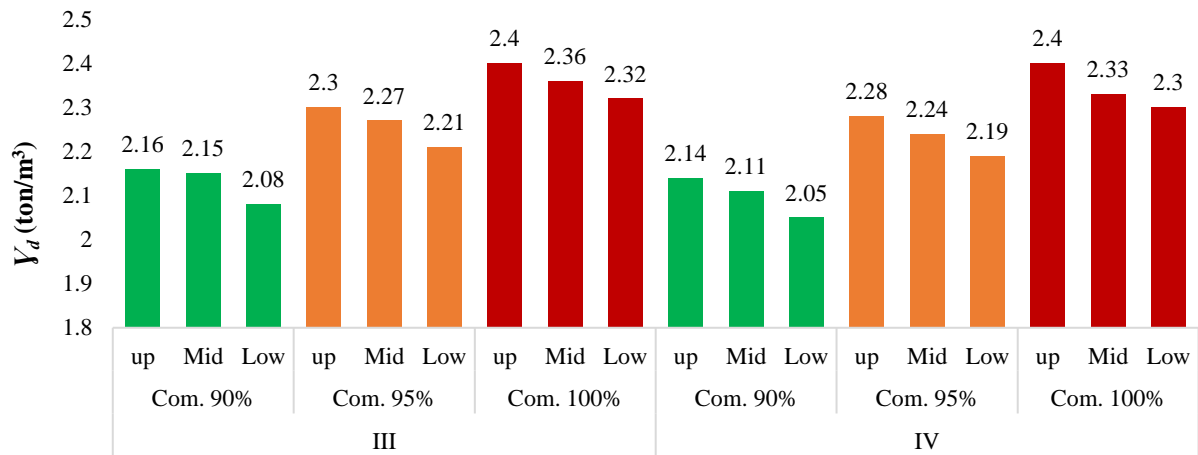
Fig. 4. The density of the base samples in different aggregate grading and compaction levels
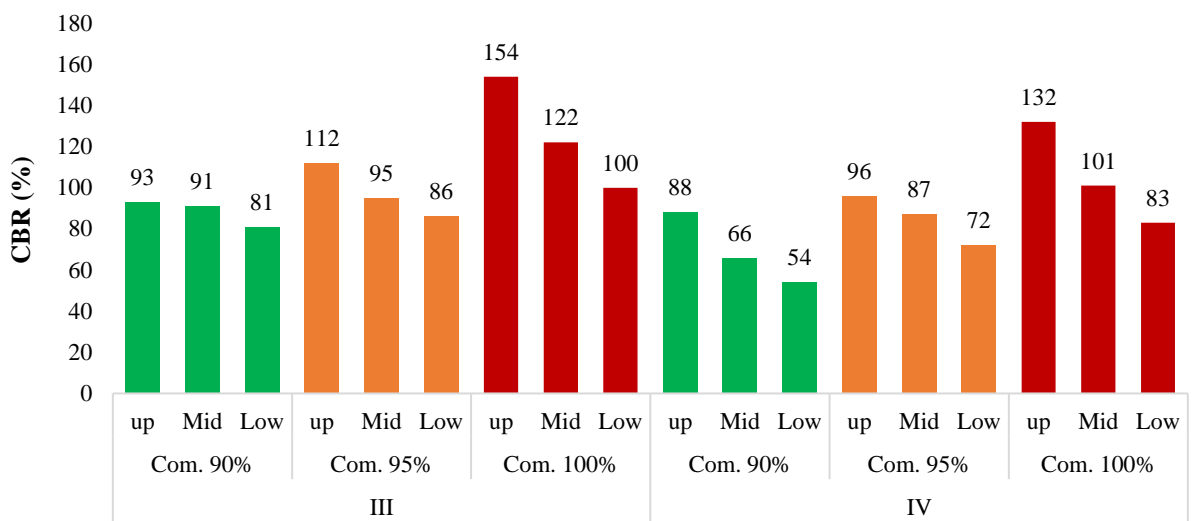
Fig. 5. The CBR of the base samples in different aggregate grading and compaction levels

3.3. The Effect of Aggregate Grading on Optimum Moisture

Comparing the data obtained from the optimum moisture experiment (Figure 6) showed that the closer the aggregate grading is to the upper limit of the aggregation diagrams (the finer the aggregate grading), the higher the optimum moisture percentage. This can also be seen in the aggregate grading change from Type 3 (coarse grain) to Type 4 (finer grain). The reason is that as the aggregate grading becomes smaller, the specific surface of the material increases, and as a result, more moisture is needed in order to moisten the surface of the stone material.

3.4. The Effect of Aggregate Grading and Compaction Level on Permeability

As can be seen in Figure 7, in the samples made according to aggregate

grading Type 3, the permeability coefficient is higher in all compaction levels (90, 95 and 100 percent) and the permeability rate has decreased as it approaches the upper limit of the diagram. In other words, the larger the grain size of the sample, the higher the permeability coefficient. As the compaction increases, the amount of cavities between the soil layers and the compaction decreases. According to the penetration rate of the prime coat in samples with aggregate grading Type 4, it can be stated that bitumen penetration coefficient has increased with increasing compaction and reduction of aggregate size (approaching the upper limit) in this type of samples. By comparing the samples with aggregate grading Types 3 and 4, it can be stated that due to the finer nature of Type 3 samples, the penetration coefficient has been lower.
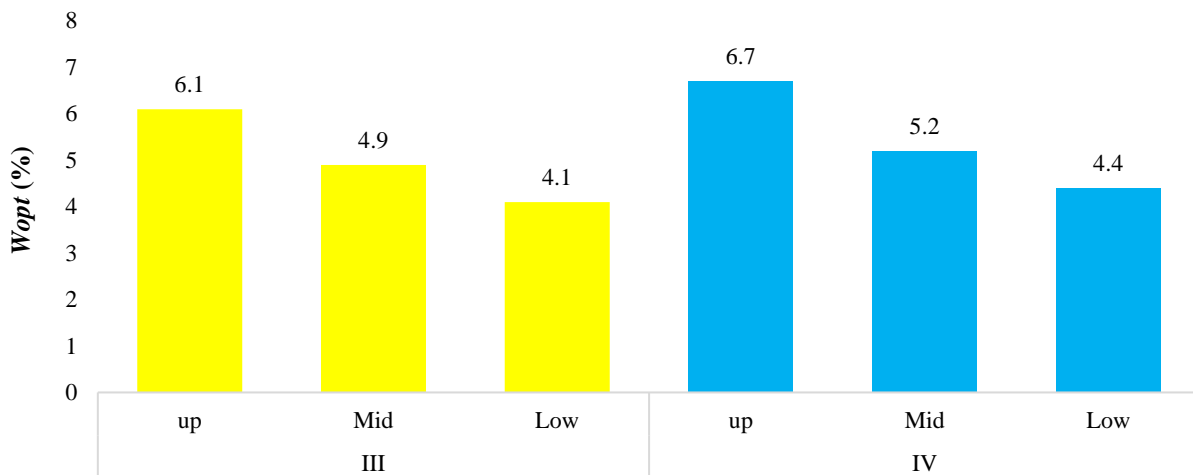
Fig. 6. Optimum moisture of the base samples with different aggregate grading
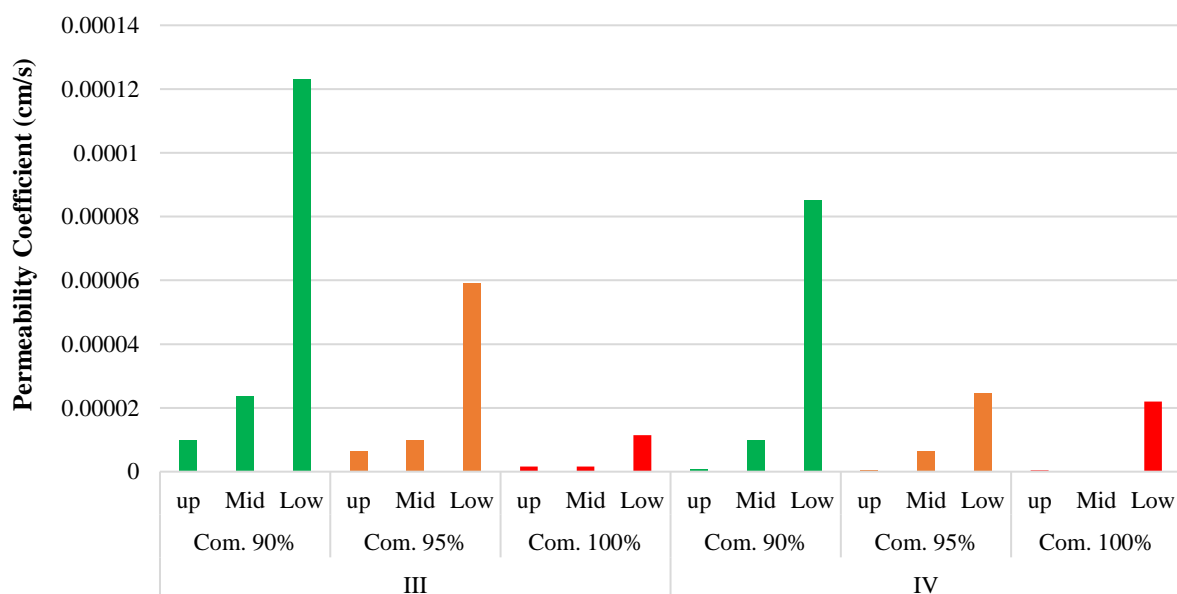
Fig. 7. Permeability of the base samples with different aggregate grading and compaction levels

3.5. Prime Coat Penetration on Dry and Wet Conditions

Figure 8 shows that samples with less compaction have higher bitumen penetration rate. Increasing the grain size in this type of aggregate grading (approaching lower limit) has led to an increase in the penetration rate. Aggregate grading Type 4 is similar to the trend of Type 3, so that the penetration rate has decreased by increasing compaction and decreasing aggregation rate. By comparing the two types of aggregate grading, it can be seen that this bitumen penetration rate in Type 4 was less than Type 3, in all compaction levels and aggregate grading, and this is due to the finer grain size of type 4.

According to Figure 9, it can be stated that the penetration rate of emulsified bitumen into the base layer has decreased by increasing the compaction and also the penetration rate has decreased by approaching the upper limit and decreasing the aggregate size. A similar trend is seen in aggregate grading Type 4 in terms of penetration due to the compaction rate and type of aggregation. Aggregate grading Type 3 has more permeability for emulsified bitumen in wet condition. By comparing wet and dry conditions in both aggregate grading (Figures 8 and 9), it can be stated that the moisture of the base layer improves the penetration rate of emulsified bitumen in all compaction levels and aggregate grading.
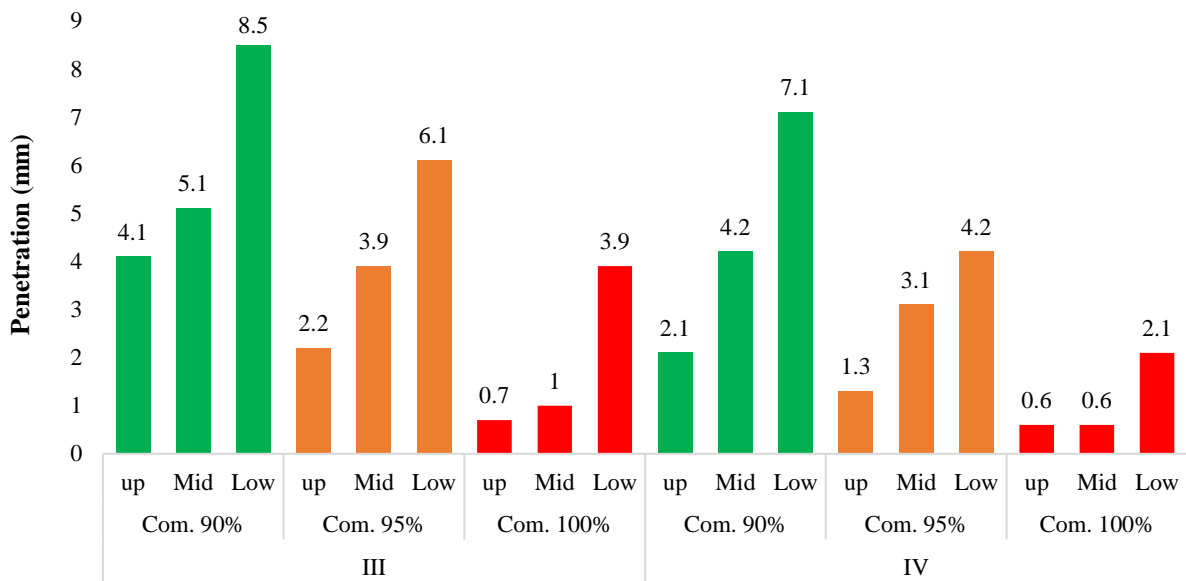
Fig. 8. Prime coat penetration rate in the base samples with different aggregate grading and compaction levels on dry condition
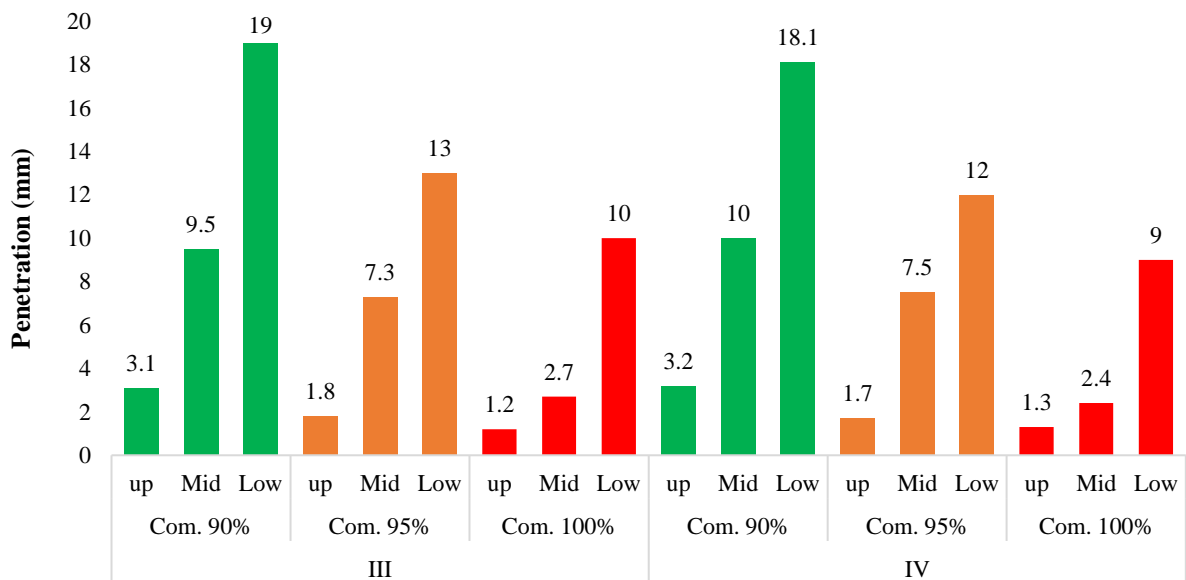
Fig. 9. Prime coat penetration rate in the base samples with different aggregate grading and compaction levels on dry condition

4. Conclusions

In this study, first the characteristics such as density, optimum CBR moisture and permeability of the samples with different compaction levels and aggregate grading were measured, and then the penetration rate of emulsified bitumen CSS-1h was investigated as a prime coat coating in samples with different compaction levels and aggregate grading, in order to evaluate the penetration rate of prime coat coatings in the grain base layer. The results of the experiments are as follows:

- With decrease in aggregation, the density and optimum water content of the samples increase. Also, increase in the compaction level increases the density of the samples.
- Samples with aggregate grading Type 3 have sufficient compressive strength in all aggregate boundaries and this resistance increases with decreasing the aggregation size (approaching upper limit) and increasing the compaction level, but in samples with aggregate grading Type 4, only samples with a 100% compaction have the required

compressive strength in all aggregate boundaries and only finer-grained samples retain their compressive strength by reducing the compaction level.

- Decreasing the grain size has reduced the permeability of the samples, but as the compaction increases, the permeability of the samples decreases.

- Coarse-grained samples (aggregate grading Type 3 or aggregation near the upper limit) and lower compactions have higher bitumen penetration on dry condition, which means that the prime coat penetration increases if the moisture increases in these samples.

5. References

AASHTO T99-10 Standard. (2015). *99: Moisture-density relations of soils using a 2.5-kg (5.5-lb) rammer and a 305-mm (12-1 in.) drop*, Standard Specifications for Transportation Materials and Methods of Sampling and Testing 2.

AASHTO (2013). *Sizes of aggregate for road and bridge construction (M 43-05)*, AASHTO, Washington, DC.

ASTM, D. (2000). *1557: Standard test methods for laboratory compaction characteristics of soil using modified effort (56,000 ft-lbf/ft³ (2,700 kN-m/m³))*, Annual Book of ASTM Standards, ASTM International, West Conshohocken, PA, United States.

ASTM, D1883-16 (2016). *Standard test method for California bearing ratio (CBR) of laboratory-compacted soils*, West Conshohocken, PA, United States.

Bastidas-Martínez, J.G., Ruge, J.C., Paba, I.J., Vasquez, F. and Rojas Suárez, J.P. (2020). "Physical mechanical performance of asphaltic emulsions in road oil for flexible pavements", *Journal of Physics: Conference Series,* 1645, 012011.

Behbahani, H., Hamedi, G.H. and Najafi Moghaddam Gilani, V. (2020). "Predictive model of modified asphalt mixtures with nano hydrated lime to increase resistance to moisture and fatigue damages by the use of deicing agents", *Construction and Building Materials,* 265, 120353.

Chhorn, C. and Lee, S.W. (2018). "Influencing compressive strength of roller-compacted concrete", *Proceedings of the Institution of Civil Engineers - Construction Materials,* 171(1), 3-10.

Chun, S., Kim, K., Park, B. and Greene, J. (2017). "Evaluation of structural benefits of prime coat application for flexible pavements using accelerated pavement testing (APT)", *KSCE Journal of Civil Engineering,* 21(1), 141-149.

Cross, S.A., Voth, M.D. and Shrestha, P.P. (2005). "Guidelines for prime coat usage on low-volume roads", *Transportation Research Record,* 1913(1), 117-125.

Freeman, T.J., Button, J.W. and Estakhri, C.K. (2010). "Effective prime coats for compacted pavement bases", No. FHWA/TX-10/0-5635-1. 2010.

Hu, X., Lei, Y., Wang, H., Jiang, P., Yang, X. and You, Z. (2017). "Effect of tack coat dosage and temperature on the interface shear properties of asphalt layers bonded with emulsified asphalt binders", *Construction and Building Materials,* 141, 86-93.

Huang, Y.H. (2004). *Pavement analysis and design*, Second Edition, Pearson Publication.

Ishai, I. and Livneh, M. (1984). "Functional and structural role of prime coat in asphalt pavement structures", In: *Association of Asphalt Paving Technologists Proceedings*, Vol. 53, 98-118.

Kucharek, A.S., Eng, P., Scarborough, O., Davidson, J.K. and Kennedy, M. (2008). "Development of a solvent-free asphalt emulsion for prime coats and granular sealing", In: *Proceedings of the Fifty-third Annual Conference of the Canadian Technical Asphalt Association (CTAA) Canadian Technical Asphalt Association (CTAA),* 84-102.

Mantilla, C.A., and Button, J.W. (1994). *Prime coat methods and materials to replace cutback asphalt*, Technical Report, Report No. FHWAffX-94/1334-lF, U.S. Department of Transportation, Virginia.

Mohan, G., Yildirim, Y., StokoeII, K.H. and Erten, M.B. (2013). "Engineering properties of prime coats applied to a granular base", *Journal of Testing and Evaluation,* 41(5), 713-718.

Motamedi, H., Amiri, H.R., Fazaeli, H. and Mohammad Aliha, M.R. (2021). "Providing a prediction model for stress intensity factor of fiber-reinforced asphalt mixtures under pure mode III loading using the Edge Notched Disc Beam (ENDB)", *Civil Engineering Infrastructures Journal,* 54(1), 43-58.

Ouyang, J., Sun, Y. and Zarei, S. (2020). "Fabrication of solvent-free asphalt emulsion prime with high penetrative ability", *Construction and Building Materials,* 230, 117020.

Šernas, O., Zofka, A., Vaitkus, A. and Gražulytė, J. (2020). "The effect of exposed aggregate concrete gradation on the texture characteristics and durability", *Construction and Building Materials,* 261, 119921.

Slaughter, G. (2004). "Environmental comparison of cutback bitumen and bitumen emulsions for sealing roads", *Towards Sustainable Land*

Transport Conference, Wellington, New Zealand.

Standard, A.A.S.H.T.O. (2009). *T265: Standard method of test for laboratory determination of moisture content of soils*, Standard Specifications for Transportation Materials and Methods of Sampling and Testing. American Association of State Highway Officials, Washington.

Taherkhani, H. (2016). "Investigating the effects of nanoclay and nylon fibers on the mechanical properties of asphalt concrete", *Civil Engineering Infrastructures Journal,* 49(2), 235-249.

Taherkhani, H. and Afroozi, S. (2017). "Investigating the performance characteristics of asphaltic concrete containing nano-silica", *Civil Engineering Infrastructures Journal,* 50(1), 75-93.

Transportation Officials. (1993). *AASHTO Guide for design of pavement structures,* Vol. 1, Aashto. Washington.

Vignarajah, M., Leaverton, M. and Senadheera, S. (2007). *Constructability review of surface treatments constructed on base courses*, Technical Report, Report No. 0-5169-2, U.S. Department of Transportation, Virginia.

Wang, G., yi Wang, D. and ning Li, D. (2017). "Laboratory study and performance evaluation of a new type of prime coat material used on cement treated base", *Construction and Building Materials,* 147, 588-597.

Xu, G., Shen, W., Huo, X., Yang, Z., Wang, J., Zhang, W. and Ji, X. (2018). "Investigation on the properties of porous concrete as road base material", *Construction and Building Materials,* 158, 141-148.

Zhang, Q., Xu, Y.-h. and Wen, Z.-g. (2017). "Influence of water-borne epoxy resin content on performance of waterborne epoxy resin compound SBR modified emulsified asphalt for tack coat", *Construction and Building Materials,* 153, 774-782.

Reviewers

The Editorial Board of the Civil Engineering Infrastructures Journal (CEIJ) would like to express sincere thanks to all reviewers of papers submitted to CEIJ during 2021 and 2022 for their time and efforts in evaluating papers for this journal.

Rezaeian, A.
Shahid Chamran University of Ahvaz
Rezaie, F.
Bu-Ali Sina University
Roozbahany, A.
University of Tehran
Sadeghi Marzaleh, A.
Swiss Federal Laboratories for Material Science and Technology, EMPA
Salehi, S.
IA University, Garmsar Branch
Samui, P.
National Institute of Technology Patna
Sert, S.
Sakarya University
Seyedi Hosseininia, E.
Ferdowsi University of Mashhad
Shahir, H.
Kharazmi University
Sharbatdar, M.K.
Semnan University
She, G.L.
Harbin Institute of Technology, China
Shekarchi Zadeh, M.
University of Tehran
Soroushian, A.
International Institute of Earthquake Engineering and Seismology
Taleb Beydokhti, N.
Shiraz University
Taghaddos, H.
University of Tehran
Taherkhani, H.
University of Zanjan
Tariverdilo, S.
Urmia University
Tehranizadeh, M.
Amirkabir University of Technology
Toloukian, A.R.
Iran University of Science and Technology
Touran, A.
Northeastern University College of Engineering
Wagner, N.
Intes GmbH Stuttgart
Zahrai, S.M.
University of Tehran
Zamani Ahari, Gh.R.
Urmia University
Zhang, B.
Glasgow Caledonian University
Zhu, J.
Southeast University

AIMS AND SCOPE

Since the College of Engineering (Former Faculty of Engineering, FOE) of the University of Tehran has renewed its policy toward scientific publication, the Civil Engineering transaction of the well- built 45 years old Persian journal of *"Nashrieh Daneshkadeh Fanni"* is to be published in English and as separate independent journal with the name of ***Civil Engineering Infrastructures Journal***.

Civil Engineering Infrastructures Journal is an international journal which publishes high quality scientific papers in all areas of engineering and management of civil infrastructures. The civil infrastructures include, but are not limited to: buildings, bridges, dams, transportation systems, geotechnical structures, underground constructions, water distribution systems, offshore platforms, pipelines, ocean structures, airports and power plants.

The scope of this journal encompasses, but is not restricted to the following aspects of engineering and management of infrastructures:

- Mathematical modeling
- Computational and experimental methods
- Environmental Impact assessment
- Passive defense and security issues
- Monitoring and assessment
- Construction and design for durability
- Deterioration modeling and aging
- Failure analysis
- Field testing
- Financial planning
- Inspection and diagnostics
- Life-cycle analysis and prediction

- Maintenance, rehabilitation, repair and replacement strategies

- Non-destructive testing

- Optimization of maintenance and management

- Specifications and codes

- Reliability and risk management

- Supervisory Control and Data Assimilation (SCADA)

- Automation and Robotics in Construction

- Smart civil infrastructure Systems

- Sustainable civil infrastructure systems

- Case studies

Audiences of *Civil Engineering Infrastructures Journal* are researchers and practitioners as well as people working in infrastructure design, construction, maintenance and operation. Papers considered for publication must contain a clear and well-defined engineering component and make a significant contribution to the engineering and management of civil infrastructures. All articles submitted to this journal will undergo a rigorous peer review by anonymous independent experts.

Additional information can be obtained from:

Civil Engineering Infrastructures Journal

College of Engineering,

University of Tehran

P.O. Box: 11155- 4563

Tehran, Iran

Tel/ Fax: +98-21-88956097

Web Site: www.ceij.ir

Email: ceij@ut.ac.ir

University of Tehran
College of Engineering

Copyright Transfer Agreement

In order to protect the author(s), from the consequences of unauthorized use, the publisher requests that all author(s) sign the appropriate statement below:

The author(s) undersigned hereby approves submission of this work and all subsequent revisions for publication and transfers, assigns, or otherwise conveys copyright ownership to the Civil Engineering Infrastructures Journal (CEIJ). I (we) acknowledge that i) the submitted material represents original material, ii) does not infringe upon the copyright of any third party, and iii) that no part of the work has been published or under consideration for publication elsewhere unless and until it is rejected by Civil Engineering Infrastructures Journal (CEIJ). I (we) agree to indemnify the publisher against any loss or damages arising out of a breach of this agreement. In the event that my (our) submission is not published, copyright ownership shall revert to the author (s).

Manuscript Title:

Corresponding Author

Author:
Date: Signature;

Author:
Date: Signature:

Author:
Date: Signature:

Author:
Date: Signature:

CIVIL ENGINEERING INFRASTRUCTURES JOURNAL (CEIJ)

is indexed and abstracted in the bibliographical databases including:

Web of Science (ESCI)
http://science.thomsonreuters.com

Scopus
https://www.scopus.com
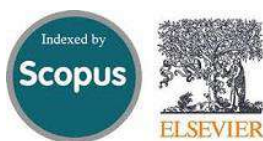
Islamic World Science Citation
Center;
http://www.isc.gov.ir

Directory of Open Access Journals
(DOAJ)
https://doaj.org

Google Scholar
https://scholar.google.com

General Impact Factor (GIF)
http://generalimpactfactor.com

Scientific Indexing Services (SIS)
http://www.sindexs.org

International Institute of
Organized Research (I2OR)
http://www.i2or.com

Information Matrix for the Analysis
of Journals (MAIR)
http://miar.ub.edu

ROAD: the Directory of Open
Access scholarly Resources
http://road.issn.org

Scientific World Index
http://www.sciwindex.com

International Innovative Journal
Impact Factor (IIJIF)
http://www.iijif.com

Science library index
http://scinli.com

Journal Factor
http://www.journalfactor.org

Open Academic Journals Index
(OAJI)
http://oaji.net

Electronic Journals Library (EZB)
https://rzblx1.uni-regensburg.de

Systematic Impact Factor
(SIF)
http://www.sifactor.org

COSMOS IMPACT FACTOR
http://www.cosmosimpactfactor.com

Polish Ministry of Science and
Higher Education (MSHE)
https://journals.indexcopernicus.com

Magiran
http://www.magiran.com

Scientific Information Database
(SID); Iran;
http://www.Sid.ir

CONTENTS: